INFN Istituto Nazionale di Fisica Nucleare

Phase a-2 Study Report
April 2009

asi agenzia spaziale italiana

GalileoGalilei (GG)

GG | A small satellite to test the equivalence principle of Galileo Newton and Einstein

ThalesAlenia Space
A Thales / Finmeccanica Company

Politecnico di Torino 1859 1906

ALTEC

DTM TECHNOLOGIES

INRiM Istituto Nazionale di Ricerca Metrologica

ALTA

In supremae dignitatis 1343
Università di Pisa

Niuna impresa, pur minima che sia
può avere
Cominciamento o fine
senza queste
Tre Cose: Senza Sapere
senza Potere
Senza con amore Volere.

(anonimo fiorentino, 1300)

GG | A small satellite to test the equivalence principle of Galileo Newton and Einstein

TABLE OF CONTENTS

EXECUTIVE SUMMARY .... **I**

1. SCIENTIFIC BACKGROUND **1**

2. SCIENTIFIC GOAL OF THE MISSION **6**

3. MISSION AND EXPERIMENT DESCRIPTION **10**

3.1 WHY TESTING THE EQUIVALENCE PRINCIPLE IN SPACE 10
3.2 THE GG EXPERIMENT CONCEPT 10
3.2.1 Passive electric grounding and the effect of electric charge patches 12
3.2.2 High frequency signal modulation with no signal attenuation 13
3.2.3 The PGB (Pico Gravity Box) space laboratory 14
3.2.4 Design of the GG differential accelerometer/s 16
3.2.5 Whirl motions and control 22
3.3 THE READ-OUT SYSTEM 23
3.4 VACUUM AT NO COST 25
3.5 SATELLITE AND ORBIT SELECTION 26
3.6 AIR DRAG: THE LARGEST EFFECT 28
3.7 BALANCING AND SIGNAL RECOVERY 29

4. EXPERIMENT DRIVERS AND REQUIREMENTS **31**

4.1 THE SIGNAL 32
4.2 EXTERNAL NON GRAVITATIONAL FORCES 33
4.3 TEST BODIES MASS MOMENTS 34
4.4 WHIRL MOTIONS 34
4.5 SATELLITE SPIN FREQUENCY 35
4.6 EARTH TIDES 35
4.7 TEMPERATURE 36
4.8 MAGNETIC COUPLING 36
4.9 ELECTRIC CHARGING 37
4.10 ERROR BUDGET 37

5. PAYLOAD DESCRIPTION **41**

5.1 PAYLOAD MAIN ELEMENTS 41
5.2 LOCK/UNLOCK MECHANISMS 45
5.3 THERMAL STABILIZATION AND CO-ROTATION 46
5.4 TEST MASSES MATERIALS 48

6. SATELLITE, ORBIT AND THE VEGA LAUNCHER **51**

6.1 LAUNCHER AND MISSION 51
6.2 SATELLITE MECHANICAL CONFIGURATION 55
6.3 THERMAL DESIGN AND ANALYSIS 60
6.3.1 TCS requirements 60
6.3.2 TCS description 60
6.3.3 Mathematical model descrption 61
6.3.4 Analysis results 66
6.3.5 Conclusions 70
6.4 ELECTRICAL AND ELECTRONIC DESIGN 71
6.4.1 On-board data handling 71
6.4.2 Electrical power system 74
6.5 TELECOMMUNICATIONS 77
6.6 BUDGETS 79
6.6.1 Mass properties 79
6.6.2 Power budgets 82
6.6.3 Data budgets 83

7. ALGORITHMS AND TECHNOLOGIES FOR FINE DRAG COMPENSATION ... 84
7.1 INTRODUCTION ... 84
7.2 FUNCTIONAL AND PERFORMANCE REQUIREMENTS ... 84
7.3 THE SIMPLIFIED MODEL ... 84
7.4 ARCHITECTURE AND ALGORITHMS FOR THE DRAG COMPENSATION ... 88
7.5 REQUIREMENTS FOR SENSORS AND ACTUTAORS ... 92
7.5.1 Rate sensors ... 92
7.6 TECHNOLOGIES ... 93
7.6.1 Actuators for fine drag compensation ... 93
7.7 SPIN RATE SENSORS ... 100
7.8 SIMULATION RESULTS ... 101
7.8.1 Simulated perturbing force ... 101
7.8.2 XY state variable trajectory without whirl and drag controls ... 102
7.8.3 XY state variables trajectory with whirl control and without drag control ... 104
7.8.4 XY state variables trajectory with whirl and drag controls ... 106
7.9 CONCLUSIONS ... 110
8. SPACE EXPERIMENT SIMULATOR ... 111
8.1 GG SIMULATOR BLOCK DIAGRAM ... 114
8.2 SIMULATOR REFERENCE FRAMES ... 115
8.2.1 Inertial Reference Frame – IRF – ... 115
8.2.2 Local Vertical Local Horizontal Reference Frame – LVLH – ... 116
8.2.3 Body Fixed Reference Frame – BF – ... 117
8.3 SIMULATOR ENVIRONMENT MODULE ... 118
8.4 SIMULATOR DYNAMICS MODULE ... 119
8.5 POST-PROCESSING MODULE ... 124
8.6 EXAMPLE OF A SCIENCE PERFORMANCE SIMULATION ... 125
8.6.1 Satellite acceleration in the LVLH reference frame ... 127
8.6.2 PGB-s/c displacement ... 128
8.6.3 Common mode motion of the test masses ... 129
8.6.4 Differential mode motion of the test masses ... 133
8.7 DYNAMICS RANGE OF THE SIMULATOR ... 135
8.8 CONCLUSIONS ... 136
9. PAYLOAD LABORATORY PROTOTYPE ... 137
9.1 GGG (“GG ON THE GROUND”) VS GG: SIMILARITIES AND DIFFERENCES ... 137
9.2 CAPACITANCE BRIDGE TRANSDUCERS, READ-OUT SYSTEM AND ELECTRONIC NOISE ... 141
9.3 MEASURED Q ... 144
9.4 WHIRL MOTIONS CONTROL ... 145
9.5 EXPERIMENTAL EVIDENCE FOR SELF-CENTERING ... 148
9.6 UNIFORMITY OF ROTATION ... 150
9.7 DEALING WITH TERRAIN TILTS ... 151
9.8 MEASURING ELECTRIC CHARGE SURFACE PATCHES ... 156
9.9 GGG SENSITIVITY TO LOW FREQUENCY DIFFERENTIAL EFFECTS ... 157
9.10 ADVANCED GGG UNDER CONSTRUCTION ... 159
10. THE GROUND SEGMENT ... 162
10.1 KEY GG OPERATIONS REQUIREMENTS ... 162
10.2 GROUND SEGMENT DESCRIPTION ... 163
10.3 USER SEGMENT DESCRIPTION ... 164
10.4 SCIENCE OPERATIONS AND SCIENCE MANAGEMENT PLAN ... 165
11. DEVELOPMENT, PROGRAMMATICS AND RISK ANALYSIS ... 168
11.1 SATELLITE DEVELOPMENT APPROACH ... 168
11.1.1 Development objectives and elements ... 168
11.1.2 Program flow ... 169
11.1.3 Model philosophy ... 170
11.1.4 Inertial Reference Frame – IRF – ... 170
11.2 PAYLOAD DEVELOPMENT PLAN ... 172

11.3 PLATFORM DEVELOPMENT PLAN 173
11.4 DEVELOPMENT PLAN FOR THE GROUND SEGMENT 174
11.5 DEVELOPMENT PLAN FOR THE USER SEGMENT 175
11.6 PROGRAM MANAGEMENT 175
11.7 MILESTONES AND MEETINGS PLAN 176
11.7.1 Phase B 176
11.7.2 Phase C/D 176
11.7.3 Phase E 177
11.7.4 Program milestone summary 177

12. REFERENCES 178

13. ACRONYMS AND ABBREVIATIONS 181

EXECUTIVE SUMMARY

GG is a small satellite which aims at testing the Equivalence Principle to 1 part in 10^{17} . It would improve by 4 orders of magnitude the best ground based laboratory tests as well as those based on Lunar Laser Ranging.

The Equivalence Principle is the founding pillar of General Relativity and testing it to very high accuracy is widely recognized as a crucial asset for fundamental physics beyond the current unsatisfactory framework. The inability so far to merge General Relativity with the Standard Model of particle physics, and the open problems of modern Cosmology –from dark matter to dark energy– all point to the need of putting General Relativity to the most stringent possible tests.

Space provides the most favorable conditions by far for testing the Equivalence Principle to very high accuracy. GG aims at reaching such a remarkable goal with a satellite carefully designed around a new concept instrument designed and optimized for this test. Overall, this makes the GG satellite small and in the low cost range. In addition, since it requires a low Earth equatorial orbit, it can be launched by VEGA (even in a dual launch) and operated from Malindi.

ASI has become interested in GG since 1996, when ESA was ready to provide financial support to a national mission devoted to testing the Equivalence Principle. At the time GG was a novel concept and it was not possible to provide sufficient experimental evidence. However, soon afterwards GG was selected as candidate for a small ASI mission, though it was not finally selected. Then, due to the difficulties emerged in procuring reasonably cheap launches in equatorial orbit, ASI funded an additional study of GG, in order to investigate the possibility to run the GG experiment in a high inclination sun synchronous orbit, for which cheaper launchers were available.

The subsequent interest of INFN in GG, made it possible to build up a dedicated laboratory for a full scale prototype of the GG payload (GG on the Ground-GGG). The GGG national experiment of INFN has provided increasing experimental evidence and a constantly improving sensitivity, even in the more hostile ground environment.

Due to these scientific results, and thanks to the support of the Italian Cosmology community, GG was included in the Piano Spaziale Nazionale of ASI 2006-2008, whereby the GG scientists and Thales Alenia Space-Italy have been supported for this Study

Throughout the GG studies, the contribution of Thales Alenia Space has been extremely important and of very high standard, thanks to their experience on fundamental physics missions and on the recently launched GOCE mission of ESA. The GG Simulator (based on the experience made with the GOCE Simulator) and the GG Drag free control –also based on heritage from GOCE– are by all standards, quite remarkable. Together with the GGG laboratory prototype, they provide strong confidence in the feasibility and success of GG.

Though the final conclusions will be presented only at the end of this Study, the GG satellite mission appears mature to enter a Phase B investigation.

1. SCIENTIFIC BACKGROUND

General Theory of Relativity (GTR) and the Standard Model (SM) of particle physics, taken together, form our current view of the physical world. While the former governs physics in the macroscopic and cosmic scales the latter governs the physics of the microcosm. According to GTR, gravity is not a force but a manifestation of space-time curvature. The relation between space-time curvature and space-time content (mass-energy and momentum) being given by Einstein's field equations. The theory has been extensively tested and no astronomical observation or experimental test (the most accurate of which have been performed in space) has been found to deviate from its predictions. Thus it is the best description we have of gravitational phenomena that we observe in nature. The Standard Model of particle physics gives a unified formalism for the other three fundamental interactions (strong, weak and electromagnetic) between the fundamental particles that make up all matter. It is a quantum field theory which is consistent with both Quantum Mechanics and Special Theory of Relativity. To date, almost all experimental tests of the Standard Model have also agreed with its predictions.

However, merging these two very successful theories to form a single unified theory poses significant difficulties. While in SM particle fields are defined on a flat Minkowski space-time, GTR postulates a curved space-time which evolves with the motion of mass-energy. The definition of a gravitational field of a particle, whose position and momentum are governed by the Heisenberg Uncertainty Principle, is unclear. In addition quantum mechanics becomes inconsistent with GTR near singularities. Attempts at reconciling these theories often lead to a violation of the Equivalence Principle on which GTR is based. Therefore tests of the Equivalence Principle address a crucial problem which is at the heart of fundamental physics today.

In addition, the need to understand the nature of dark matter, the recent remarkable discoveries of observational cosmology and the puzzle of dark energy, all indicate that physics beyond the Standard Model and the General Theory of Relativity is needed. Invoked by most astronomers, dark matter probably consists of undiscovered elementary particles whose aggregation produces the gravitational pull capable of holding together galaxies and clusters of galaxies. It should account for more than 20% of the total mass in the universe but is not understood as yet. Dark energy is an even deeper mystery. Recent measurements show that the expansion of the universe is speeding up rather than slowing down, thus contradicting the fundamental idea that gravity is always attractive and calling for the presence of an unknown form of energy (the "dark energy") –whose gravity is repulsive and whose nature determines the evolution of the universe– which should contribute by about 70% to its total mass.

The major questions now being asked about the universe at its two extremes –the very large and the very small– appear to be inextricably intertwined.

The National Research Council of the US National Academies has appointed a specific “Committee on the Physics of the Universe” to investigate the subject and advise the major national research funding agencies. The results of the panel’s work have been published in the book ”Connecting Quarks with the Cosmos: Eleven Science Questions for the New Century” [1].

The 3rd of the eleven questions identified in the book is “Did Einstein Have the Last Word on Gravity?” and reads:

“Black holes are ubiquitous in the universe, and their intense gravity can be explored. The effects of strong gravity in the early universe have observable consequences. Einstein’s theory should work as well in these situations as it does in the solar system. A complete theory of gravity should incorporate quantum effects—Einstein’s theory of gravity does not—or explain why they are not relevant.”

The last chapter of the book, under the title “Realizing the Opportunities”, is devoted to giving recommendations as to how to proceed in order to answer the 11 questions identified. The recommendations focus on very large scientific projects; however, a specific Section called “Striking the Right Balance” reads (p. 162):

“In discussing the physics of the universe, one is naturally led to the extremes of scale –to the largest scales of the universe as a whole and to the smallest scales of elementary particles. Associated with this is a natural tendency to focus on the most extreme scale of scientific projects: the largest space observatories, the most energetic particle accelerators. However, our study of the physics of the universe repeatedly found instances where the key advances of the past or the most promising opportunities for the future come from work on a very different scale. Examples include laboratory experiments to test gravitational interactions, theoretical work and computer simulations to understand complex astrophysical phenomena, and small-scale detector development for future experiments. These examples are not intended to be exhaustive but to illustrate the need for a balanced program of research on the physics of the universe that provides opportunities for efforts that address the scientific questions but that do not necessarily fit within major program themes and their related large projects.

Two of our scientific questions –"Did Einstein have the last word on gravity?" and "Are there additional space-time dimensions?"– are being addressed by a number of laboratory and solar-system experiments to test the gravitational interaction. Tests of the principle of equivalence using laboratory torsion balances and lunar laser ranging could constrain hypothetical weakly coupled particles with long or intermediate range. These experiments have reached the level of parts in 10^{13} and could be improved by another order of magnitude. Improvement by a factor of around 10^{5}

could come from an equivalence principle test in space. …….. null experimental results provide important constraints on existing theories, and a positive signal would make for a scientific revolution."

In addition to the "Committee on the Physics of the Universe", a Dark Energy Task Force (DETF) has been established in the US by the Astronomy and Astrophysics Advisory Committee and the High Energy Physics Advisory Panel to advise the Department of Energy, NASA and the National Science Foundation on future dark energy research. In 2006 the DETF published its final report [2], where the Executive Summary begins as follows:

"Over the last several years scientists have accumulated conclusive evidence that the Universe is expanding ever more rapidly. Within the framework of the standard cosmological model, this implies that 70% of the universe is composed of a new, mysterious dark energy, which unlike any known form of matter or energy, counters the attractive force of gravity. Dark energy ranks as one of the most important discoveries in cosmology, with profound implications for astronomy, high-energy theory, general relativity, and string theory.

One possible explanation for dark energy may be Einstein's famous cosmological constant. Alternatively, dark energy may be an exotic form of matter called quintessence, or the acceleration of the Universe may even signify the breakdown of Einstein's Theory of General Relativity. With any of these options, there are significant implications for fundamental physics. "

A few pages below, the Section of the Report on "Goals and Methodology for Studying Dark Energy" ends with the following sentence:

"Just as dark-energy science has far-reaching implications for other fields of physics, advances and discoveries in other fields of physics may point the way toward understanding the nature of dark energy; for instance, any observational evidence for modifications of General Relativity."

The principle of equivalence has historically played a major role in the development of gravitation theory. It is possible to ascribe two conceptually different kinds of mass to a body: an inertial *mass* and a gravitational *mass*. The inertial mass is the proportionality factor between a force (any kind of force) applied to the body and the acceleration it acquires in response to it in an inertial laboratory. The gravitational mass is a measurement of the property of the body to attract gravitationally any other body (gravitational *active* mass), or to be gravitationally attracted by any other body (gravitational *passive* mass). Assuming the validity of the action–reaction principle (which leads to conclude that the center of mass of an isolated system must move with constant velocity in an inertial frame of reference) also implies that the gravitational passive and active mass of a body must be the same. The gravitational mass is the analog in a gravitational field, of the electric charge in an electric field –it can be viewed as a gravitational charge– and it has no apparent relation (in spite of the name) with the concept of inertial mass. Using Newton's law of gravitation to write the equation of motion of a body of inertial mass m_i and gravitational mass m_g in the field of a source body of gravitational mass M_g (for instance, the Earth), if $m_i \propto m_g$ the resulting acceleration is the same for all bodies. With the measured value of the gravitational constant *G* and a proportionality factor +1 ($m_i = m_g$) , the local acceleration of gravity on the surface of the Earth –the same for all bodies regardless of their mass and composition– amounts to about 9.8 m/s^2. This is the so called Universality of Free Fall (UFF). No such thing holds for all other fundamental forces of Nature. For instance, a proton and an electron do not have –in the same electric field– the same (in modulus) acceleration, because the inertial mass of the proton is much larger than the inertial mass of the electron and no proportionality holds between the inertial mass of a body and its electric charge.

Galileo was most probably the first one to provide experimental evidence for the UFF [3]. However, he was not aware of the law which rules the gravitational interaction. Therefore, he had no awareness either of the equivalence between inertial and gravitational mass, and of the link between this concept and his own experimental results on the UFF. The fact that the two concepts of inertial and gravitational mass refer in fact to the same physical quantity was first stated by Newton in the opening paragraph of the *Principia* [4]: "*This quantity that I mean hereafter under the name of ... mass ... is known by the weight ... for it is proportional to the weight as I have found by experiments on pendulums, very accurately made... "*

At the beginning of the 20th century, almost 300 years since Galileo's work, Einstein realized that because of the proportionality between the gravitational mass and the inertial mass, the effect of gravitation is locally equivalent to the effect of an accelerated frame and can be locally canceled. This is known as the Weak Equivalence Principle (WEP) which Einstein introduced in 1907 [5] as the "hypothesis of complete physical equivalence" between a gravitational field and an accelerated reference frame: in a freely falling system all masses fall equally fast, hence gravitational acceleration has no <u>local</u> dynamical effects. Any test mass located inside the famous Einstein elevator –falling with the local acceleration of gravity g near the surface of the Earth– and zero initial velocity with respect to it, remains motionless for the time of fall. An observer inside Einstein elevator will not be able to tell, before hitting the ground, whether he is moving with an acceleration g in empty space, far away from all masses, or else he is falling in the vicinity of a body (the Earth) whose local gravitational acceleration is also g.

Einstein's formulation of the Weak Equivalence Principle whereby the effect of gravity disappears in a freely falling reference frame, holds only <u>locally</u>. The elevator is free falling <u>in the vicinity</u> of the Earth, which amounts to saying that the height of fall is much smaller than the radius of the Earth. The cancellation of gravity in a freely falling frame holds locally for each frame, but the direction of free fall is not the same in all of them. Which is a direct consequence of the fact that the gravitational field of a body (like Earth) is non uniform, giving rise to the so called tidal forces between test particles whose centers of mass are not coincident. With the WEP Einstein has moved from Newton's concept of one global reference frame with gravitational forces and the UFF, to many free falling local frames without gravitational forces.

In his further development of the General theory of Relativity Einstein formulated what is known as the Einstein Equivalence Principle (EEP), which is an even more powerful and far reaching concept. EEP states the following (see e.g.[6]): i) WEP is valid; ii) The outcome of any local non-gravitational experiment is independent of the velocity of the freely-falling reference frame in which it is performed (Local Lorentz Invariance); iii) The outcome of any local non-gravitational experiment is independent of where and when in the universe it is performed (Local Position Invariance). The Einstein Equivalence Principle –which assumes the weak one– is regarded as the "heart and soul" of the General Theory of Relativity because it is the validity of this "principle" to ensure the fact that in General Relativity the effects of gravity are replaced by a curved 4-dimensional space-time.

Quantitative comparisons between the "probing power" of equivalence principle tests and tests of the PPN-Parametrized Post Newtonian parameters (such as the Eddington parameter, best measured with the space mission Cassini [7]) have been performed [8,9]. They show the superior probing power (by several orders magnitude) of equivalence principle tests, thus indicating that a breakdown of General Relativity (if any) is more likely to be detected by putting to more and more stringent tests the foundations of the theory (hence the equivalence principle), rather then its numerous predictions.

2. SCIENTIFIC GOAL OF THE MISSION

From an experimental point of view, a violation of the Universality of Free Fall would invalidate the Weak Equivalence Principle, hence the Einstein Equivalence Principle, thus placing a limit on the validity of the General Theory of Relativity itself. This is the physical motivation behind a continuing interest within the scientific community worldwide in performing more and more accurate experimental tests of the UFF –on Earth and hopefully also in space.

In an experiment to test UFF the observable physical quantity is the differential acceleration Δa of two test masses of different composition, relative to each other, while falling in the gravitational field of a source body with an average acceleration a (also referred to as the "driving acceleration"). A deviation from UFF is therefore quantified by the dimensionless parameter

$$\eta = \frac{\Delta a}{a} \quad . \tag{2.1}$$

The finding of a value $\eta \neq 0$ would disprove the UFF and indicate a violation of the Weak Equivalence Principle on which General Relativity ultimately relies. Instead, $\eta = 0$ –as reported by all experiments so far– confirms the basic assumption of General Relativity. By writing the equations of motion of each individual test mass without assuming a priori the equivalence of their inertial and gravitational mass, the parameter η given by (1) becomes

$$\eta = \frac{2[(m_g/m_i)_A - (m_g/m_i)_B]}{[(m_g/m_i)_A + (m_g/m_i)_B]} \tag{2.2}$$

where subscripts A and B refer to the individual test masses and allow them to be distinguished by their different composition. This parameter η is also known as the Eötvös parameter and it has additional profound significance.

The total mass–energy of a body can be expressed as the sum of many terms, corresponding to the energy of all the conceivable interactions and components: $m = \Sigma_k m_k$. For instance, at the atomic level, the rest mass contributes (as a fraction of the total) for $\cong 1$; the nuclear binding energy for $8 \cdot 10^{-3}$ (for light elements), the mass difference between neutron and proton for $1.4 \cdot 10^{-3} (A-Z)/A$ (A being the number of protons plus neutrons and Z the number of protons in the nucleus), the electrostatic energy of repulsion in the nuclei for $6 \cdot 10^{-4} Z^2 A^{-4/3}$, the mass of electrons for $5 \cdot 10^{-4} Z/A$, the antiparticles for $\cong 10^{-7}$, the weak interactions responsible of β decay for 10^{-9} or less. For an extended spherical body of radius R and (homogeneous) density ρ, the gravitational self–energy contributes by the fraction

$-(4/5)\pi\rho GR^2/c^2$. The conventional Eötvös parameter (2.2) can therefore be generalized into:

$$\eta_k = \frac{2[(m_g/m_i)_{A_k} - (m_g/m_i)_{B_k}]}{[(m_g/m_i)_{A_k} + (m_g/m_i)_{B_k}]} \tag{2.3}$$

such that a non-zero value of η_k would define the violation of equivalence between the inertial and gravitational mass-energy of the k^{th} type. From the point of view of conventional field theory, the verification of all these separate "Equivalence Principles" corresponds to a very peculiar coupling of each field to gravity; whether and why it should be so in all cases is a mystery.

It is apparent from (2.1) that –for any given experimental apparatus– the larger the driving acceleration, the more sensitive the UFF test (hence the EP test) that it provides. In a Galileo-type mass dropping experiment the driving acceleration is the gravitational acceleration of the Earth along the local vertical ($9.8\,ms^{-2}$). If the test masses are suspended on a torsion balance the driving acceleration is $0.017\,ms^{-2}$ (at most) in the field of the Earth –directed along the North-South direction of the local horizontal plane– and $0.006\,ms^{-2}$ in the field of the Sun (with components along the North-South and East-West directions of the horizontal plane). Yet, the first experimental apparatus to provide very accurate EP tests (to $10^{-8}-10^{-9}$) was the torsion balance used by Eötvös [10] at the turn of the 20th century, and later on by his students to detect an EP violation in the field of the Earth. This is because torsion balances are extremely sensitive; moreover, they are inherently differential instruments, and although in reality perfect rejection of common mode effects is impossible, the advantages of a differential instrument for detecting differential accelerations are enormous.

The next leap in sensitivity (to $10^{-11}-10^{-12}$) came in the 60s and early 70s using again a torsion balance but also recognizing that by taking the Sun as the source mass rather than the Earth, any differential effect on the test masses of the balance would be modulated by the 24^{hr} rotation of the Earth on which the balance sits [11,12]. Indeed, the modulation frequency should be as high as possible, in order to reduce $1/f$ electronic noise. The best and most reliable results in EP testing (to about 1 part in 10^{13}) have been achieved by the "Eöt-Wash" group at the University of Seattle in a systematic series of experiments using torsion balances placed on a turntable which modulates the signal with a period down to about 20 minutes [13-15].

Despite the much larger driving acceleration, Galileo-type mass dropping tests of UFF have been unable to compete with rotating torsion balances [16]. The success of torsion balances relies on 3 main properties: i) high sensitivity to differential accelerations; ii) long time duration of the experiment; iii) up-conversion of the signal (DC from the Earth and 24-hr from the Sun) to higher frequency. Flying an instrument with these properties in low orbit around the Earth would add the only advantage of mass dropping, namely the very large driving acceleration from Earth. This fact alone would provide –assuming the same sensitivity to differential accelerations as achieved in ground tests– an improvement in η by about 3 orders of magnitude. The difficulties related to running the experiment in space, with no direct access to it, can be compensated by exploiting those peculiarities of the space environment which are relevant for experiments to test UFF, most importantly, absence of weight and isolation of the satellite/experiment once in orbit. Throughout this Report we shall see how absence of weight and system isolation can significantly contribute to improving the current best tests of EP by several orders of magnitude.

Torsion balance tests indicate that considerable progress beyond the current level is extremely hard to achieve. A new type of experiments based on interferometry of free falling cooled atoms is in preparation [17] with the very ambitious goal of performing in the lab an EP to 10^{-15} and even to 10^{-17} sometime in the future. So far a measurement of the local acceleration of falling atoms has been performed achieving $\Delta g / g \simeq 3 \cdot 10^{-9}$ [18]. The proposed EP tests with cold atoms interferometry will measure the differential acceleration between isotopes ^{85}Rb and ^{87}Rb, whose difference in composition is unfortunately limited to two neutrons only.

All other experiment proposals aiming at a considerable improvement over the results achieved by rotating torsion balances are to be performed inside a capsule dropped during a balloon flight [19], in a suborbital flight with a sounding rocket [20] or inside a spacecraft in low Earth orbit [21-23].

Theoretical predictions have been made as to what level an EP violation is likely to occur [24, 25, 9]. In [9] it is shown with a rigorous calculation, within a classical framework which does not postulate any new interaction, that if gravity couples anomalously to the energy of neutrino-antineutrino exchange, its contribution to the mass-energy of the nucleus would lead to an Equivalence Principle violation to the level of about 10^{-17}. The most recent work [9] indicates that, for test masses made of Be-Cu and Pt-Ti, a violation might occur at a level which should be observed with the rotating torsion balances of the "Eöt-Wash" group. However, it is apparent from the speculative nature of these analyses that only a very high accuracy EP test will provide a major breakthrough or –if not– severely constrain the theoretical framework. In this context, tests of composition dependent effects and of post-Newtonian ones are quantitatively compared –as mentioned above [9]– to conclude that UFF tests put much more stringent limits than solar system or binary-pulsar test, by several orders of magnitude.

Equivalence principle experiments involving man made test masses do not allow to test it for gravitational self-energy itself because the contribution from gravitational binding energy –mentioned above in relation to the generalized Eötvös parameter

(2.3)– is negligible for artificial bodies. This form of equivalence is often referred to as the Strong Equivalence Principle (SEP) and can be tested only with experiments in which the test masses are celestial bodies –as in the case of the Earth and the Moon falling in the gravitational field of the Sun, the lunar orbit being determined by laser ranging to the Moon. In addition to differing in composition, Earth and Moon have a significant component of gravitational binding energy ($4.6\cdot 10^{-10}$ for the Earth and $1.6\cdot 10^{-11}$ for the Moon) whose equivalence can be tested with the current sensitivity of Lunar Laser Ranging (LLR) tests which have reached the level of 10^{-13} as tests of the weak equivalence principle [26]. In this sense LLR tests are unique, though they need to be combined with composition dependent tests of laboratory size bodies of Earth-like and Moon-like composition in order to remove their ambiguity as tests of the SEP [14].

The new APOLLO (Apache Point Observatory Lunar Laser-ranging Operation) facility in southern new Mexico [27] will provide –together with an improved physical model of all perturbations involved– a better determination of the lunar orbit and a more accurate test of the equivalence principle, confirming LLR once more as the most important scientific legacy of the Apollo project to the Moon.

As a test of the equivalence principle, lunar laser ranging is ultimately limited by the non uniformity of the gravity field of the Sun, a limitation expressed by the dimensionless quantity $3\Delta a_{sma}/d$ (Δa_{sma} being the measurement error in the semimajor axis of the orbit of the Moon around the Earth and d the distance of the Earth-Moon system from the Sun) [28]. A $1cm$ error in semimajor axis (due to $1cm$ accuracy of lunar laser ranging) is consistent with the current level of LLR tests to 10^{-13}, 1 order of magnitude improvement is expected with the capability of the APOLLO facility to perform laser ranging to the Moon at $1mm$ 1 level.

The effect of non uniformity of the gravitational field is a real limitation to EP tests with laser ranging because they rely on absolute distance measurements from Earth. However, it is apparent from (2.1) that EP tests require to measure only differential accelerations –and the displacements they give rise to– of the test masses relative to one another. If artificial test masses are placed inside a spacecraft and differential measurements are performed in situ, displacement sensors are available to measure their relative displacements many orders of magnitude more accurately than by laser ranging from Earth. For testing the equivalence principle there is no need for a very accurate measurement of the absolute distance of the spacecraft from Earth. This is why differential accelerometers to fly inside a spacecraft in low Earth orbit can aim at a far more accurate EP test than lunar laser ranging so as to put General Relativity to the most stringent test ever.

3. MISSION AND EXPERIMENT DESCRIPTION

3.1 WHY TESTING THE EQUIVALENCE PRINCIPLE IN SPACE

The GG mission is designed to measure the relative acceleration of two test masses of different composition suspended inside the spacecraft and orbiting around the Earth at low altitude (520 km nominal). Thus, GG tests the Universality of Free Fall (UFF) whereby all bodies should fall with the same acceleration regardless of their mass and composition, which is a direct consequence of the Equivalence Principle.

The target of GG is to detect a fractional differential acceleration of the falling bodies, hence an EP violation, to the level of 1 part in 10^{17}. If successful, it would improve by 4 orders of magnitude the best results achieved in the lab with rotating torsion balances [13-15]

In case of EP violation, test bodies in low Earth orbit are subjected to a signal from the Earth more than a thousand times larger than that due to the Sun acting on torsion balances on the ground (see e.g. [29])

Extremely weak suspensions can be used in orbit –because of weightlessness– to suspend and couple the test masses inside the spacecraft, thus resulting in a much higher sensitivity than at $1g$.

In space, the entire “laboratory” (i.e. the experimental apparatus and the spacecraft) is an isolated system. This fact eliminates altogether numerous local disturbances unavoidable on Earth (such as terrain tilts and nearby mass anomalies). With such an isolated system, rotation of the apparatus in order to up-convert the signal to higher frequency (similarly to the rotating torsions balances of the “Eöt-Wash” group) can be performed by rotating the entire spacecraft, with no need of motor and bearings, and therefore with greatly reduced noise.

3.2 THE GG EXPERIMENT CONCEPT

Searching for a new composition dependent differential effect in space requires the test masses to be well centered on each other, as classical tidal effects due to non uniformity of the gravitational field of the Earth would otherwise mask any small deviation from known Physics. Thus, the generally preferred design in satellite tests of EP is that of concentric, co-axial test cylinders. Only in GG they are arranged so as to be sensitive in the plane perpendicular to the cylinders common axis, rather than along the axis itself (see Figures 3.1 and 3.2).

This turns out to be a crucial choice, as discussed below.

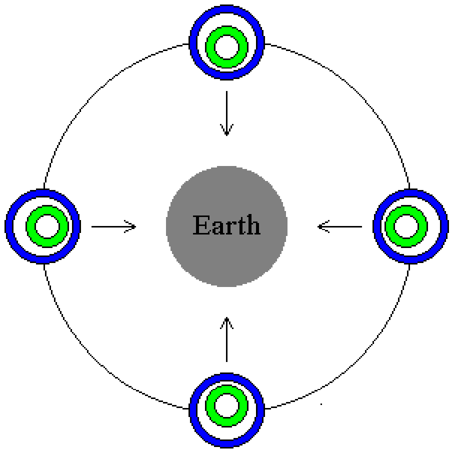

Figure 3.1: The EP violation signal in GG. Section in the plane perpendicular to the spin/symmetry axis of the GG outer and inner test cylinders (of different composition and weakly coupled in the plane) as they orbit around the Earth inside a co-rotating, passively stabilized spacecraft (not shown). The centers of mass of the test cylinders are shown to be displaced towards the center of the Earth as in the case of a violation of the equivalence principle in the field of the Earth (indicated by the arrows). The signal is therefore at the orbital frequency $(1.75 \cdot 10^{-4}\ Hz)$. Figure 3.2 below shows how this signal is modulated by rotation around the symmetry axis. (The figure is not to scale).

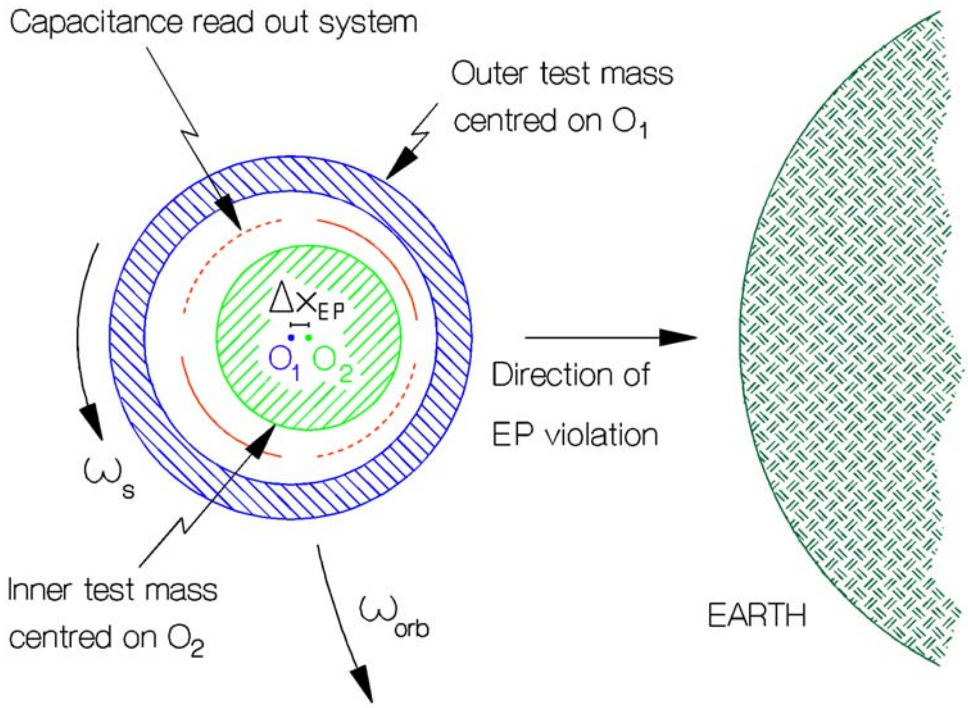

Figure 3.2: Modulation of the violation signal at the spin frequency. Section of the GG coaxial test cylinders and capacitance sensors in the plane perpendicular to the spin axis (not to scale). The capacitance plates of the read-out are shown in between the test bodies, in the case in which the centers of mass of the test bodies are displaced from one another by a vector $\Delta\vec{x}_{EP}$ due to an Equivalence Principle violation in the gravitational field of the Earth (e.g., the inner test body is attracted by the Earth more than the outer one because of its different

composition). Under the (differential) effect of this new force the test masses, which are weakly coupled by mechanical suspensions, reach equilibrium at a displaced position where the new force is balanced by the weak restoring force of the suspension (the weaker the coupling, the larger the displacement), while the bodies rotate independently around O_1 and O_2 respectively. The vector of this relative displacement has constant amplitude (for zero orbital eccentricity) and points to the center of the Earth (the source mass of the gravitational field); it is therefore modulated by the capacitors at their spinning frequency with respect to the center of the Earth ($1Hz$ in the current GG baseline).

Two driving needs are compelling when attempting to test the Equivalence Principle. The concentric test cylinders should:

(i) be coupled very weakly to each other –whatever the physical nature of the coupling– in order to increase sensitivity to differential accelerations, such as that caused by an EP violation;
(ii) spin as fast as possible in order to provide signal modulation at frequency as high as possible, and thus reduce the well known $1/f$ electronic noise

As for weak coupling, GG relies on the absence of weight in space which allows us to use mechanical suspensions of very low stiffness and high quality factor.

3.2.1 Passive electric grounding and the effect of electric charge patches

It is very important to stress that mechanical suspensions ensure passive electric grounding of the test masses. Thus, there is no need in GG for active electric discharging of the masses as in GP-B and LISA-PF where a control loop is used applying UV radiation on the surfaces of the bodies. Passive discharging is preferred in GG because of the possibility, when actively controlling effects much stronger than the tiny target signal, of leaving too large residual disturbances [30].

Electric charge patches are known to exist even on the surface of grounded bodies, and they have been found to slowly wander around. In all small force experiments, both on ground and in space, electric patches are minimized by gold coating all conductive surfaces, and this is planned for GG too. More importantly, in GG residual patches on the surface of the bodies will co-rotate with them and the entire system; therefore, they will be detected by the rotating sensors as DC or low frequency effects, while an EP violation would be detected at the $1Hz$ frequency of spin, as shown in Figure 3.2. In any case, a rigorous method has been set-up for direct measurement in the lab of residual charge patches with the full scale GGG (“GG on the Ground”) payload prototype (see Section 9) to ensure beyond question that they will not interfere with the expected signal.

3.2.2 HIGH FREQUENCY SIGNAL MODULATION WITH NO SIGNAL ATTENUATION

As for signal modulation, the GG solution sketched in Figure 3.2, with the spin frequency much higher than the natural coupling frequency (by a factor 540 in the current design), makes the GG system in essence a supercritical rotor in 2D. Indeed, requesting both weak coupling and fast spin leads to the very definition of a supercritical rotor. Supercritical rotors are known to be unstable if the masses are constrained to one direction only [31, p. 228]. Instead, in 2D a well defined position of relative equilibrium exists, dictated by physical laws for a rotor with given construction and mounting errors. The GGG laboratory prototype has experimentally demonstrated this prediction in the case, never demonstrated before by a precision experiment, of a multibody rotor (see Section 9). The 2D design of GG satisfies this classical requirement, while accelerometers designed to be sensitive in 1D only (along the symmetry axis of the test cylinders, rather than in the transverse plane) do not.

In addition, a 1D accelerometer will up-convert the signal to higher frequency by rotating the sensitive axis itself in the orbit plane, and in doing so it will necessarily respond to a differential driving signal from the Earth as a forced oscillator (it is equivalent to the accelerometer being still and the Earth rotating around it). In which case a forcing effect at frequency higher than the natural one would be attenuated as the ratio of the frequencies squared. (The same happens on the ground for rotating torsion balances, seeking for an EP violation signal either in the field of the Sun or the Earth). The GG design is unique because, as it is clearly shown in Figure 3.2, the violation signal not affected by the system spinning. Indeed, the figure shows that in principle the signal could be modulated at the spin frequency by rotating the displacement transducers (i.e. the capacitance plates) only, and not the test cylinders themselves, thus proving that in GG the differential displacement caused by an EP violation is not affected by rotation. Obviously, this choice would not be wise, especially in space.

Fast modulation frequencies are therefore utterly impossible with 1D accelerometers. In point of fact, the first proposal to test the Equivalence Principle in space with a fast rotating platform, so as to modulate the signal at its rotating frequency, goes back to 1970 [32]; however, in that apparatus the test bodies were constrained to move along one diameter of the rotating platform. Being 1 dimensional, the system was strongly unstable and the idea was abandoned.

It is to be added that since GG is sensitive in 2D, the use of a capacitance read out in two orthogonal directions of the plane doubles the amount of scientific data for a given integration time, thus reducing the noise level of the measurement in that timespan by a factor $\sqrt{2}$. It also preserves the cylindrical symmetry of the system.

3.2.3 THE PGB (PICO GRAVITY BOX) SPACE LABORATORY

In GG two test masses of different composition are arranged to form a differential accelerometer. The accelerometer is not directly connected to (suspended from) the spacecraft. It is located inside an intermediate cylindrical "laboratory" named PGB (Pico Gravity Box) because it is in essence a passive attenuator of spacecraft vibration noise [33, 34]. In this case the PGB has the shape of a cylindrical lab suspended from the GG spacecraft at the two ends of its symmetry axis by means of specifically designed springs (sketched in Figure 3.3). The PGB springs ensure low stiffness for oscillations in the plane perpendicular to the axis of the cylinder (which is the plane of sensitivity of the accelerometer) and high stiffness along the symmetry Z axis. Along its axis the PGB has a shaft (tube) from which, at its center of symmetry, the GG differential accelerometer –the core instrument of the mission– is suspended, as shown in Figure 3.4.

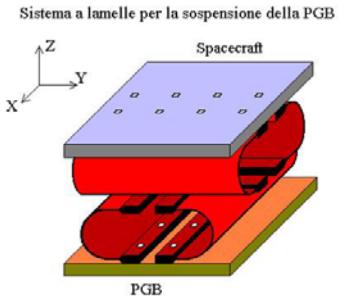

Figure 3.3 (left): Sketch of the suspension springs to be used for suspending the PGB laboratory (see text above) from the GG spacecraft

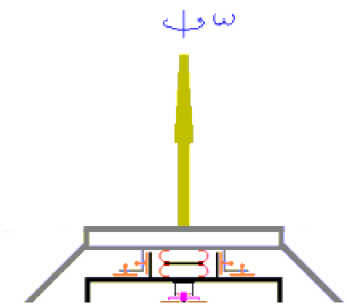

Figure 3.3 (right): Sketch showing –in a section along the symmetry axis of the satellite (one dipole antenna is also visible)– how, on one end of its axis, the PGB lab is connected to the spacecraft. Small capacitance plates are also visible –in between the PGB and the spacecraft– to sense their relative in all 3 directions

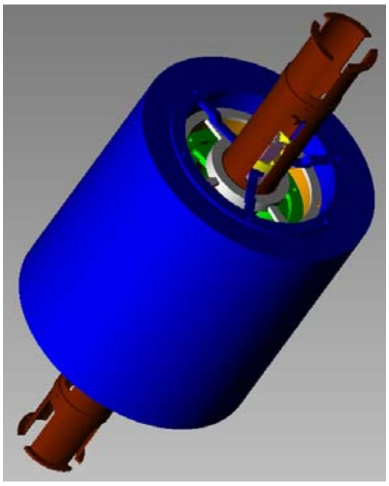

Figure 3.4: The GG differential accelerometer assembled around the PGB shaft (tube), which is shown in brown. Only the outer test of the accelerometer is visible (the inner one inside is hardly visible). The figure is obtained from the engineering drawings of the system.

An overall view of the entire GG system formed by the solar panels, the spacecraft (with its components), the PGB and the accelerometer, is shown in Figures 3.5 and 3.6 below.

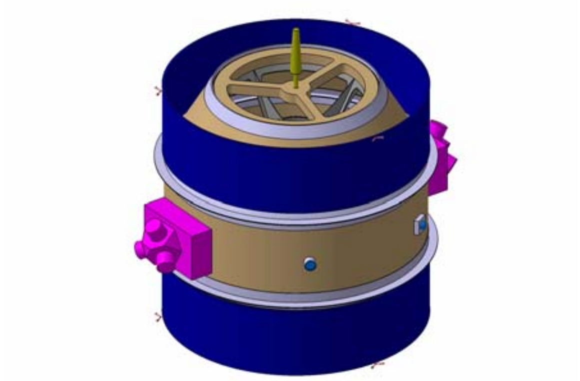

Figure 3.5 (left): The GG spacecraft in its current design, with the cylindrical solar panels (in blue), the "spinning top" compact structure (in light brown) and the thrusters (in magenta) for drag compensation (see Section 7). The satellite spins around the symmetry axis at 1 Hz. One dipole antenna (at the top) is visible along the axis. The cylinder has 1.45 m diameter and 1.42 m height. The whole system is very compact to ensure a low area-to-mass ratio and thus minimize the effect of all non gravitational forces acting on its external surface (primarily drag due to residual atmosphere along the orbit).

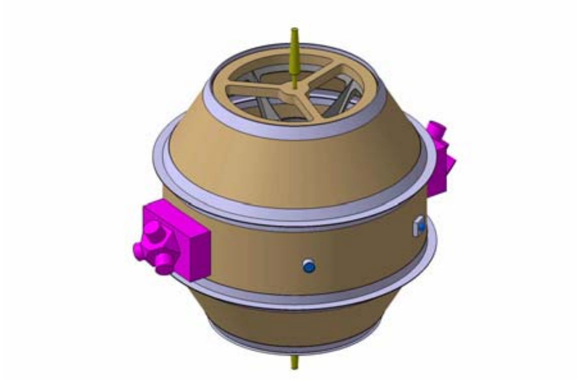

Figure 3.5 (right): The very compact "spinning top" housing the entire experimental apparatus. It is made in carbon fiber composite in order to minimize thermal disturbances.

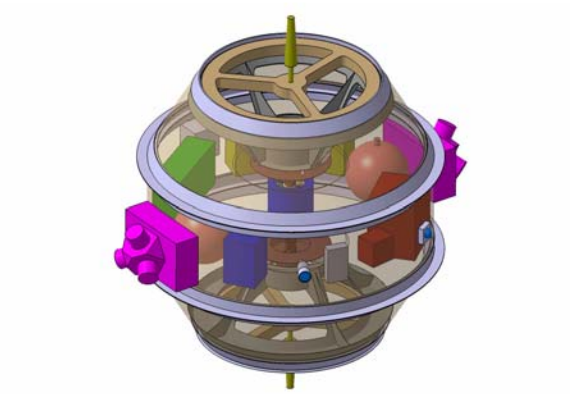

Figure 3.6 (left): A view inside the "spinning top" showing (in light gray) the PGB inside it and the GG differential accelerometer (with the outer test cylinder visible in blue) at the center.

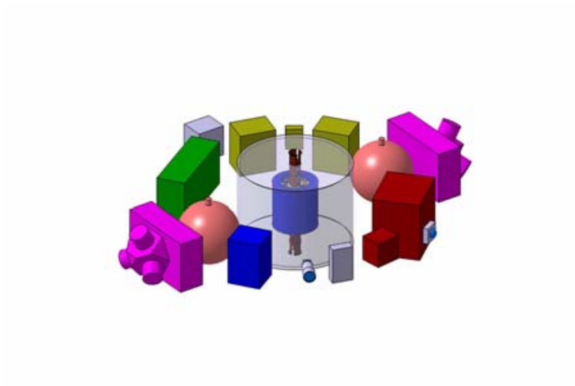

Figure 3.6 (right): From the panel on the left the "spinning top" has been removed; the cylindrical PGB (in light gray) is now visible with its central tube; (in brown) and the accelerometer (outer test cylinder in blue). Note that all electronics boxes are located outside the PGB, as far away as possible from the test masses of the accelerometer, attached to the inner side of the "spinning top".

The PGB serves several very important functions in the GG mission:

(i) It provides an attenuation stage for the spacecraft vibration noise acting in the sensitive plane of the accelerometer –perpendicular to the spin/symmetry axis– at frequencies higher than the natural oscillation frequency of the PGB ($1/360\,Hz$ in the current baseline). Note that the EP signal is not attenuated because it acts at the satellite orbital frequency of $1/5700\,Hz$ (as shown in Figures 3.1 and 3.2) which is below the PGB natural frequency.

(ii) It serves as test mass whose relative motion w.r.t the “spinning top” (sensed by means of small capacitance plates –located as sketched in Figure 3.3) drives the drag compensation control loop (Section 7) at low frequencies such as the orbital one (above the natural frequency of the PGB, active compensation is not needed because passive it attenuation is provided by the PGB itself)

(iii) It provides the test masses inside it with passive magnetic shield (by mu-metal layer), thermal shield (by multi layer thermal blankets) and electric grounding

(iv) Its weak coupling with the spacecraft provides “nutation damping” for the the satellite 1-axis rotation

The relevance of these functions will become apparent throughout this Report. A simple glance at Figure 3.6 shows how the accelerometer, thanks to the PGB, is essentially decoupled from all the subsystems of the spacecraft which are needed to provide the simple services needed in low Earth orbit (such as communication with the ground and data transmission) and, in the case of GG, also drag compensation.

3.2.4 Design of the GG differential accelerometer/s

From the conceptual point of view the test cylinders of the GG differential accelerometer are arranged as in a beam balance, the beam being directed along the symmetry axis. A crucial property of this balance is that the masses are concentric, which is a must for using it in space where non concentric masses are subjected to classical differential (tidal) forces. Beam balances are known for their property to “balance”, i.e. to reject common mode forces extremely well (to 10^{-8} and even better). The GG accelerometer has been conceived to retain as much as possible such property of beam balances, while at the same time being suitable for space.

As shown in Figure 3.7, the test masses of the GG accelerometer (10 kg each) are concentric, co-axial, hollow cylinders. The two cylinders are mechanically coupled by attaching them, at their top and bottom, to two ends of a coupling arm by means of flexible lamellae. The coupling arm is made of two concentric tubes similarly attached at their midpoints to a single shaft (the PGB). This assembly preserves the overall symmetry of the apparatus, when the two parts of the arm are taken together. The masses are mechanically coupled through the balance arm such that they are free to move in the transverse XY plane and stiff in the direction of the symmetry axis; all of them taken together form the physical system. The masses oscillate in a two dimensional harmonic potential defined by the suspension springs at the ends of the balance arm while free falling around the Earth. A differential acceleration of the masses would thus give rise to a displacement of the equilibrium position in the XY plane. The displacement of the test masses is sensed by two sets of capacitance plates located between the test cylinders, one set for each orthogonal direction (X and Y). Each set of capacitance plates is placed in an AC-bridge configuration such that a displacement of the masses causes an unbalance of the bridge and is thus converted into a voltage signal. When the physical system is mechanically well balanced it is (almost) insensitive to "common-mode" accelerations. In addition, the capacitance bridges are predominantly sensitive to differential displacements. Thus, the differential nature of the accelerometer is ensured by the dynamics of the physical system and also by the displacement transducer.

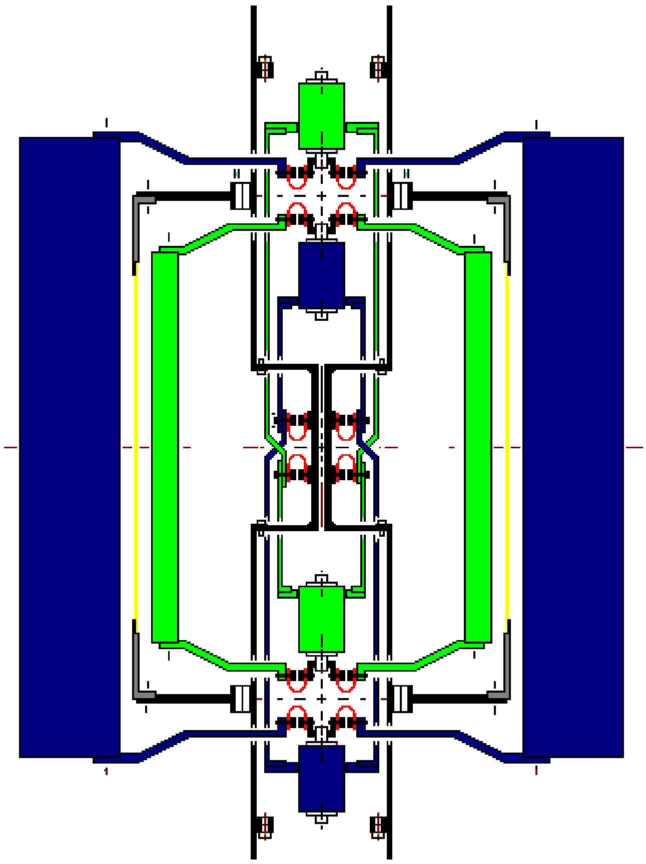

Figure 3.7: Baseline design of the GG accelerometer made of two test cylinders of different composition for EP testing (section through the spin/symmetry axis). The system is sensitive to differential forces acting on the cylinders in the plane perpendicular to the symmetry axis (plane of sensitivity). The coupled test cylinders (green and blue; 10 kg each) are suspended from the PGB central shaft (shown here as a black tube) at their center of symmetry. All the suspensions, including those used for coupling the test cylinders to each other, are thin,

curved laminar suspension strips (shown in red). There are 3 of them at each level, symmetrically placed around the axis (shown in green and blue inside the PGB shaft tube). The particular geometry of mounting them ensures that the pivoting points of the two balancing arms are well defined and that those at the center of the accelerometer, which suspend it all from the PGB shaft, coincide well one with the other (at the cross shown). These suspensions are very soft for lateral differential oscillations of the two test masses and at the same time are particularly rigid for unwanted motions, like common mode lateral oscillations and rotational oscillations around the spin axis. They have enlarged ends for clamping (so as not to add dissipation at the clamps), and those in the central part of the rotor are fastened by electrically insulating clamps, so that these suspensions can be used as conducting leads between the PGB tube and the two balancing arms for the driving voltages of the four axial inch-worms (shown in blue and green respectively), which are used for balancing the two rods and for adjusting the axial position of the two test masses. Once the desired balancing has been achieved the driving voltages of the inch-worms are switched off, leaving them blocked; in this way they will not disturb the EP measurements nor produce joule heating inside the PGB laboratory. The capacitance plates of the transducer designed to read the displacements of the test cylinders relative to each other in two orthogonal directions of the sensitive plane, are shown in yellow between them. They are rigidly attached to the PGB shaft and respect the cylindrical symmetry of the whole system. Much smaller capacitance sensors/actuators (not shown here for simplicity) are designed to sense and damp whirl motions. The figure is to scale

The effect of a differential force, such as the one arising form an EP violation, is sketched in Figure 3.8.

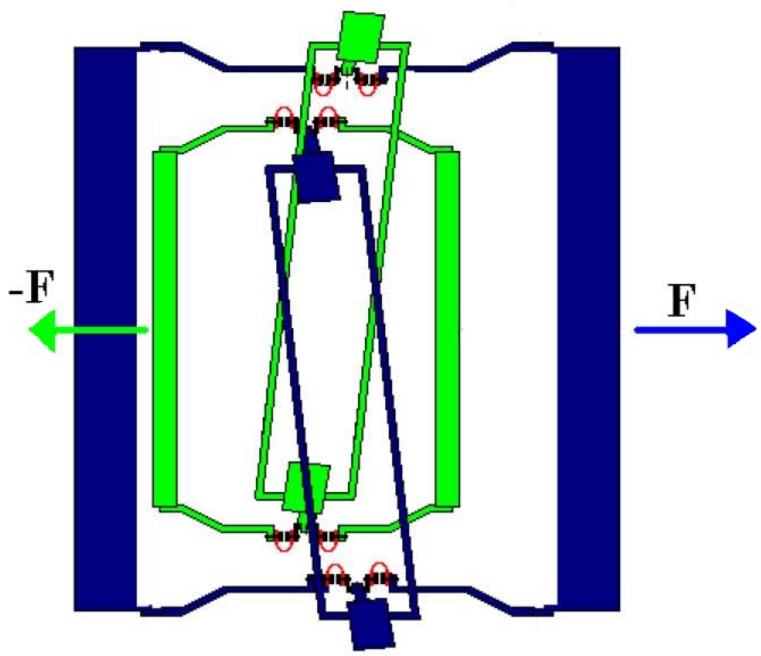

Figure 3.8: Conceptual view of the effect of a differential force acting in the sensitive plane on the GG test cylinders coupled and arranged as shown in Figure 3.7. The effect is a displacement of the centers of mass of the test cylinders relative to one another (simplified, largely exaggerated). This differential displacement is read by a capacitance transducer located in between the cylinders (not shown here)

A better understanding of the instrument can be obtained from Figure 3.9 where several 3D charts derived from the construction drawings of the accelerometer show its structure, and how the cylindrical symmetry is respected.

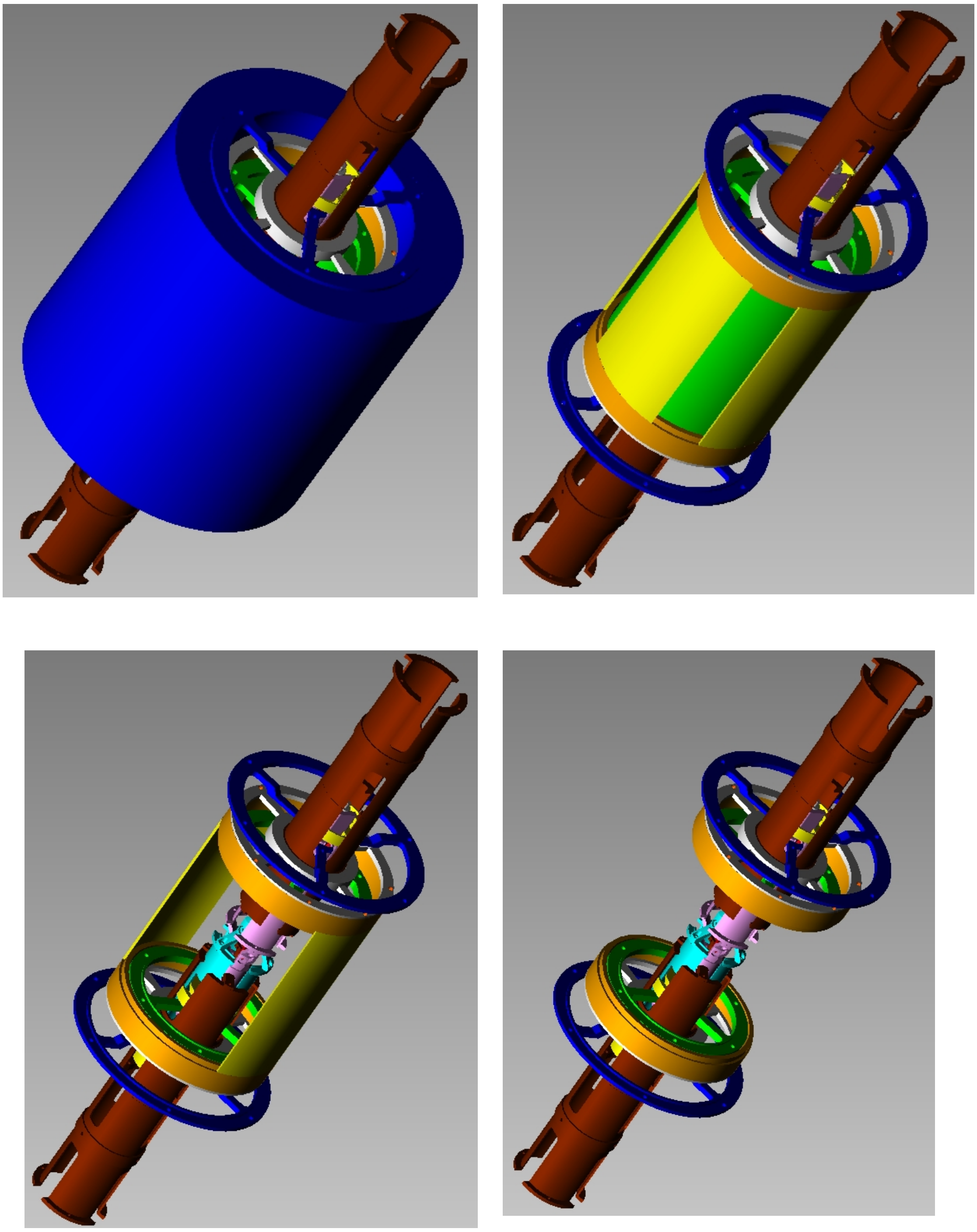

Figure 3.9: Details from the engineering drawings of the GG differential accelerometer showing the instrument parts from the "outside" (top figure) to the "inside". The brown central tube is the PGB shaft. The blue and green cylinders are the test masses, the yellow plates are the capacitance bridge plates designed to measure the relative displacements of the test cylinders.

In the current baseline the GG satellite features one single accelerometer with 2 test cylinders of different composition, as shown in Figure 3.5. The instrument is designed to achieve a sensitivity to an Equivalence Principle violation in the field of the Earth 4 orders of magnitude better than the best laboratory tests. Securing this goal is the must –and would be the great achievement of the GG mission– because both frequency and phase of the violation signal are both well known (see Figures 3.1 and 3.2) and therefore it can be distinguished from classical gravitational or non gravitational effects.

Additional accelerometers are considered for other satellite missions devoted to EP testing, only one being centered on the center of mass of the spacecraft, thus casting doubts on the reliability of the check because tidal forces would be different on different locations, to name just one important difference to be concerned with.

Since there is only one center of mass of the spacecraft, the only solution is for any additional accelerometer to be concentric with the original one.

For GG a design featuring one additional, concentric accelerometer with the test cylinders made of the same material to serve as a zero-check, has been investigated. As shown in Figure 3.10, both accelerometers are centered on the center of mass of the spacecraft, and they can fit inside the PGB and the GG spacecraft of Figure 3.5: A composition dependent signal, violating the Equivalence Principle, should be sensed by the inner accelerometer and not by the outer one. Instead, a classical differential signal, not depending on the composition of the test masses, would be detected by both accelerometers. It is also worth stressing that the whole system is symmetric around the spin axis as well as top/down.

So far all efforts have been concentrated in ensuring with theoretical analysis, with a space experiment simulator and by building a full scale payload prototype in the laboratory, that the GG target can be achieved with one single accelerometer. The 2-accelerometer design of Figure 3.10 has no conceptual difference with respect to the one with a single accelerometer; indeed, both accelerometers work with the same principles and the decision . The concern at this point is the additional complexity (hence the additional cost and development time) of the mission

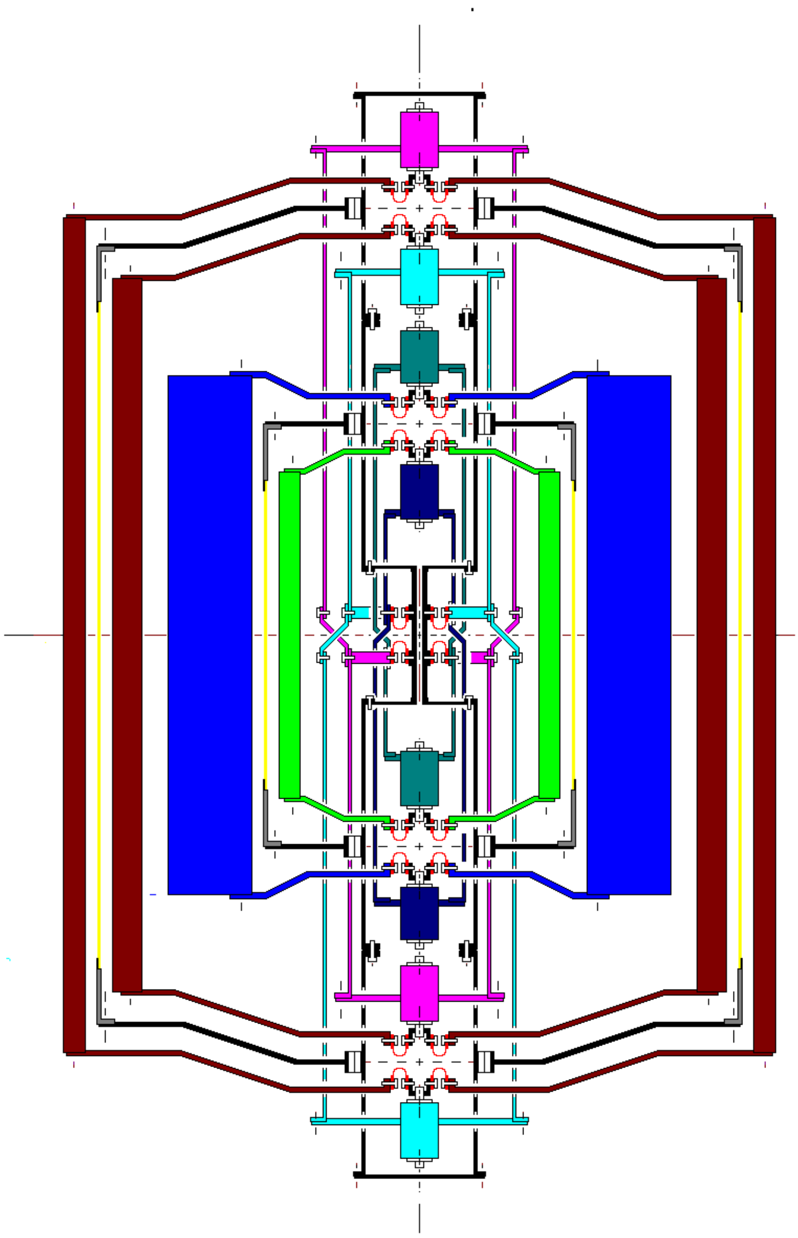

Figure 3.10: Section through the spin axis of 2 co-axial, concentric, differential accelerometers for the GG mission, which could be considered in alternative to the single EP testing accelerometer of Figure 3.7. (Figure is to scale; the external diameter of the blue test cylinder is 23 cm). There are 4 test cylinders (weighing 10 kg each), one inside the other, all centered at the same point (nominally, the center of mass of the spacecraft) forming 2 differential accelerometers: the inner one for EP testing (cylinders of different composition; shown in green and blue respectively) and the outer one for zero check (cylinders made of the same material; both shown in brown). In each accelerometer the 2 test cylinders are coupled to form a beam balance by being suspended at their top and bottom from the 2 ends of a coupling arm made of 2 concentric tubes (each tube suspends one test cylinder at each end, which makes it asymmetric top/down; however, the two of them together form a symmetric coupling). All 4 tubes (2 for each coupling arm) are suspended at their midpoints from the same suspension shaft (the longest vertical tube in figure). In all cases the suspensions are $\cup$-shape (or $\cap$-shape) thin strips (shown in red), to be carved out of a solid piece of CuBe. At each connection there are 3 of them, at 120° from one another (the planar section in figure shows 2 for explanatory purposes only). There are capacitance plates (connected to the suspension shaft) for the read-out of differential displacements in between each pair of test cylinders (shown as yellow lines in section). The 8 small cylinders drawn along the symmetry axis are inchworms for the fine adjustment of the lengths of the coupling arms in order to center each test mass

on the center of mass of the spacecraft. The whole system is symmetric around the spin axis as well as top/down. The two accelerometers are both centered at the center of mass of the spacecraft in order to reduce common mode tidal effects and improve the reliability of the zero check.

3.2.5 WHIRL MOTIONS AND CONTROL

Supercritical rotation, namely rotation at a frequency higher than the natural frequencies of the suspended bodies, is known to ensure self centering of the centers of mass of the rotors on the rotation axis (see e.g. [31]). The initial offset vectors $\vec{\varepsilon}$ due to construction and mounting (hence, fixed on the rotor) will be reduced by the factor $(\omega/\omega_n)^2$ (spin-to-natural-to frequency squared):

$$\Delta\vec{r}_{cc} \simeq -\vec{\varepsilon}\cdot\frac{1}{(\omega/\omega_n)^2}$$

giving rise to an equilibrium position $\Delta\vec{r}_{cc}$ (also fixed on the rotor) closer to the rotation axis but on the opposite side of it with respect to the initial offset vector. Incidentally, this is the reason why 2 degrees of freedom are required for the center of mass of the rotor to reach its equilibrium position, while in 1 dimension only it would be unstable and eventually break the suspension. The larger the ratio $(\omega/\omega_n)^2$, the better the centering: the center of mass of ideal free rotor would be perfectly centered on the spin axis. With a large spin-to-natural frequency ratio, the GG supercritical rotation is very close to that of ideal, unconstrained rotors.

The existence of an equilibrium position uniquely determined (for a given dynamical system) by physical laws is a very important property: the test masses do not need to be maintained concentric on one another at an arbitrary defined location by applying forces on them.

However, suspensions are not perfect, which means that, as they undergo deformations at the frequency of spin, they also dissipate energy. The higher the mechanical quality of the suspensions, the smaller the energy losses. Energy dissipation causes the spin rate to decrease, hence also the spin angular momentum will decrease; and since the total angular momentum must be conserved, the suspended bodies will develop whirl motions around their relative equilibrium position (at their slow natural frequencies). It is well known in rotordynamics that the forces needed to damp whirl motions are smaller than the elastic forces coupling the bodies by a factor equal to the mechanical quality factor of the system ($Q_{TMs} \geq 20000$ for the GG test masses); moreover, they act at about 90° from the radial direction along which the effect of an EP violation would be sensed. In GG whirl motions are damped actively with small capacitance sensors/actuators and appropriate control laws taking into account that the whole system co-rotates (see [35], Section 7 and

Section 9). Since whirls grow very slow, data taking will take place while they are small and whirl control is switched off.

3.3 THE READ-OUT SYSTEM

It is a must for small force gravitational experiments that the sensing apparatus be as passive as possible.

However, a transducer is needed to read the relative displacement of the test cylinders. In GG the transducers are two capacitance bridges, along the two directions X, Y of the plane perpendicular to the symmetry axis, whose plates are located halfway in between the inner and outer test cylinder as sketched (for a single bridge) in Figure 3.11. The better the plates are centered in between the test cylinders, the better the bridge will reject common mode forces acting on the them; ideally, a perfectly balanced bridge would be totally insensitive to common mode displacements and give a signal only if the bodies move relative to one another (see Figure 3.12).

In is way the sensitivity of the GG accelerometer to differential effects is ensured by its mechanical design and also by the transducer design.

The capacitance bridges are rigidly connected to the PGB tube. Since the whole system is co-rotating (unlike in the ground prototype) the analog and digital electronics required by the read-out can be located away from the test masses on the PGB, with an optical link between the PGB and the spacecraft for data transmission. Power is transmitted to the PGB through its suspension springs (which are fastened by electrically insulating clamps and serve as electric wires). Close to the test masses only the inch-worms need to be powered when used for balancing (see caption of Figure 3.7); in this case, since they are located on the coupling arms, the U-shape central suspensions will serve as wires. Once balancing has been achieved, the inch-worms will be switched off, they will maintain the desired position and the system will be passive again. As for the small capacitance sensors/actuators to be used to damp the whirl motions of the test masses relative to the PGB, they will be connected to the PGB tube and no wiring is required.

With all this care, the test masses are almost completely passive (they are totally passive when whirl damping is switched off) and free to move around their physical position of relative equilibrium with the capacitance bridge transducers measuring their relative displacements. High frequency modulation ensures that 1/f electronic is minimized.

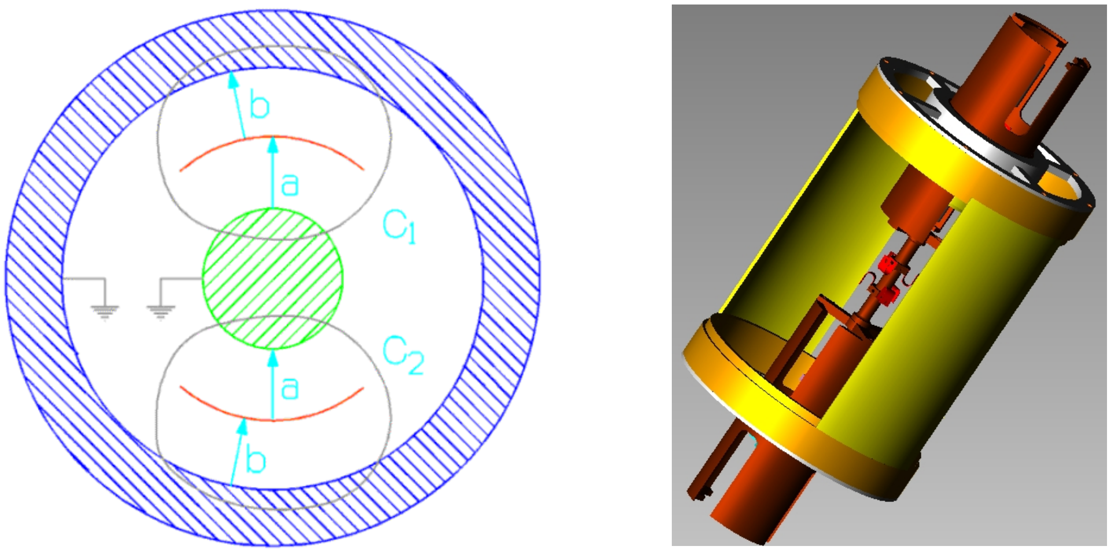

Figure 3.11: (Left) Schematic drawing of the capacitance bridge transducer for detecting relative displacements of the inner and outer test body with respect to one another (only the bridge in one direction shown). The capacitors of the bridge (indicated here as C_1 and C_2) are formed by two surfaces –one for each of the two grounded bodies– and one plate, to which a sinusoidal voltage is applied; the other two capacitors of the bridge are fixed capacitors. Any differential displacement of the test masses with respect to the plates causes a loss of balance of the bridge and therefore an output voltage signal. (Right) 3D engineering drawing showing the two plates of one capacitance bridge transducer designed for the GG accelerometer (the other bridge is at 90° from this one). Note that for each bridge the plates are rigidly attached to the PGB tube (shown in brown). The test cylinders (to be located one inside and the other outside of the plates) have been removed from this drawing to make the plates visible.

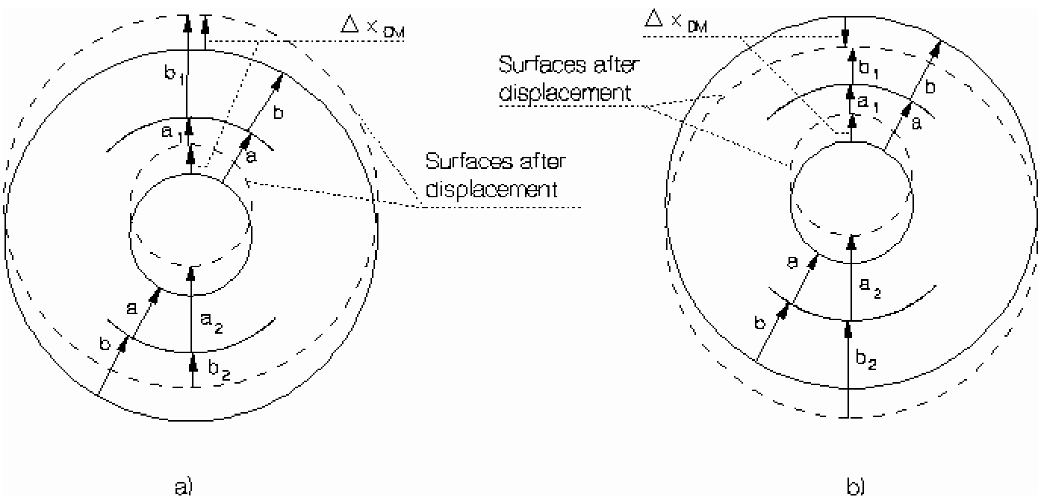

Figure 3.12: This drawing shows the surfaces of the capacitors depicted in Figure 3.11 before and after: a) a common mode displacement and b) a differential mode displacement. For a non zero value of *(a-b)* both a differential and a common mode displacement would contribute to the (capacitance) unbalance of the bridge, hence to the output potential. An EP violation signal would produce a differential displacement. For it to be detected the contribution coming from a common mode displacement (e.g. caused by air drag) must be smaller than the contribution of the EP violation, hence leading to the constraint on the mechanical unbalance of the bridge *(a-b)/a*.

3.4 VACUUM AT NO COST

More than 4 centuries ago Galileo wrote: "…se si levasse totalmente la resistenza del mezzo, tutte le materie descenderebbero con eguali velocità" ("…if one could totally remove the resistance of the medium, all substances would fall at equal speeds"), thus he was already aware that in order to test what later became known as the "Universality of Free Fall (UFF)" one should perform the experiment in vacuum.

In ground laboratory turbomolecular pumps usually provide the required vacuum inside carefully manufactured vacuum chambers. In space, even at low Earth altitude, good vacuum is already there, which would be sufficient for the requirements of the GG experiment. By opening 2 holes at the two ends of the symmetry axes of both the "spinning top" and the PGB communication with space will ensure that all the spacecraft interior is evacuated. By appropriately choosing the size of the openings on the basis of the amount of outgassing expected (and measured in the lab) inside the spacecraft, vacuum can be maintained at no cost for the entire duration of the mission (2 years nominal) with no need of even getter pumps.

This is very important because in GG vacuum is needed inside the whole spacecraft, the reason being that the PGB itself is the "test mass" (co-centered on the center of mass of the spacecraft like the test masses of the GG accelerometer) whose relative motion with respect to the spacecraft allows the effect of non gravitational forces acting on the outer surface of the spacecraft (mostly air drag along the orbit) and not on the masses inside it, to be detected and partially compensated. In other words, the PGB is the test mass whose motion relative to the spacecraft drives the Drag Free Control system of GG (to which the entire Section 7 is devoted), and therefore it should not be disturbed by large air pressure.

Payloads for fundamental physics experiments in space are often housed in chambers that are evacuated in the lab and sealed before launch (with some additional provision to take care of vacuum degradation afterwards because of outgassing). This is known to be an expensive procedure, which must be avoided in small, low cost missions like GG. In fact, even though in space the difference of pressure that the chamber must sustain is very small, this is not the case on ground before launch, when a large gap exists between atmospheric pressure outside and vacuum inside.

The choice of GG to obtain vacuum at no cost is therefore very interesting. However, we point out that care should be taken when opening a connection hole between the spacecraft and outer space. Even at low Earth orbit as in the case of GG some plasma already exists which gives rise to a current on the satellite surface, which in turn, because of the Earth magnetic field, will produce a (non gravitational) force on it which in turn will be felt as an equal and opposite inertial force (in common mode) by all bodies suspended inside the spacecraft. It has been demonstrated [36] that at typical GG altitudes such a force –even under extremely conservative assumptions– is below 1/1000 of the typical residual air (neutral) drag force, and therefore poses no problems to the drag free control system of GG.

This is correct as long as the outside plasma is not allowed inside the spacecraft. A non gravitational acceleration 1000 times smaller than drag, acting directly on the PGB and the test masses, would leave a residual differential effect larger than the signal. This would likely happen because some plasma might get inside the spacecraft through the openings mentioned above. A cure for that has been proposed, based on 2 appropriate grids for each opening (one neutral and one charged) so as to keep the plasma out [36]. It has already been used, for other reasons, within the BeppoSax mission to protect its sensors. A detailed grid design is in preparation and will be tested inside the Plasma Chamber facility of IFSI-INAF in Rome, where ionospheric plasma at the GG orbiting altitude can be reproduced and the shielding capability of the grids can be demonstrated beyond question.

3.5 Satellite and orbit selection

As it is often the case with space experiments in Fundamental Physics, the satellite and the orbit are driven by the experiment to be performed. In GG the driving concept is the high frequency modulation of the expected EP violation signal, which has been a must in all ground experiments on the Equivalence Principle from the 1960s to date.

The GG satellite is therefore designed to have cylindrical symmetry, enclosing the test cylinders and co-rotating with them. Rotation around its symmetry axis (also the axis of maximum moment of inertia) provides passive stabilization. Weak coupling between the spacecraft and the PGB provides the dissipation needed for the so called “nutation damping” of one-axis passively stabilized satellites.

Thus, the experiment need for high frequency modulation leads to passive satellite attitude stabilization, which is undoubtedly less complex, less expensive (and also less disturbing for the experiment itself) than active attitude stabilization would be.

In space it is possible to realize an isolated rotor made of multiple macroscopic bodies in a nested configuration, all co-rotating, with no motor or bearings, no nearby moving mass anomalies, no local terrain tilt disturbances. This would never be possible on the surface of the Earth. A simple minded way to appreciate the advantages, in terms of low noise, of such an isolated co-rotating system is to think at the diurnal co-rotation of the Earth and its atmosphere, whereby we have no perception of moving (at mid latitudes) at about 1,200 km/h.

The orbit of GG is also driven by the experiment and the signal it is designed to detect ([22, Section 2.1.2]). It must be low and equatorial (with the spacecraft axis of spin close to the orbit normal) in order to maximize the signal. A sun-synchronous high inclination orbit would require periodic attitude maneuvers to keep the spin axis close to the orbit normal. The orbit should also be almost circular in order to reduce effects at orbital period (see Figure 3.13). However, none of these requirements need to be met very stringently.

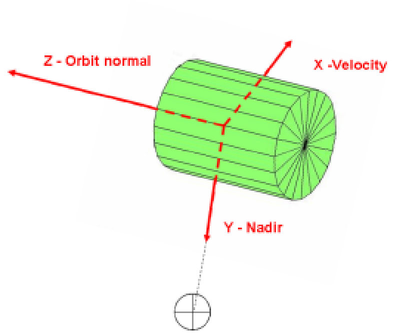

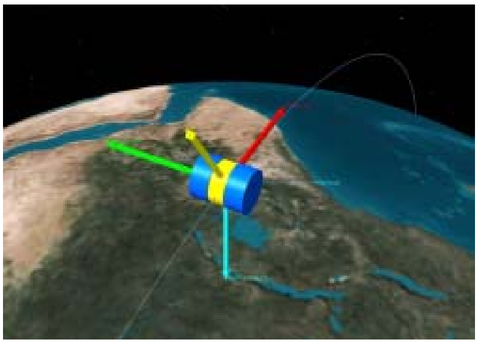

Figure 3.13: A simple sketch of the GG satellite on its orbit around the Earth –almost circular, almost equatorial, with the spin axis almost perpendicular to the orbit plane.

For the GG satellite to be placed in low altitude equatorial orbit the selected preferred launcher is VEGA. In the past GG was designed for the Pegasus launcher, which posed considerable constraints; as VEGA As it is apparent from figures 3.14 and 3.15 the Vega bay allows a much better accommodation of GG (a dual launch would also be possible). This fact has been exploited to reduce the cost of the satellite (by selecting standard, less expensive components typically designed for bigger satellites, such as electronic boxes etc…). The satellite size has also been increased (room being available) so that the GG sensitive accelerometer would be farther away from the spacecraft structure itself, as shown in Figure 3.6. Naturally, care has been taken in keeping the area-to-mass ratio of the GG satellite small (it is a very compact satellite, in order to reduce the effect of drag.

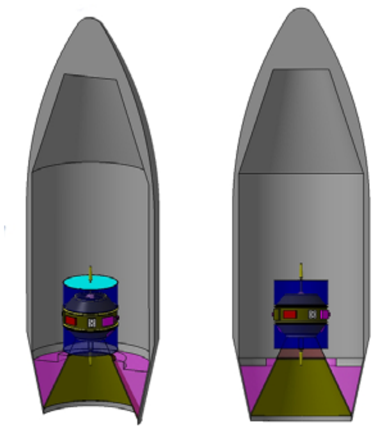

Figure 3.14: View of the GG spacecraft in the bay of the VEGA launcher (Figure to scale)

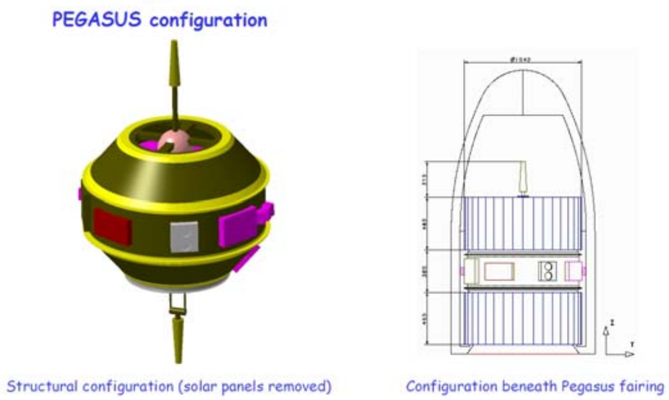

Figure 3.15: View of the GG spacecraft in the bay of the PEGASUS launcher (Figure to scale). The comparison shows the advantage of using VEGA launcher; the much larger room available makes the possiibility of a dual launch worth pursuing

3.6 AIR DRAG: THE LARGEST EFFECT

An apparatus designed to test the Equivalence Principle must be capable to detect extremely small differential forces acting between its test masses. It would therefore be desirable that the apparatus itself not be subjected to much larger forces, especially in the same plane and direction as the expected EP violation force

In space, drag on the outer surface of the spacecraft due to the residual atmosphere along the orbit is the largest force on the satellite. It is many orders of magnitude smaller than local gravity on the ground, but it is much larger than the target signal of GG.

By acting on the spacecraft outer surface (and not on the bodies suspended inside it), atmospheric drag gives rise to an inertial common mode acceleration of the test masses (equal and opposite to the drag acceleration of the satellite). Though it is mostly directed along the orbit, hence at about 90° from the signal (which acts in the radial direction), and it is common mode (while the signal is differential) it cannot just be taken as it is.

Should the GG accelerometer perfectly reject common mode forces, the problem would be solved with no need to implement drag free control on GG. In reality, relying solely on common mode rejection would increase the difficulty of the experiment and limit the achievable sensitivity in EP testing.

A good strategy if for drag (as well as other, smaller non gravitational external forces) to be partially compensated by an appropriate drag free control system, and than partially rejected by a good design of the differential accelerometer and its transducer. The thrusters needed for drag free control should not in turn disturb the experiment, which in this case rules out conventional impulsive thrusters and leads to choose finely tunable micro thrusters.

The entire Section 7 is devoted to Drag Free Control (DFC) for the GG space experiment, reporting the very good results which have been obtained by Thales Alenia Space in Torino.

3.7 Balancing and signal recovery

Once all GG rotors have been properly unlocked (see Section 5.2), and whirl control and DFC are in operation data taking can begin from the main read-out capacitance sensors (Section 3.3) through a synchronous demodulation of the *2*-phase 1Hz signal, since we know that the signal of interest is modulated at the 1Hz frequency of spin.

Large relative displacements of the test bodies will be detected at first. This means that either the test masses are not balanced (i.e. disturbances in common mode are not sufficiently rejected), or the axial misalignment between the centers of mass is too large. The balancing phase consists in applying changes with the inch-worm actuators (shown in Figure 3.7), detecting the corresponding effect and from it deciding about the next change. The largest acceleration against which the system is balanced is due to air drag. It is helpful that its effect is at a rather large phase difference from the signal. Once no further reduction of the differential signal can be obtained, the GG accelerometer is balanced, i.e. no further reduction of common mode forces acting on its test masses is possible and the common mode rejection capability of the instrument has been reached.

Note that the property of a balance to be balanced (i.e. to reject common mode forces) is a property of the balance, not of the common mode force applied. Therefore, once the GG accelerometer is balanced against drag, it will be balanced for any type of common mode force acting on it (in any direction of its plane of sensitivity).

Figure 3.15 describes graphically how the signal is demodulated and the balancing is carried out. The procedure is very clearly outlined in the figure caption.

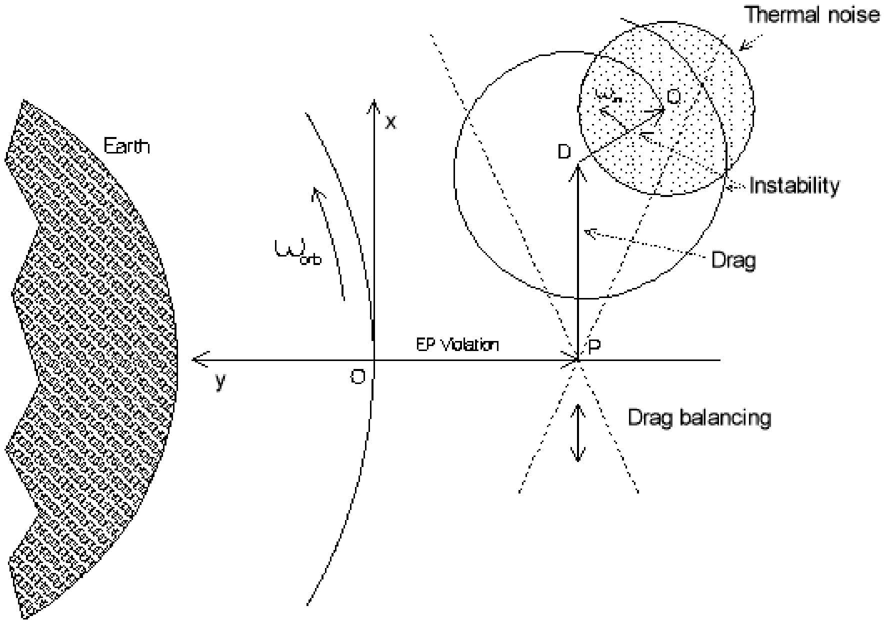

Figure 3.15: Qualitative representation, in the orbital plane, of the differential displacements obtained from the synchronous demodulation of the 2-phase 1 Hz signal. The *X* axis is fixed in the Earth-to-satellite direction; in this non spinning frame the *OP* vector represents the expected signal, namely a differential displacement, directed along the *X* axis and constant in amplitude (for zero orbital eccentricity, otherwise changing from perigee to apogee in a well knwon manner), of the two masses due to a violation of the Equivalence Principle. The perturbation *PD* due to an unbalanced atmospheric drag will be found in the area between the two dotted lines crossing in *P*: The angle between them is roughly 0.8 rad (which would slightly change with the satellite orbiting altitude), due to the fact that the drag has a variable component in the radial direction because of solar radiation pressure. Smaller contributions to the *PD* vector come from the Earth albedo, the Earth infrared radiation and, by a smaller amount, from the eccentricity of the orbit. By finely adjusting the lengths of the suspension arms (by means of the inchworms depicted in Figure 3.7) the point *D* is displaced up or down inside this area, and brought close to *P.* In doing so, also the radial component of the drag is automatically balanced. The low frequency variations of the drag (not shown) will oscillate inside the same area. The vector *DQ* shows here the whirl instability before it is damped by the whirl control whose period in this (non spinning) frame is the natural frequency of oscillation. The circle around point Q represents the error in the measurement due to thermal noise of the mechanical oscillations built up during the integration time.

4. EXPERIMENT DRIVERS AND REQUIREMENTS

The major experiment drivers are:

- The signal
- External non gravitational forces
- Test bodies mass moments
- Whirl motions
- Satellite spin frequency
- Earth tides
- Temperature
- Magnetic coupling
- Electric charging

Each driver leads to derived requirements which must be met in order to achieve the GG mission goal of testing the Equivalence Principle to 1 part in 10^{17}. Below, for each driver a table lists the derived requirements that can be fulfilled at present.

A detailed physical explanation for all the entries in the tables is not reported here. However, all the requirements have been embedded in the very powerful GG Simulator tool and a full scientific simulation of the GG experiment has been performed (see Section 8.6). The resulting systematic errors in the relative displacements of the test cylinders provide a very realistic error budget for GG. They are reported in a self explanatory graphical manner in Section 4.10.

4.1 THE SIGNAL

DRIVER #1: THE SIGNAL

$\eta = 10^{-17}$	EP test GG mission target expressed in terms of the Eötvös parameter	
$h = 5.2 \cdot 10^{5}\ m$ $(a = 6.898 \cdot 10^{3}\ km)$ $(\nu_{orb} = 1.754 \cdot 10^{-4}\ Hz \quad P_{orb} = 5.7 \cdot 10^{3}\ s)$	Orbit altitude satellite tracking accuracy no issue	
	$g(h) = 8.38\ ms^{-2}$	driving gravitational acceleration
	$a_{EP} = g(h) \cdot \eta = 8.38 \cdot 10^{-17}\ ms^{-2}$	signal acceleration
$e \simeq 0.01$	orbital eccentricity (standard)	
$I \simeq 5°$	orbital inclination (typical for launch from Kourou)	
$\theta_i \leq 1°$	spin axis to orbit normal angle at start (after spin up)	
$P_{dm} = 540\ s$	Natural period of test masses oscillations in differential mode	
	$\Delta x_{EP} = \frac{a_{EP}}{4\pi^2} \cdot P_{dm}^2 = 0.62 \cdot 10^{-12}\ m$	Signal displacement
$SNR = 2$	Signal to noise ratio	
$T_{int} = 7 \cdot 86400\ s$	Minimum Integration time	

4.2 EXTERNAL NON GRAVITATIONAL FORCES

DRIVER #2: EXTERNAL NON GRAVITATIONAL FORCES

$(A/M)_{GG} \le 0.05\ m^2 kg^{-1}$	Maximum area to mass ratio of GG satellite
$a_{NG} \le 2 \cdot 10^{-7}\ ms^{-2}$	Maximum external non gravitational acceleration on GG in the sensitive plane
$(a_{NG})_z \le 5 \cdot 10^{-8}\ ms^{-2}$	Maximum external non gravitational acceleration on GG along axis
$\chi_{DFC} \le 1/50000$	Maximum compensation of non grav acc in the sensitive plane
$(\chi_{DFC})_z \le 1/500$	Maximum compensation of non grav acc along axis
$a_{i\_cm} = a_{NG} \cdot \chi_{DFC} \le 4 \cdot 10^{-12}\ ms^{-2}$	maximum common mode non grav acc on test masses in sensitive plane
$(a_{i\_cm})_z = (a_{NG})_z \cdot (\chi_{DFC})_z \le 10^{-10}\ ms^{-2}$	maximum common mode non grav acc on test masses along axis
$P_{cm} = 30\,s$	Natural period of test masses oscillations in common mode
$P_z = 30\,s$	Natural period of test masses oscillations along axis
$\Delta r_{cm} = \frac{a_{i\_cm}}{4\pi^2} \cdot P_{cm}^2 \le 9.1 \cdot 10^{-11}\ m$	maximum common mode displacement of test masses in sensitive plane
$\Delta z_{cm} = \frac{(a_{i\_cm})_z}{4\pi^2} \cdot (P_{cm})_z^2 \le 2.3 \cdot 10^{-9}\ m$	maximum common mode displacement of test masses along axis
$\chi_{CMR} \le 1/100000$	Maximum rejection of common mode effects in the sensitive plane
$(\chi_{CMR})_z \le 1/50$	Maximum rejection of common mode effects along axis
$\chi = \chi_{DFC} \cdot \chi_{CMR} \le 2 \cdot 10^{-10}$	Maximum total reduction of non grav acc in the sensitive plane
$\chi_z = (\chi_{DFC})_z \cdot (\chi_{CMR})_z \le 4 \cdot 10^{-5}$	Maximum total reduction of non gav acc along axis
$a_{dm} = a_{NG} \cdot \chi \le 4 \cdot 10^{-17}\ ms^{-2}$	maximum perturbing differential acceleration on test masses in sensitive plane
$(a_{dm})_z = (a_{NG})_z \cdot \chi_z \le 2 \cdot 10^{-12}\ ms^{-2}$	maximum perturbing differential acceleration on test masses along axis
$\Delta r_{dm} = \frac{a_{dm}}{4\pi^2} \cdot P_{dm}^2 \le 0.3 \cdot 10^{-12}\ m$	maximum differential displacement of test masses due to external non gravitational forces in sensitive plane
$\Delta z_{dm} = \frac{(a_{dm})_z}{4\pi^2} \cdot (P_{dm})_z^2 \le 4.6 \cdot 10^{-11}\ m$	maximum differential displacement of test masses due to external non gravitational forces in sensitive plane
$\chi_{bridge} \le \frac{\Delta x_{EP}}{\Delta r_{cm}} \simeq 6.8 \cdot 10^{-3}$	Maximum fractional mechanical unbalance of capacitance bridges
$d_{bridge} = 2.5 \cdot 10^{-3}\ m$	bridge gap
$\Delta d_{bridge} \le d_{bridge} \cdot \chi_{bridge} \le 1.7 \cdot 10^{-5}\ m$	Maximum mechanical unbalance of capacitance bridges
$P_{PGB} = 360\,s$	Natural oscilaltion period of PGB in the sensitive plane
$(P_{PGB})_z = 30\,s$	Natural oscilaltion period of PGB along axis

4.3 Test bodies mass moments

Driver #3: Test bodies mass moments

$\left(\frac{\Delta J}{J_x}\right)_{TMs} < 1.2 \cdot 10^{-2}$		Maximum fractional difference between the principal moments of inertia of the test bodies
	$a_{qp}^{\oplus} < 0.5 \cdot a_{EP}$	maximum differential acceleration from Earth monopole coupling to quadrupole moments of test bodies
	$\Delta x_{qp}^{\oplus} < 0.5 \cdot \Delta x_{EP}$	maximum differential displacement from Earth monopole coupling to quadrupole moments of test bodies

4.4 Whirl motions

Driver #4: Whirl motions

$Q_{TMs} \geq 20000 \quad (at\ spin\ frequency)$	Minimum quality factor of the test masses suspensions for losses occurring at the spin frequency (1Hz)
$Q_{PGB} = 90 \quad (at\ spin\ frequency)$	quality factor of PGB suspensions at spin frequency (1Hz)
$(r_w)_{TMs} \leq 10^{-8}\ m$	Maximum whirl displacement of test masses
$(r_w)_{PGB} \leq 10^{-8}\ m$	Maximum whirl displacemnet of PGB
$k_{safety} = 1.5$	safety factor of whirl control to ensure damping of whirl velocity
$\varphi_{error} \leq 0.14°$	maximum phase error of applied control force

4.5 SATELLITE SPIN FREQUENCY

DRIVER #5: SATELLITE SPIN FREQUENCY

$\nu_s = 1Hz \quad (in\ LVLH\ reference\ frame)$ $\nu^* = \nu_s + \nu_{orb} = 1.0001754\ Hz \quad (in\ the\ IRF)$	Nominal spin frequency of GG satellite
$\left(\Delta\nu_s / \nu_s\right) \le 10^{-5} \div 10^{-4}$	Maximum fractional measurement error in the satellite spin frequency (whatever its nominal value)

4.6 EARTH TIDES

DRIVER #6: EARTH TIDES

$\varepsilon_{mech} \le 10^{-5}\ m$	Initial offset (by contruction and mounting) of the centers of mass of the cylinders from their rotation axes
$\Delta z_{TMs} = \frac{(a_{dm})_z}{4\pi^2} \cdot (P_{dm})_z^2 \le 4.6 \cdot 10^{-11}\ m$	Maximum dispalcement along axis between the test masses (gives rise to tidal displacement in sensitive plane)

4.7 TEMPERATURE

DRIVER #7: TEMPERATURE

$N_{days} \geq 20\ d$	Minimum number of days after which rebalancing of the test masses is needed
$\dot{T} \leq 0.2\quad K/d$	Maximum test masses temperature daily variation
$\Delta T / \Delta z \leq 4\ Km^{-1}$	Maximum temperature gradient along axis
$(\alpha_{CTE})_{TMs} \leq 2 \cdot 10^{-5}\ K^{-1}$	Maximum thermal expansion coefficient of test masses
$(\alpha_{CTE})_{ca} \leq 10^{-5}\ K^{-1}$	Maximum thermal expansion coefficient of coupling arms
$\Delta k / k \leq 4 \cdot 10^{-4}\ K^{-1}$	Maximum fractional thermal variation of suspensions stiffeness
$\chi_k \leq 1/100$	Maximum relative change in stiffness of suspensions with temperarure
$p_{PGB} \leq 10^{-7}\ torr\quad (p_{PGB} \leq 1.333 \cdot 10^{-5}\ Pa)$	Maximum air pressure inside OGB
$\varepsilon_{goldcoating} \leq 3 \cdot 10^{-2}$	Emissivity of goald coating

4.8 MAGNETIC COUPLING

DRIVER #8: MAGNETIC COUPLING

$\chi_{\mu shield\_PGB} \leq 1/100$	Minimum magnetic field reduction provided by mu-metal shielding of PGB
$(\chi_m)_{TMs} \leq 10^{-6}$	Maximum magnetic susceptibility of test masses
$\mu_{TMs} \leq 10^{-6}\ Am^2$	Maximum magnetic moment of test masses

4.9 Electric charging

As far as electric charging is concerned, we rely on passive electric grounding of the test masses and the co-rotation of the test masses and the capacitance transdusers, (see Section 3.2.1), in addition to gold coating of all the conductive surfaces. Moreover, surface charge patches can be measured in the GGG laboratory prototype, as we have recently shown (see Section 9.8)

4.10 Error budget

As reported at the beginning of the Section, all the requirements above have been embedded in the GG Simulator tool to run a full scientific simulation of the GG experiment (see Section 8.6). From that, we get a time history of the relative displacements of the test cylinders (they should be zero for perfectly free falling bodies and in absence of an EP violation!!) which allows us to establish both systematic and random errors.

The systematic errors in the relative displacements of the test cylinders provide a very realistic error budget for GG, as depicted graphically in Figures 4.1 and 4.2 below, and described in detail in the figure captions.

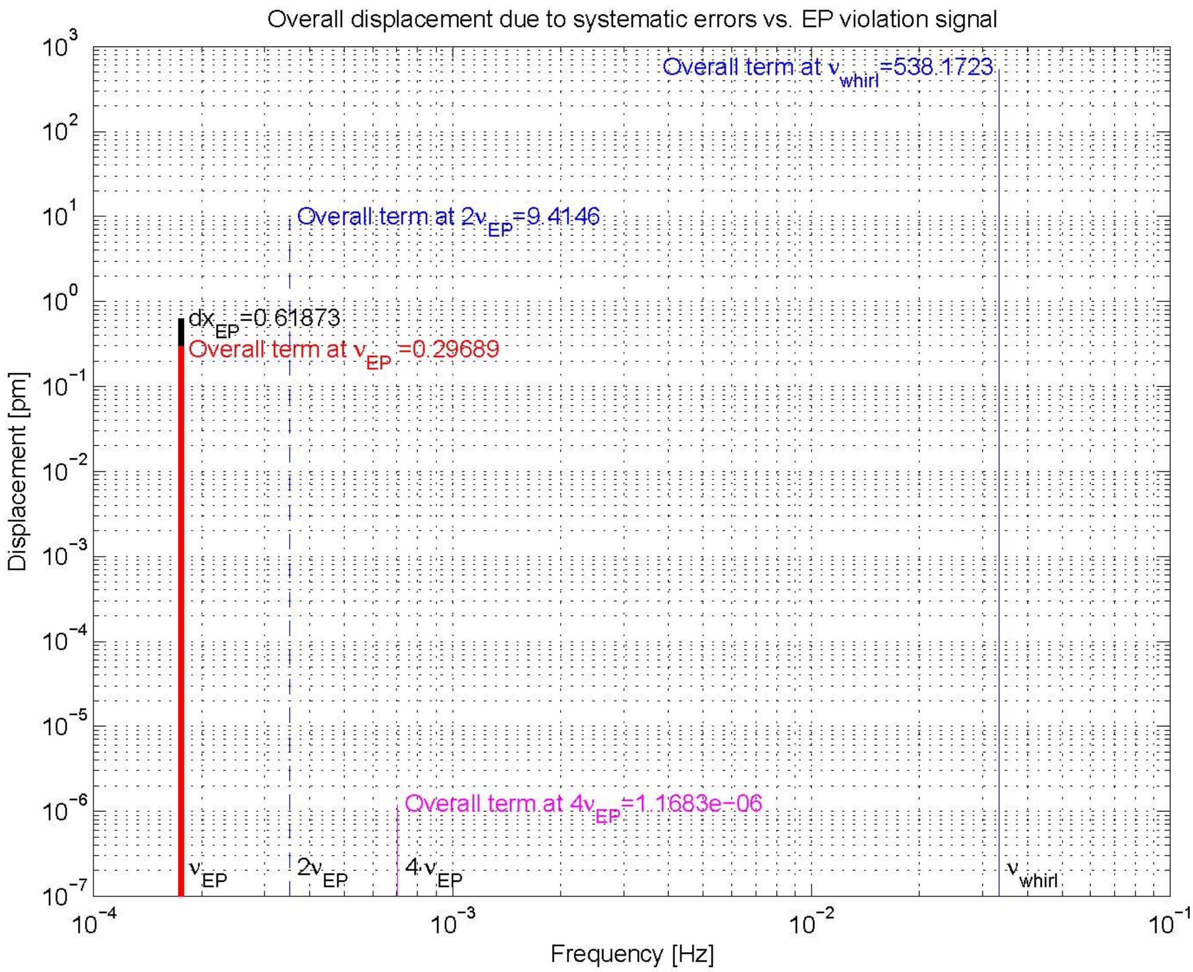

Figure 4.1: Amplitude Spectrum of the test masses differential displacement due to the main systematic errors vs the target EP violation signal $\Delta x_{EP} = 0.61\,pm$ (at the orbit frequency $\nu_{EP} = 1.7538 \cdot 10^{-4}\,Hz$ w.r.t. the inertial reference frame IRF). The amplitude of the error at the orbit frequency is smaller than the signal by a factor about 2. The closest error line is at twice the orbit frequency, with an amplitude one order of magnitude bigger of the signal: this error can be easily distinguished from the signal during data processing, since the duration of each elementary experiment is about one week (the provided minimum step in frequency is about one millionth of Hz). The amplitude of the error at 4 times the orbit frequency is negligible. The error at the whirl frequency is easily removed during the synchronous demodulation of the post-processing.

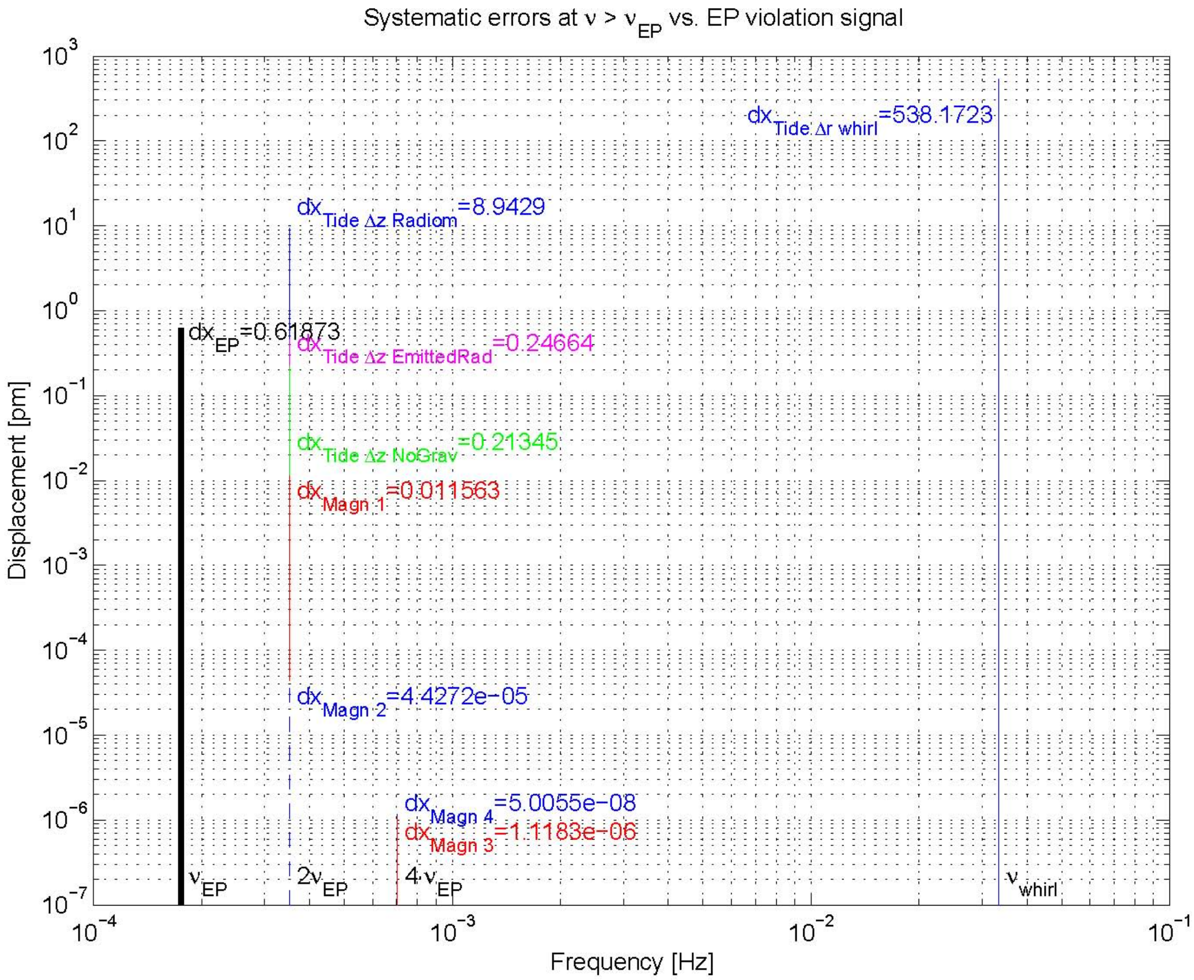

Figure 4.2: Detailed view of the Amplitude Spectrum of the main systematic errors (the target EP violation signal $\Delta x_{EP} = 0.61\,pm$ at the orbit frequency is reported for direct comparison). At $2\nu_{EP}$ the errors due to magnetic coupling are negligible. At this ferquency the main component of the displacement is due to the test masses differential displacement along the spin axis which through the gravity gradient generates a displacement in the plane of the science measurement. The differential displacement along z is due mainly to the radiometric effect (worst case assumption for the residual pressure inside the PGB is made, and a better value is expected); smaller contributions are due to the residual s/c non-gravitational acceleration and to the proof masses emitted radiation. At $4\nu_{EP}$, the two different magnetic induced displacements are negligible.The whirl, and the Earth tides coupled with whirl generate three lines: at frequencies: ν_{whirl} and $\nu_{whirl} \pm 2\nu_{EP}$. The three lines appear here as a single line at ν_{whirl} due to their negligible separation in the loghartmic frequency scale. All three lines do not affect the signal detection, due to their large separation in frequency w.r.t. the orbit frequency ν_{EP}.

Random noise is also available from the simulator, but is not reported here.

A theoretical calculation of the thermal noise to be expected as the ultimate limitation, it has been shown in the past (see Section 2.2.7 in [22]). In GG the large mass of test bodies (10 kg) and the long period of their natural differential oscillations help in reducing thermal noise. Moreover, in supercritical rotation the relevant losses take place at the (high) spin frequency, at which they are small (see Section 9.3 for losses measured with the laboratory prototype)

5. PAYLOAD DESCRIPTION

5.1 PAYLOAD MAIN ELEMENTS

The GG payload is housed inside the "spinning top (see Figure 3.6). It contains in a nested configuration –and always respecting the cylindrical symmetry, as well as "top/down" symmetry with respect to the center of mass of the whole system– the following main elements:

- the PGB laboratory, with its central shaft, connected to the "spinning top" by mechanical springs at its "top" and "bottom" (see Figure 3.3 and details on the springs in Figures 5.1 , 5.2)
- the differential accelerometer for EP testing (see Figure 3.7) with U shaped laminar suspensions connecting its coupling arm (see below) to the PGB shaft/tube at its center
- a perfectly symmetric coupling arm (see Figure 3.7) made of two pieces, arranged inside each other in order to guarantee the required symmetry; each piece is connected at the center to the PGB shaft via U shaped laminar suspensions (see Figure 5.3 and 5.4)
- two coaxial concentric test cylinders, each one connected to the coupling arm described above via U shaped laminar suspensions. Note that the test cylinders are not directly connected to the PGB, otherwise they could not form a balance and reject common mode effects. They are connected to the PGB only through the coupling arm, which is indeed the beam of the balance
- two opposite pairs of capacitance plates located halfway in between the test cylinders forming two capacitance bridges and rigidly connected to the PGB shaft
- small capacitance plates (arranged as capacitance bridges) to sense the relative motion (in all 3 directions) of the PGB wrt the spacecraft which provides the input signal to the drag free control loop. They also serve as actuators to damp the whirl motion of the PGB (see Figure 3.21 (right) where they are labeled as "active dampers"; a better view is given in Figure 3.22)
- small capacitance plates (arranged as capacitance bridges) similar to those described above, between each test cylinder and the PGB shaft. They are used as sensors and actuators within the whirl control loop (to damp the whirl motion of the test cylinders relative to the PGB)

The PGB accommodates also the electronics of the capacitance read-out system (see for instance Figure 9.1 for the laboratory prototype), while data from the accelerometer will be transmitted by an optical link (the same in the lab prototype). The PGB springs will allow the required power to be provided from the spacecraft to the accelerometer (read out electronics and inchworms; note at present the GGG rotating electronics –read out only- requires 4 Watt)

The Figures below show several details of the components just described.

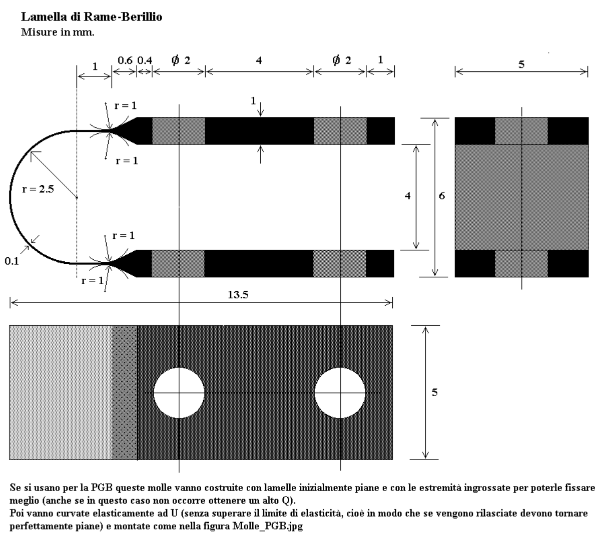

Figure 5.1: Construction details of the springs connceting the PGB to the spacecraft (see also Figure 3.3)

Flessione di una sbarretta con un'estremita' fissa

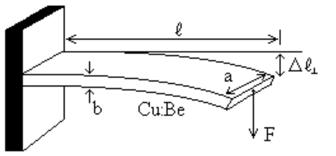

$$\Delta\ell_\perp = \frac{4}{Y}\cdot\frac{F\,\ell^3}{a\,b^3}$$

Y = Young's modulus

Energia elastica del sistema

$$E = \int_0^{\Delta\ell_\perp} F(x)dx$$

Y(Pure Cu) = $12\cdot10^{11}$ dyne/cm²
Y(Cu:Be) ~ $19\cdot10^{11}$ dyne/cm²
Y(Steel) = $21\cdot10^{11}$ dyne/cm²

Def. $F \equiv k\cdot\Delta\ell$ $\qquad k_\perp = \frac{Y\,a\,b^3}{4\,\ell^3}$

Per una molla a forma di U e con un braccio rigido di lunghezza L si ha:

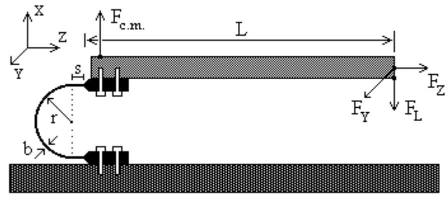

$r = 0.25$ cm
$s = 0.1$ cm
$\ell = \pi\cdot r + 2s \cong 1$ cm
$b = 5\cdot10^{-3}$ cm
$L = 20$ cm
$a = 0.5$ cm

$k_\ell = \frac{Y\,a\,b^3}{4\,\ell^3} \cong 3\cdot10^4$ dyne/cm $\qquad k_L = \frac{Y\,a\,b^3}{4\,\ell\,L^2} \cong 74$ dyne/cm

$k_Z \cong \frac{1}{2}\,\frac{Y\,a\,b^3}{4\,r^3_{+s}} \cong 9.5\cdot10^5$ dyne/cm $\qquad k_{c.m.} \cong k_Z$

$k_{c.m.}/k_\ell \cong 32$ $\qquad k_{c.m.}/k_L \cong 12800$ $\qquad k_Y \cong k_L$

Prove sperimentali effettuate con un pezzetto di lamella di Cu:Be di spessore $b = 50\,\mu$

Con: $a = 1$ cm $r = 0.4$ cm $s = 0.1$ cm $L = 8$ cm $F_L = 50$ mgr $\simeq 50$ dyne
si ha: $\Delta\ell \simeq 0.5$ cm $\Rightarrow$ $k_L \simeq 100$ dyne/cm $\quad Y \sim 19\cdot10^{11}$ dyne/cm²

Con $F_Y = 1$ gr	si ha:	$\Delta\ell_Y \simeq 1.54$ cm	$k_Y/k_L \simeq 6.5$
Con $F_{c.m.} = 8$ gr	si ha:	$\Delta\ell_{c.m.} = 0.05$ cm	$k_{c.m.}/k_L \cong 1600$
Con $F_Z = 10$ gr	si ha:	$\Delta\ell_Z = 0.1$ cm	$k_Z/k_L \cong 1000$
Con: $a = 0.5$ cm	$F_Y = 1$ gr	$\Delta\ell_Y \simeq 2.6$ cm	

Per una lamella fatta con un nastro di Rame-Berillio inizialmente piano, poi curvata a forma di U senza superare il suo limite di elasticita' e tenuta compressa fra due piani paralleli da una forza F_Z si ha:

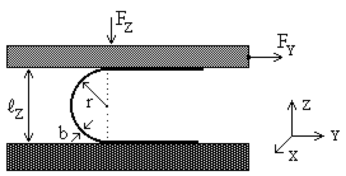

$\ell_Z = 2r$

$$\Delta\ell = \frac{4}{Y}\cdot\frac{F\,\ell^3}{a\,b^3}$$

Per far scorrere in direzione Y la superficie superiore rispetto all'altra, come se fosse su una ruota, non occorre nessuna forza F_Y. Infatti durante tale moto la molla mantiene inalterata la sua energia elastica (se r non varia) in quanto si flette ad una estremita' del diametro verticale aumentando l'energia elastica, e si rilascia (si srotola) dall'altra, diminuendo l'energia di una uguale quantita'.

Percio', in linea di principio, se le superfici sono piane, pulite, e se la molla e' omogenea, il k_Y di questa molla e' zero.

In pratica si potra' ottenere un k_Y positivo o negativo se le superfici sono rispettivamente un po' concave o un po' convesse.

Figure 5.2: Mechanical properyties of the springs designed to conncet the PGB to the spacecraft

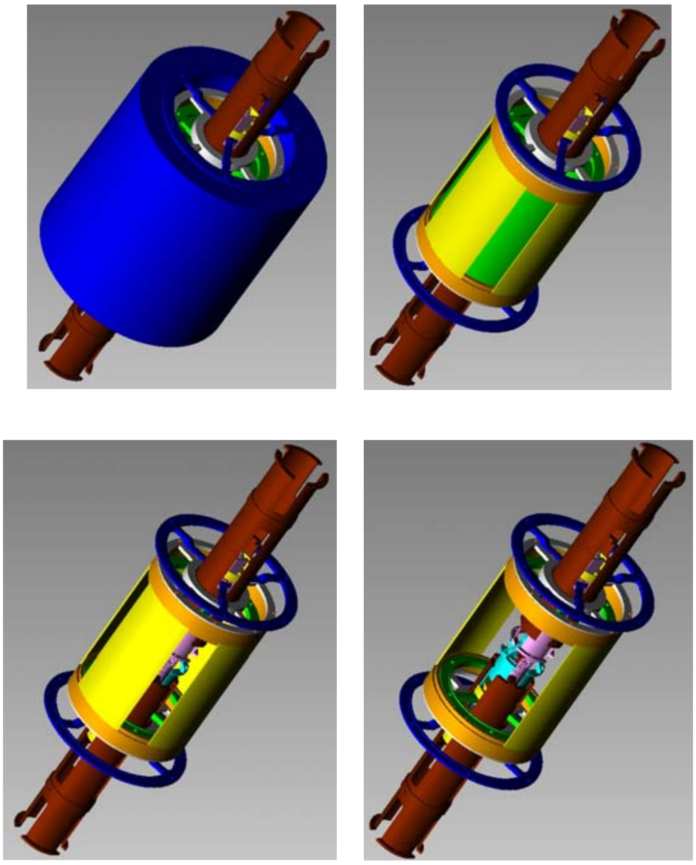

Figure 5.3: Details from the engineering drawings of the GG differential accelerometer showing further and further parts going from “outside” to “inside”. The brown central tube is the PGB shaft. The blue and green cylinders are the test cylinders, the yellow plates are the capacitance bridge plates to measure the relative displacements of the test cylinders. Note that the outer diameter of the blue test cylinders is about 23 cm

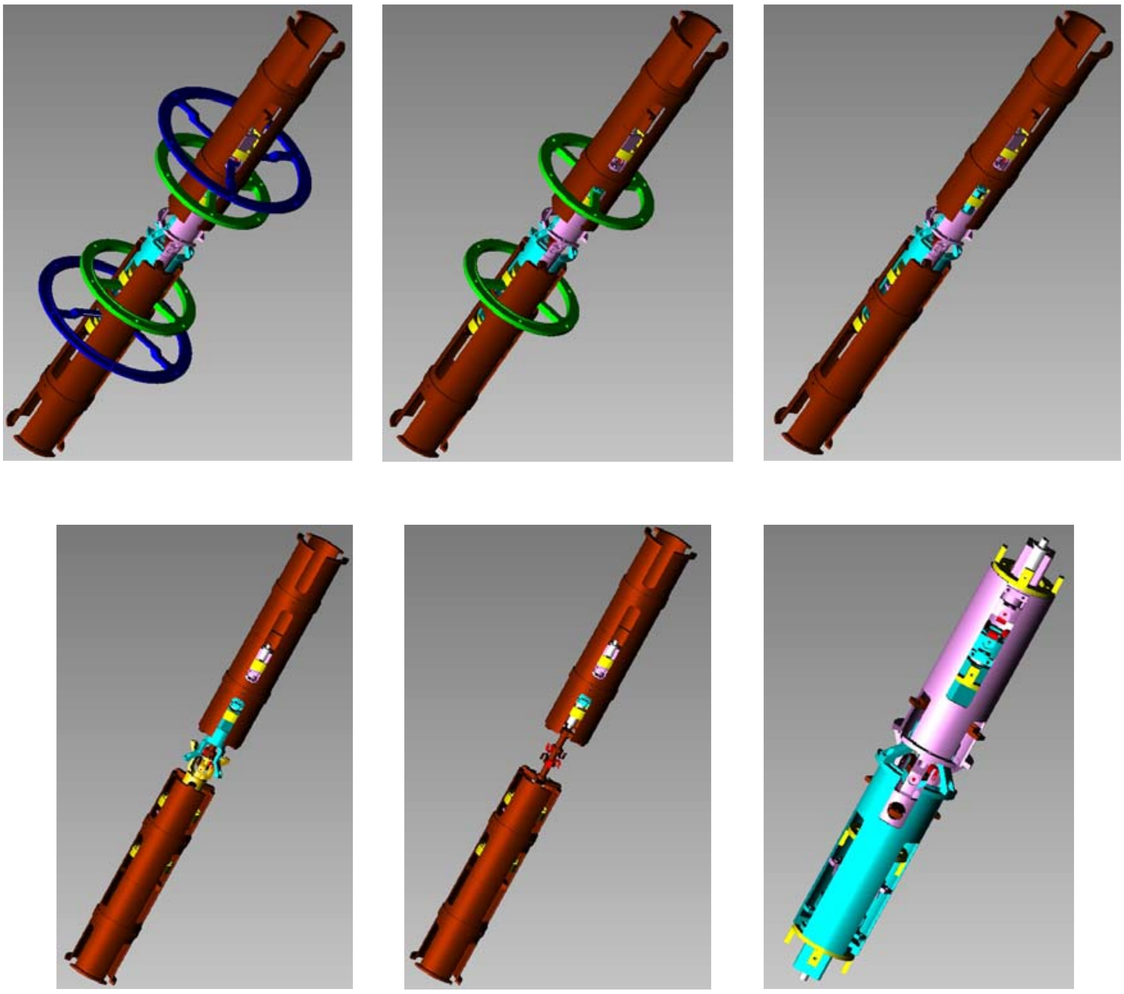

Figure 5.4: From previous figure: further details after removing components one by one. In the last picture only the coupling arm remains, a dn it is clear how it is made symmetric by putting together the two parts (pink and light blue). In the figure before the last, the PGB shaft is well visible, showing its center where the two pieces of the coupling are connected, each one with 3 U shaped laminar suspensions at 120° from each other.

5.2 LOCK/UNLOCK MECHANISMS

The PGB, the test cylinders and the coupling arms –being weakly suspended– will have: a static lock mechanism in order to withstand large accelerations at launch, to be unlocked once in orbit (1-shot). In addition, by design, each suspended mass is constrained to only slight movements in all directions (mechanical stops) as it is apparent from the 3D drawings shown in Figures 5.3 and 5.4.

Finally a refined lock/unlock system, with inch-worms and pressure sensors, has been designed for the system in orbit (shown and described in Figure 5.5) in order to gently release the test masses and the PGB in absence of weight. Unlike the static lock, this system can be re-used during the whole mission to lock/unlock the bodies in orbit should the need occur.

The latter mechanism is finely designed but is no matter of concern because of the very small forces involved at zero-g and the high reliability of inch-worms (based on PZTs). The single shot static lock is a “brute force” lock to be used only once but obviously crucial to the experiment; special care is being devoted to it by DTM Technologies, a company with considerable expertise and a long successful record of collaboration with Thales Alenia Space for issues related space mechanics and Ferrari for ground mechanics.

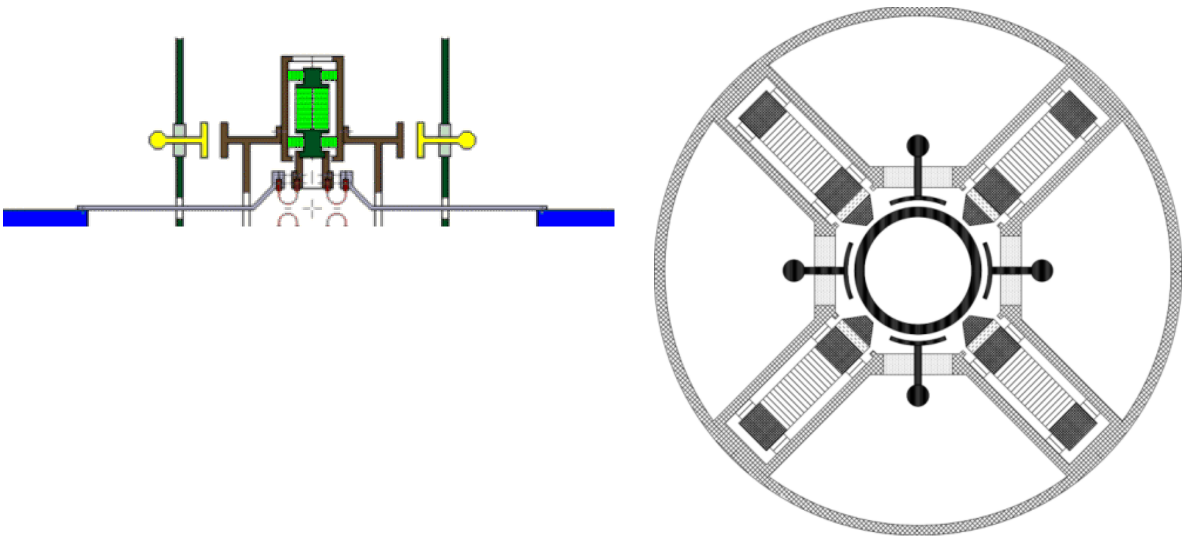

Figure 5.5: (right) Top view (across the spin/symmetry axis) of one set of 4 inch-worm actuators for fine unlocking of the suspended GG bodies; this figure refers to unlocking the PGB from the spacecraft. The inner tube of about 10 cm radius (belonging to the PGB) encloses one of the PGB suspension spring (as shown in Figure 3.3). This system is located at the top (or bottom) of the PGB suspensions. Each suspended cylinder needs 2 sets like the one shown here placed at its two axial ends. (left) Section through the symmetry axis (as in Figure 3.7) showing the detailed location of this fine lock/unlock device for one of the test cylinders.

5.3 THERMAL STABILIZATION AND CO-ROTATION

Thermal stability of the GG accelerometer is very important as temperature induced distortions may unbalance the test masses, unbalance the capacitance bridge transducers, displace the test masses along the axis direction. The high symmetry of the entire system and its rapid rotation help considerably in reducing such effects (most importantly the radiometer effect, [37, 38)]).

However, the low equatorial orbit causes a strong thermal stress on the GG satellite as it goes in and out of the Earth shadow every orbit. This orbit has been selected, instead of a high-inclination sun-synchronous orbit, in order to avoid re-aligning the spin axis of the satellite with the orbit normal during the mission, so as to perform a more passive and less disturbed experiment, and also to reduce the complexity and cost of the mission (see [39, 40]). It definitely turns out to be the best choice with the availability, in the near future, of the VEGA launcher (see Section 3.5 and Section 6).

Considerable effort has therefore been devoted to the thermal stabilization of the GG payload. The thermal control shall provide a suitable thermal conditioning of the PGB environment, in terms of high stability in time of the test mass temperatures, and low axial as well longitudinal temperature gradients of the test masses themselves.

The thermal control subsystem is entirely designed on material-standard equipments and a classical passive approach is used to counter the external (direct Sun, albedo, Earth infrared radiation) as well internal (equipment power dissipations) thermal loads and their oscillations, aiming at maintaining as constant and uniform as possible the thermal environment around and inside the PGB.

MLI blankets are used to decouple loads and attenuate oscillations. They are used both to protect the external surface of S/C from external environment and to decouple the PGB from inside of S/C where the electronic units are installed. The connections of dissipating equipment to equatorial radiators are provided (all the boxes are located around the equatorial cylinder surfaces), via thermal fillers, to increase their contact conductance at the boxes radiator contact baseplates; heaters are employed when necessary to trim or maintain the necessary temperature levels.

The “spinning top” structure (shown many times in this Report; see e.g Figure 3.5) will be made of carbon fiber composite to reduce thermal distortions.

It is worth stressing that so far no need has arisen for active heaters.

An issue has arisen about co-rotation of the PGB with the outer spacecraft. The spin rate of the outer shell will change if the moment of inertia of the shell changes while the spin angular momentum remains constant. This happens due to temperature variations of the outer shell as the GG satellite gets in and out of the Earth shadow, which is not the case for the PGB since it is very well insulated and thermally de-coupled from the spacecraft. The resulting phase difference is very large, because of the rapid rotation. However, the absolute change in the moment of inertia is indeed very small. This means that it can be balanced by a small compensation mass. Moreover, compensation can be passive; the idea is to have a mass which expands and contracts in anti-phase with respect to the outer shell of the spacecraft so as to keep the total moment of inertia (of the outer shell plus the compensation mass) essentially constant.

Co-rotation between the PGB and the spacecraft shell with be sensed by placing a small mirror on the PGB tube and a photo-detector on the spacecraft (it adds no wire to the PGB). Should a residual phase lag be detected, it will drive the thrusters of the drag free control loop for compensation.

Several solution for passive mass compensation are available and a final choice will be made by the end of this Study.

Note that no such phase lag will take place between the PGB and the test bodies because of the very good thermal insulation; spring coupling will take care of eliminating residual small phase lags (e.g. left out by the unlocking procedure) during the initial phase of the mission

5.4 TEST MASSES MATERIALS

The choice of the test masses composition should be made in order to maximize the possibility that an EP violation may occur.

Since one does not expect that hypothetical EP violations can depend on such macroscopic properties of matter like density, and on chemical, mechanical, electric or magnetic characteristics, one should look for other properties of matter for deciding what substances to choose for the test. In [41], for all the elements of the periodic table, are calculated and plotted the three properties that are considered as the most likely sources of a possible EP violation, namely

- B/μ ($B = N + Z$ being the number of barions, N the number of neutrons, Z the number of protons, μ the mass in units of the mass of the H atom)
- L/μ (L the lepton number; for neutral atoms $L = Z$)
- I_z/μ ($I_z = N - Z$ the z component of Isospin)

Figure 5.6, 5.7 and 5.8 are adapted from the corresponding plots reported in [41]. According to Figures 5.7 and 5.8, CH_2 and Pb are the best possible choice, while from Figure 5.6 this choice is about equivalent to the typical choice of Be for one mass and Cu or Ti for the other.

With CH_2 we indicate all solid polymers like polyethylene $(C_2H_4)_n$, polypropylene $(C_3H_6)_n$ etc.., all with the same proportion of Protons and Neutrons as CH_2

It is very important to stress that in GG, due to the fast rotation of the test masses there is no need to manufacture them to need to very high precision, as small anomalies would give DC effects not competing with the signal. This is also why the GG test bodies can be 10 kg each, that is, considerably more massive than test masses typically used for ground experiments or proposed for space. The case for larger masses is obviously to reduce thermal noise.

We are therefore considering using CH_2 and Pb since this choice would maximize the possibility for an EP violation for the same target sensitivity of the GG experiment.

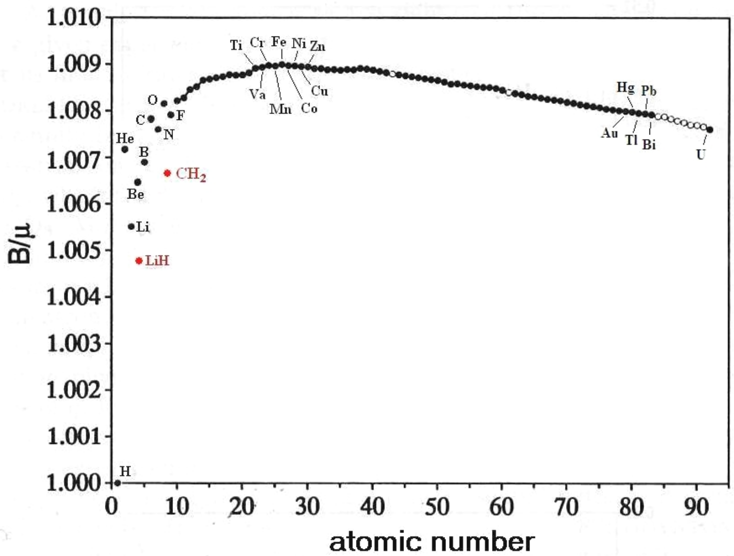

Figure 5.6: B/μ as function of the atomic number (the red dots have been added to the original plot in [41])

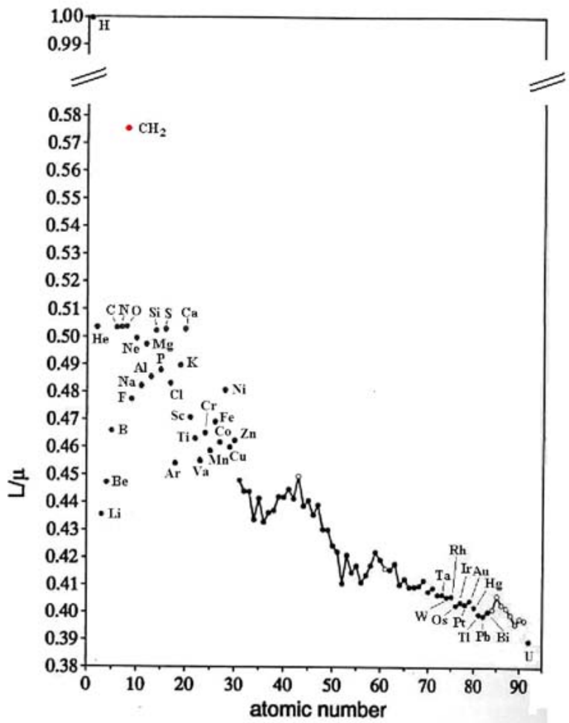

Figure 5.7 : L/μ as function of the atomic number (the red dot has been added to the original plot in [41])

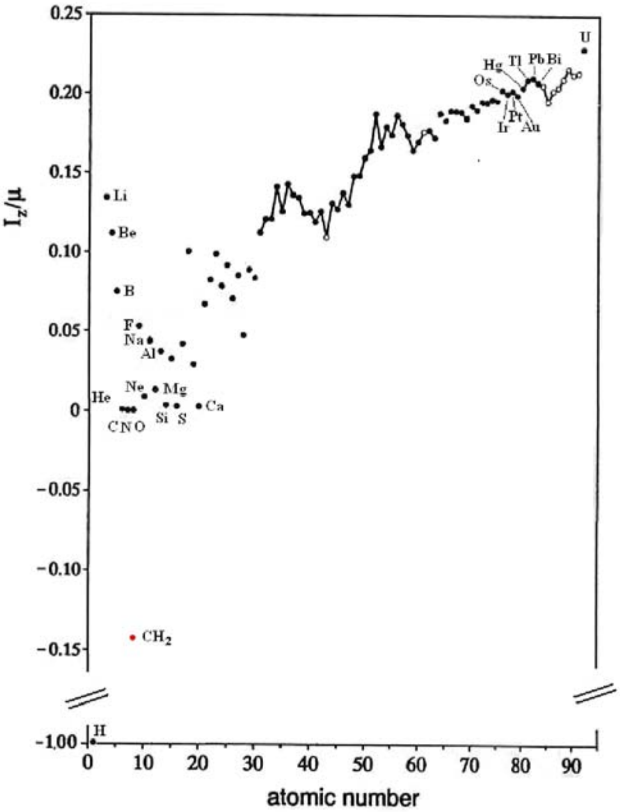

Figure 5.8: I_z/μ as function of the atomic number (the red dots have been added to the original plot in [41])

6. SATELLITE, ORBIT AND THE VEGA LAUNCHER

6.1 LAUNCHER AND MISSION

The satellite will be launched directly into near-circular, near-equatorial orbit by a small / medium launcher such as Vega (baseline) or PSLV (backup). Both launchers have capability much in excess of a small spacecraft such as GG, and a dual launch might be taken into consideration (Figure 6-1).

The design launch altitude will be between 520 km and 600 km, according to the strategy discussed below. No orbit maintenance is planned, and the spacecraft altitude will be allowed to decay gently in time, with negligible impact on the satellite mission and operations.

A preliminary sequence of events is in Table 6-1. Once set up and initialized, the experiment will run in a regular way without any changes to either orbit or attitude. Given the near-equatorial orbit, the satellite will experience a regular once-per-orbit sequence of eclipses (35 minutes) and passes above the equatorial ground station of San Marco near Malindi, Kenya (about 10 minutes, with small variations depending on the selected altitude).

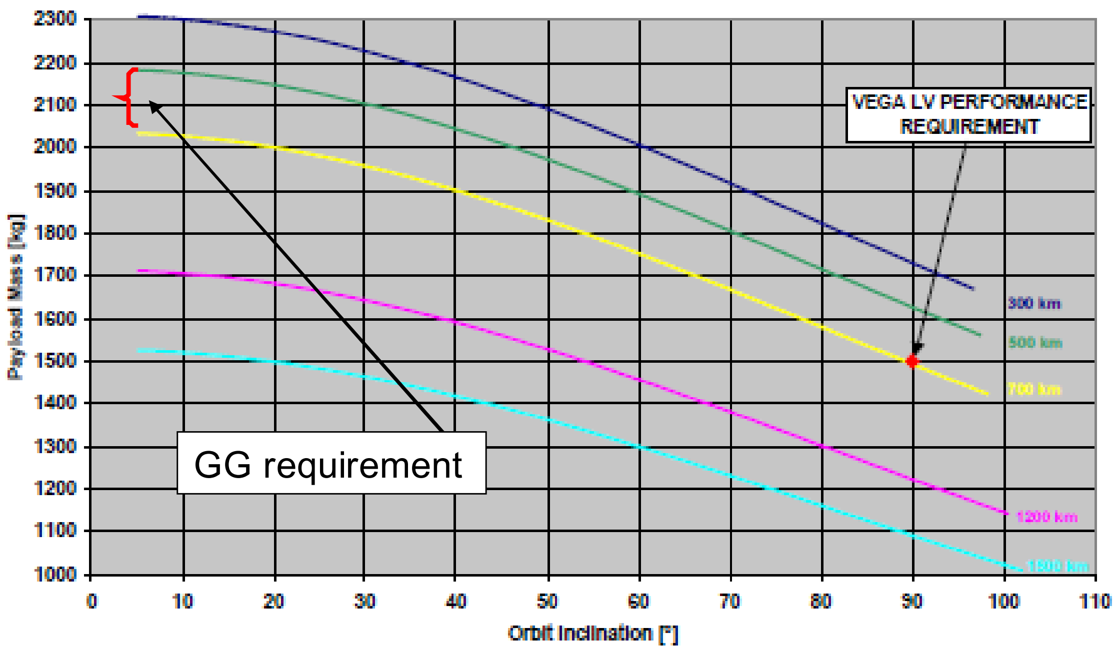

Figure 6-1: VEGA performance for circular orbits. The launcher requirement is 1500 kg in a 700-km altitude polar orbit. The lower limit to the orbit inclination is about 5°, and is set by the latitude of the Kourou launch site (5°N). For such a near-equatorial orbit, as required by GG, the VEGA performance is in excess of 2000 kg, much above the needed spacecraft mass.

Launch and Ascent Phase	
duration: ≈1 hour	3-axis stabilized release by the launcher satellite off on lift-off; activation of OBDH and RF by separation switch
Early Orbit Phase	
duration: ≈1 day	sun acquisition, rate damping and coarse spin attitude stabilization (autonomous) satellite acquisition by the EOP ground station network satellite health check
Satellite Commissioning	
duration: ≈1 week	satellite control handed over to the dedicated ground station subsystem commissioning satellite spin-up (semi-autonomous, assisted by the ground station)
Payload Switch-on and Calibration	
duration: ≈3 weeks	FEEP thruster switch on (pre-calculated thrust profile) Coarse thruster calibration Activation of electrostatic dampers common-mode sensing PGB unlocking Activation of common-mode sensing Activation of drag-free control Activation of spin rate control Test mass unlocking Test mass centering & alignment Fine test mass set-up / iteration
Scientific Mission	
duration: 2 years	Routine data collection Calibration
Scientific Mission Extension (optional)	
duration: until consumables are exhausted	Same sequence as in the Scientific Mission

Table 6-1: Sequence of events in the GG mission

The magnitude of the drag acceleration experienced by the satellite is a key to its performance, via the common-mode rejection ratio of the experiment and the drag-free control. As is well known, the scale height of the Earth's upper atmosphere (and thus the drag on low Earth orbit satellites) is very sensitive to the intensity of the short-wavelength solar radiation and the level of geomagnetic activity. Both parameters are function of epoch and are routinely forecast by a number of organizations, with sufficient accuracy for satellite lifetime and perturbation studies. In this study, we have used the 95% confidence level NASA forecast of the solar activity index F10.7, and of the daily global index of geomagnetic activity Ap, for the time period [2013, 2020], which encompasses atmosphere conditions ranging from near-solar maximum to solar minimum (see Figure 6-2).

In order to design the on-board systems independently of the epoch, a maximum acceleration threshold of 2×10^{-7} m/s^2 is specified, and the launch altitude is selected in such a way that the threshold will not be exceeded, in the time span of interest for the mission, at the 95% probability level. Given the downward trend of the solar flux from 2012 on, this criterion shows (Figure 6-3) that the mission design altitude needs to be >600 km if the launch occurs before 2015, and can be 550 km or lower if the launch occurs in 2016 or after. This range of variation of the altitude is of no consequence to either the launch mass or the scientific mission performance.

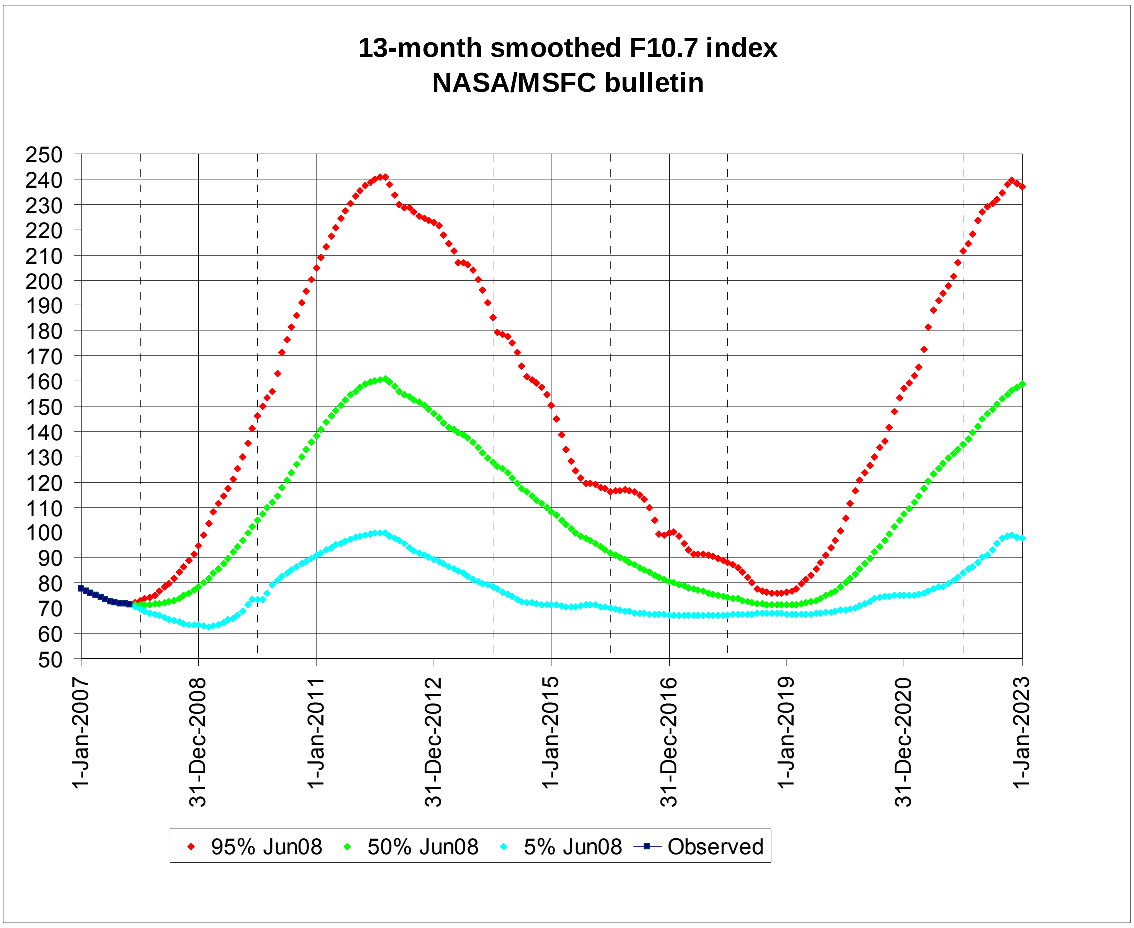

Figure 6-2: NASA forecast of F10.7 solar flux index [June 2008 NASA MSFC bulletin]

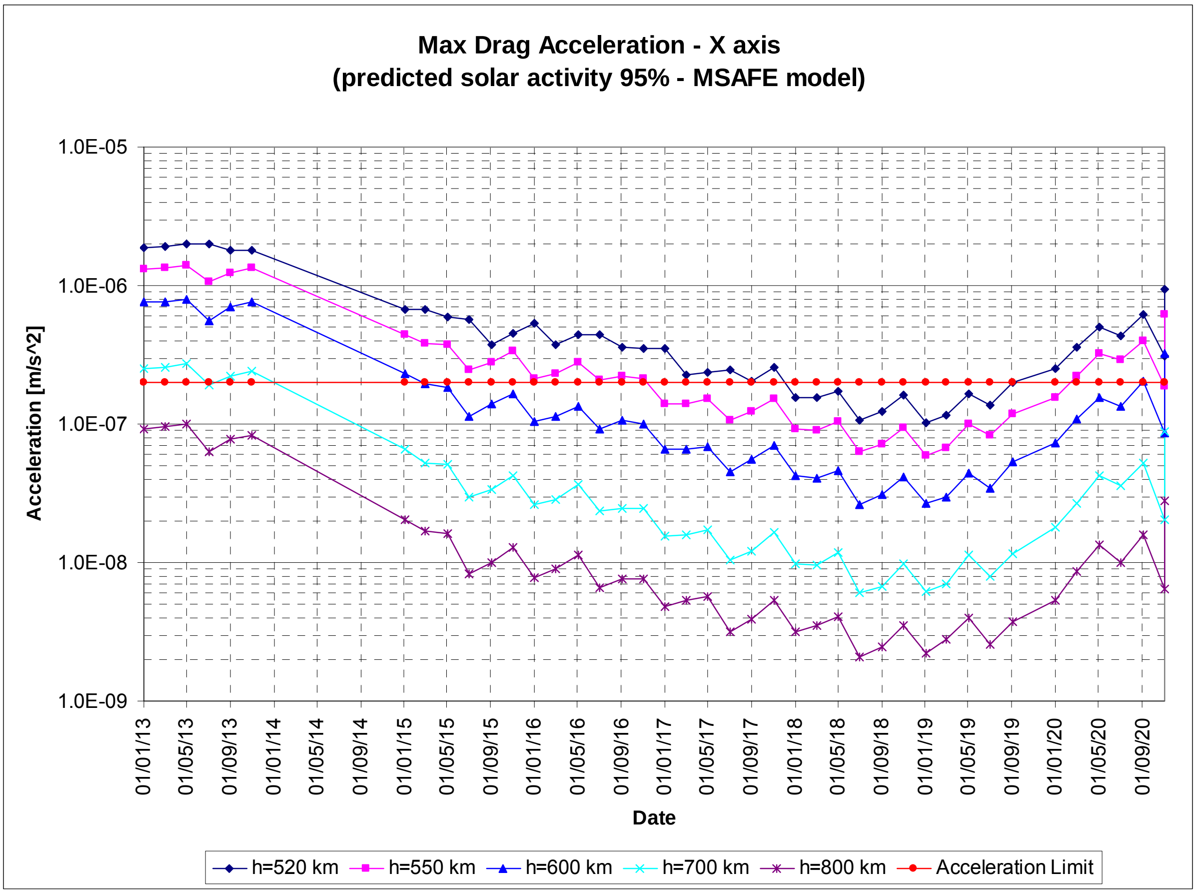

Figure 6-3: Parametric analysis of the drag acceleration. The atmospheric density is taken at the 95% probability level according to the NASA forecast of June 2008. The area-to-mass ratio is 0.0046 m²/kg. A maximum drag acceleration level < 2.0E-7 m/s² first becomes available at mean orbit altitude < 600 km in January 2015.

6.2 SATELLITE MECHANICAL CONFIGURATION

The cylindrical symmetry of the test masses and their enclosure, the Pico-Gravity Box, and the spin required to provide high frequency signal modulation, lead to a spacecraft of cylindrical symmetry, stabilized by rotation about the symmetry axis.

The main configuration requirements of the GG spacecraft are as follows.

- The GG experiment implies an ad-hoc configuration; reuse of an existing platform cannot be proposed. Conversely, many pieces of equipment may be inherited from the PRIMA complement.

- The spacecraft must be made compatible with the Vega launch vehicle (the previous design exercise was focused on Pegasus). In particular, the configuration shall fit the Vega fairing envelope, and the standard Vega 937 B adapter shall be used for launcher separation.

- The configuration shall allow easy integration of the PGB, with mounting/dismounting possible even during the last steps of the satellite integration.

- Low area-to-mass ratio is required ($\leq 0.005\ m^2/kg$). The spacecraft shape and its mass distribution must have a degree of cylindrical symmetry. The spin axis must be a principal axis of inertia, with the following constraints
  - $J_{spin} > J_{trans}$
  - $\beta = (J_{spin} - J_{trans})/J_{trans} \sim 0.2 \div 0.3$.

The proposed solution is therefore a dedicated “spinning-top” structure supporting the PGB and equipment, plus two cylindrical solar panels; sensors and electric thrusters are mounted to a central belt, while the two S-band antennas, both fixed, are mounted on booms aligned with the spin axis.

The GG structural configuration is depicted in Figure 6-4. The external structure, completely enclosing the PGB laboratory, is made from CFRP, for minimum thermal distortions, and is made up of three parts:

- central cylinder with 1.4 m diameter, with thermal radiators cutouts;
- upper truncated cone, with the dismountable interface to the PGB suspension system;
- lower truncated cone, symmetrically placed, hosting the launcher interface ring.

The upper cone is removable to allow PGB integration. Equipment items are mounted internally to the central belt; thrusters and sensors are mounted externally. The solar array is made of two cylinders separated by a central belt for mounting equipment, including thrusters and sensors; this solution also allows a convenient distribution of thermal covers and radiators to achieve an efficient thermal control.

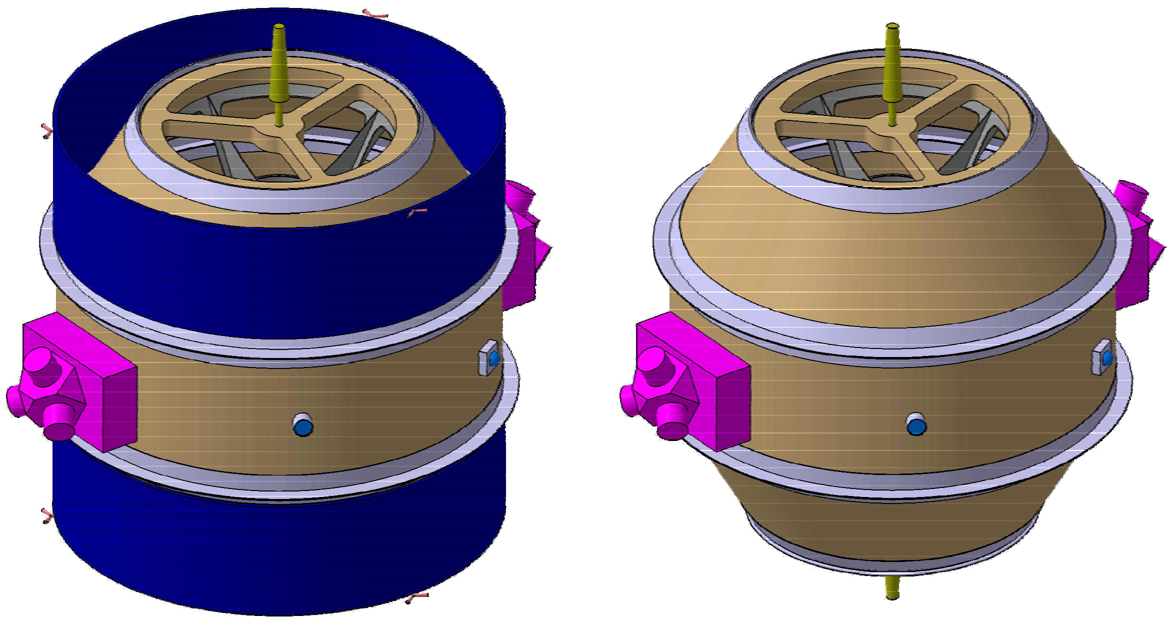

Figure 6-4: GG Spacecraft Configuration. Left: integrated configuration. Right: solar panels removed to show underlying structure.

The details of the configuration are listed below, from bottom to top, together with their component materials:

- interface ring with the launcher (7075 Al-alloy TBC);
- lower payload support cone (CFRP structure);
- lower circular plate with cut-outs, to support the lower LGA antenna;
- lower truncated cone (Al honeycomb with CFRP skins);
- lower cylindrical solar panel;
- central cylinder for mounting the equipment (Al honeycomb with Al skins);
- the equipment (see relevant s/s);
- upper truncated cone (Al honeycomb with CFRP skins);
- upper payload support cone (CFRP structure);
- upper circular plate with cut-outs, to support the upper LGA antenna;
- upper cylindrical solar panel;
- PGB assembly with the on-orbit suspension springs devices;
- two PGB launch-lock mechanism sets, released after launch;
- two antennas aligned with the spin axis, both fixed.

Figure 6-6 shows a 3D view of the satellite. The spacecraft body is about 1.45 m in outer diameter and about 1.42 m high. The experimental apparatus is accommodated in a nested arrangement inside the body, as shown in outline in the transparent view of Figure 6-6. As shown by Figure 6-5, there is plenty of mass and volume available for double launch with Vega, should it become possible.

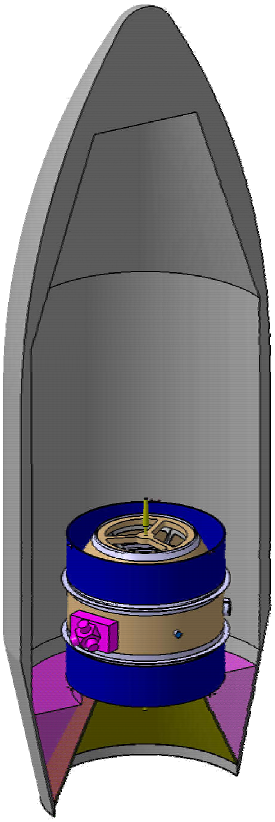

Figure 6-5: View of GG Spacecraft beneath Vega fairing

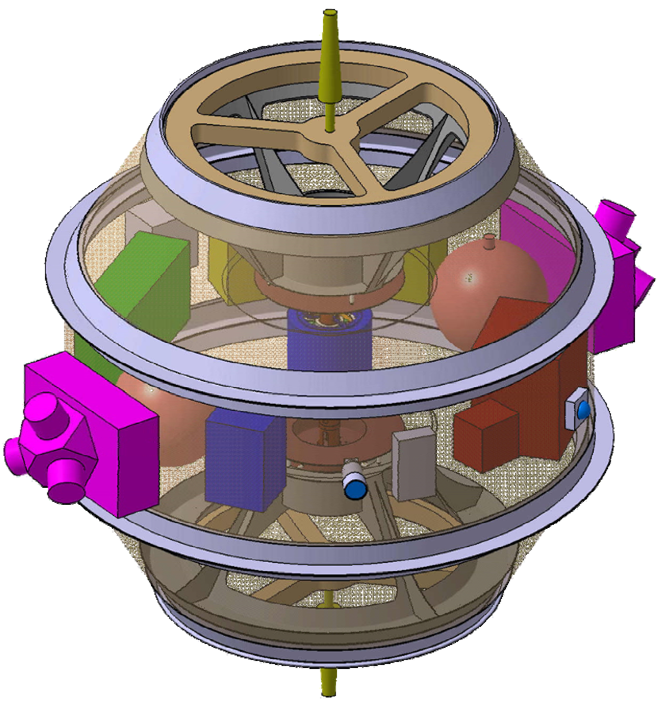

Figure 6-6: View of GG Spacecraft (transparent view)

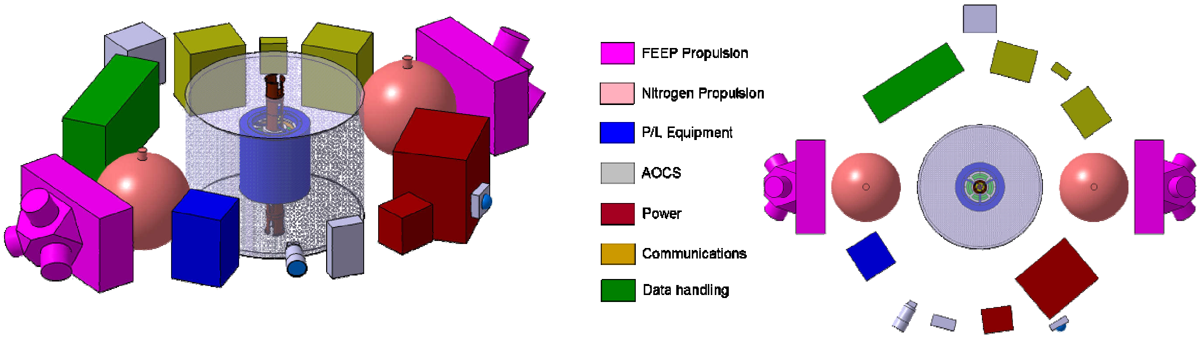

Figure 6-7: GG Spacecraft Preliminary Layout

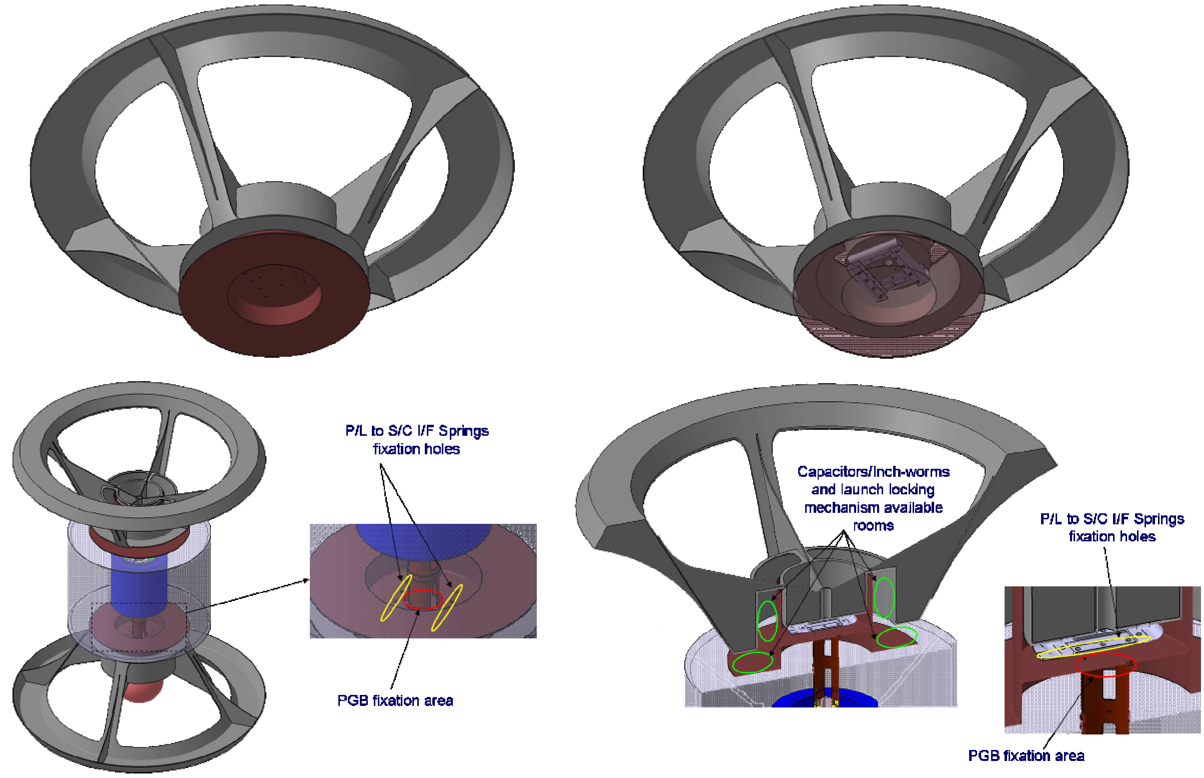

Figure 6-8: GG Experiment mechanical interface concept

Details about the equipment layout experiment mechanical interface concepts are provided in Figure 6-7 and Figure 6-8 respectively.

The current design maximizes the moment of inertia J_{spin} with respect to the symmetry axis, thereby providing passive spin stabilization around it, and meets the requirement with a $(J_{spin} - J_{trans})/J_{trans}$ ratio of ~ 0.3.

The spacecraft structure, similar to a spinning top, is exceptionally compact and stiff. Carbon fiber is used to the maximum extent to minimize thermal distortions. The central belt alone is composed of Aluminum honeycomb with aluminum skins for accommodation of the thermal radiators.

The total structural mass is 122.5 kg, including 20% subsystem margin. The launcher stiffness requirements are fulfilled with a satisfactory margin. The calculated first axial mode with the structure constrained at launch is 43.7 Hz (against > 20 Hz and < 45 Hz required by the launcher, see Figure 6-9). The first lateral mode is 26.2 Hz (>15 Hz required, see Figure 6-10).

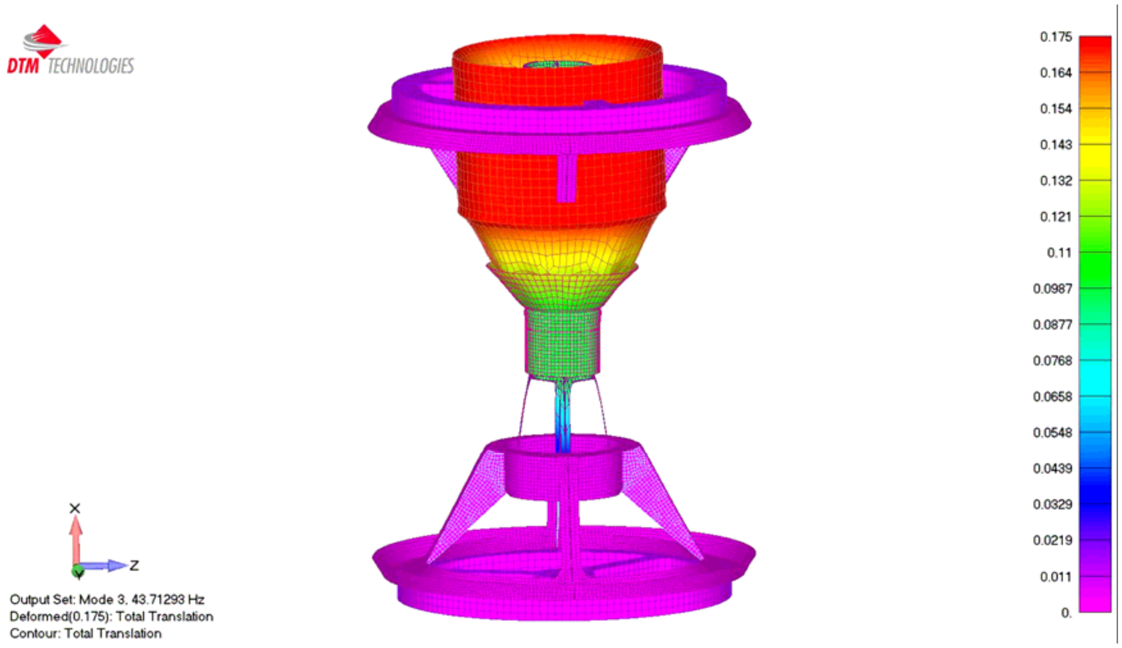

Figure 6-9: GG FEM Model first axial eigenfrequency (43.7 Hz, preliminary data)

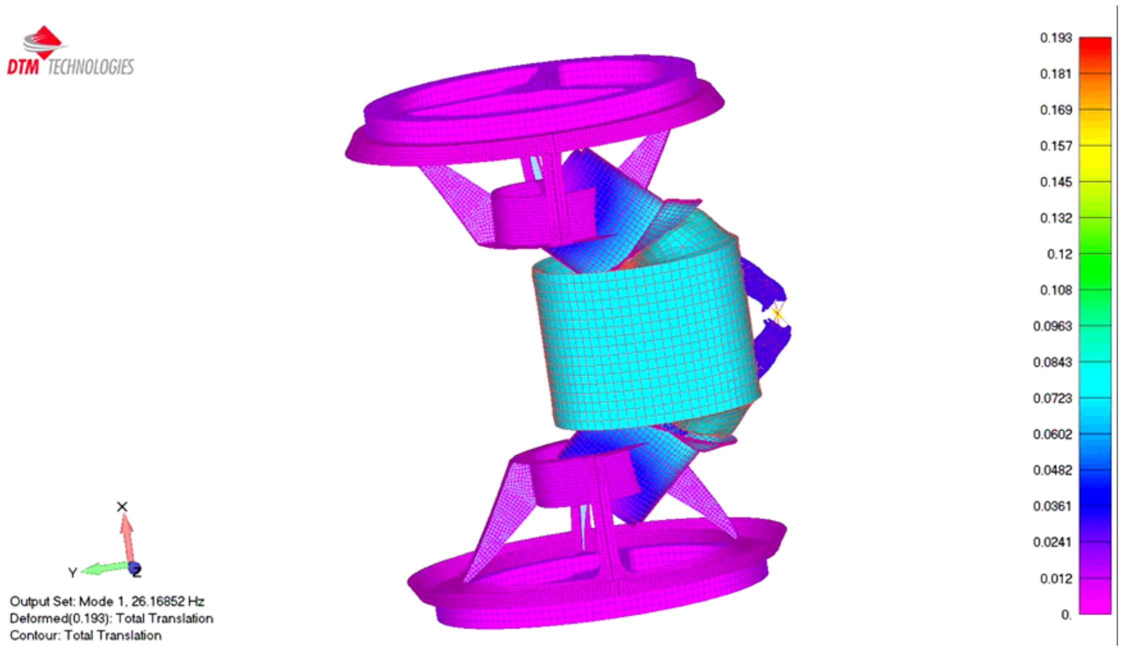

Figure 6-10: GG FEM Model first lateral eigenfrequency (26.2 Hz, preliminary data)

6.3 THERMAL DESIGN AND ANALYSIS

6.3.1 TCS REQUIREMENTS

The thermal requirements derive from the goal to maintain a thermal configuration able to perform the needed scientific measures. The high spin frequency value makes negligible the azimuthal temperature difference, while the axial effect shall be limited. Moreover it is important to maintain the temperature stable. The mechanical suspensions are sensitive to the temperature variation and this variation shall not degrade the common mode rejection of the mechanical suspension.

The following temperature requirements shall be met:

- test mass mean temperature stability better than 0.1°C/day;
- Axial temperature gradient at the level of the proof masses shall not exceed 1 °C/arm length;
- Temperature fluctuations in the proof masses shall not exceed 0.2 °C in 1 day;
- Linear temperature drift in the proof masses shall not exceed 0.2 °C/day.

As for the electronic units, the following temperature requirements were assumed:

- -20/+50 °C operating temperature;
- -30/+60 °C non operating temperature.

6.3.2 TCS DESCRIPTION

A classical passive approach plus heaters has been selected:

- The external side of the S/C will be covered by MLI blankets to counter the environment loads; painted radiators areas are distributed on the cylindrical structure following the footprint of the electronic boxes mounted inside the structural cylinder; solar arrays cells are placed on two dedicated cylindrical sections.
- The internal side of the S/C will be black-painted as much as possible where power is generated (internal cylindrical section and electronic boxes) in order to minimize temperature gradients, while a low-emissivity surface finish has been selected for both the external and the internal side of the PGB in order to radiatively decouple the payload from the remaining parts of the S/C.
- Electronics are mounted on the internal cylindrical structure via thermal fillers to increase the baseplates contact conductances; the PGB is conductively decoupled as much as possible from the remaining parts of the S/C, and the core of the payload is connected to the support structures via springs.
- The use of standard electrical heaters to trim or maintain the necessary temperature levels is under evaluation; if applied, this solution will be limited to the electronic boxes area, that is no heaters are envisaged inside the PGB enclosure in order to limit oscillation and temperature disturbances to the test masses.

The following thermal hardware is foreseen at this level of analysis.

MLI Blankets

Multi Layer Insulation blankets will be 20-layers ITO Kapton 3 mil with Dacron net spacers; the MLI will cover all the external surfaces except the radiators, solar cells and mechanical I/F with launch adapters. The S/C parts exposed to high heat input, i.e. plumes, will be shielded by 0.3 mil aluminised Kapton.
MLI blankets will also be used on the PGB cylinder, both on the external and the internal side.

Surface Finishes

Black paint Aeroglaze Z306 will be used for the internal side of the structural cylinder and as finish of the electronic boxes.
All the remaining parts of the internal environments will have a low-emissivity finish, not exceeding 0.05.
The external radiator areas will be covered with silvered Teflon tape.

Thermal fillers

Sigraflex-F will be used to increase thermal coupling between equipments and the mounting surfaces (brackets or structural panels).

6.3.3 Mathematical model description

Geometrical Mathematical Model (GMM)

Esarad 6.2 has been used to build up the Geometrical Mathematical model and to run the radiative analysis. The GMM includes all the main structural elements, the payload components, and the equipments both inside and outside the S/C:

- Structural main cylinder, cones, flanges and payload support structures
- Internal electronic boxes
- PGB protective cylinder, I/F flanges and springs
- Payload internals: Mass 1, Mass2, Capacitive Plates, and support cylinders brackets and flanges
- External MLI blankets, sensors, antennas and Solar Arrays.

The following figures depict the modeled elements.

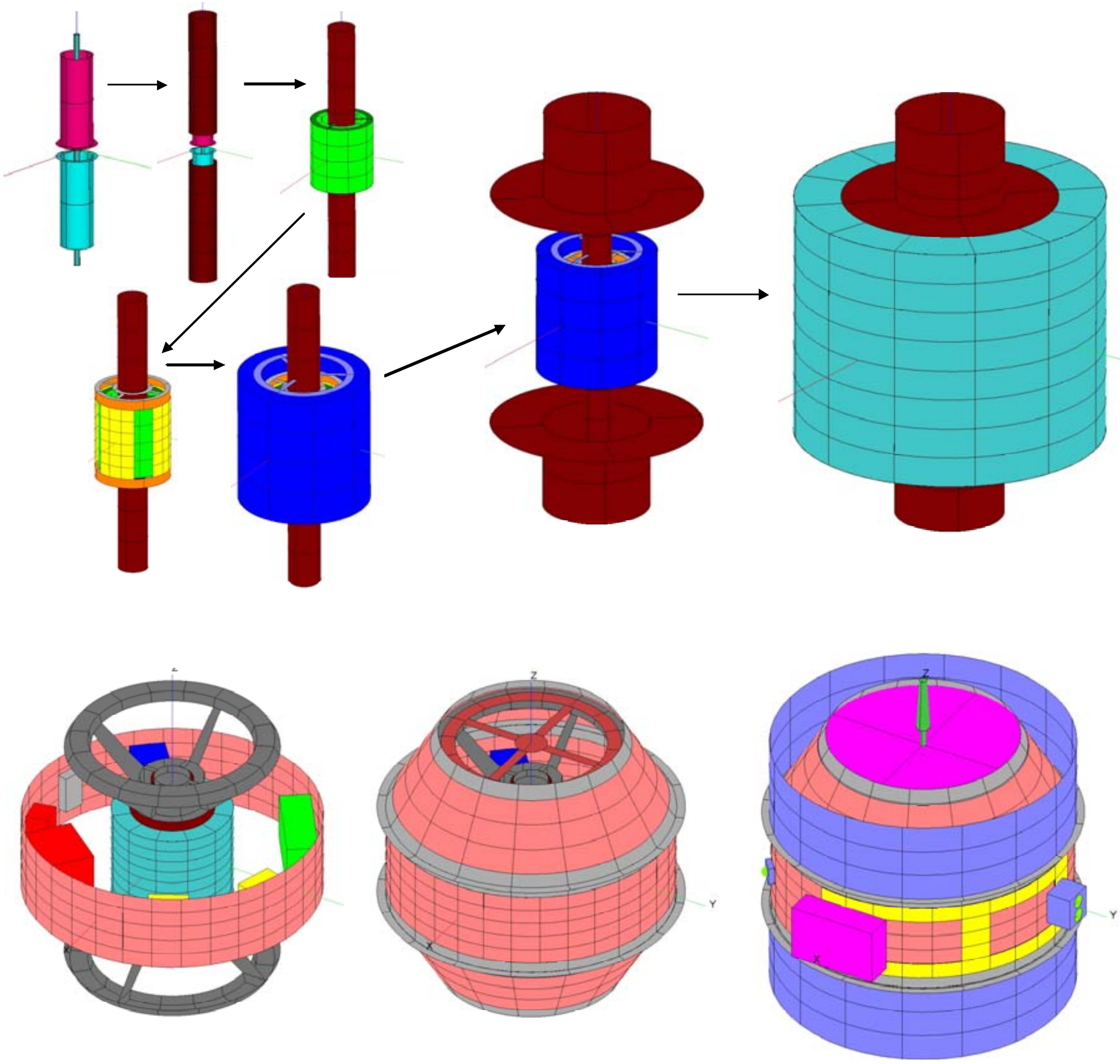

Figure 6.11: Overall GG Geometrical Mathematical Model component breakdown

The radiator areas have been positioned only on the outer cylindrical part of the structure, and in general follow the arrangement of the internal boxes. Radiator areas implemented in the GMM are listed in Table 6.1.

Unit	Radiator area [m^2]
Battery	0.067
PCE	0.122
CDMU	0.234
TRANSP 1	0.100
TRANSP 2	0.100
PCU	0.300
Tot Radiative area [m^2]	**0.923**

Table 6-2: Radiator areas

The GMM is made of 2090 nodes and 509804 radiative conductors are calculated as output. A summary of the thermo-optical properties and the main orbit data is given in the following two tables.

Thermo-Optical properties			
Surface finish	ε	α BOL	α EOL
MLI ITO Kapton	0.77	0.30	0.43
MLI Aluminised Kapton	0.05	0.14	0.14
Black paint Z306	0.88	0.96	0.96
Silvered Teflon tape	0.75	0.14	0.30
Bare aluminium	0.05	0.21	0.21
Solar Array Cell Side	0.82	0.75	0.75
Solar Array Back Side	0.71	0.51	0.51

Table 6-3: Thermo-optical properties

Orbit and Attitude data		
Orbit	Orbit case	EOL
	Earth-Sun distance	149.5979 E06 Km
	Sun temperature	5770 K
	Orbit eccentricity	0
	Orbital altitude	520 Km
	Orbital period	5699.35 s
	Earth albedo factor	0.35
	Earth temperature	263 K
Attitude	Attitude	+Z normal to orbit spin axis
	Number of orbital positions	10
	Spin rate	720 deg/s
	Spin results averaged over	12 positions

Table 6-4: Orbit and Attitude properties

Thermal Mathematical Model (TMM)

The Thermal Mathematical Model has been written to run in Esatan 10.2 code. The linear thermal network is made by 4309 conductors. The material properties used in the TMM (thermal conductivity, heat capacity, mass density) are listed in the Table 6-5 and Table 6-6.

A very conservative approach has been used for the units power dissipation evaluation. For each orbit, the maximum value of power dissipation has been considered when the S/C is exposed to the Sun flux, while the minimum value has been taken into account during the eclipse phase. A summary of the figures used is given in Table 6-7.

The electronic units are placed on the internal side of the main structural cylinder; in the TMM, units are coupled directly to the cylinder H/C. Brackets and mounting structures have not been taken into account at this level of analysis.

Element	Material	Thermal conductivity	Heat capacity	Density	Comments
Structural panels: cylinder, cones, solar arrays	Honeycomb	KXY=10.8 W/K KZ=1.8 W/m2/K	900 J/kg/K	2.5 kg/m2	Al skin 2*0.4 mm Al core 15 mm
Structure: Rings, flanges, PGB I/F, Payload support structures, S/C launcher I/F Payload: TM1, TM2, Capacitive Plates brackets, flanges, support cylinders	Al 7075	150 W/K	900 J/kg/K	2700 Kg/m3	
Test Mass 1	Pb	35 W/K	129 J/kg/K	11340 Kg/m3	
Test Mass 2	Al 7075 (1)	150 W/K	900 J/kg/K	2700 Kg/m3	
Capacitive Plates	Cu	390 W/K	380 J/kg/K	8920 Kg/m3	
Propellant tanks	Ti	10 W/K	520 J/kg/K	4500 Kg/m3	
MLI blankets	20-lay Kapton	temperature dependent (see Table 6.6)	0	0	

(1) In a conservative approach, only the Aluminium box containing the Polypropylene Mass 2 has been considered.

Table 6-5: Materials thermal properties

Structure	Element	Material	Thickness [mm]
Payload inner support cylinders	cylinders	Al 7075	1.609
	cylinders flanges	Al 7075	3.0
Payload outer support cylinders	cylinders	Al 7075	1.565
Test Mass 1 support structure	circular flange	Al 7075	5.0
	brackets	Al 7075	6.5
	mass cylinder	Al 7075	23.1
Test Mass 2 support structure	circular flange	Al 7075	3.0
	brackets	Al 7075	3.0 - 4.5
	mass cylinder	Al 7075	37.8
Capacitive Plates support structure	circular flange	Al 7075	2.0 – 11.04.0
	brackets	Al 7075	4.0
	plates supports	Al 7075	6.0
	plates	Al 7075	2.0
PGB	I/F structure	Al 7075	2.5
	protective cylinder (1)	Al 7075	3.0
H/C structural supports	cylinder ring	Al 7075	2.5
	cylinder flange	Al 7075	5.0
	cone flanges	Al 7075	2.5
	upper/lower platforms	Al 7075	60.0

(1) Two Protective Cylinder configurations have been analysed: one made of Aluminium (shown in this table) and one made of MLI (without any support structure)

Table 6-6: Structure panels thermal conductivity

Unit	Power in Sun [W]	Power in Eclipse [W]	Remarks
BATTERY	11	0	
SRS	1	0	
CPE	23	0	
CDMU	45	14.4	
TRSP2	20	6	TX (10 min/orb) = 20W RX = 6W
RFDN	0	0	
TRSP1	6	6	
PCU	55	14	
EPSA+PPCU+NEUTRAL	30	0	
ECE (1)	12	12	
Tot without ECE	191	40.4	
Tot with ECE	203	52.4	

(1) ECE has been considered only in one analysis case, see Results chapter for details

Table 6-7: Units power dissipations

6.3.4 ANALYSIS RESULTS

Esatan 10.2 was used for a first series of transient analyses. The purpose is to gain sensitivity over the driving parameters of the models and to explore the response of the payload to variations of the boundary conditions.

At this level of the analysis, a hot orbital environment (direct Solar flux peak 435 W/m^2, albedo factor 0.35, Earth temperature 263K), and a conservative power dissipation profile during the orbits were assumed.

A summary of the analysis cases is given in Table 6-8. A detailed description is given of Case 1 (baseline); the results of other cases are summarized in the conclusions. The results of analysis are given always for 20 orbits after 180 orbits of stabilization.

Case ID	Description	Remarks
1	EOL environment and thermo-optical properties PGB with Aluminum finish (ε=0.05) Standard power dissipation profiles No heater power applied	Baseline case
2	EOL environment and thermo-optical properties PGB with Black Paint finish (ε=0.88) Standard power dissipation profiles No heater power applied	Evaluation of radiative environment of the internal payload
3	EOL environment and thermo-optical properties PGB with Aluminum finish (ε=0.05) Standard power dissipation profiles, but TRSP2 in TX (20W) only for 10min/orbit instead of the entire sunlit phase No heater power applied	Evaluation of power dissipation profiles of electronic units
4	EOL environment and thermo-optical properties PGB with Aluminum finish (ε=0.05) Standard power dissipation profiles + ECE power inside the PGB (12W) No heater power applied	Evaluation of power dissipation on the internal payload
5	EOL environment and thermo-optical properties PGB with Aluminum finish (ε=0.05) Standard power dissipation profiles PGB with of MLI No heater power applied	Evaluation of insulation of the internal payload

Table 6-8: Analysis cases for sensitivity

Results of Case 1

As baseline configuration, all the internal S/C environment is considered black painted (ε=0.88), except the PGB interior, which has a bare aluminum finish (ε=0.05) for all the items contained; the PGB protective cylinder is made of aluminum (ε=0.05 both for the external and the internal side).

Test Mass 1, Test Mass 2 and the Capacitance Plates nodes show a temperature drift, but both the spatial (ΔT<1°C/arm length) and the temporal (ΔT<0.2°/day) temperature requirements are met. See Figure 6-11 to 6-13.

All the spacecraft units remain within limits even if no heater power is applied:

time	BATTERY	SRS	CPE	CDMU	TRSP2	RFDN	TRSP1	PCU
T MIN	*-3.99*	*-6.34*	*2.01*	*4.62*	*10.84*	*-6.02*	*-1.21*	*7.99*
T MAX	*4.38*	*-3.35*	*7.40*	*7.93*	*14.08*	*-3.50*	*-0.42*	*11.14*

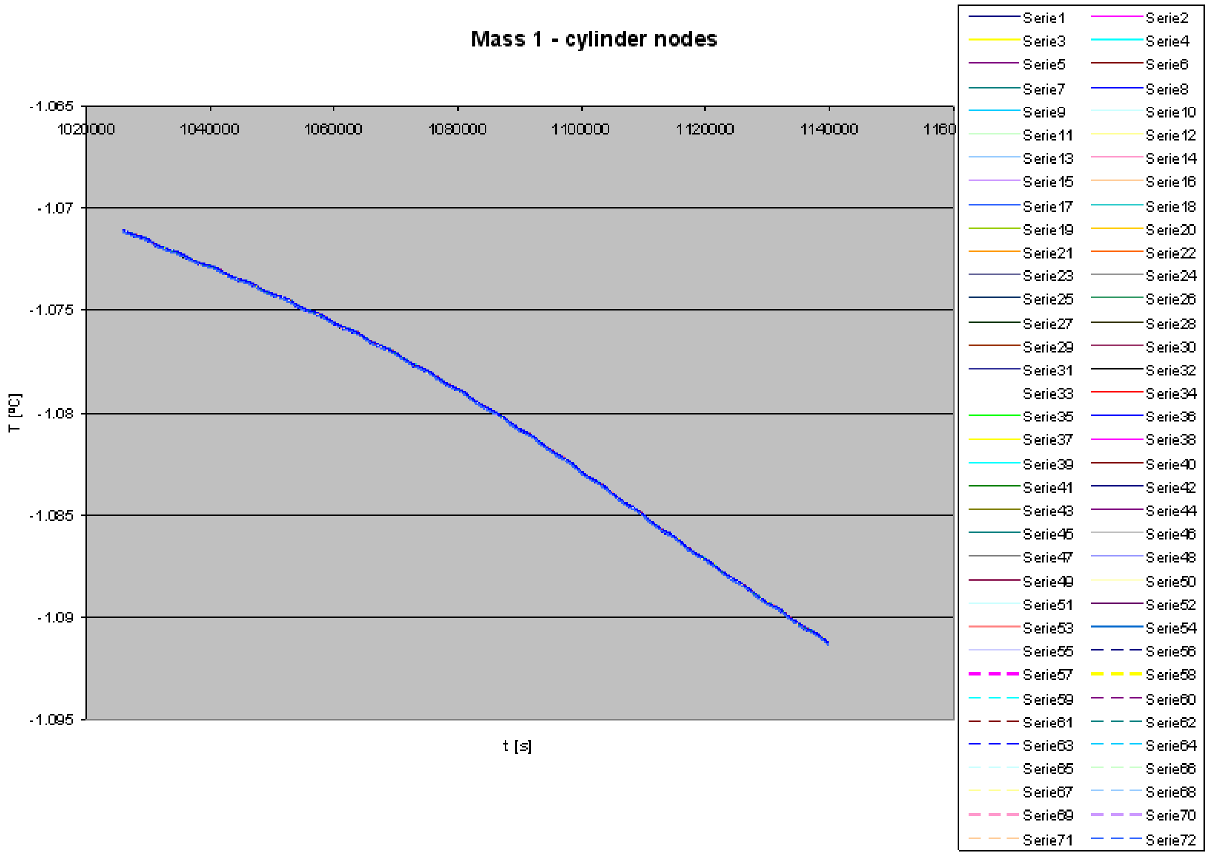

Figure 6-11: Thermal analysis of Case 1: Test mass 1 thermal nodes

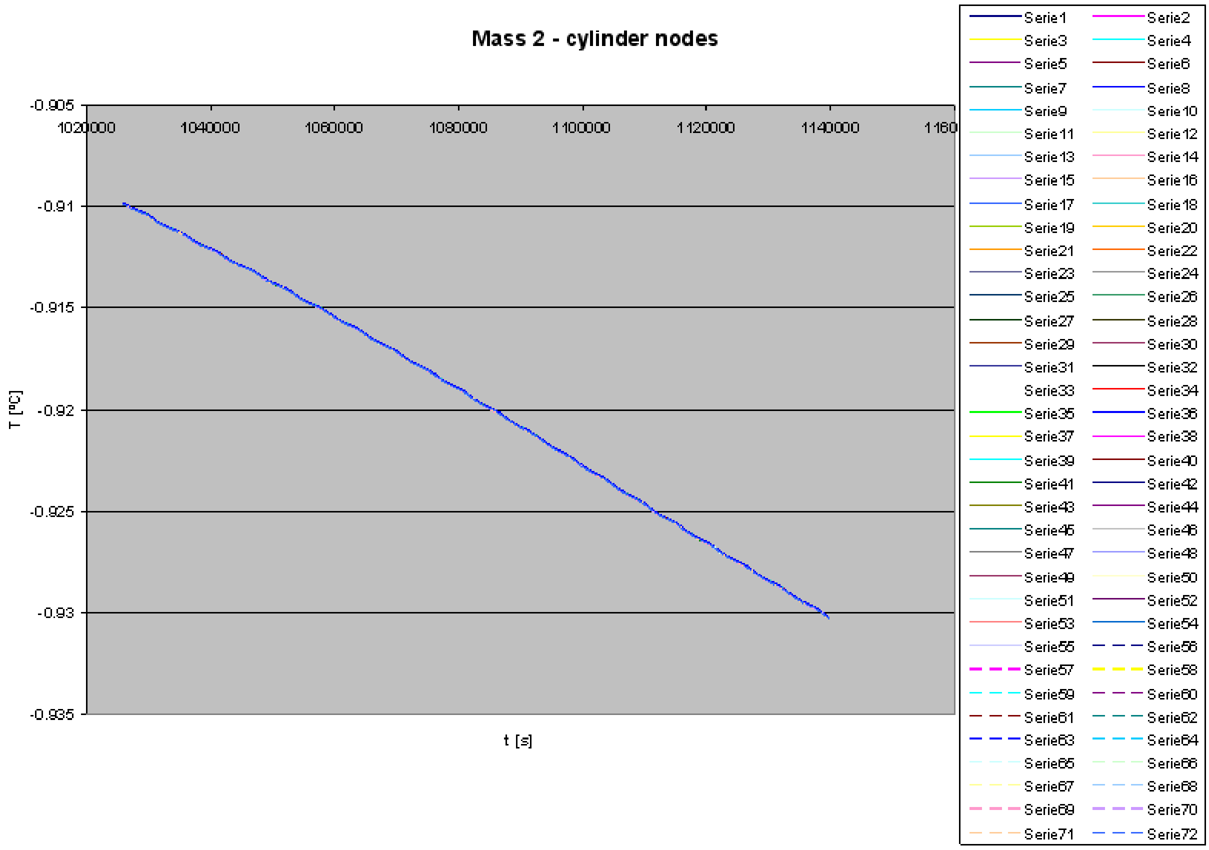

Figure 6-12: Thermal analysis of Case 1: Test mass 2 thermal nodes

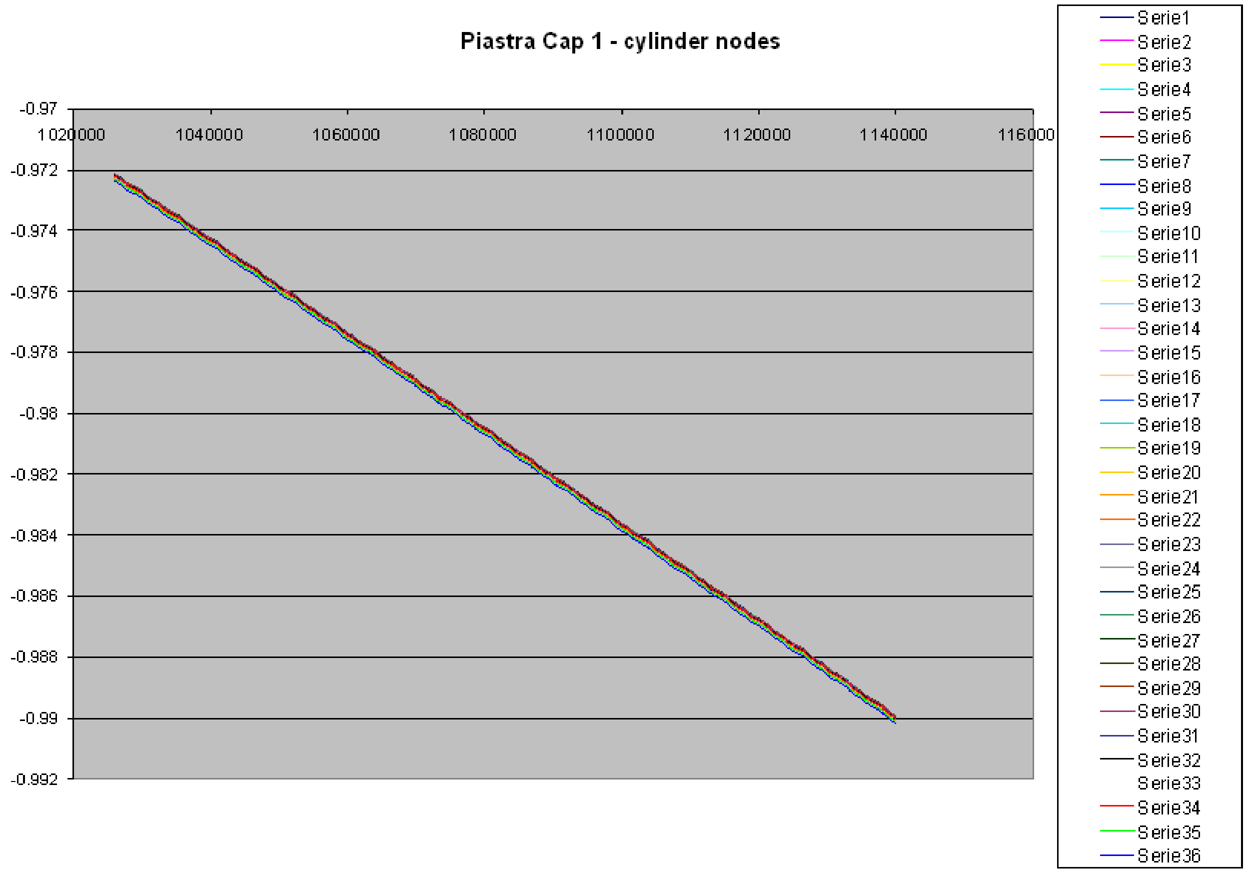

Figure 6-13: Thermal analysis of Case 1: capacitance plate 1 thermal nodes

6.3.5 Conclusions

After the described preliminary analysis campaign, the following remarks are made.

A number of assumptions have been introduced in the mathematical models:

- For Test Mass 2 body aluminum has been considered as material in the TMM; the foreseen Polypropylene mass contained inside an aluminum body will be implemented in the TMM as soon as this configuration will be confirmed;
- Conservative power dissipation profiles have been considered: maximum dissipation power is considered while the S/C is in sunlight, while minimum dissipation power is considered while the S/C is in eclipse, leading to a wide variation in the internal produced heat for each orbit (191W in sunlight and 40.4W in eclipse in the case without ECE dissipation);
- Calculations take into account 180 orbits for stabilization and 20 orbits for output;
- The PGB support structure is made of aluminum, conductively connected to the satellite structure by two laminar CuBe alloy springs sets only (GL = 0.0021 W/K each).

These assumptions need to be reviewed and harmonized with the final payload design.

At the current level of analysis, no need to use electrical heaters is foreseen.

Use of black paint inside the PGB makes the payload elements more sensitive to the external disturbances; on the other hand, black paint allows the internal components of the payload to approach the equilibrium conditions faster.

The design of the protective cylinder seems adequate even if simulated by an aluminum cylinder (conservative approach).

Power dissipation inside the PGB should be minimized, as it affects the performance both in terms of space (temperature gradients between two points of the test masses) and in terms of time (temperature drift in the test masses).

Due to the high decoupling of the internal payload from the rest of the S/C, long times are needed to approach the equilibrium temperatures, even if the temperature variations during this time are within the requirements. A more detailed analysis is mandatory to estimate the time constant of the system.

MLI, structural elements and solar panel temperatures show normal temperature levels and are of no concern.

6.4 ELECTRICAL AND ELECTRONIC DESIGN

Figure 6-14 shows the GG avionic system architecture, comprising both payload electronics units and service module units.

The Payload Electronics is composed by two major subsystems:
- PGB Control and Processing Electronics (CPE)
- Experiment Control Electronics (ECE).

The PGB Control and Processing Electronics, located on the spacecraft platform, manages PGB motion control (whirl sensing, whirl damping) and the processing of all signals coming from the test masses (motion control and EP sensing). Moreover, the CPE performs:
- TC reception from spacecraft and decoding;
- execution of payload timelines and commands;
- Science data collection, compression and formatting;
- Formatting of TM packets and their transmission to the spacecraft.

The Experiment Control Electronics, housed inside the PGB, communicates with the CPE via an optical link. It performs readout of the EP chain and, under control by the CPE processor, manages locally the whirl sensing and damper activation.

The service module electrical architecture includes:
- On Board Data Handling
- Electrical Power System including PCDU, solar array and battery.

6.4.1 ON-BOARD DATA HANDLING

The GG on-board data handling system will be based on a single CDMU, derived from the standard LEONARDO unit, developed via the ASI PRIMA program and based on an ERC32 CPU. A dedicated CPU board, equipped with LEON2FT processor, based on a standard ASIC, is under qualification by TAS-I. If necessary this board could replace the ERC processor board.

The CDMU acts as the central communication node between the Spacecraft and the active Ground Station, distributing or executing commands received from ground and collecting, formatting and transmitting the satellite telemetry.

The CDMU provides: telecommand acquisition, decoding, validation and distribution; scientific and HK data acquisition and storage; distribution of time reference signals for the Central Reference Time generator and synchronization with the local timers of the other processors; autonomy supervision and management.

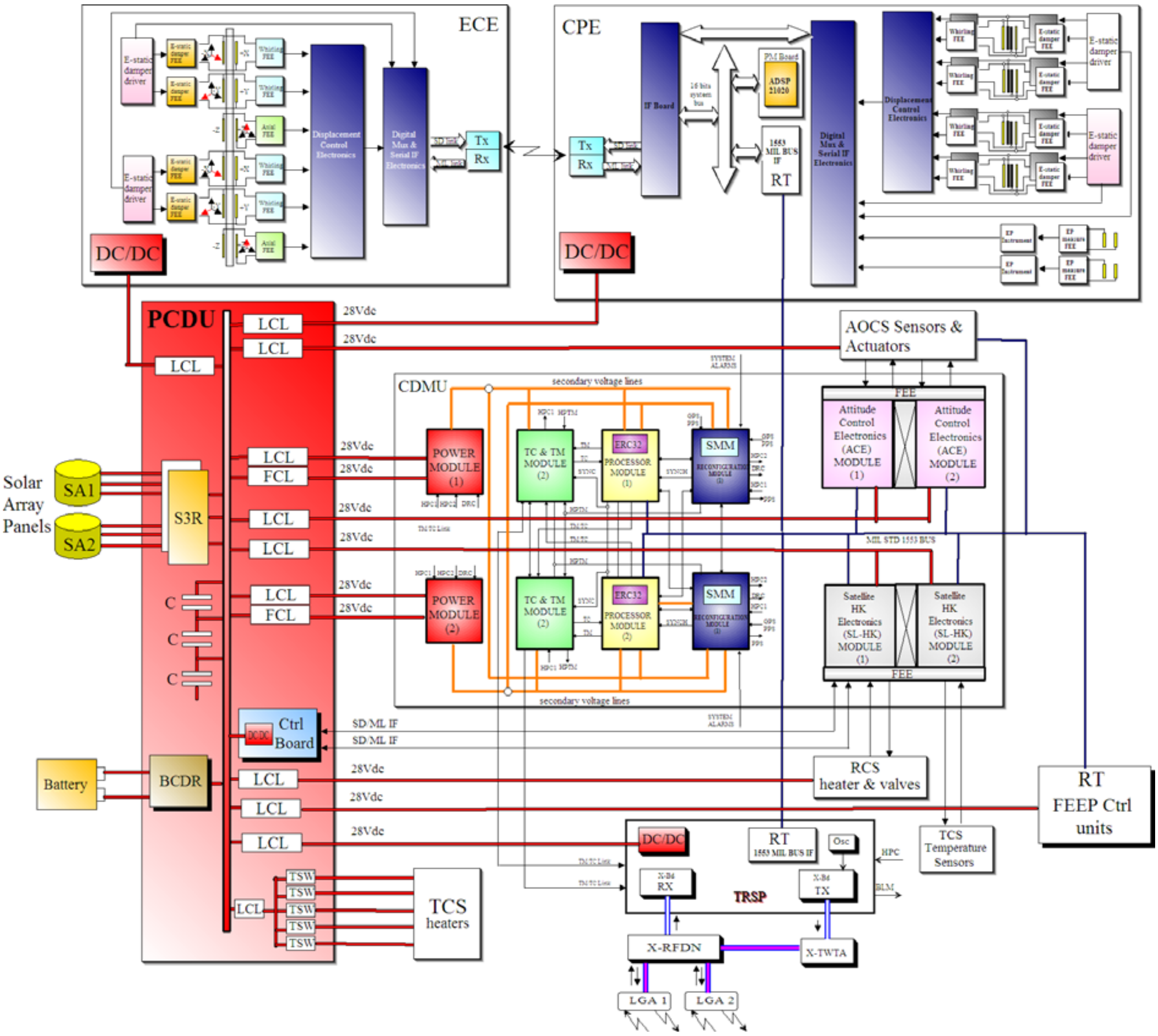

Figure 6-14: GG avionic architecture block diagram.

Within the centralized CDMU computer, all the application software will be executed, including the software implementing the AOCS and drag free control algorithms.

The CDMU provides a number of discrete telecommand lines for reconfiguration purposes. It provides condition inputs for discrete telemetry lines which will be used for housekeeping, to acquire status monitors and temperatures from the Thermal Control sensors. Power to Thermal Control heaters is provided by the PCDU, under CDMU commands received on the 1553 bus.

Decoding and validation of telecommands uplinked from ground is performed by the TC decoder embedded in the CDMU. A set of High Priority Commands is available to command directly the end users from the decoders, by-passing any on board processor. These commands are used for time critical functions such as activation/deactivation of units, on board computers re-initialization, back-up initiation of post-separation sequences.

The CDMU includes a Reconfiguration Module, functionally independent from the Processor Module and the On Board Software, capable of processing some alarm signals via dedicated links and of commanding directly the end users via the High Priority Commands.

Moreover, the CDMU will be equipped with internal power supply dedicated boards, based on standard FPGAs (Actel RTSX), to drive all the required mechanisms and actuators. Finally, the box will implement an acquisition module dedicated the internal HK and the conditioning of the sensors and acquisition needed to control the mechanisms.

The GG CDMU will be based on dedicated tailoring of a TAS-I heritage architecture (Figure 6-15), based on the experience gained with the development of many control units.

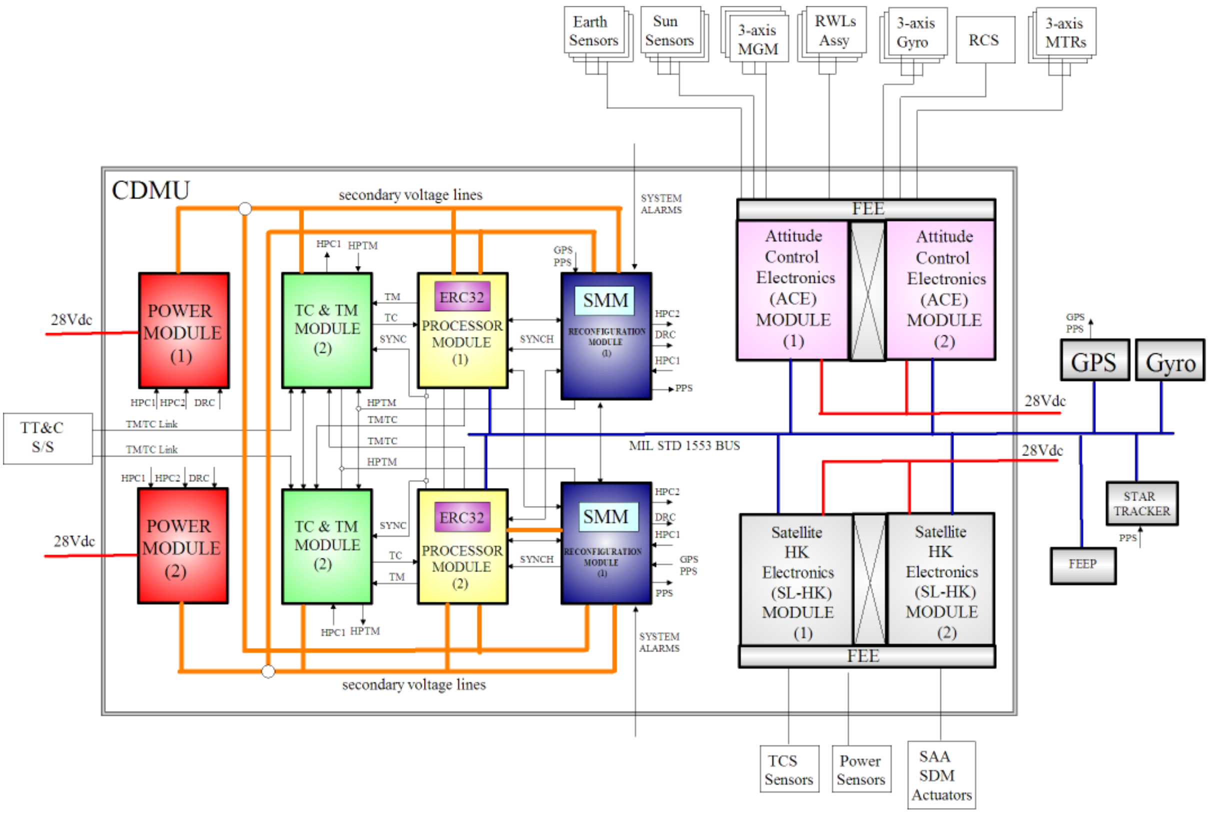

Figure 6-15: Functional block diagram of a generic CDMU based on TAS-I heritage.

6.4.2 ELECTRICAL POWER SYSTEM

The Electrical Power System (EPS) is implemented by a dedicated Power Distribution and Control Unit (PCDU), plus power generators and a battery.

On the basis of the power budget, the EPS is required to provide around 520W for both payload and S/C equipment, constantly along the whole mission duration of 2 years.

A fully regulated 28V power bus was adopted, compliant with the ESA power standard, under the assumption that the payload electronics only allow operation in a limited range of bus voltage variation. This design also increases the power conversion efficiency in the EPS system and reduces EMC noise.

For the Solar Array power regulation, either an S3R regulator or an MPPT regulator could be considered. An S3R regulator design is preliminarily assumed, considering its simple operation (constant attitude to the sun), the simplicity and robustness of the design and the good flight heritage. By regulating the number of SA sections connected to the bus, the bus is controlled to be at fixed voltage value.

In series to the S3R regulator there are two buck DC/DC converters, providing the required 28 V power bus voltage conversion and regulation using a majority voted Main Error Amplifier (MEA).

Taking into account the regulated bus topology, a single BCDR module can be implemented, consisting of two power regulators, a Battery Change Regulator (BCR) and a Battery Discharge Regulator (BDR).

<u>PCDU configuration</u>

The PCDU provides the following functions:

- it controls the electrical power generated by the solar array;
- conditions the energy stored in the battery when required;
- controls, monitors and maintains the health of the EPS;
- distributes power to the scientific instruments and spacecraft equipment;
- protects the power bus from external faults and prevents failure propagation;
- provides heater switching control in response to commands;
- interfaces for AIV and Launch support EGSE.

The proposed modular PCDU, derived from the ASI PRIMA PCDU (SMU) design, has the following features.

- 28V regulated Power Bus
- Up to 700 W distributed power
- At least 4 I/F with independent Solar Array sections and 1 Li-Ion Battery
- S3R concept
- SD/ML TM/TC I/F

- Outputs:
  - 12 FCL (Fold-back Current Limiters)
  - 24 LCL (Latching Current Limiters)
  - 60 heater lines.

The PCDU will include the following main boards:
- Array Power Regulation modules;
- Battery charge/discharge regulator modules;
- Command and Monitoring modules;
- Back Plane;
- Heater Distribution module.

<u>Battery configuration</u>

The battery provides a store for the excess solar array energy, and a source of energy whenever there is insufficient power from the array (e.g. during launch, transient power demands and eclipse periods). The selected equatorial orbit leads to eclipse on every orbit with duration of about 36 minutes over a period of 95 minutes.

The Sony 18650HC Li-Ion cell technology is considered for the battery. The battery sizing case is energy supply of the satellite during the entire LEOP phase assuming a power load of 171 W for 120 minutes. Considering a battery with 27 Ah capacity (18px7s), initial State of Charge (SoC) of 98% and 1 failed string, the final SoC after the LEOP will be 69.7 % with the voltage of the battery at 26.74V.

The battery discharge and charge profiles, and the expected SoC degradation at end of Life (EoL) were calculated assuming maximum Depth of Discharge (DoD) of 30%. The resulting SoC degradation at EoL is 13 % with 11,100 charge/discharge cycles over the expected mission lifetime.

The assumed efficiencies are 94% (BDR) and 96% (BCR). Summarizing, the calculated battery characteristics under the assumptions listed above are:
- Capacity of 27 Ah
- Energy 633.15 Wh @3.35 V
- Configuration: 18p7s
- Mass: 6.35 kg (including 20% maturity margin)
- Dimensions: 200mm x 120mm x120mm.

<u>Solar array configuration</u>

The Solar Array consists of two cylindrical surfaces equipped with RWE 3G-ID2L/150-8040 cells. They will be used to generate the power necessary to supply the S/C and P/L electronic units and heaters during the sunlit period, while spinning at 1 Hz.

Cells shall be organized in strings to achieve the required voltage, but as the current delivered by each string is limited by the least illuminated cell, it is necessary to grant constant illumination over the entire string in order to both optimize the power conversion efficiency and minimize cell degradation. Cells shall be stacked vertically on the cylinder surface to form strings. The length of a single cell determines how many such stripes can be disposed while the height limits the number of cells per string.

As first approximation the collected solar flux of the cylindrical surface can be approximated by its projection:

$$\eta_{area} = \frac{\Pr ojectedsurface}{HalfLateralSurface} = \frac{2Rh}{\pi Rh} = 2/\pi \cong 0.637$$

Unfortunately this approximation is not conservative as below specific incidence angles the conversion efficiency degrades more than the cosine projection and becomes negligible around 85°. The relative power of solar cells has therefore been calculated according to the following empirical formulation:

$$\begin{array}{ll} \gamma < 50° & P/P_o = \cos(\gamma) \\ 50° \le \gamma < 85° & P/P_o = 1.149 - 5.99e-3 \cdot \gamma - 8.65e-5 \cdot \gamma^2 \\ \gamma \ge 85° & P = 0 \end{array}$$

The γ angles have been calculated for every string exposed to the Sun on the cylindrical surface. The collected and usable flux on the exposed cells area results in the order of 780W/m^2, which, including a packing factor of 0.9, translates into an area exploitation efficiency of η_{area}=0.48.

For the S3R an equivalent efficiency of 95 % is considered. Given the available surfaces and the cell characteristics, the following SA configuration is found: 15 cells per string, 38 strings per cylinder, 2 cylinders. This SA configuration requires a total used area of 3.6 m² to supply a maximum power load of 519 W.

6.5 TELECOMMUNICATIONS

An S-Band architecture derived from the PRIMA platform is proposed for the Galileo Galilei TT&C. The architecture, shown below, consists of:

- 2 transponders with low output power (23 dBm, i.e., 200 mW) and diplexer embedded;
- RFDN miscellanea in coaxial technology:
  - 3-dB hybrid coupler
  - Connection cables;
- 2 LGAs with circular polarization and hemispherical coverage (gain = -3 dBi at ±90° boresight offset angle)

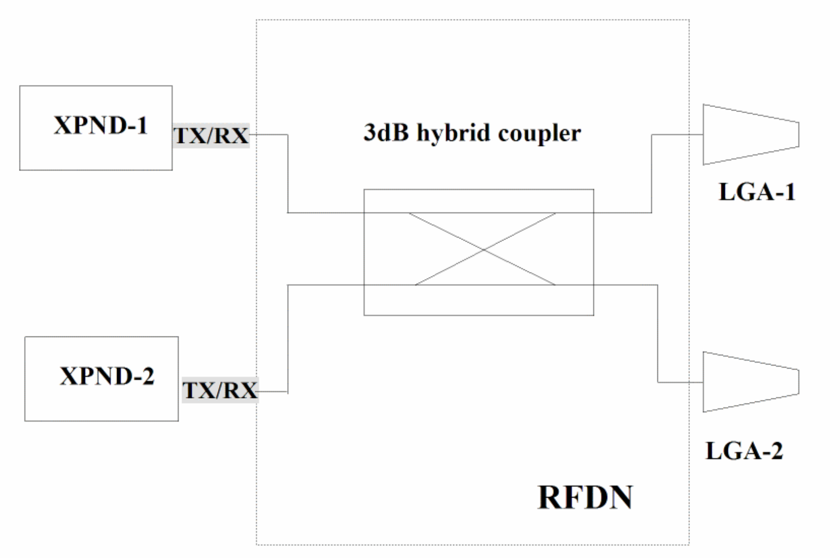

Figure 6-16: GG TT&C block diagram

The telemetry data generated by the GG system, including overheads and margins, is 2350 Mbit/day (see §6.6). This amount of data may be downloaded on each ground station pass, once per orbit, minimizing the telemetry rate, or the number of contacts per day can be reduced in order to reduce Malindi ground station occupation time. The guideline for re-use of PRIMA hardware limits the TM symbol rate to 512 kbps, and leads to adoption of Reed-Solomon coding and SP-L modulation.

Assuming the data volume generated in one day of science operations must be downloaded within the next day, Table 6-9 shows, as function of number of contacts per day, the minimum TM data rate allowing data volume downlink. The values in red exceed the limit of 512 kbps, so they are not allowed.

Number of contacts/day	No data compression		Compression factor 1.5 (zip		Compression factor 2.8	
	TM data rate [kbps]	TM symbol rate [kb/s]	TM data rate [kbps]	TM symbol rate [kb/s]	TM data rate [kbps]	TM symbol rate [kb/s]
1 / orbit	263	300	175	200	94	107
10	392	447	261	298	140	159
9	435	496	290	331	155	177
8	490	558	326	372	175	199
7	560	638	373	425	200	228
6	653	744	435	496	233	266
5	783	893	522	595	280	319
4	979	1116	653	744	350	399
3	1306	1489	871	992	466	532
2	1959	2233	1306	1489	700	797
1	3917	4466	2612	2977	1399	1595

Table 6-9: TM data rates with limitation to 512 kbps

The conclusions from the table above are that:

- without data compression 9 contacts per day are necessary;
- with “zip file” technique (compression factor = 1.5) this number can be reduced to 6;
- using a Rice algorithm (compression factor = 2.8), 4 contacts per day are enough to download the whole mass memory content.

Link budget calculations have been performed for the worst case, i.e. no data compression, with and without ranging. With the architecture proposed, margins are such that ranging operations are guaranteed as well (Table 6-10). The TC link will be established at 4 kbps following the PCM/PSK/PM modulation scheme, according to standard ECSS-E-50-05A. Ranging too will be implemented in accordance with standard ECSS-E-50-02A.

Distance [km]	UP-LINK				DOWN-LINK						
	Data Rate [kbps]	Nom. Margin [dB]			Information Rate [kbps]	TM Coding	TM symbol rate [kbps]	Flux	Nom. Margin [dB]		
		RX power	Carrier Rec.	TC Recovery					Carrier Rec.	TM Recovery	Ranging
600	4	35.72	53.65	44.27	435	R-S	496	7.48	34.55	3.43	45.19
600	4	35.72	54.45	45.07	435	R-S	496	6.93	35.10	3.98	No RG

Table 6-10: Link budget summary

6.6 BUDGETS

6.6.1 MASS PROPERTIES

In the following, mass and inertia tables are provided, as follows.

- CoG, MoI and PoI budgets in Figure 6-17;
- GG Experiment mass budget in Table 6-11;
- GG Spacecraft Subsystems Mass Budget in Table 6-12;
- GG Spacecraft System Mass Budget in Table 6-13.

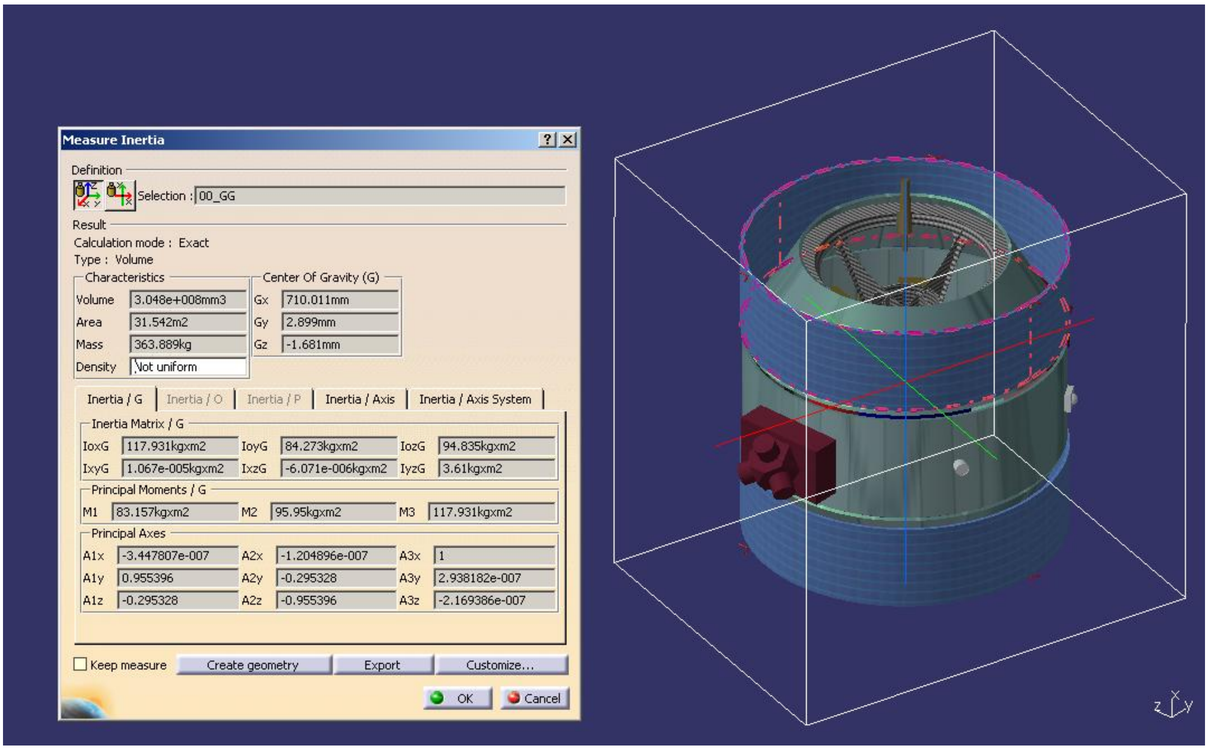

Figure 6-17: GG Spacecraft CoG, MoI and PoI budgets

Name	No.	Unit Mass [kg]	Total Mass [kg]	Margin [%]	Margin [kg]	Total Mass with margin [kg]
Inner Test Mass	**1**	**10,168**	**10,168**	**0**	**0,00**	**10,17**
Outer Test Mass	**1**	**10,183**	**10,183**	**0**	**0,00**	**10,18**
PGB Shaft			**2,879**	**20**	**0,58**	**3,45**
Mollette giunto 1	1	0,102	0,102			
Mollette giunto 2	1	0,071	0,071			
Mollette supporto piezo 1	1	0,098	0,098			
Mollette supporto piezo 2	1	0,030	0,03			
Assy supporto centrale	1	0,060	0,06			
Cilindro Giunto interno 1	1	0,161	0,161			
Cilindro Giunto interno 2	1	0,049	0,049			
Cilindro portante	1	1,082	1,082			
Piastre capacitive	1	1,164	1,164			
Piastrine capacitive	1	0,062	0,062			
PGB Shell allocation (TBC)	**1**	**7,60**	**7,60**	**20**	**1,52**	**9,12**
Locking mechanisms allocation (TBC)	**1**	**8,40**	**8,40**	**20**	**1,68**	**10,08**
Inch Worms allocation (TBC)	**12**	**0,10**	**1,20**	**20**	**0,24**	**1,44**
Thermal control allocation (TBC)	**1**	**3,00**	**3,00**	**20**	**0,60**	**3,60**
PAYLOAD TOTALS			**43,43**	**10,6%**	**4,62**	**48,05**

Table 6-11: GG Experiment Mass Budget

Element 1 - Galileo Galilei						
FUNCTIONAL SUBSYSTEM	#	Mass (kg) per unit	Total Mass (kg)	Margin (%)	Margin (kg)	Mass (kg) with Margin
Structure			**102,11**	**20,00**	**20,42**	**122,53**
Upper Platform	1	1,23	1,23	20	0,25	1,48
Upper Cone	1	7,08	7,08	20	1,42	8,50
Outermost Cylinder	1	11,35	11,35	20	2,27	13,62
Lower Cone	1	7,08	7,08	20	1,42	8,50
Lower Platform	1	1,23	1,23	20	0,25	1,48
Cone to Cylinder I/F ring	2	14,58	29,16	20	5,83	34,99
Cone to Platform I/F ring	2	4,03	8,06	20	1,61	9,67
Lock/Unlock mechanism	2	2,50	5,00	20	1,00	6,00
Separation system ring	1	2,50	2,50	20	0,50	3,00
Miscellaneous (inserts. cleats. etc.	1	9,00	9,00	20	1,80	10,80
Mass Compensation System	1	7,50	7,50	20	1,50	9,00
Payload support cone	2	4,80	9,60	20	1,92	11,52
PGB interface	2	1,66	3,32	20	0,66	3,98
Thermal Control			**15,75**	**20,00**	**3,15**	**18,90**
S/C Thermal control allocation	1	15,75	15,75	20	3,15	18,90
Communications			**9,60**	**10,00**	**0,96**	**10,56**
XPDN S-Band 1	1	3,60	3,60	10	0,36	3,96
XPDN S-Band 2	1	3,60	3,60	10	0,36	3,96
RFDN S-Band	1	1,20	1,20	10	0,12	1,32
S-Band Antenna 1	1	0,60	0,60	10	0,06	0,66
S-Band Antenna 2	1	0,60	0,60	10	0,06	0,66
Data Handling			**16,00**	**20,00**	**3,20**	**19,20**
CTU+RTU	1	16,00	16,00	20	3,20	19,20
AOCS			**3,95**	**20,00**	**0,79**	**4,74**
Coarse Sun Sensor	1	0,65	0,65	20	0,13	0,78
Spin Rate Sensor	1	1,00	1,00	20	0,20	1,20
Earth Sensor	1	2,30	2,30	20	0,46	2,76
Propulsion			**33,50**	**13,32**	**4,46**	**37,96**
FEEP Thrusters	2	1,60	3,20	20	0,64	3,84
FEEP Electronics	2	5,60	11,20	20	2,24	13,44
Nitrogen Thrusters	6	0,10	0,60	5	0,03	0,63
Nitrogen Tank	2	7,16	14,32	5	0,72	15,04
Lines & Valves	1	1,80	1,80	20	0,36	2,16
FEEP Neutralizer	2	0,12	0,24	20	0,05	0,29
FEEP Miscellanea	1	2,14	2,14	20	0,43	2,57
Power			**34,40**	**12,88**	**4,43**	**38,83**
Solar Array	2	4,95	9,90	20	1,98	11,88
PCDU	1	20,00	20,00	10	2,00	22,00
Battery	1	4,50	4,50	10	0,45	4,95
Harness			**12,50**	**20,00**	**2,50**	**15,00**
Harness	1	12,50	12,50	20	2,50	15,00
Payload			**56,03**	**12,74**	**7,14**	**63,17**
Inner test mass	1	10,17	10,17	0	0,00	10,17
Outer test mass	1	10,18	10,18	0	0,00	10,18
PGB Shaft	1	2,88	2,88	20	0,58	3,45
PGB Shell allocation	1	7,60	7,60	20	1,52	9,12
ECE	1	5,40	5,40	20	1,08	6,48
CPE	1	7,20	7,20	20	1,44	8,64
Locking Mechanisms allocation	1	8,40	8,40	20	1,68	10,08
Inch Worms allocation	12	0,10	1,20	20	0,24	1,44
P/L Thermal Control allocation	1	3,00	3,00	20	0,60	3,60
Propellant						**3,75**

Table 6-12: GG Spacecraft Subsystems Mass Budget

Galileo Galilei					
			Target Spacecraft Mass at Launch	1000,00	kg
			Below Mass Target by:	535,43	kg
	Without Margin	Margin		Total	% of Total
Dry mass contributions		%	kg	kg	
Structure	**102,11 kg**	**20,00**	20,42	**122,53**	26,38
Thermal Control	**15,75 kg**	**20,00**	3,15	**18,90**	4,07
Communications	**9,60 kg**	**10,00**	0,96	**10,56**	2,27
Data Handling	**16,00 kg**	**20,00**	3,20	**19,20**	4,13
AOCS	**3,95 kg**	**20,00**	0,79	**4,74**	1,02
Propulsion	**33,50 kg**	**13,32**	4,46	**37,96**	8,17
Power	**34,40 kg**	**12,88**	4,43	**38,83**	8,36
Harness	**12,50 kg**	**20,00**	2,50	**15,00**	3,23
Payload	**56,03 kg**	**12,74**	7,14	**63,17**	13,60
Total Dry(excl.adapter)	**283,84**			**330,89 kg**	
System margin (excl.adapter)		**20,00 %**		**66,18 kg**	
Total Dry with margin (excl.adapter)				**397,07 kg**	
Other contributions					
Wet mass contributions					
Propellant	**3,75 kg**	**100,00**	3,75	**7,50**	1,61
Adapter mass (including sep. mech.), kg	**60,00 kg**	**0,00**	0,00	**60,00**	0,13
Total wet mass (excl.adapter)				**404,57 kg**	
Launch mass (including adapter)				**464,57 kg**	

Table 6-13: GG Spacecraft System Mass Budget

6.6.2 Power budgets

The power demand of the satellite is about 519 W including maturity margins and a system margin of 20%, as reported in Table 6-14.

Equipments	No.	Power [W]	Contingency [%]	Contingency [W]	Nominal Power [W]
ECE	1	9,12	20%	2,28	11.40
CPE	1	18,4	20%	4,6	23.00
Total P/L					**34.40**
Spacecraft Management Unit	1	18	10%	1,8	19.8
Transponder 1 (TX & RX)	1	20	10%	2	22
Transponder 2 (RX)	1	6	10%	0.6	6.6
PCDU	1	20	10%	2,00	22
Battery (max charging)	0	180	-	-	190
TCS Heaters	1	40	20%	8	48
Coarse Sun Sensor	1	0.5	10%	0.1	0.6
Earth & Sun Sensor	1	6	10%	1.2	7.2
Harness loss + PCDU loss	1	20	20%	4	22
FEEP Electronics (assuming an thrust average of 300 uN)	1	100	10%	10	60
Total Service Module					**398.2**
Total Satellite					**432.60**
System margin			**20%**		**86.52**
G R A N D T O T A L					**519.12**

Table 6-14: Satellite power demand

6.6.3 DATA BUDGETS

The mass memory budget and hence the telemetry data rates depend on the data collection mode. The total science data rate in the normal scientific mode is about 158 Mbit/orbit including all overheads and margins (Table 6-15).

An on board mass memory sized for 24-hour autonomy would amount to about 1.6 Gbit. The whole 24-hour memory contents could be downloaded to the ground station in one single pass of 10' duration at a rate of about 186 kbps that is compatible with the maximum data rate permitted by the ESA S-band stations.

Data description	Variable list	Number of variables	Freq. [Hz]	Record length [bit]	Data rate [kbit/s]
Diff. TMs displacement	Δx, Δy	2	50	16	1.6
Tme/PGB displacement	Δx, Δy, Δz	3	50	16	2.4
Tmi/PGB displacement	Δx, Δy, Δz	3	50	16	2.4
PGB/Spacecraft displac.	Δx, Δy, Δz	3	50	16	2.4
ω_{SPIN}	ω_x, ω_y, ω_z	3	50	16	2.4
Reference time	t	1	50	16	0.8
Science data					**12.0**
PGB whirl monitoring	Sensing + actuation	6	1	16	0.096
Tme whirl monitoring	Sensing + actuation	6	1	16	0.096
Tmi whirl monitoring	Sensing + actuation	6	1	16	0.096
ADC monitoring	Number of ADC	9	1	16	0.144
Inchworm monitoring	Number of inchworms	6	1	16	0.096
Piezo monitoring	Number of piezo	6	1	16	0.096
PGB Inner temperature monitoring	Number of temperature sensors	20	0.10	16	0.03
Capacitance bridge monitoring	Number of capacitance bridges	9	0.10	16	0.01
Payload HK					**0.7**
Commands to FEEP	Number of commands	6	1	16	0.096
PGB/Spacecraft phase lag	Number of lag sensors	1	0.10	16	0.0016
Commands to actuators	Number of commands	6	50	16	4.8
Sun sensor	1 (2 in case o redundancy)	2	50	16	1.6
FEEP monitoring	Number of FEEP	6	1	16	0.096
SVM (DFACS + other sub-systems)					**10.0**
			Total Data Rate	kbps	**22.7**
			Overhead		**20.0%**
			Total Data Rate with margins	kbps	**27.2**
			Altitude	km	**600**
			Period	s	**5801**
			Data volume	Mbit/orbit	**158**
			Pass duration	minutes	**10**
			Telemetry rate	kbit/s	**263**
			Passages/day		**14**
			Telemetry data volume	Mbit/day	**2350**

Table 6-15: Satellite data budgets

7. Algorithms and technologies for fine drag compensation

7.1 Introduction

The chapter is dedicated to the part of the Attitude and Control Subsystem (ACS) used during the scientific observations and providing the fine drag compensation. This operating phase is covered at system level by a dedicated operating mode (Drag-Free Mode, DFM) during which:

- the spacecraft is spinning nominally at 1 Hz (360 deg/s), along the Z axis of the body frame;
- the atmospheric drag, the solar pressure and other perturbing actions at spin rate shall be reduced in such a way to permit the reliable detection and measurement of a possible Equivalence Principle violation.

After recalling of the requirements that drive the design of the operating mode, focus will be given on the architecture, designed algorithms, specific technologies and simulation results.

At it will be shown, the design of the algorithms for fine drag compensation is completed. The proposed solutions permit to meet requirements considering already available technologies.

7.2 Functional and performance requirements

The requirements for the drag-compensation sub-system are:

1. rejection of the overall environmental perturbation at spin frequency (space environmental and spacecraft induced disturbances) to detect and recover the EP signal violation. The required rejections are:
   1.1 X and Y axes : 2 10^{-5};
   1.2 Z axis: 2.5 10^{-3}.

2. to maintain the relative position and rotation magnitudes between spacecraft and PGB well below the bounds for PGB suspension integrity, and dynamic range of the sensors. It means that the linear displacement between PGB COM and spacecraft COM shall be lower than 0.15mm, and that the angular displacement shall be lower than 0.1 rad.

Design driver is the required rejection on the X and Y axes, particularly considering the limitations on the response time of the state of the art actuators (key aspect). The above limitations strongly impact on the complexity of selected algorithms.

7.3 The simplified plant model

The model to be considered for the control design (control law, equipment requirement specification) starts from the following assumptions:

- the spacecraft is a rigid body;
- the PGB is a rigid body;
- coupling between spacecraft and PGB is provided by suspension.

Let be:

x, y, z : the coordinates of the PGB COM with respect to the spacecraft COM;

m_S : the spacecraft mass

m_{PGB} : the PGB mass

m_r : the reduced mass

$$m_r = \frac{m_S\, m_{PGB}}{m_S + m_{PGB}}$$

F_P : perturbing force (drag, solar pressure, thruster's noise)

F_T : thruster assembly control force

F_C : capacitors' control force

Q : quality factor of the PGB suspension

ω_S : spacecraft spin rate

ω_0 : natural frequency of the suspension

The following differential equations describe the dynamics of the PGB-spacecraft COMs relative motion with respect to an inertial observer positioned at the orbital reference frame at the init time:

$$\ddot{x} = -\omega_0^2 x - \left(\frac{\omega_0^2}{Q\omega_S}\right)\dot{x} + \left(\frac{\omega_0^2}{Q\omega_S}\right)\omega_S y - \frac{F_{PX} + F_{TX}}{m_S} - \frac{F_{CX}}{m_r}$$

$$\ddot{y} = -\omega_0^2 y - \left(\frac{\omega_0^2}{Q\omega_S}\right)\dot{y} - \left(\frac{\omega_0^2}{Q\omega_S}\right)\omega_S x - \frac{F_{PY} + F_{TY}}{m_S} - \frac{F_{CY}}{m_r}$$

$$\ddot{z} = -\omega_0^2 z - \left(\frac{\omega_0^2}{Q\omega_S}\right)\dot{z} - \frac{F_{PZ} + F_{TZ}}{m_S} - \frac{F_{CZ}}{m_r}$$

The model shows coupling between the movements on the XY plane, while the movement on z axis is independent. The coupling occurs by the parameter $\left(\frac{\omega_0^2}{Q\omega_S}\right)\omega_S$ that is equal to about $2\ 10^{-5}$ (weak coupling) (see Table 7-14).

The poles of the 4th order system describing the dynamics on XY plane are:

$$p_{1,2} = -0.000234 \pm j0.0419 = -0.000234 \pm j\omega_0$$

$$p_{3,4} = 0.000231 \pm j0.0419 = 0.000231 \pm j\omega_0$$

The poles of the 2th order system describing the dynamics along Z-axis are:

$$p_{5,6} = -1.551\ 10^{-6} \pm j0.0419 = -1.551\ 10^{-6} \pm j\omega_0$$

Without any external control action the movement on the plane X-Y is unstable. Figure 7-18 shows the magnitude of the transfer function between the force applied in X axis (Y axis) and the movement along X (along Y).

The following equations describe the dynamics of the PGB-spacecraft COMs relative motion with respect to an observer fixed with the spacecraft body frame:

$$\ddot{x} = -\left(\omega_0^2 - \omega_S^2\right)x - \left(\frac{\omega_0^2}{Q\omega_S}\right)\dot{x} + 2\omega_S\dot{y} - \frac{F_{PX} + F_{TX}}{m_S} - \frac{F_{CX}}{m_r}$$

$$\ddot{y} = -\left(\omega_0^2 - \omega_S^2\right)y - \left(\frac{\omega_0^2}{Q\omega_S}\right)\dot{y} - 2\omega_S\dot{x} - \frac{F_{PY} + F_{TY}}{m_S} - \frac{F_{CY}}{m_r}$$

$$\ddot{z} = -\omega_0^2 z - \left(\frac{\omega_0^2}{Q\omega_S}\right)\dot{z} - \frac{F_{PZ} + F_{TZ}}{m_S} - \frac{F_{CZ}}{m_r}$$

As in previous reference frame, the model shows coupling between the movements on the X and Y, while the movement on Z axis is independent. The coupling occurs by the parameter $2\omega_S$ that is equal to about 12.6 (strong coupling) (see Table 7-14).

The poles of the 4th order system describing the dynamics on XY plane are:

$$p_{1,2} = -0.000234 \pm j6.3251 = -0.000234 \pm j\left(\omega_S + \omega_0\right)$$

$$p_{3,4} = 0.000231 \pm j6.2413 = -0.000231 \pm j\left(\omega_S - \omega_0\right)$$

The poles of the 2th order system describing the dynamics along Z-axis are (same for inertial reference frame):

$$p_{5,6} = -1.551\ 10^{-6} \pm j0.0419 = -1.551\ 10^{-6} \pm j\omega_0$$

Without any external control action the movement on the plane X-Y is unstable.

Figure 7-19 shows the magnitude of the transfer function between the force applied in X axis (Y axis) and the movement along X axis (Y axis). Figure 7-20 provides a zoom around spin rate (1 Hz) of the magnitude of the above transfer function: it is possible to recognize the effect of frequency shift of the suspension transfer function due to spacecraft and PGB spin rate. The disturbances at spinning frequency are not attenuated by the PGB suspension (natural frequency around 6.7 mHz). This is the reason why so fine drag compensation is required to the drag-free controller: drag is not attenuated by the PGB suspension but only by CMRR of the balance connecting the proof masses.

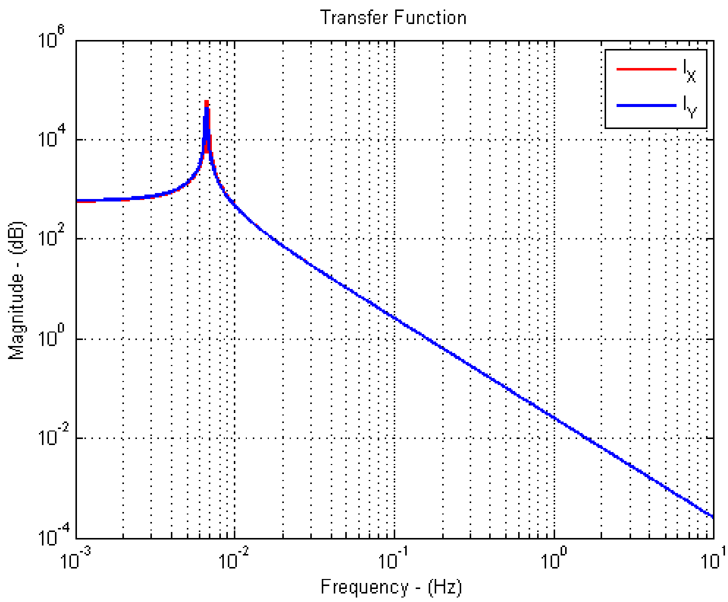

Figure 7-18 - Magnitude of the transfer functions between X force and X displacement (red), Y force and Y displacement (blu) in Inertial reference frame.

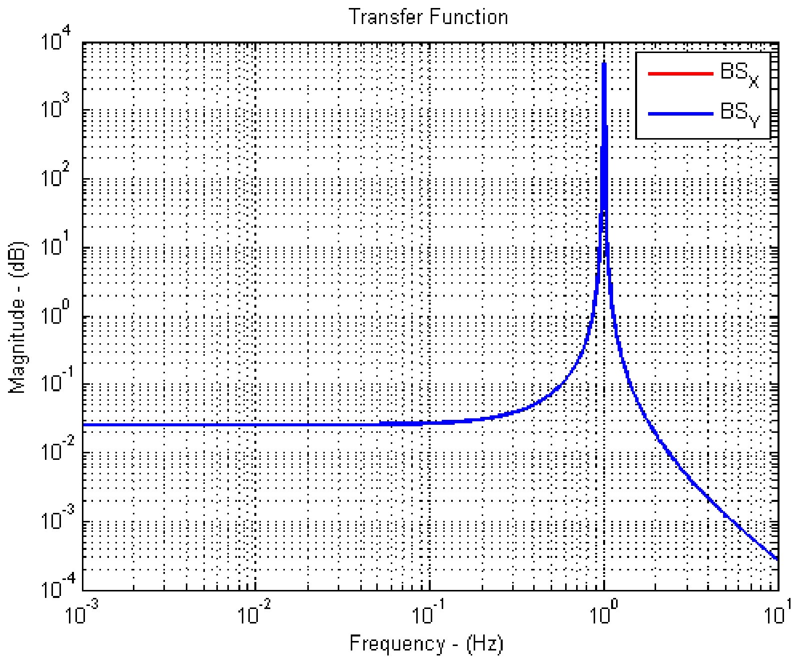

Figure 7-19 - Magnitude of the transfer functions between X force and X displacement (red), Y force and Y displacement (blu) in Body reference frame.

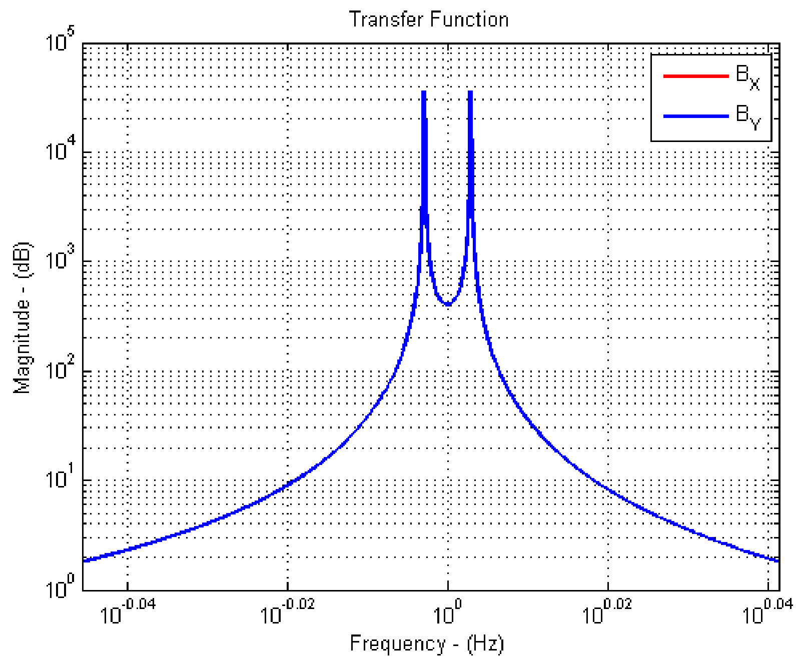

Figure 7-20 - Zoom around 1 Hz of the magnitude of the transfer functions between X force and X displacement (red), Y force and Y displacement (blu) in Body reference frame.

No	Parameter	Unit	Value	Comments
1	Spacecraft mass	kg	500	
2	PGB mass	kg	45	
3	PGB suspension quality factor		90	
4	Period of the PGB suspension	s	150	
5	Natural frequency of PGB the suspension	rad/s	0.0419	
6	Spacecraft spin angular rate	rad/s	6.2832	

Table 7-14 – Nominal values of relevant spacecraft and suspension parameters used as reference for control design

7.4 Architecture and algorithms for the drag compensation

According to previous analysis, the designed controller has in charge:

1. the stabilization of the relative displacement in the plane XY, limiting the magnitude;
2. the rejection of any disturbances (drag is the expected major one, but others are solar pressure, thrusters noise, etc.) at spinning rate (1Hz) on overall axis.

The overall controller has been organized according to the architecture provided in Figure 7-21. There are three independent controllers:

- *XY drag-free controller* for drag compensation on the XY plane. The controller shall reduce the drag disturbances at spinning rate providing a rejection lower than 2 10^{-5};
- *XY whirl controller* for the stabilization of the movement in the plane XY. The controller shall stabilize the movement introducing a low-frequency action.
- *Z drag-free controller* for drag compensation and displacement reduction along Z axis.

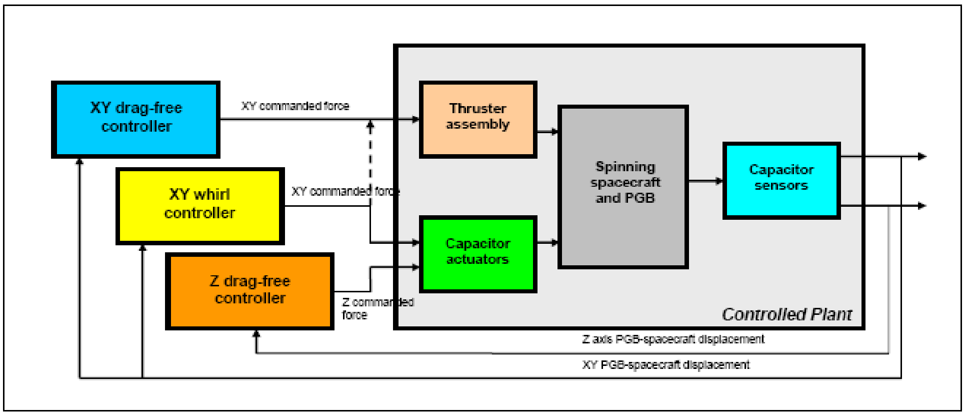

Figure 7-21 – Linear axis control architecture

XY drag-free controller is feed by measurement on relative XY displacement between PGB and spacecraft COM provided by capacitors sensors. The fine compensation occurs thank to micro-thrusters assembly.

Also XY whirl controller is feed by measurement on relative XY displacement between PGB and spacecraft COM as for XY drag-free controller, and the actuation is realized by capacitors (out from DFM, when PGB is released by mechanism and micro-thrusters assembly disabled) and/or micro-thrusters assembly (during DFM, as alternative).

Z drag-free controller is feed by measurement on relative displacement along Z axis between PGB and spacecraft COM provided by capacitors sensors. Actuation is realized always by capacitors.

XY drag-free controller is the most challenging one considering the required very fine drag compensation and the limitations on the response time of the available actuators that reduces the useful command update rate. Two control design approaches have been envisaged for it:

- controller designed directly in body reference frame (see Figure 7-22);
- controller designed in the inertial reference frame (see Figure 7-23):
  1. The controller commands the required force in an inertial reference frame;
  2. The actual thrusters commands (in body reference frame) are computed by modulation starting from above commanded force ;
  3. The acquired measurements (in body reference frame) are reported in body reference frame by de-modulation.

The above approaches are equivalent for what concern the thruster's requirements and the performances. Both solutions need the estimated spacecraft orbital and spin rates in order to provide required rejection. For the spin rate measurement, a specific equipment has been considered (see chapter 7.7)

The first solution in principle is the better one since the "natural one". It permits to work directly in the body reference frame where the measurements are available and the commands shall be provided. At the same time, using the body reference frame, the observer (see next in the chapter) may be shared between XY drag-free controller and XY whirl controller. As drawback, the plant model envisages strong coupling between X and Y axes requiring higher measurement sampling frequency and greater care shall be put building the discrete model.

Using instead the inertial reference frame, the coupling between X and Y axes is weak and numerical problem are simpler to be managed. The draw-backs are in the necessity to introduce demodulation and modulation schemes at spinning rate. This solution has been selected.

XY drag-free controller and XY whirl controller are Multi Input Multi Output (MIMO) controller, and Z drag-free controller is a Single Input Single Output (SISO) controller.

All controllers have been designed according to the state variable approach building four lower level functions:

6. reference state trajectory generator;
7. state variable observer;
8. control law;
9. command distribution.

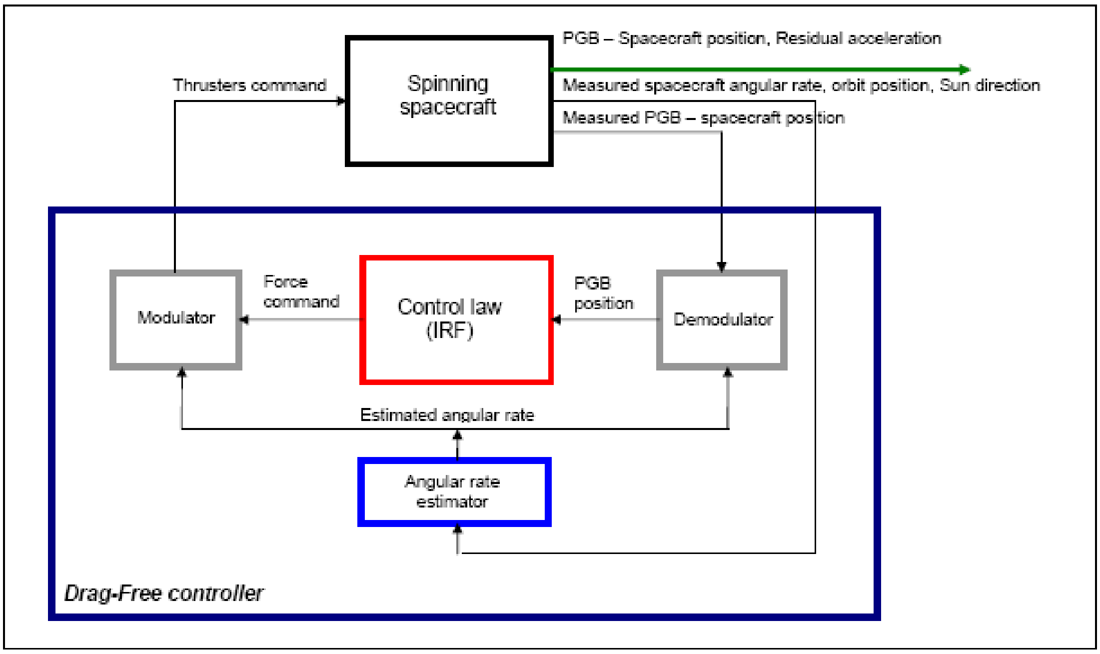

Figure 7-22 - Controller designed in Body frame – block diagram

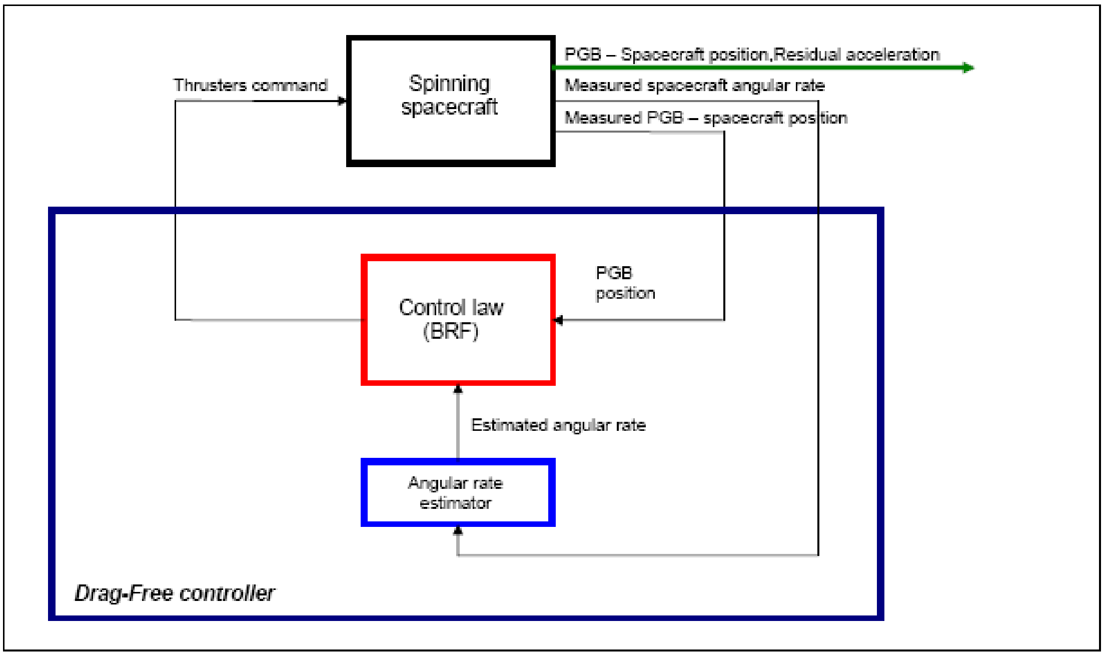

Figure 7-23 - Controller designed in Inertial frame – block diagram

Reference state trajectory generator computes the desiderata state variable trajectory. For the specific applications, the state variables are the relative position and velocity that are all zeros.

State Observer has in charge the reconstitution in real-time of all relevant plant state variables. It embeds:

10. the dynamic and kinematics plant models with acceptable and/or convenient simplifications;
11. relative disturbance force model acting on the spacecraft and PGB;
12. feed-forward by commanded force.

XY drag-free observer has been designed neglecting the coupling between X and Y axes obtaining two one-axis observers (the model errors are recovered by higher observer bandwidth). The model state variables are 5 for X axis observer and 5 for Y axis observer. They are the relative position and velocity, disturbance acceleration constituted by an integrator preceded by a harmonic oscillator.

Z drag-free observer has been designed as for X and Y axes. The general model embedded in the one-axis observer is shown in . X_0 represents the relative position, X_1 the relative velocity, X_2 the disturbance acceleration. Depending on the considered axis and the reference frame, specific values have been considered for α, β, ω_X and m_X.

XY whirl observer is based on the plant model written in the body reference frame, with the addition of a simple disturbance force model. The overall plant model state variables are 6.

Usually, the control law function computes the required force based on the sum of the following terms:

- proportional to the difference between reference relative position and estimated one;
- proportional to the difference between reference relative velocity and estimated one;
- estimated disturbance force.

In the XY and Z drag-free controllers the above approach has been totally followed. Instead in the XY whirl controller, the commanded force is proportional to the actual linear velocity in the inertial reference frame and it takes into account the estimated disturbance force.

Starting from the required force provided by control law the command distribution computes:

- the command to be send to each actuator in the assembly;
- the resultant commanded force taking into account actuator resolution, saturations, etc. Resultant commanded force is fed to the observer.

Observers' gains and control law gains have been computed according to pole placement approach. Controllers sampling frequency has been fixed to 10Hz (1 order of magnitude higher than the spacecraft spin rate).

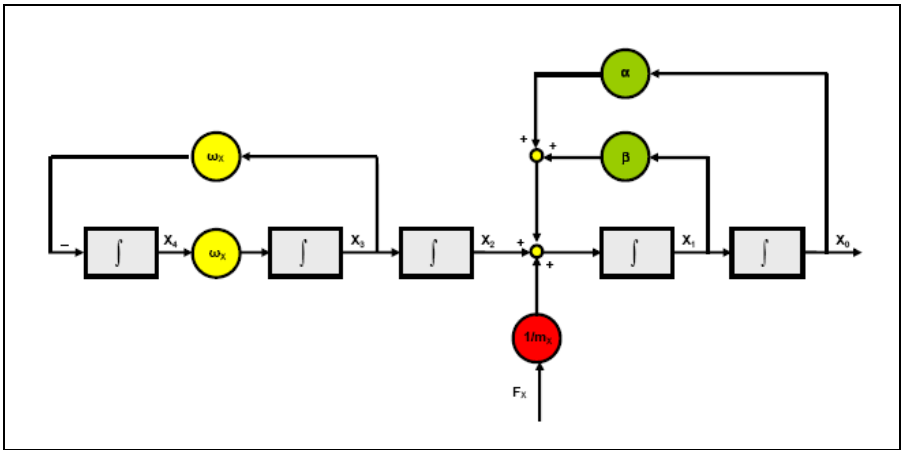

Figure 7-24 – Model embed in the one-axis observer (X , Y and Z axes).

7.5 Requirements for sensors and actuators

Capacitor sensors for PGB and spacecraft COM displacement

Capacitor sensors are used to measure the displacement between PGB and spacecraft COM. Measurement accuracy at frequency in a neighbour of the spacecraft spin rate shall be:

- XY plane

  $N_{MDF\_XY} \leq 0.5\,10^{-6}$ m/$\sqrt{Hz}$

- Z channel

  $N_{MDF\_Z} \leq 4\,10^{-6}$ m/$\sqrt{Hz}$

From those requirements, taking into account the stage of the program, the following requirement shall be considered for the design:

- XY plane

  $N_{MDF\_XY} \leq 0.05\,10^{-6}$ m/$\sqrt{Hz}$

  bias < 10^{-5} m

- Z channel

  $N_{MDF\_Z} \leq 0.4\,10^{-6}$ m/$\sqrt{Hz}$

  bias < 10^{-5} m

Scale factor and not orthogonality errors in the location of the capacitor sensors are not critical.

7.5.1 Rate sensor

Rate sensor is used to tune at the actual spacecraft spin-rate the frequency of the harmonic oscillator in the observer (Z drag-free controller), and for modulation/demodulation functions (XY drag-free controller).

Requirements on this equipment have been put considering the results out coming from previous study phase. At the end of the study, when the overall controller algorithms will be frozen, the rate sensor requirements will be updated. At the time being, the following requirement shall be considered:

- full performance for angular rate in the range: 50÷70 rpm;
- relative accuracy: $\left|\frac{\Delta\omega}{\omega}\right| < 10^{-5} \div 10^{-4}$

Micro-thrusters

As already said, the micro-thrusters are a key technology for the performances of Galileo Galilei. Table 7-15 reports the performance requirements derived for each thruster in the assembly, considering 1Hz spin rate.

No	Parameter	Unit	Value	Comments
1	Maximum thrust	μN	>=150	50% margin

2	Max thruster response time[1]	ms	40	@ commanded step (up and down) >= 60 μN
3	Resolution (quantization)	μN	24	TBC, not critical
4	Max noise	μN/√Hz	18	Around 1Hz
5	Scale factor error	%	12	Peak
6	Update command rate	Hz	10	TBC
7	Total impulse	Ns	4500	20 % margin
8	Minimum thrust	μN	<=10	TBC, not critical
9	Vector stability	rad	0.17	Peak, at 60 μN
10	Centrifugal acceleration	g	<4.4	20 % margin, 0.75m spacecraft radius

Table 7-15 – Thrusters requirements - Spin rate: 1Hz

7.6 Technologies

7.6.1 Actuators for fine drag compensation

The capability to compensate the disturbances at spinning rate strongly depends on the actuator performances. Low thrust, low noise and resolution thrusters are required.

Two technologies have been considered, both leaded by Italian industries:

1. Field Emission Electrical Propulsion (FEEP) from ALTA S.p.A.;
2. Cold gas propulsion system (CGPS) from TAS-I S.p.A.

FEEP is an electrostatic propulsion concept based on field ionization of a liquid metal and subsequent acceleration of the ions by a strong electric field. They are characterized by high specific impulse, very low noise and resolution, fast response time (tens of milliseconds) but also high electric power consumption.

Cold gas micro-propulsion is based on the well-know cold-gas technology, with significant improvements and new concepts on pressure regulation stage, mass flow-sensor, thrust valve, control algorithms. They are characterized by low specific impulse (about two orders of magnitude lower than FEEP), very low noise and resolution, slow response time (hundreds of milliseconds).

The status of both technologies with respect to the requirement reported in Table 7-15 will be provided in the next chapters.

FEEP thrusters

FEEP Thrusters are being developed for the ESA Lisa Pathfinder (LPF) mission and the CNES Microscope mission (see Figure 7- 25).

Thruster development is nearly completed, and the preparation of the Lisa Pathfinder FEEP Cluster Assembly (FCA) Qualification Model is ongoing. Manufacturing of FM parts for LPF was also released. Microscope programme is currently on hold, pending completion of thruster's development.

During thrusters development phase, the following results were achieved:

[1] Thrust response time is defined as the time required to achieve the 90% of the commanded step, and to remain definitively over this threshold.

- demonstration of priming principle and repeatability (6 thrusters in a row were successfully activated and fired);
- full performance characterization;
- demonstration of endurance up to more than 1000 Ns (> 3200 hours firing);
- successful performance of environmental testing (sine + random vibration, thermal balance);
- direct thrust measurement (ongoing at TAS-I Turin);
- neutral flow measurement characterization (ongoing at ONERA Palaiseau).

Table 7-16 permits the comparison of the GG requirements with the currently available FEEP performances. It is possible to see that the major not compliant of already available Lisa Pathfinder equipment are related to the response time and the centrifugal accelerations. Both are not considered critical by manufacturer, pending additional activities to be executed during phase B. ALTA has already outlined possible design solutions.

LISA Pathfinder (ESA – Technology demonstration for LISA)

Microscope (CNES - Equivalence principle)

Figure 7- 25 – ESA missions based on FEEP micro-propulsion.

No	Parameter	Unit	Value	FEEP status
1	Maximum thrust	μN	>=150	Thruster is designed and currently being qualified for a maximum thrust of 150 μN. Command capability is, at present, greater than 204.8 μN, and thrust up to 540 μN was recorded during one test
2	Max thruster response time	ms	40	Current response time (for 60 μN step from 0 to 60 μN) is about 80 to 150 ms, (depending on thrust and up or down command), with command frequency at 10 Hz. Step response can be improved up to 30-40ms reducing internal delay, fall time, by biasing minimum thrust (e.g. working with thrust higher than 70 μN) and/or adding some internal dissipation.
3	Resolution (quantization)	μN	24	Thruster/PCU are designed and currently being qualified for a thrust resolution of 0.1 μN (see Figure 7- 27).
4	Max noise	μN/√Hz	18	The thruster is being qualified for 0.03μN/√Hz (range 0.006 to 5 Hz)
5	Scale factor error	%	12	PCU allows scale factor correction and re-calibration with a 12 bit resolution (individual command correction). Requirement is not deemed critical.
6	Update command rate	Hz	10	Already available for Lisa Pathfinder
7	Total impulse	Ns	4500	Thruster is designed vs. a requirement of 2900 Ns (Lisa Pathfinder). Life test (on QM) will be performed up to 1100 Ns (with possible extension to higher total impulse). Analysis will be performed to predict EOL performance. At present, > 1000 Ns were verified at EM level.
8	Minimum thrust	μN	<=10	Thruster is designed and currently being qualified for a minimum thrust of 0.3 μN.
9	Vector stability	rad	0.17	For thrust greater than 10 μN is always met.
10	Centrifugal acceleration	g	<4.4	Not met by current design. Modification of thruster design, and, in particular, of tank position and shape, to minimize hydrostatic head will permit to achieve the requirement.

Table 7-16 – Status of FEEP thrusters with respect to GG requirements

Figure 7- 26 shows the FEEP cluster assembly designed for Lisa Pathfinder and representatives for the GG design. Each cluster consists of:

- 4 thrusters;
- the supporting and interface structure;
- the required thermal control hardware;
- the necessary harness, including low voltage connectors and high voltage flying leads.

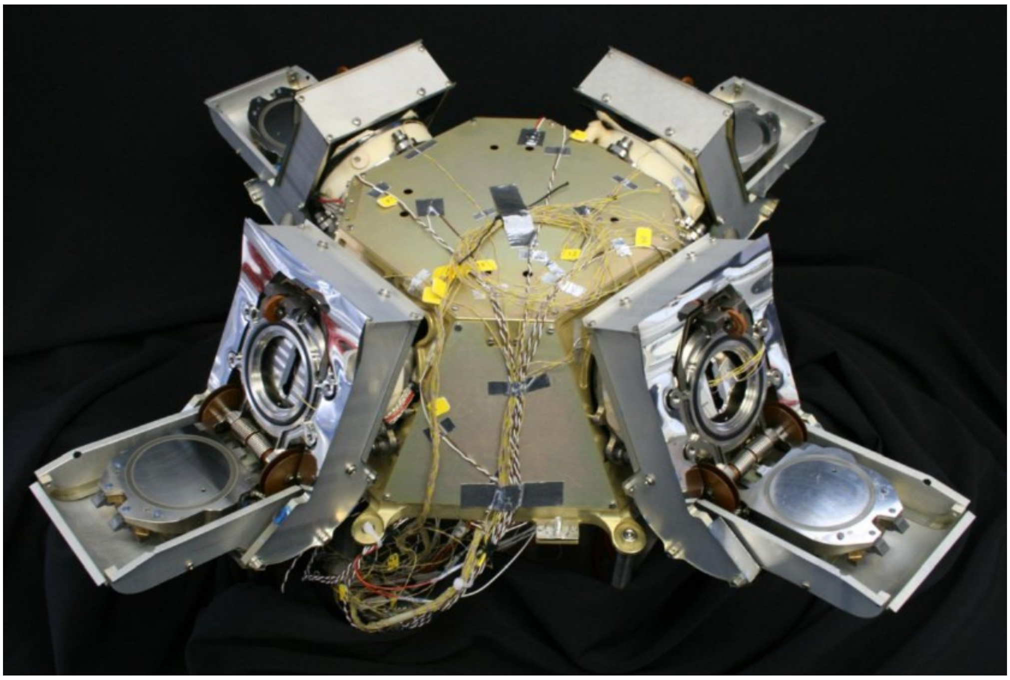

Figure 7- 26 – FEEP cluster assembly for Lisa Pathfinder.

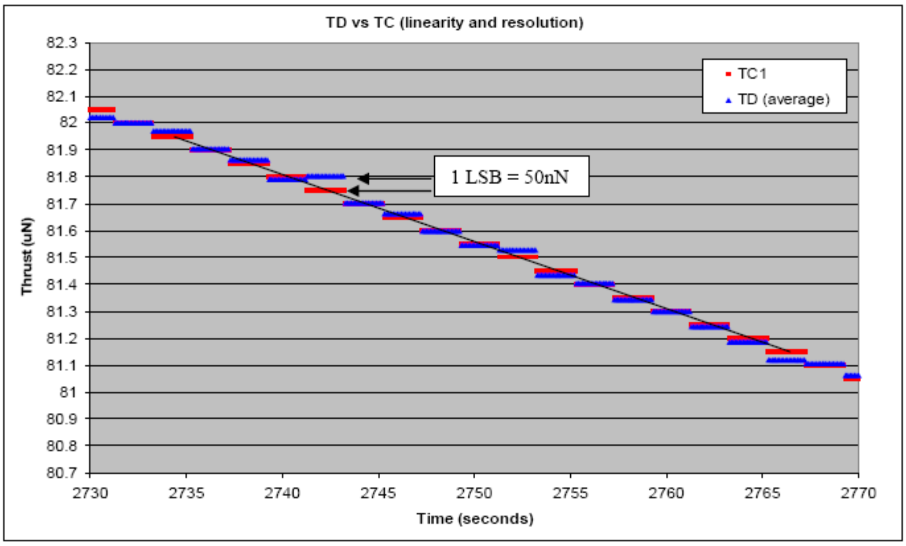

Figure 7- 27 – FEEP thrusters resolution.

As every ion thrusters, FEEP is prone to arc discharge events (arcing). Arc discharge occurs usually between emitter and accelerator electrodes (i.e., it is an event internal to the thruster). The discharge event lasts between 2 and 10 µs. After that, voltage drops down and thrust is temporarily interrupted. Thrust is recovered after the capacitors of PCU are recharged. Typical time is that of thrust command response (for a 0 to nominal thrust step).

Figure 7- 28 shows the observed percentage of sparks versus time between sparks. Figure 7- 29 shows the spark rate versus the thrust level. Taking into account the frequency of arcing occurrence and the duration, the expected effect will be the introduction of a transient in drag-compensation that will increase the noise to be considered for post-processing. In a case, this aspect will be considered in the next study phase.

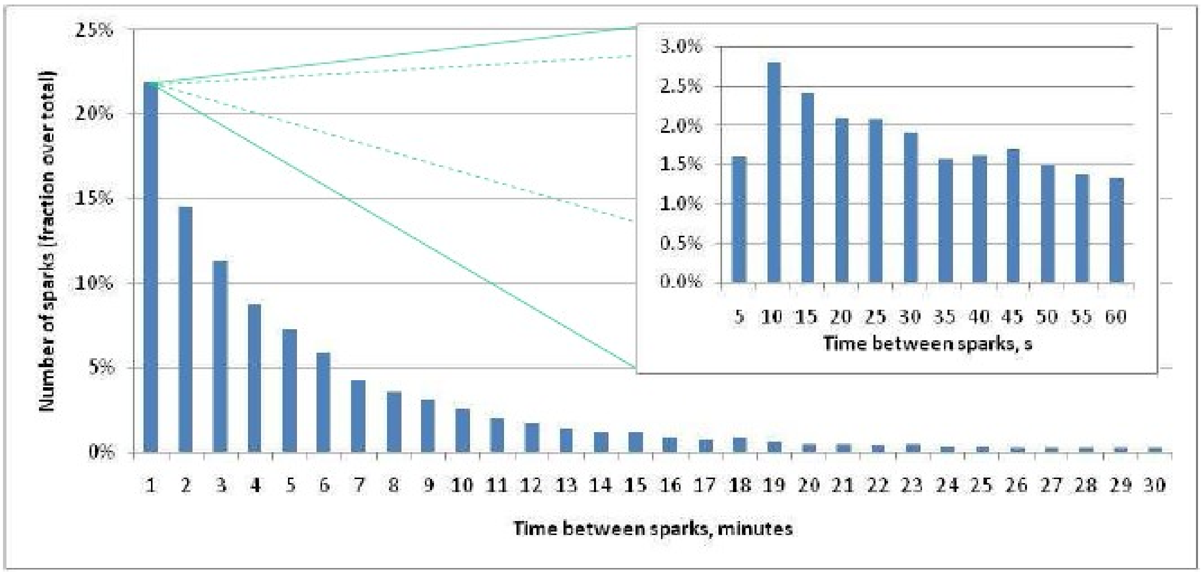

Figure 7- 28 – Percentage of sparks vs. time between sparks

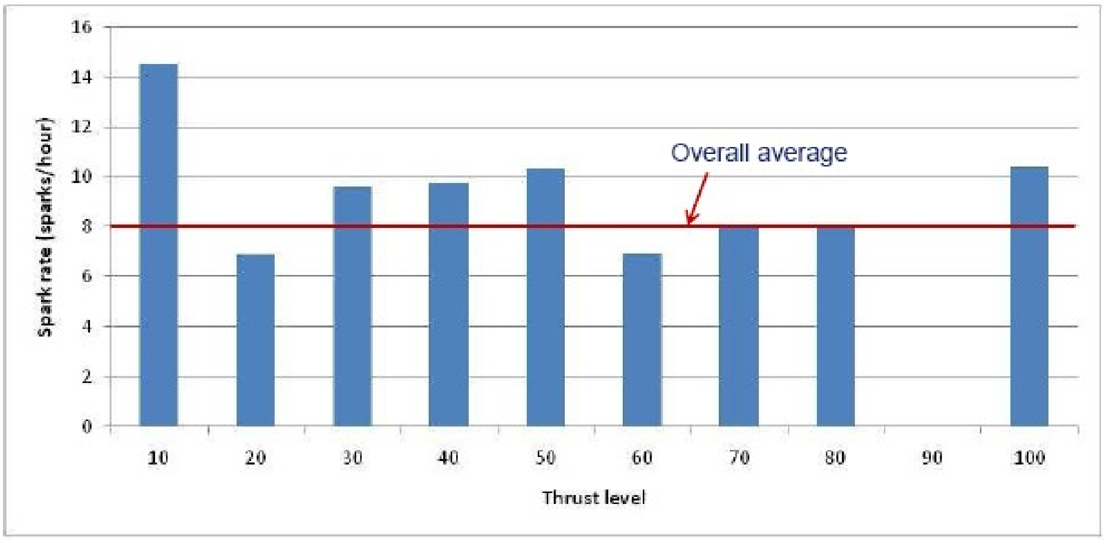

Figure 7- 29 – Spark rate vs. thrust level.

GAIA Micro Propulsion system (MPS), currently under qualification at TAS-I, represents the reference design and technology starting points for configuring/realizing both Microscope and GG.

Improvement will be provided using an EPR (Electronic Pressure Regulator) instead then a MPR (Mechanical Pressure Regulator) for realizing the PRS (Pressure Reduction & Regulation Stage)

The main advantages of an EPR based on regulation valves as actuating elements are.

- fully European technology (key components are TAS-I products);
- no ITAR exportation/importation problems;
- extremely low leakage (at least one order of magnitude better than the MPR);
- very low ripple in the regulated low pressure;
- high degree of flexibility (regulated low pressure selectable according to a specified set point);

- contained mass and dimensions.

Table 7-17 permits the comparison of the GG requirements with the currently available CGPS performances. It is possible to see that the major not compliant of already available GAIA equipment are related to the response time and the command rate. Both are not considered particularly critical by manufacturer, pending additional activities to be executed during phase B for electronic box and control algorithm re-design.

No	Parameter	Unit	Value	CGPS Status
1	Maximum thrust	μN	>=150	Thrust levels up to 500 mN achievable
2	Max thruster response time	ms	40	about 100 ms: commanded thrust level below 50 mN: 100 to 200 ms: commanded thrust level in the 50 to 500 mN range
3	Resolution (quantization)	μN	24	1 μN achievable with the current GAIA Design
4	Max noise	μN/√Hz	18	1 μN/√Hz from 0.01 Hz to 1 Hz 0.045 μN/√Hz from 1 Hz to 150 Hz achievable with GAIA design (see Figure 7- 30)
5	Scale factor error	%	12	1 for GAIA
6	Update command rate	Hz	10	1 Hz for GAIA
7	Total impulse	Ns	4500	Same Total impulse figure required for GAIA 700 million cycles at 10 Hz, in open loop, performed on the TV EM
8	Minimum thrust	μN	<=10	1 μN achievable with the current GAIA Design
9	Vector stability	rad	0.17	No data available at the moment, not critical
10	Centrifugal acceleration	g	<4.4	No risk of valve opening induced by the centrifugal force has been recognized. In fact, the centrifugal force (0.174 kg) is lower than the spring strength (1 kg).

Table 7-17 – Status of Cold Gas Propulsion System with respect to Galilelo Galilei requirements

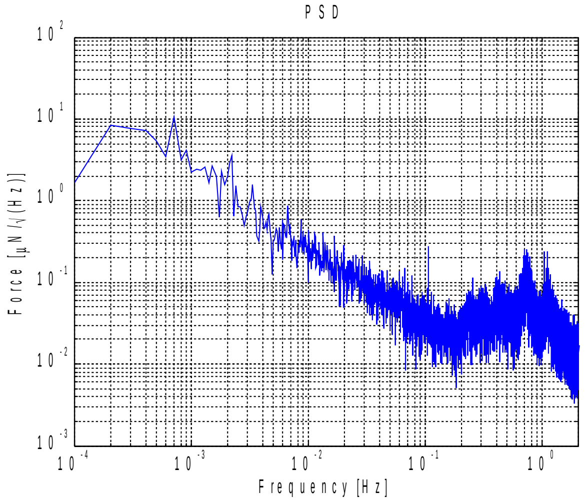

10 µN thrust

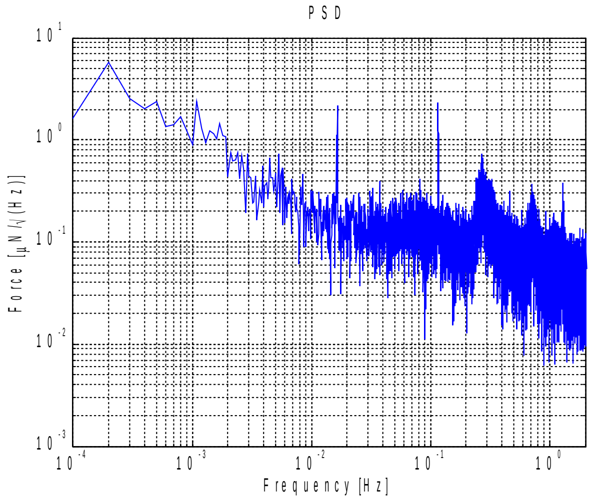

100 µN thrust

Figure 7- 30 – Spectral density of the cold gas thrusters noise measured by Nanobalance facility (TAS-I).

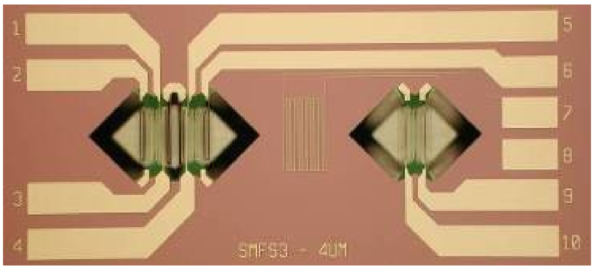

Mass Flow Sensor implemented in a Si Chip (new layout)

Micro Thruster EQM model assembled in view of qualification Campaign vs. GAIA requirements

Thrust Valve EQM for GAIA MPS

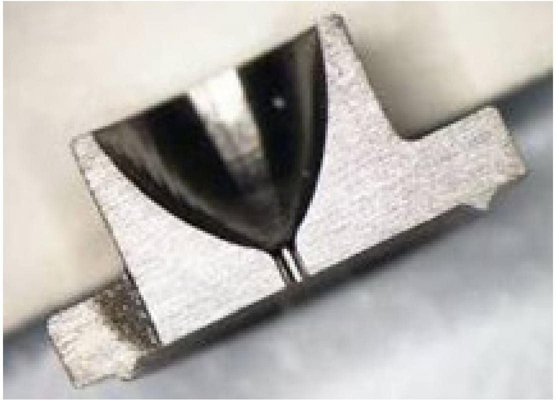

Low Pressure Regulation Valve with Nozzle (cutaway) close up

Figure 7- 31 – Pictures of the major CGPS component.

7.7 Spin rate sensor

Taking into account the unavailability of off-the-shelf equipment due to high relative accuracy and high angular rate, specific equipment has been designed by TAS-I in cooperation with SILO.

A small telescope endowed with Position Sensing Detectors (PSD) as focal plane detects Sun position from the position of the light spot focused on the PSD.

Sensor main features are:

1. square camera design to detect Sun for the whole year
    1. Field Of View (FOV) corresponding to Sun annual declination range i.e. ± 25°
2. optical system focusing light spot on PSD sensing area
3. PSD outputs:
    1. Optical power of detected light source i.e. Sun
    2. Coordinates of light spot focused on PSD sensing plane, translating into angular measurement of Sun position

The sensor accommodation will be normal to the satellite spin axis.

The internal section view is provided in Figure 7- 32.

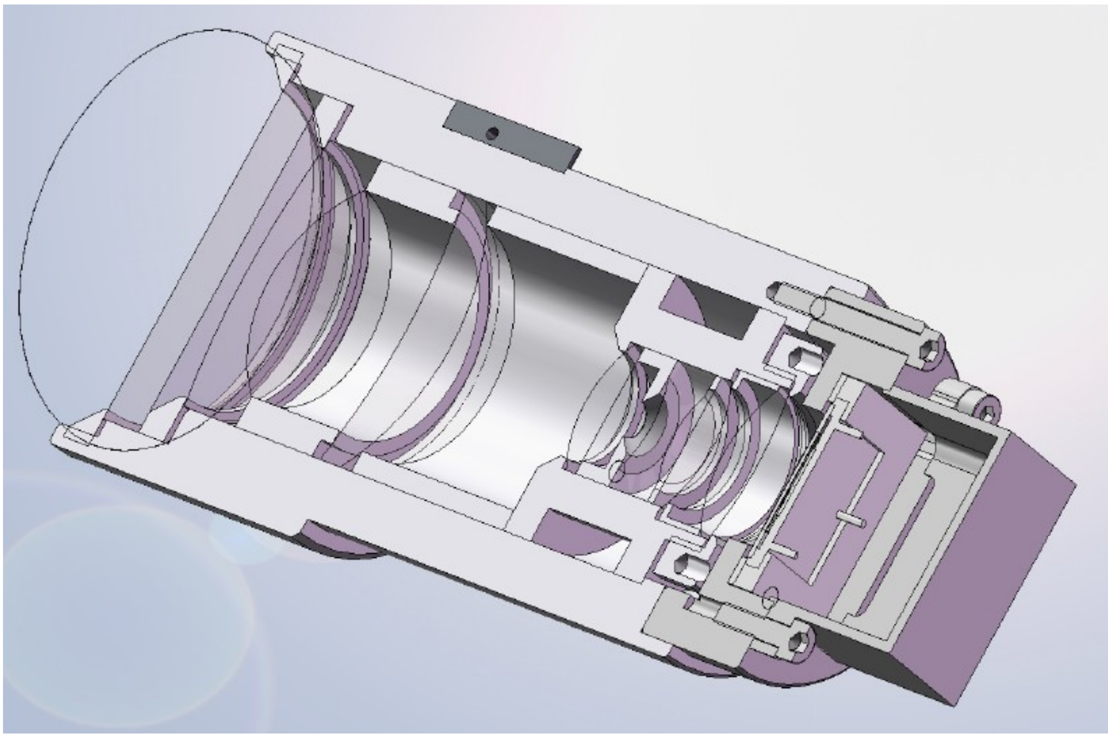

Figure 7- 32 – Spin rate sensor - Internal section view

7.8 Simulation results

In the following, the major results related to most challenging XY drag-free and XY whirl controllers will be provided. Equipment parameters have been considered in agreement with the specified values.

The presentation has been organized in lower level chapters devoted to:

- simulated perturbing force;
- XY state variables trajectory without whirl and drag controls;
- XY state variables trajectory with whirl control and without drag control;
- XY state variables trajectory with whirl and drag controls.

7.8.1 Simulated perturbing force

The simulated perturbing force takes into account the drag only. The drag force profile time series and its amplitude spectrum both given in the inertial reference frame are shown in Figure 7- 33 and in Figure 7- 34 respectively. Figure 7- 35 shows the drag force in body reference frame with spacecraft spin rate equals to 1Hz.
Drag force amplitude has been scaled in order to provide a maximum linear acceleration equals to 0.2 10-6 m/s2. The orbital period is about 5800s (600km).

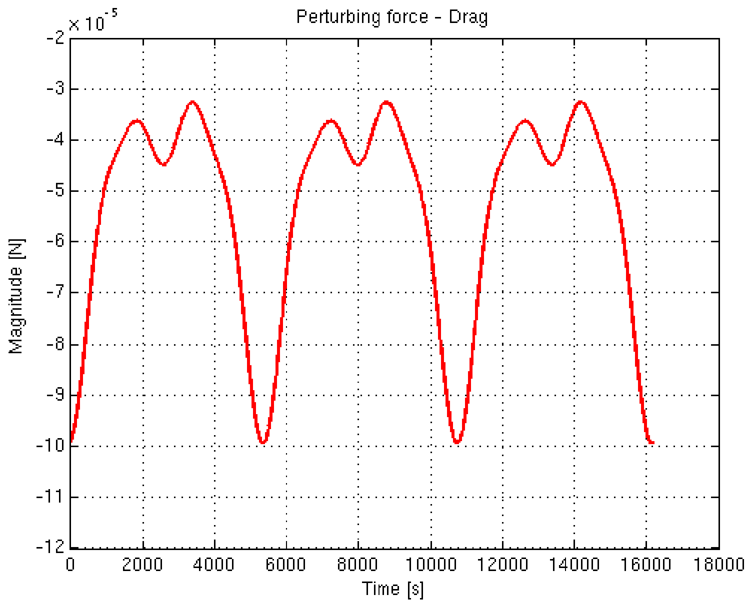

Figure 7- 33 – Time series of the XY plane perturbing force (inertial reference frame)

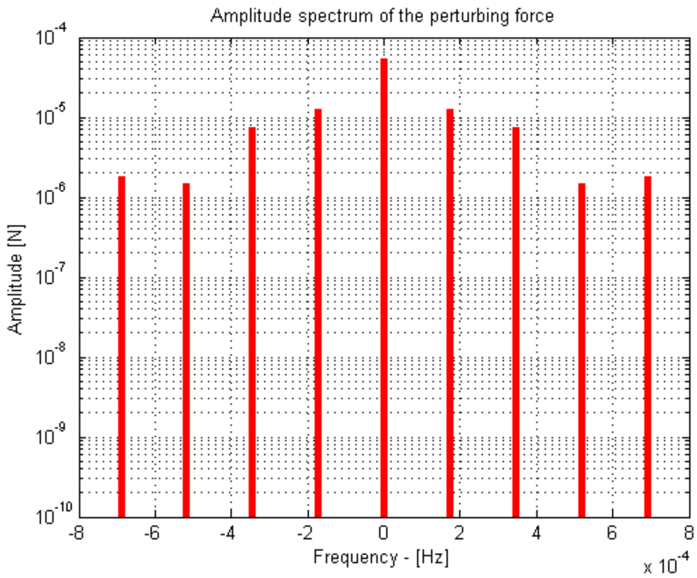

Figure 7- 34 – Spectrum of the XY plane perturbing force (inertial reference frame)

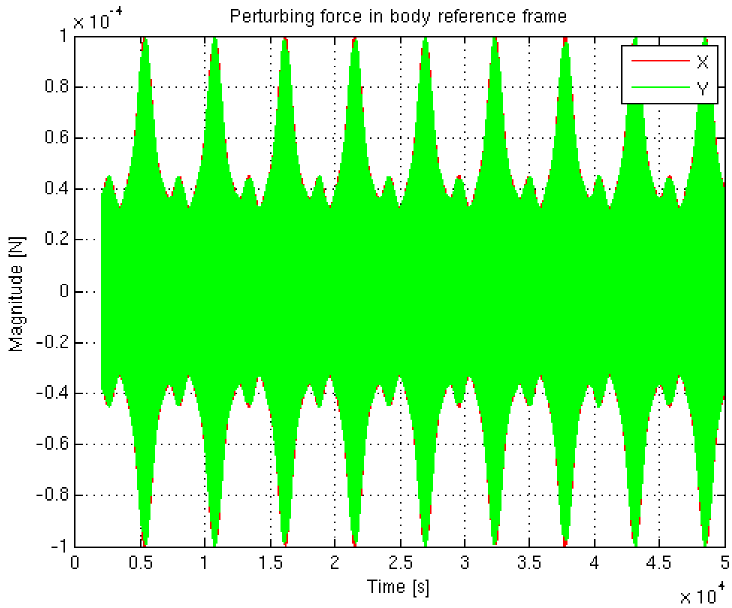

Figure 7- 35 – Time series of the XY plane perturbing force (body reference frame)

7.8.2 XY STATE VARIABLE TRAJECTORY WITHOUT WHIRL AND DRAG CONTROLS

Figure 7- 36 shows the XY displacements as function of time without whirl and drag-free controllers. The growing of magnitude of X and Y relative positions due to instability is evident. Figure 7- 37 shows a zoom of the XY movements.

Figure 7- 37 and Figure 7- 38 provide the XY displacements in phase diagram.

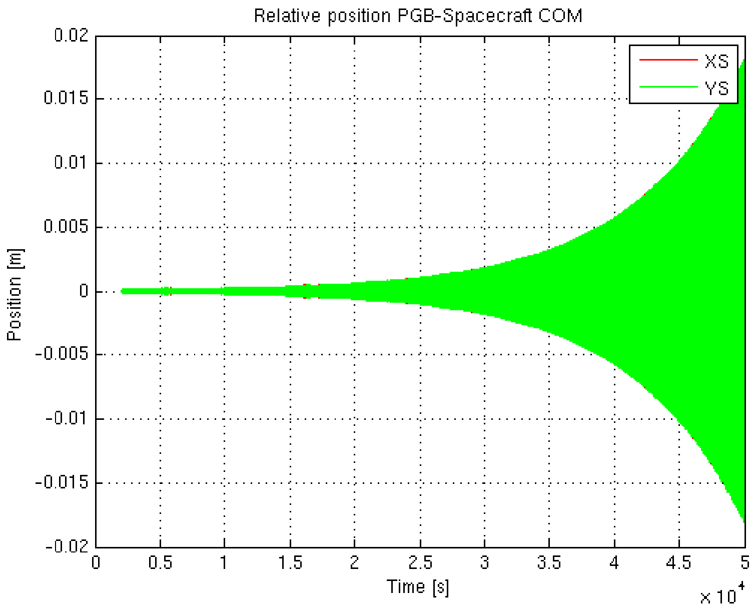

Figure 7- 36 – Time evolution of the PGB- spacecraft COMs relative position

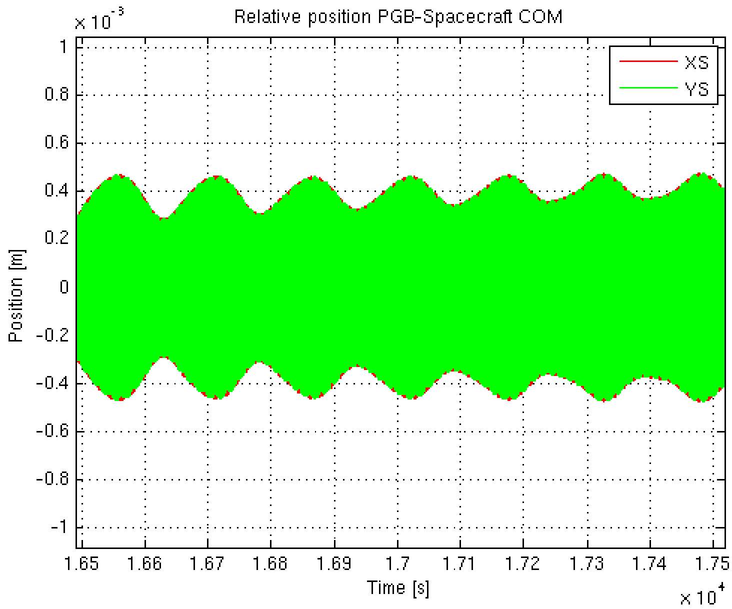

Figure 7- 37 – Time evolution of the PGB- spacecraft COMs relative position (zoom)

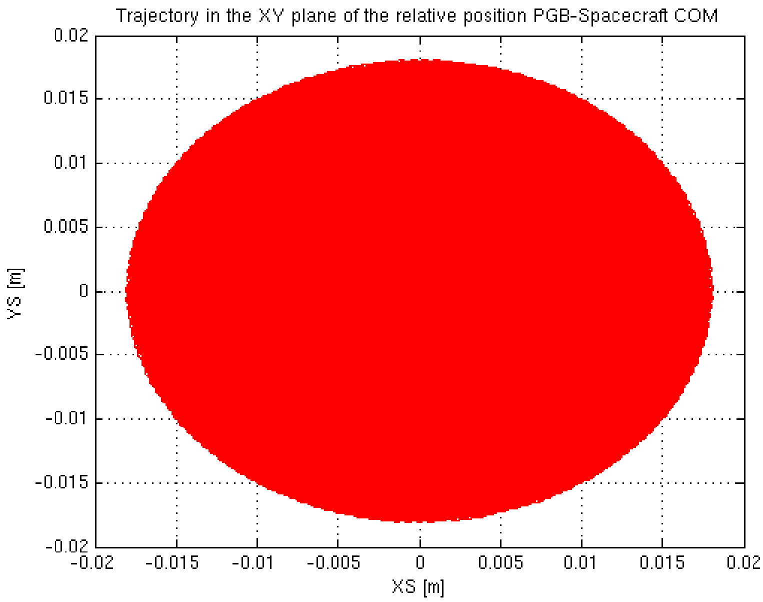

Figure 7- 38 – Phase diagram of the PGB- spacecraft COMs relative position

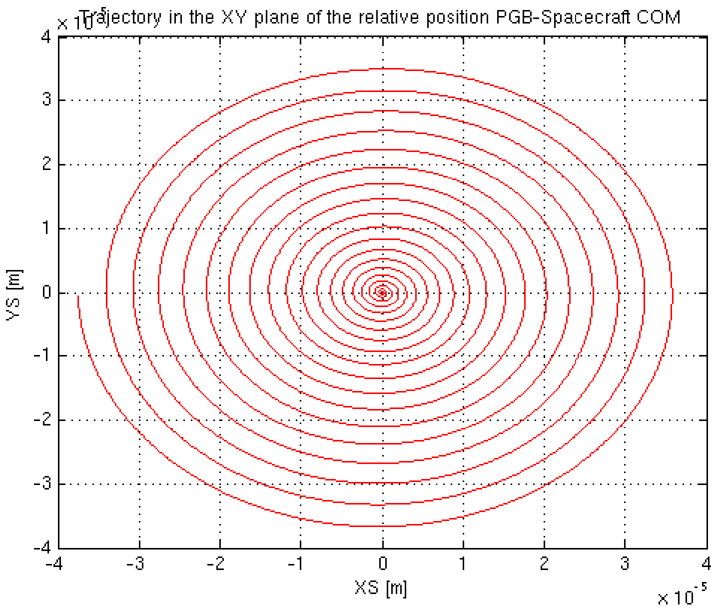

Figure 7- 39 – Phase diagram of the PGB- spacecraft COMs relative position (zoom)

7.8.3 XY STATE VARIABLES TRAJECTORY WITH WHIRL CONTROL AND WITHOUT DRAG CONTROL

Figure 7- 40 and Figure 7- 41 show the XY displacements as function of time with whirl control and without drag-free control. The pictures show the effectiveness of the stabilization introduced by control law.

Figure 7- 42 and Figure 7- 43 show the one-side spectral density of the XY PGB-spacecraft relative position given in body reference frame. It is possible to recognize around 1 Hz the rows due to the perturbing force spectrum (see also Figure 7- 34). The maximum value of

the relative position spectral density around 1Hz, computed with a frequency resolution equals to about 2 10^{-5} Hz, is 7 10^{-3} m/√Hz.

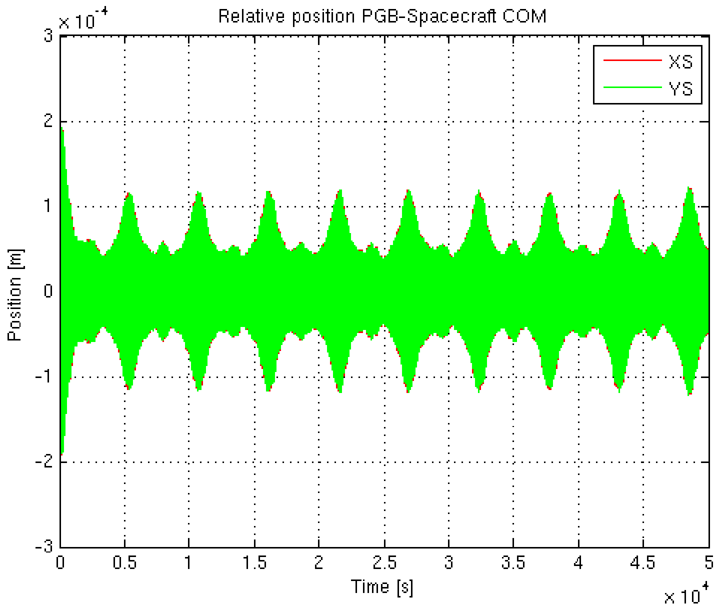

Figure 7- 40 – Time evolution of the PGB- spacecraft COMs relative position (body reference frame)

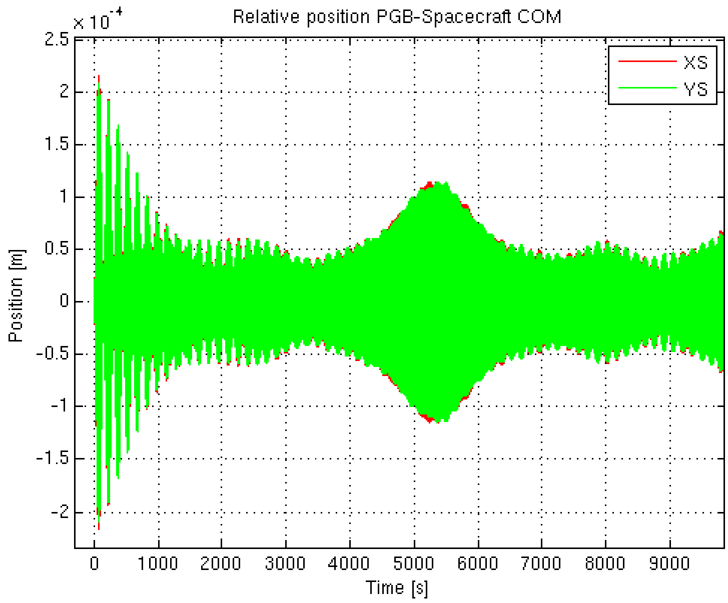

Figure 7- 41 – Zoom of the PGB- spacecraft COMs relative position (body reference frame)

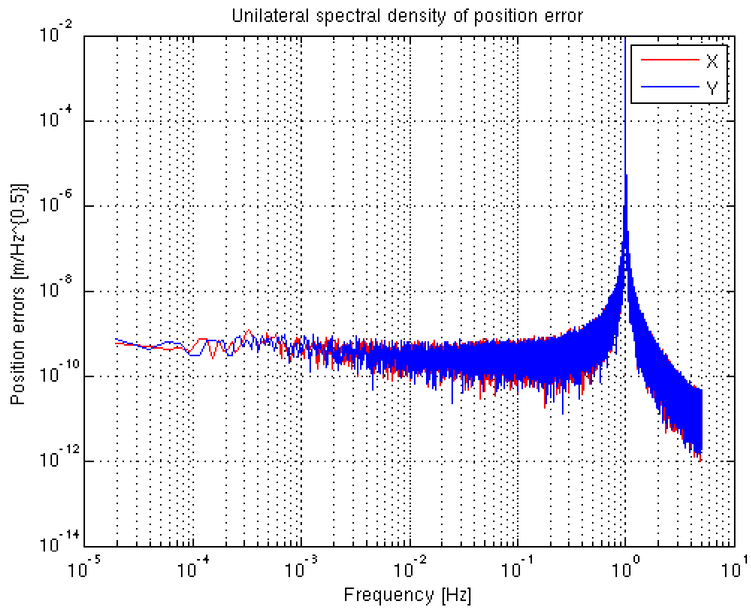

Figure 7- 42 – One-side spectral density PGB- spacecraft COMs relative position (body reference frame)

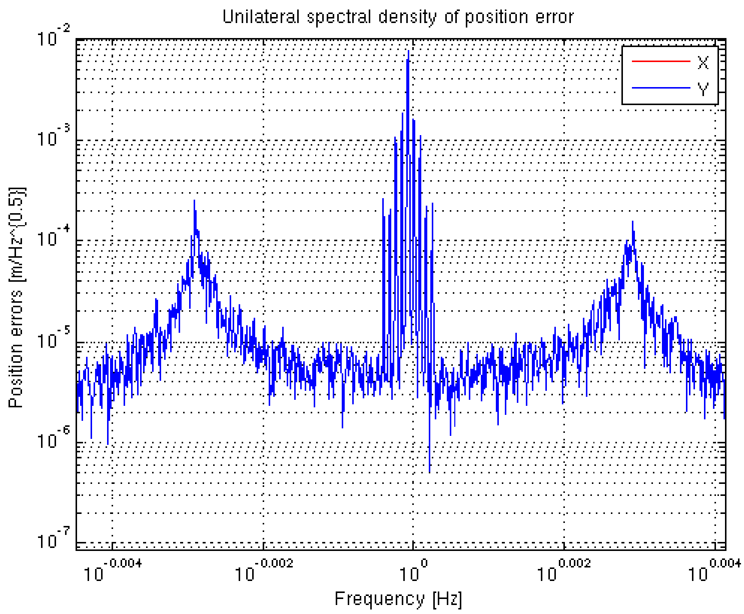

Figure 7- 43 – Zoom around 1Hz of the one-side spectral density PGB- spacecraft COMs relative position (body reference frame)

7.8.4 XY STATE VARIABLES TRAJECTORY WITH WHIRL AND DRAG CONTROLS

Results provided in the pictures below have been obtained considering a relative uncertainty on spacecraft spin rate equals to 10^{-4} Hz (one order of magnitude worse that the required value).

Two cases have been considered:

- without capacitor sensors measurement noise (Figure 7- 44, Figure 7- 45, Figure 7- 46 and Figure 7- 47). This case is relevant to appreciate the drag compensation capabilities provided by the designed control;
- with capacitor sensors measurement noise (Figure 7- 48 and Figure 7- 49). It permits to see the end performances, to be considered for scientific post-processing.

Comparing the maximum spectral density around 1Hz given in Figure 7- 43 and Figure 7- 47, it is possible to observe that the rejection on drag-disturbances provided by XY drag-free controller is lower than 1/150000 with a relative uncertainty on angular rate knowledge equals to 10-4.

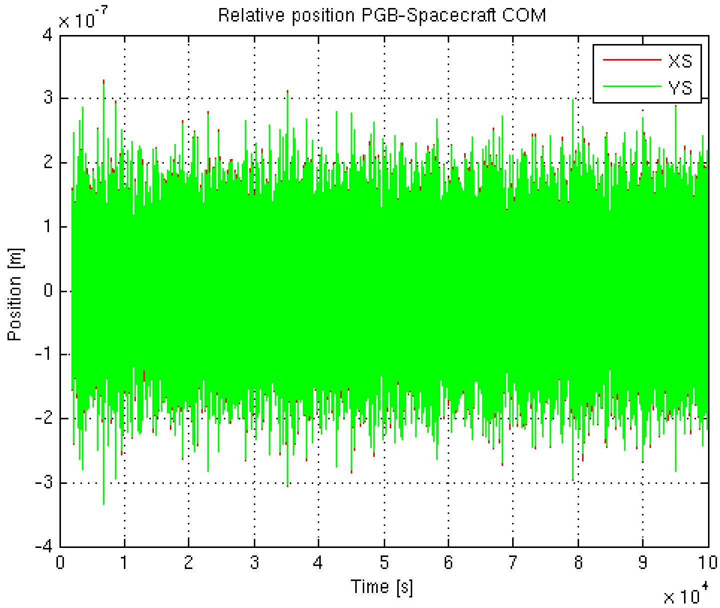

Figure 7- 44 – Time evolution of the PGB- spacecraft COMs relative position (body reference frame, without measurement noise)

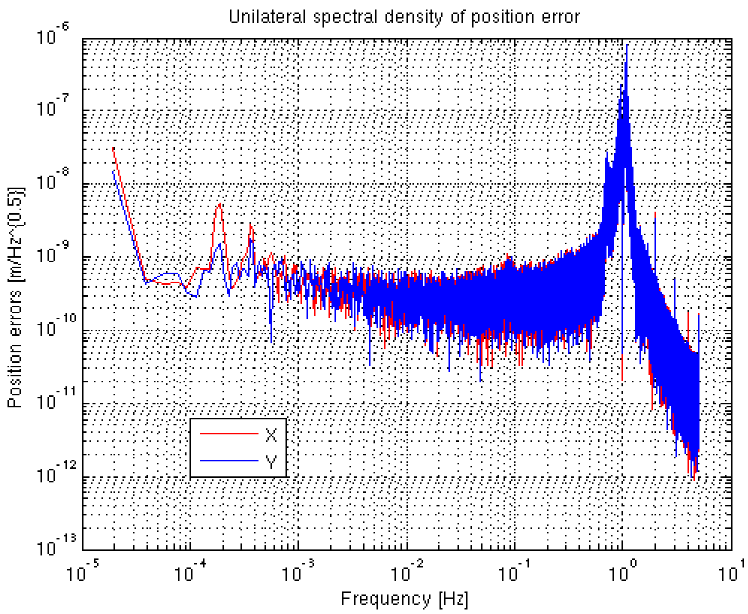

Figure 7- 45 – One-side spectral density PGB- spacecraft COMs relative position (body reference frame, without measurement noise)

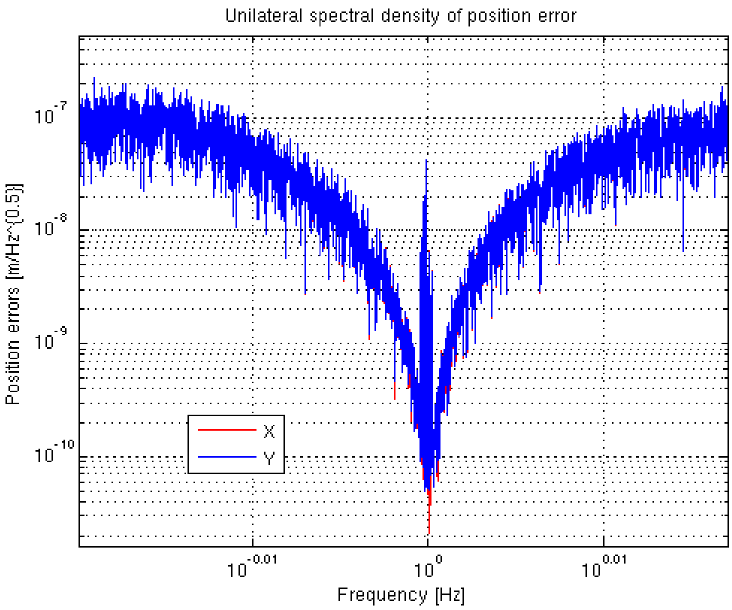

Figure 7- 46 – Zoom around 1Hz of the one-side spectral density PGB- spacecraft COMs relative position (body reference frame, without measurement noise)

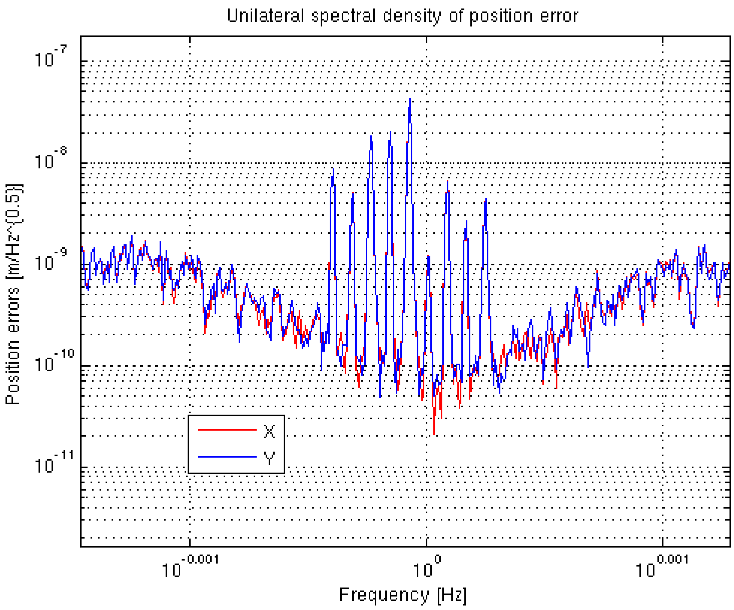

Figure 7- 47 – Zoom around 1Hz of the one-side spectral density PGB- spacecraft COMs relative position (body reference frame, without measurement noise)

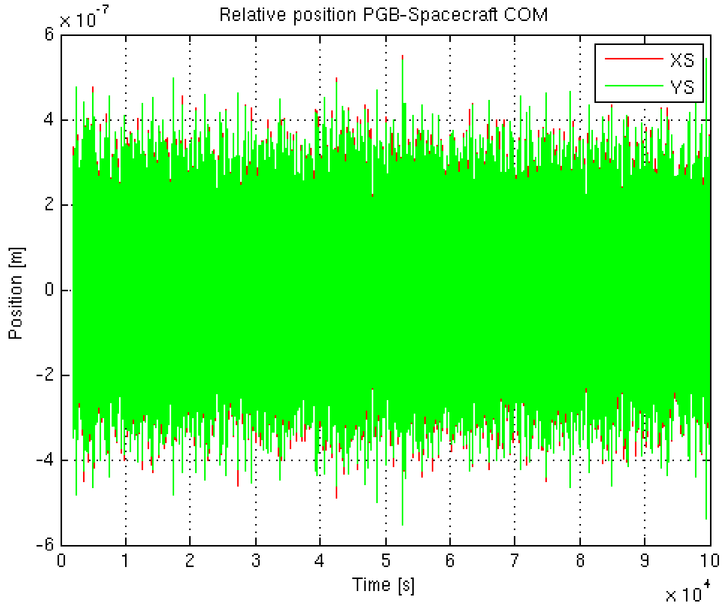

Figure 7- 48 – Time evolution of the PGB- spacecraft COMs relative position (body reference frame, with measurement noise)

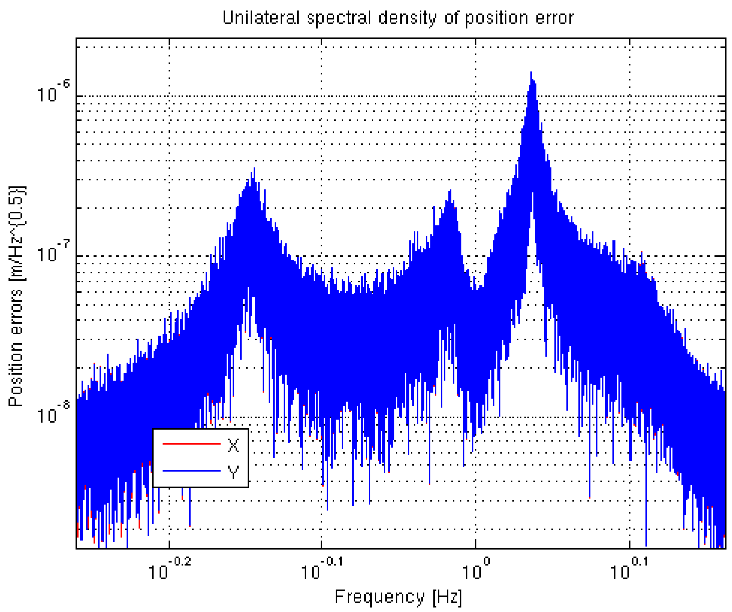

Figure 7- 49 – Zoom around 1Hz of the one-side spectral density PGB- spacecraft COMs relative position (body reference frame, with measurement noise)

7.9 CONCLUSIONS

The chapter has summarized the requirements, the architecture, the algorithms, the specific technologies and the results for the fine drag compensation sub-system.

At it has been shown, the design of the basic algorithms for fine drag compensation is completed. As usually, they will be completed with additional logics not relevant for the performance but relevant for system robustness (failure detection and isolation, sensors monitoring, etc.) during the Phase B.

Results from simulation clearly show that:

- the proposed solutions permit to meet requirements with margins considering already available technologies.
- during Phase A-2 of the study, improvements in the control performances has been achieved.

Minor open points are still present on thrusters' performances (particularly for response time, and maximum centrifugal acceleration). Two technologies have been considered, both led by Italian industries:

3. Field Emission Electrical Propulsion (FEEP) from ALTA S.p.A.;
4. Cold gas propulsion system (CGPS) from TAS-I S.p.A.

FEEP Thrusters are being developed for the ESA Lisa Pathfinder (LPF) mission and the CNES Microscope mission. Thruster development is nearly completed, and the preparation of the Lisa Pathfinder FEEP Cluster Assembly (FCA) Qualification Model is ongoing. Manufacturing of FM parts for LPF was also released.

GAIA Cold-gas Micro Propulsion system (GCPS), currently under qualification at TAS-I, represents the reference design and technology starting points for configuring/realizing both Microscope and GG.

ESA Lisa Pathfinder FEEP are almost in line with required response time, but need modifications of tank positioning and shape to meet the requirement on maximum centrifugal acceleration. Additional activities during Phase B are needed to extend the performances of already available LPF FEEP to GG FEEP.

GAIA CGPS are compliant with required maximum centrifugal acceleration, but need modifications on electronic box and control algorithms to meet the requirement on response time. Additional activities during Phase B are needed to extend the performances of already available GAIA CGPS to GG CGPS.

8. SPACE EXPERIMENT SIMULATOR

Space missions in Fundamental Physics like GG require high precision experiment to be performed in space with no direct access to the apparatus once in orbit. Though this is commonplace for all space missions, space missions at large do not rely on weightlessness as a key feature for the experiment performance. To the contrary, GG as well as other missions in this field (e.g. GP-B, Goce, μScope, Lisa-PF, Step, Lisa …), are designed to perform experiments in absence of weight. Therefore, the experimental apparatus is designed and built to work at zero-g, not at 1-g, and the issue arises as to how effectively such an apparatus can be tested in the lab before launch, and what are the chances for the space mission to perform as expected.

Since flight opportunities are scarce˜ especially for basic science˜ and flying a mission, even in Low Earth Orbit, is typically as expensive as large ground projects, it is a must to provide firm evidence before launch that chances to succeed are high.

Considerable effort has been devoted during several years in order to provide strong evidence for the success of the GG mission.

This is done by proceeding along the 3 following 3 lines:

- Build up a numerical Space Experiment Simulator of the GG mission in space based on the best know-how available to the most advanced space industries, particularly those with direct expertise in missions which fly zero-g designed payloads
- Build up a prototype in the lab which is demonstrated to have the key physical features of the payload to fly, and provide experimental evidence that the major requirements of the space mission are met
- Feed the values of the physical parameters measured in the lab into the Space Experiment Simulator to assess the overall performance of the GG mission

It is apparent that this is a very challenging plan. Space industry should have the capability required; the payload should have been designed so that a 1-g version of it can be built which maintains its key features; the scientific and industrial teams should be able to work in very close collaboration.

In this Section we are going to show why and how this is actually the case for GG, in terms of space industry specific know-how, of physical design of the experimental apparatus for it to be significantly tested in the lab, as well as for what concerns a well established tradition of close collaboration between scientists and space industry.

Thales Alenia Space Italy (TO) is certainly the best candidate to perform the task of building a GG Space Experiment Simulator.

In its capacity as prime contractor of the Goce mission of ESA, it has just built a complete Space Experiment Simulator for this mission (that has been launched on March 17th from the Plesetsk cosmodrome in northern Russia), which has considerable commonalties with GG. Goce is a high tech very challenging mission devoted to measuring the gravitational field of the Earth to very high degree and order. It is therefore equipped with very sensitive accelerometers arranged in diamond configuration to accurately measure gravity gradient effects. The accelerometers designed and built by Onera (Chatillon, France) are based on a “free floating” test mass with electrostatics bearing and pick up. Though a tiny mechanical connection is added in order to provide passive electrostatic grounding, the accelerometers as such can work only at zero-g and no full test is possible in the lab. Onera with the support of Cnes has indeed already flown similar accelerometers (onboard the Space Shuttle, as well as in previous satellite geodesy mission such as Champ and Grace). However, being the tasks of Goce more challenging, a Space Experiment Simulator was built by Thales Alenia Space in Torino to check the consistency of spacecraft and payload specifications with the overall system requirements, to support trade-off, sensitivity and worst-case analyses, to support design and pre-validation testing of the Drag-Free and Attitude Control (DFAC) laws, to prepare and test the on-ground and in-flight gradiometer calibration concepts, to prototype the post-processing algorithms, and to validate the performance of the mission. The GOCE simulator has been extensively used during the design and construction of the spacecraft and payload.

A delay in the readiness of the launcher has postponed the launch of Goce by several months, but the satellite is now flying in its low Earth orbit, thus allowing in particular putting the numerical Simulator itself under the most stringent test.

The GG Space Experiment Simulator was initiated with ASI support since the first study of the mission, precisely because it was immediately rated as a crucial validating tool. This preliminary simulator allowed the basic physical features of the GG system to be identified and checked; however, it was still too simplified (e.g., it was mostly a 2-dimensional model).

Building up on the expertise acquired with the Goce Simulator, the GG Space Experiment Simulator has been pushed to a very advanced level as it is demonstrated by the results reported here, to be brought to full completion by the end of the Study (see the Conclusions on Section 8.8)

8.1 GG SIMULATOR BLOCK DIAGRAM

The GG simulator solves for the satellite dynamics along an orbit resulting from the application of the Earth's gravity field, the non-conservative environmental disturbances (atmospheric drag, wind, solar radiation pressure, coupling with Earth's magnetic field, etc.) and the DFAC control forces and torques.
The GG simulator is based on three different main modules: the Environment, the Dynamics and the Post-Processing ones. Figure 8-1 shows a description of the GG simulator logical breakdown, highlighting the main data sets exchanged.

The *Environment Module* is in charge of computing the gravity field, the gravity gradient and the non-gravitational forces/torques acting on the spacecraft. These forces and torques are added to the forces of the DFAC and AOCS actuators, in order to realize the GG orbit.

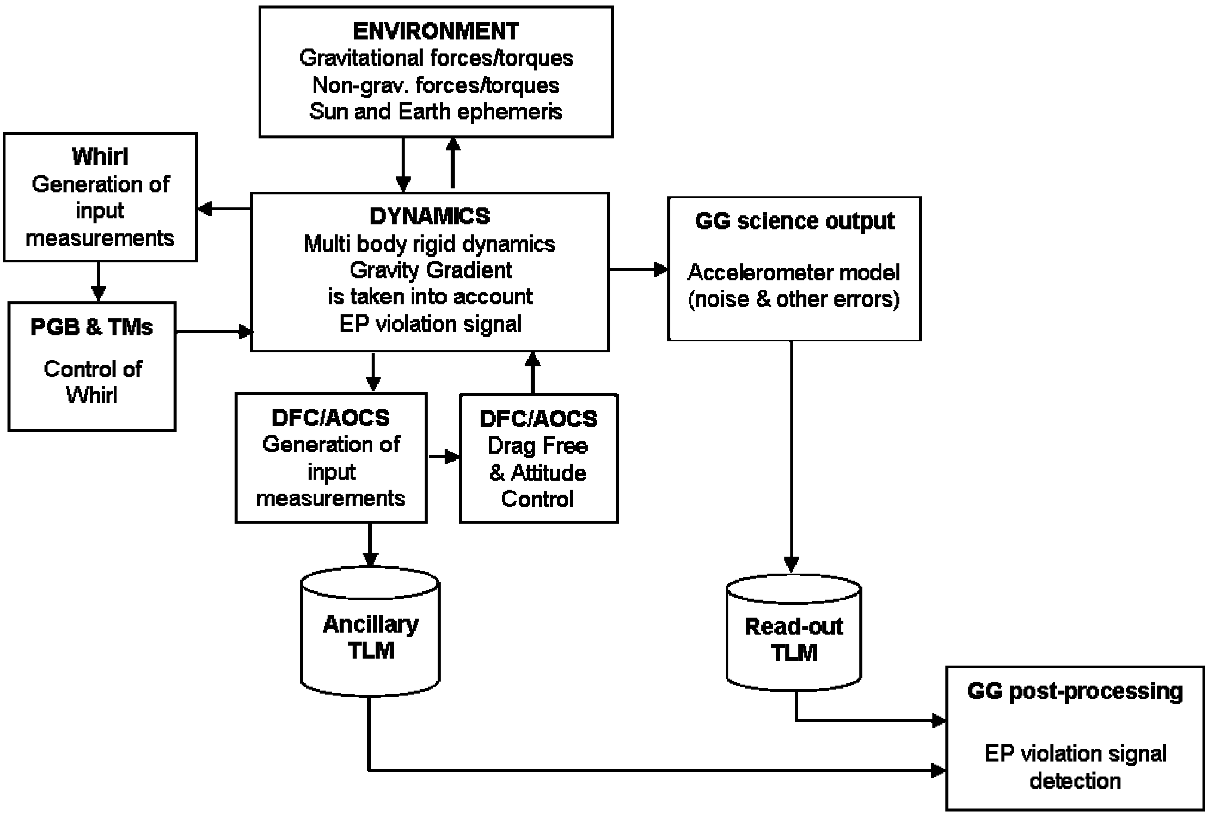

Figure 8-1: GG simulator block-diagram. The three main modules of the simulator are the Environment, the Dynamics and the Post-Processing ones. The blocks containing the controllers for the damping of the whirling motion of PGB and of the test masses, the Drag Free and the Attitude and Orientation of the satellite are components of the Dynamics module.

The *Dynamics Module* is in charge of computing the GG orbit and the relative dynamics of PGB w.r.t. the spacecraft, and of test masses w.r.t. PGB. This module has to take into account the gravity gradient acting on each body inside the GG spacecraft, and of the EP violating signal acting on the test masses. The control laws for the damping of the PGB and test masses whirling motion, for the drag free and the AOCS are also dedicated blocks of the dynamics module. It is also in charge of computing:

- the capacitance measurements used to feed the Whirl control of the PGB and of the test masses (simulation of the capacitance sensors, which feed the whirl controller)
- the forces necessary to damp the PGB and test masses whirl motions (simulation of the actuators, which realise the whirl controller commanded forces)
- the effects due to temperature variations on the inertia properties of spacecraft, PGB and test masses
- the effects due to temperature variations on the mechanical suspension (degrade of the $CMRR_{xy}$ and $CMRR_z$) and on the mechanical balancing of the read-out capacitance bridge
- the effects of the temperature gradients on the mechanical suspension (degrade of the $CMRR_{xy}$ and $CMRR_z$) and on the mechanical balancing of the read-out capacitance bridge
- the DFAC and AOCS sensors' measurements
- the DFAC and AOCS actuators' forces and torques (simulation of the FEEP/cold gas thrusters)
- the ancillary telemetry data and the other spacecraft data
- the GG science output (simulation of the science capacitance sensors measurements, which feed the post-processing module)

The *Post-Processing Module* is a self standing off line post-processor, which is in charge of detecting the EP violating signal in terms of differential test mass displacement starting from the science output (and ancillary telemetry if needed). It is also used to compute accelerations, displacements and other useful vectors in the hereafter defined different reference frames.

8.2 Simulator Reference Frames

The GG simulator describes the satellite orbit w.r.t. the most relevant reference frames for the science mission, which have been also used for the assessment of the Scientific Requirements and of the Error Budget: the Inertial Reference Frame, the Local Vertical Reference Frame and the Body Fixed Reference Frame.

8.2.1 Inertial Reference Frame – IRF –

The fundamental Inertial Reference Frame of the mission is currently realised by the J2000 Equatorial Reference Frame (JERF), which is a Cartesian frame defined as follows (see Figure 8-2):

- Origin, O_{J2000}, located at the centre of the Earth

- X_{J2000} axis at the intersection of the mean ecliptic plane with the mean equatorial plane at the date of 01/01/2000 and pointing positively towards the vernal equinox
- Z_{J2000} axis orthogonal to the mean equatorial plane at the date 01/01/2000
- Y_{J2000} axis completing a right-handed reference frame

The satellite initial conditions (position, velocity and attitude) are defined w.r.t. the Inertial Reference Frame. At t= 0 s, the satellite is lying along the X_{J2000} axis, and its velocity is along the Y_{J2000} one.

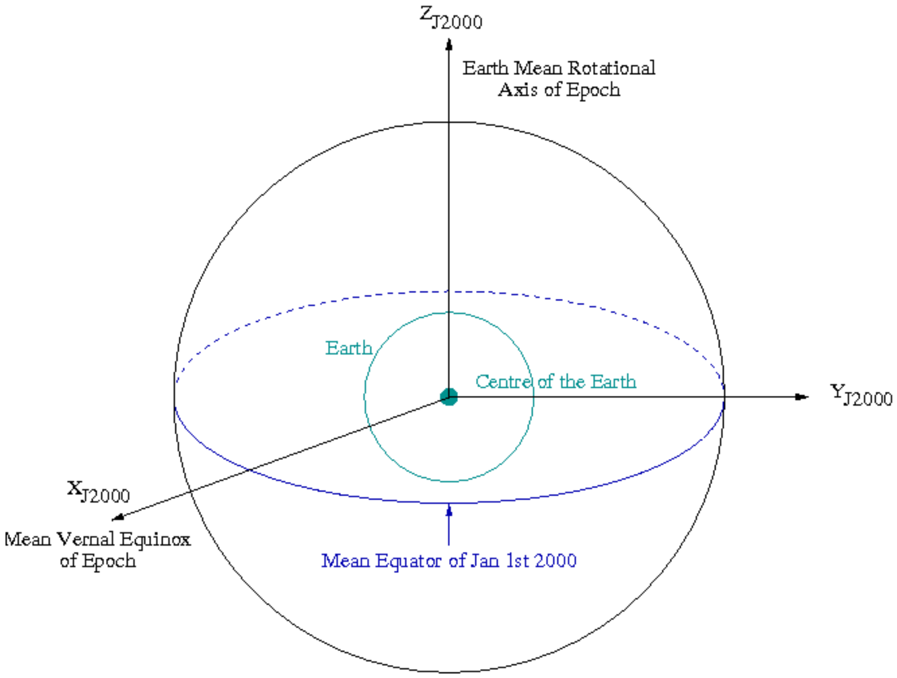

Figure 8-2: The Inertial Reference Frame is the J2000 Equatorial Reference Frame. The centre is coincident with the Earth centre, the X axis is at the intersection of the mean ecliptic plane with the mean equatorial plane (at the date Jan 1st 2000), the Z axis is perpendicular to the mean equatorial plane (at the date Jan 1st 2000), and the Y axis completes a right-handed reference frame.

8.2.2 Local Vertical Local Horizontal Reference Frame – LVLH –

The LVLH reference frame is the second fundamental frame: in this frame the EP violating signal always appears along a fixed direction (in case of a perfect circular orbit, the Earth is fixed in this reference and the EP violating signal appears as a DC effect). In order to have the EP violating signal along the X_{LVLH} axis, this reference frame is so defined (see Figure 8-3):

- Origin, O_{LVLH}, located at the satellite centre of mass (COM)
- X_{LVLH} axis directed from the centre of mass of the Earth to the satellite centre of mass (X_{LVLH} axis identifies the local vertical from the point of view of the satellite COM)

- Y_{LVLH} axis points toward the direction of motion (it identifies the local horizontal projection of the velocity)
- Z_{LVLH} axis is perpendicular to the orbital plane and completes the right-handed coordinate system.

Notice that because the spacecraft velocity vector rotates, to remain tangential to the orbit, the LVLH system also rotates about the Earth. The LVLH does not take into account the GG spinning about its symmetry axis.

The Post-Processing module of the GG simulator aims to compute the test masses differential displacement due to the EP violating signal w.r.t. the X_{LVLH}, while the main component of the non-gravitational accelerations acting on the spacecraft external surface is along Y_{LVLH}, i.e. 90° out of phase.

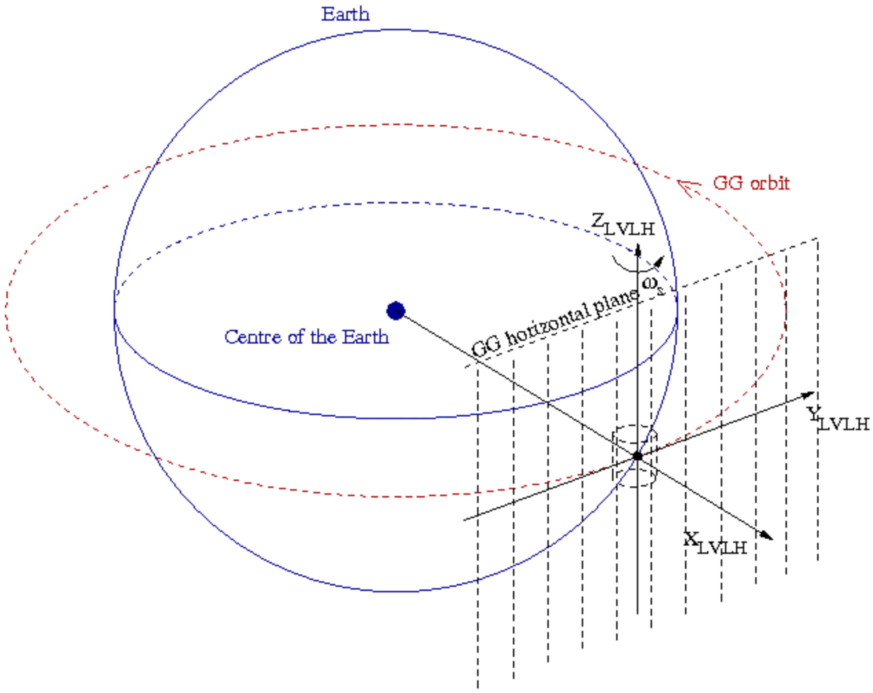

Figure 8-3: The Local Vertical Local Horizontal Reference Frame (LVLH) is a frame co-rotating with the spacecraft. Its origin is coincident with the satellite COM, its X axis is always from the Earth centre of mass to the satellite centre of mass, Y is pointing in the direction of orbit motion (it identifies the local horizontal plane) and its Z axis is perpendicular to the orbital plane and completes the right-handed coordinate system.

8.2.3 Body Fixed Reference Frame – BF –

The Body Fixed Reference Frame is the frame "attached" to the spinning satellite and defined by means of physical markers on the true structure. The necessity of assuming one spacecraft fixed reference frame is dictated by the fact that DFC sensors and actuators are fixed with respect to the satellite structure (PGB and test masses are mechanically suspended and during science operations are not fixed with respect to the satellite structure). The BF frame is defined according to the following prescription:

- The Z_{BF} axis corresponds to the central axis of the PGB connecting cylindrical tube (when the PGB is locked to the satellite). It is nominally the spinning axis of the satellite, and the positive direction is the same of the angular rate vector. In the GG simulator the Z_{BF} axis is the satellite spin axis and it is coincident with the PGB symmetry axis at t=0 s.
- The reference origin, O_{BF}, is located on the Z_{BF} axis. When PGB and test masses are locked with respect to the satellite, the origin marker is placed in order to individuate the position along the Z_{BF} axis of the test masses equatorial plane. O_{BF} is nominally coincident with the satellite centre of mass (when PGB and proof masses are locked). In the GG simulator, O_{BF} is coincident with the satellite centre of mass.
- X_{BF} and Y_{BF} axes lie on the plane containing O_{BF} and perpendicular to the Z_{BF} axis. Each axis passes through the median plane of the two pairs of capacitance plates in between the test masses. A dedicated marker identifies the axes X_{BF} and Y_{BF}, which are chosen to complete with the Z_{BF} axis a right-handed coordinate system. In the GG simulator, it is assumed that the capacitance plates defining the X_{BF} axis are the ones on the X_{J2000} at t = 0.

8.3 SIMULATOR ENVIRONMENT MODULE

This block is dedicated to the computation of the forces and torques acting on the spacecraft and resulting from the interaction with the orbital environment. As such, this module computes the gravity force, the gravity gradient torque, the aerodynamic force and torques, the magnetic torque, the solar radiation pressure force and torque. It includes:

- the Earth gravity field, with gravitational constant GM = 3.986004418·1014 m^3/s^2, according to the EGM96 Earth Gravity field solution, and Earth Mean Radius = 6378144 m. The gravity gradient torque taking into account for J2 effect is also applied on each body.
- the MSIS86 atmospheric model for the computation of the air density, temperature and chemical composition along the satellite orbit. The F10 and F10.B indexes related to the Solar activity and the Geomagnetic indexes Ap and Kp are used to feed the MSIS model.
- a model of the Earth’s magnetic field derived from the Oersted satellite measurements
- the celestial bodies ephemeredes computation

The solar radiation pressure and Earth albedo are computed modeling the satellite surface as a set of one cylinder and two simple flat surfaces. The pressures due to the solar and Earth albedo, which depend mainly on the distance from the Sun, on the altitude of the satellite during its orbit, and on the angle between the Sun direction and the local-vertical direction, is computed for each elementary surface. Once the pressures have been computed, the corresponding forces for each surface are obtained considering the normal and tangent components depending on the surface extension and on the aspect angle of the surface with respect to fluxes direction. The force is computed for each surface and applied to the surface's centre of pressure. The resulting force and torque on the centre of mass of each body is then computed.

8.4 SIMULATOR DYNAMICS MODULE

The complete GG system, which takes into account the spacecraft, the Pico Gravity Box, the inner and outer test masses, has been simulated by using the DCAP (Dynamics and Control Analysis Package) software package developed by Thales Alenia Space under ESA contract. An additional dummy body has been introduced in order to solve for the orbit without introducing numerical errors due to the high spinning frequency of the spacecraft itself (the orbit is solved in the reference frame of the first body of the kinematics chain). The dummy body is a massive point coincident with the spacecraft centre of mass: its motion w.r.t. the Inertial Reference Frame is defined by the degrees of freedom (3) of the Hinge 1, which connects it (Node 1) to the origin of the IRF. Moreover, the dummy body identifies the origin of the LVLH reference frame: the vector pointing towards the Earth identifies the X-axis, its velocity identifies the Y-axis (along-track direction), and the orbit angular velocity is along the Z-axis. The bodies are characterized by the up-to-date values of the mass and inertia properties, while the dummy body – Body 1 - is a unitary massive point coincident with the spacecraft centre of mass (Node 10). The bodies of the GG dynamical model (schematically represented in Figure 8-4) and the degrees of freedom (summarised in Table 8-1) are defined as follows:

- Body 1 is the dummy body. Its representative node (Node 1) is coincident with the spacecraft centre of mass. The Hinge 1, which connects the IRF to Node 1, has 3 degrees of freedom: its translation completely describes the orbit motion of the spacecraft.
- Body 2 is the spacecraft. The satellite has its centre of mass (Node 10) coincident with the dummy body (Node 1). The null-length Hinge 2, which connects the LVLH origin to the s/c centre of mass, permits satellite rotations only. In particular, the rotation about the Z axis defines the spin w.r.t. the LVLH.
- Body 3 is the Pico-Gravity Box (PGB). The Hinge 3, which connects the s/c centre of mass (Node 10) to the PGB centre of mass (Node 20), provides the 6 degrees of freedom (3 rotations and 3 translations) of the PGB-s/c relative motion.
- Body 4 is the outer (external) test mass (TMe). The Hinge 4, which connects the PGB centre of mass (Node 20) to the TMe centre of mass (Node 30), provides the 6 degrees of freedom (3 rotations and 3 translations) of the TMe-PGB relative motion.
- Body 5 is the inner test mass (TMi). The Hinge 5, which connects the PGB centre of mass (Node 20) to the TMi centre of mass (Node 40), provides the 6 degrees of freedom (3 rotations and 3 translations) of the TMi-PGB relative motion.

This type of multi-body connection grants an open-loop kinematics topology, with no need for cut-joint hinges. All hinges are described by a Euler sequence Type 1, x-y-z. The active degrees of freedom (DoF) defined by hinges can be differently set depending on the required type of simulation.

Hinge Id.	Transl. Dofs (x,y,z)	Rotational Dofs (x,y,z)
1	F, F, F	L, L, L
2	L, L, L	F, F, F
3÷5	F, F, F	F, F, F
Note : L = Hinge DoF Locked F = Hinge DoF Free		

Table 8-1: Translation and rotational degrees of freedom of the hinges defining the kinematics chain of the GG system. Hinge 1 connects the IRF to the dummy body, and the null-length Hinge 2 connects the dummy body to the spacecraft centre of mass.

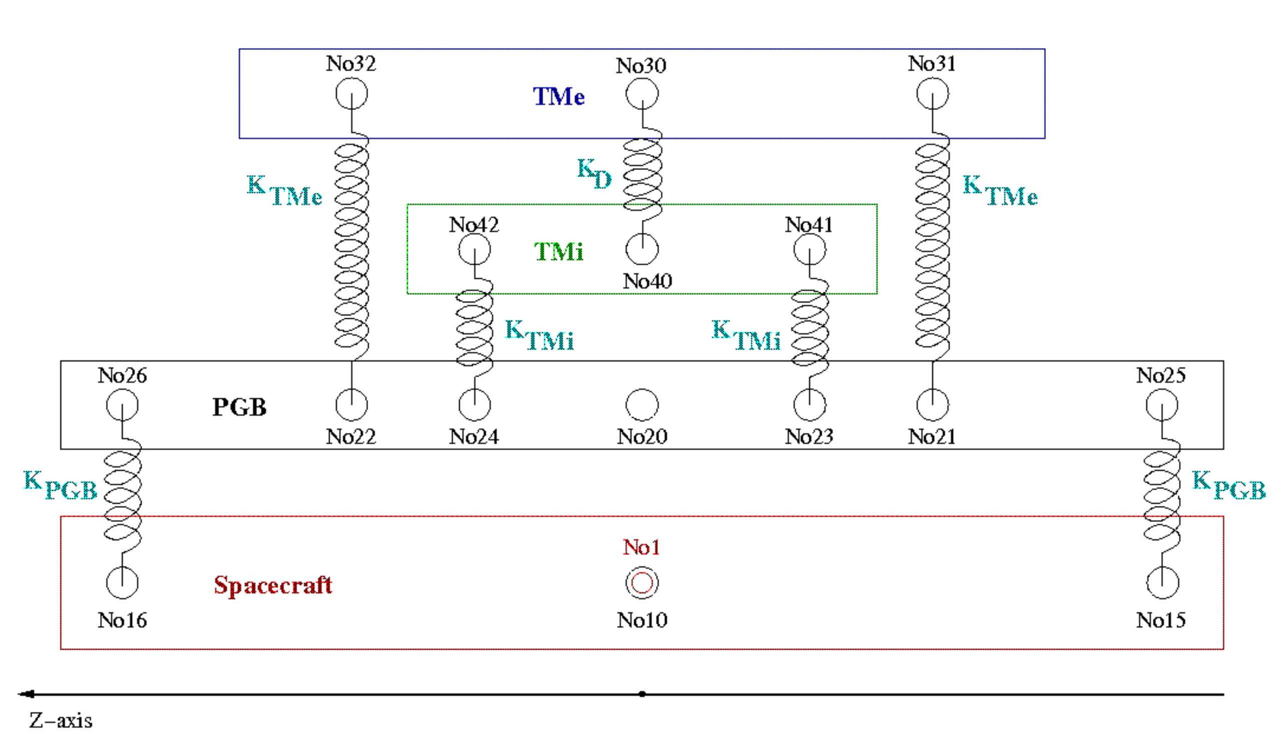

Figure 8-4: Schematic model of the GG dynamics system. Logical scheme of the dynamical model implemented within DCAP software code for finite element simulation of the space experiment. The z axis is the spin/symmetry axis of the system; all elastic connections along z are very stiff; the plane of sensitivity is perpendicular to z. The model encompasses all bodies (spacecraft, PGB and 2 test masses), each one with its 6 degrees of freedom in 3D (3 for translation and 3 for rotation), mass and moments of inertia. All non rigid components of the system (sketched as springs) are implemented with their designed stiffness (in the sensitive plane as well as in the z direction) and mechanical quality factors Q for simulation.

The Hinge 1 defines also the initial condition for the GG orbit (w.r.t. the IRF), with the convention that at t = 0 the satellite position is ($R_\oplus$ + h, 0, 0) and the satellite velocity is (0, v_y, 0), with $R_\oplus$ the Earth equatorial radius and h the GG orbit altitude. The

Hinge 2 defines instead the satellite spin w.r.t. the IRF: initially it has been assumed to be 2 Hz, but it is going to be updated to 1 Hz, according to the last analyses, which have been performed in order to verify the capability of FEEPs and cold gas thrusters for the drag free compensation.

The mass and inertia properties used in the simulator have been fixed at the beginning according to the last Phase A Report description (2000); then, they have been updated according to the March review mass budget. At the end they shall be updated according to the last mass budget. The mass and inertia properties are not continuously updated in order to make more efficient the “growth” of the simulator (the main job is adding all the possible spurious effect masking or competing with the EP signal).

The mechanical suspensions connecting the PGB to the spacecraft and the test masses to the PGB, which are schematically represented by springs in Figure 8-4, are implemented in order to provide realistic suspension modes (according to the GG on the Ground measured values) and transfer function (see Table 8-2). The PGB-s/c suspension is also characterised by its realistic dissipative term, corresponding to a mechanical quality factor $Q_{PGB} \cong 90$, in order to provide the most realistic representation of the PGB-s/c dynamics behaviour: the PGB-s/c relative motion not only must be measured in order to feed its control of the whirl motion, but provides also the input of the DFAC control, which is a key point for the GG science performance.

GG sub-system	Planar oscillation period [s]	Axial oscillation period [s]
s/c-PGB	360	30
PGB-TMe	$30 < T_{CMxy} < 120$	30
PGB-TMi	$30 < T_{CMxy} < 120$	30
TMe-TMi	540	0

Table 8-2: Oscillation periods of the various GG subsystem along the satellite spin axis and in the plane perpendicular to it.

The dissipation of the PGB-test masses suspensions is instead assumed to be greater and greater than the true one, by adopting a corresponding mechanical quality factor $Q_{TM} \cong 500$ (vs. a true value of $Q_{TM} \cong 20000$): this choice is necessary in order to have a whirl-radius doubling time t_{rw2} of the order of $t_{rw2} \approx 10000$ sec (vs. a true value of $t_{rw2} \approx 500000$ sec). This shorter t_{rw2} permits to carry out simulations covering a mission time duration not longer than 200000÷300000 sec, but which cover all the relevant aspects in terms of disturbing effects and science performance (the EP signal is in fact detected). The adoption of the true value for the mechanical quality factor of the PGB-test masses suspension would force the length of one science performance simulation to several millions of seconds, just to verify the growth of the whirling motion! It is apparent that there is nor loss of generality, neither a “favourable” assumption in this choice.

The EP violating signal is simulated with a force with amplitude $F_{EP} = m_{TM} \cdot g(h) \cdot \eta$ N, which is directed from the Earth centre of mass to the centre of mass of the outer test body only (it is a pure differential force for the test masses). This mean that the EP violating force is always directed along the X_{LVLH} axis. The mass of the proof body is 10 kg, the value of the local gravity sensed from the test mass depends on the GG altitude, and it is about 8÷8.4 m/s^2. The Eötvös parameter η is an input value for the simulator, with η in the range of $10^{-17} \div 10^{-13}$.

High-fidelity models represent sensors feeding the control algorithms and the actuators (FEEPs/cold gas thrusters and spinning-up gas thrusters), which are in charge of generating the DFAC and AOCS commanded forces and torques. The high-fidelity models for sensor and actuators have to account for intrinsic noises, transfer functions, non linearity, mounting errors, sensor/actuators inner geometrical imperfections (see Figure 8-5), temperature fluctuations, quantization and all the other effects which can degrade the scientific performance of the sensors/actuators, since the goal of the simulation is predicting the realistic mission scientific performance.

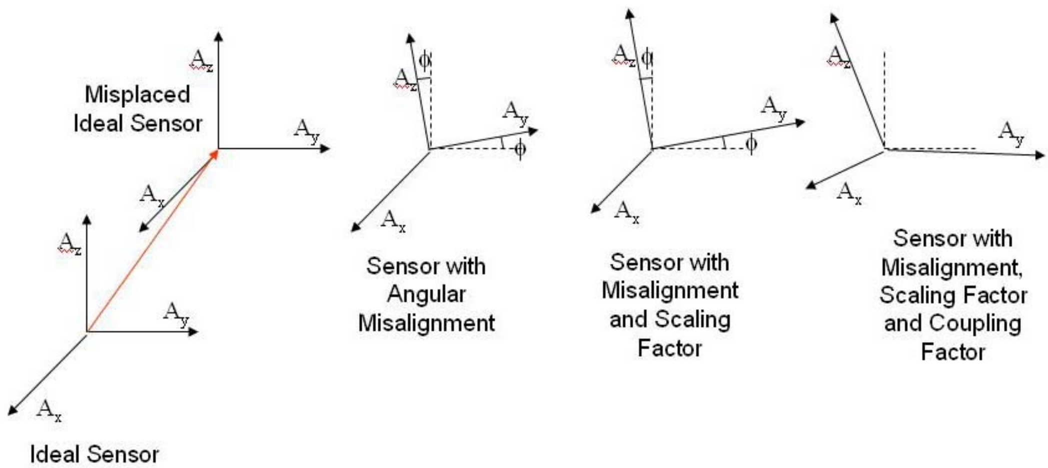

Figure 8-5: Sensor/actuator geometrical imperfection: mis-positioning, misalignment, scale factor error and coupling error.

The simulation of sensor/actuator noise and of temperature fluctuation is based on the superposition of deterministic noise (implemented by sinusoidal terms) and of stochastic noise (implemented by noise shaping technique). With the noise shaping technique, a properly devised (in the frequency domain) noise shaping filter is used to provide the desired shape to its feeding unitary band limited white noise. The block-diagram of the white noise shaping technique is reported in Figure 8-6: a unitary (one-sided) white noise is passed through an analog/digital filter that builds up the requested noise Spectral Density and which integrates also an anti-aliasing filter (if necessary). The output of the filter is then decimated (if requested) and saved into a dedicated variable.

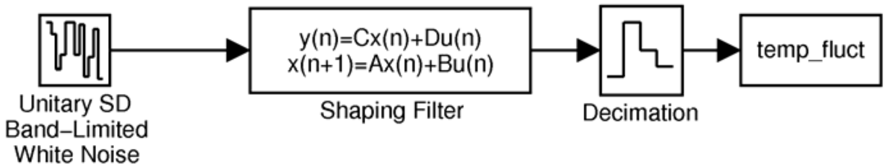

Figure 8-6: Block diagram of the white noise shaping technique. A white noise with unitary (one-sided) Spectral Density is passed through a shaping filter (applying also the anti-aliasing, if necessary) and decimated (if required) before saving the output into a dedicated variable.

Figure 8-7 shows as example the time histories of the fluctuating temperature, temp_fluct, realized according to the white noise shaping technique. Figure 8-8 shows the Spectral Density (SD) as computed from the simulated time history, vs the desired analytic SD: the desired analytic SD can be superimposed to the computed one.

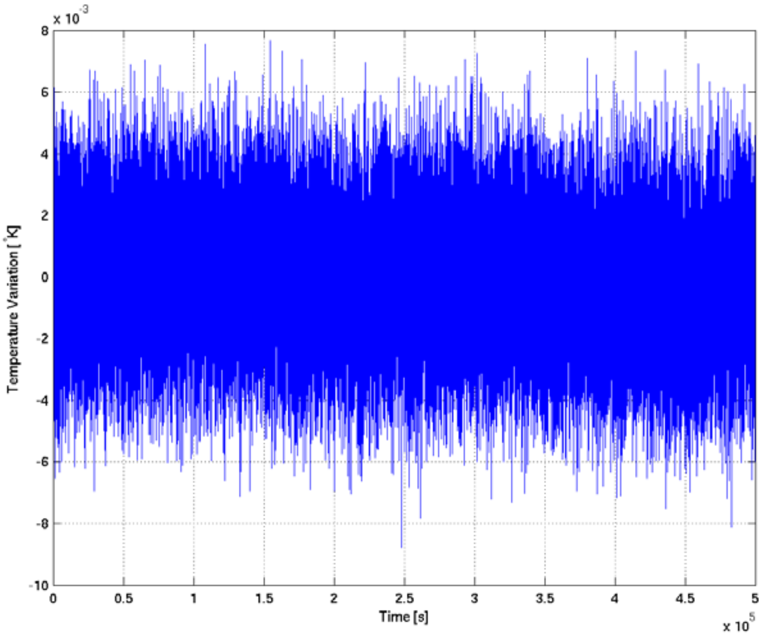

Figure 8-7: Time history of the fluctuating component of temperature obtained with the white noise shaping technique

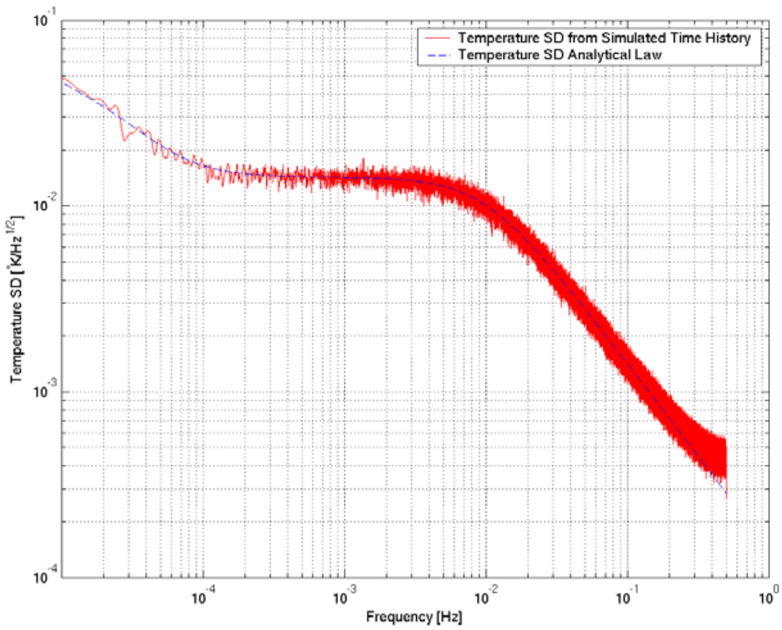

Figure 8-8: Spectral density of the temperature fluctuation computed from the simulated time history vs. the Spectral density desired analitic law.

The above cited technique provides the capability of adding the temperature effects sensed at the level of the test masses (thermal noise, temperature fluctuation), of the mechanical balancing of the science read-out, and of the $CMRR_{xy}$ and $CMRR_z$ variation due to temperature.

An analytic function for the temperature variation sensed from spacecraft and PGB shall be instead modelled in order to introduce their inertia variations.

The simulator architecture allows easy incorporation of models generated by a wide range of software tools, such as DCAP-RT (Dynamics and Control Analysis Package for Real Time, TAS-I developed dynamics package), and commercial off the shelf tools like Matlab/Simulink and Real Time Workshop.

8.5 Post-Processing Module

The GG sensor and actuators are fixed w.r.t. the spinning satellite: this means that the detection of the EP violation signal and of the other interesting information (non-gravitational acceleration, whirling motion, temperature effects, gravity gradient contributions, etc.) is completely masked by the GG spinning frequency.

The Post-Processing module, which is in embryonic status (Phase A level), consists of a Matlab macros package, which has been implemented in order to allow the transformation of all the sensor measurements from the BF to the IRF and to the LVLH reference frames. Also the ancillary information about the satellite, PGB and test masses dynamics is provided in all the reference frames, in order to allow the science performance check by using the time histories generated by the simulator. The implemented macro package requires the Signal Processing and Statistics Matlab Toolboxes. The coding of this module is such that it should be easy a full porting to the GNU Octave environment, which is a free Matlab clone providing also packages equivalent to the Signal Processing and Statistics Toolboxes.

The Post-Processing module allows the analysis on both the time and frequency domain, providing results in terms of Amplitude Spectrum and Spectral Density of the interesting signals (e.g. Fourier analysis of the non-gravitational accelerations w.r.t to IRF and Spectral Density accelerations and displacements).

A further development of this module is foreseen in case of advance in Phase B of the GG science mission.

8.6 EXAMPLE OF A SCIENCE PERFORMANCE SIMULATION

The results of one science performance simulation have been hereafter reported in order to validate the GG simulator and to show its capabilities and usefulness. This simulation was carried out in order to check the real basis of the experiment, i.e. the capability to detect the EP violating signal, taking into account:

- the gravity field and the gravity gradient acting on the spacecraft
- the non gravitational forces acting on the spacecraft surface
- the dissipation of the mechanical suspensions (whirling motions and whirl controls of PGB and test masses)
- the gravity gradient acting on the proof masses

For this exercise, the sensors' and actuators' noise and imperfections have been neglected, in order to compare the simulator's results vs. the analytical predictions. Moreover, it is assumed a perfect Common Mode Rejection Ratio of the mechanical suspensions ($\chi_{CMRRxy} = 0$, $\chi_{CMRRz} = 0$), and a perfect mechanical balancing of the science capacitance bridge ($\chi_{bridge} = 0$). Due to the perfect rejection of the common mode by means of the mechanical suspension, the DFC for the partial compensation of the non-gravitational disturbances is not working in this simulation. The satellite spin frequency has been updated to the new default value: 1 Hz. For this exercise the oscillation periods of the test masses and of PGB have been modified (compare Table 8-3 vs. Table 8-2) in order to largely amplify the displacements due to the inertial acceleration sensed by the bodies (this is due to the fact that the adopted environment cannot be considered a worst case scenario).

GG sub-system	Values of simulated Planar oscillation period [s]	Values of simulated axial oscillation period [s]
s/c-PGB	295.04	295.04
PGB-TMe	T_{CMxy} = 113	113
PGB-TMi	T_{CMxy} < 113	113
TMe-TMi	500	0

Table 8-3: Oscillation periods of the various GG subsystem along the satellite spin axis and in the plane perpendicular to it adopted for this science performance simulation.

The orbit altitude for this simulation has been chosen to be 520 km, which is not the reference altitude of the science mission, but the one for which the local gravity is 8.4 m/s^2: this value of local gravity was the driver for the EP violating signal for this simulator run. The implemented EP violating signal is the minimum detectable one, i.e. it is due to $\eta=10^{-17}$. Such a signal is simulated with a force with amplitude $F_{EP} = m_{TM} \cdot g(h) \cdot \eta = 8.4 \cdot 10^{-16}$ N, always directed along X_{LVLH} and acting on the outer test mass only. The initial time for the orbit has been assumed to be 2013 July 7th, 6 a.m.: the solar radiation indexes used for this simulation are F10 = F10.B = 120, the geomagnetic index is 8: Figure 8-9 shows the GG orbit and the initial conditions of the simulation (satellite on the X_{IRF} axis). The solar radiation pressure has been taken also into account. The spacecraft area to mass ratio used for the simulation is 0.0032 m^2/kg, which is slightly better than the up-to-date true one (0.005 m^2/kg), but still representative.

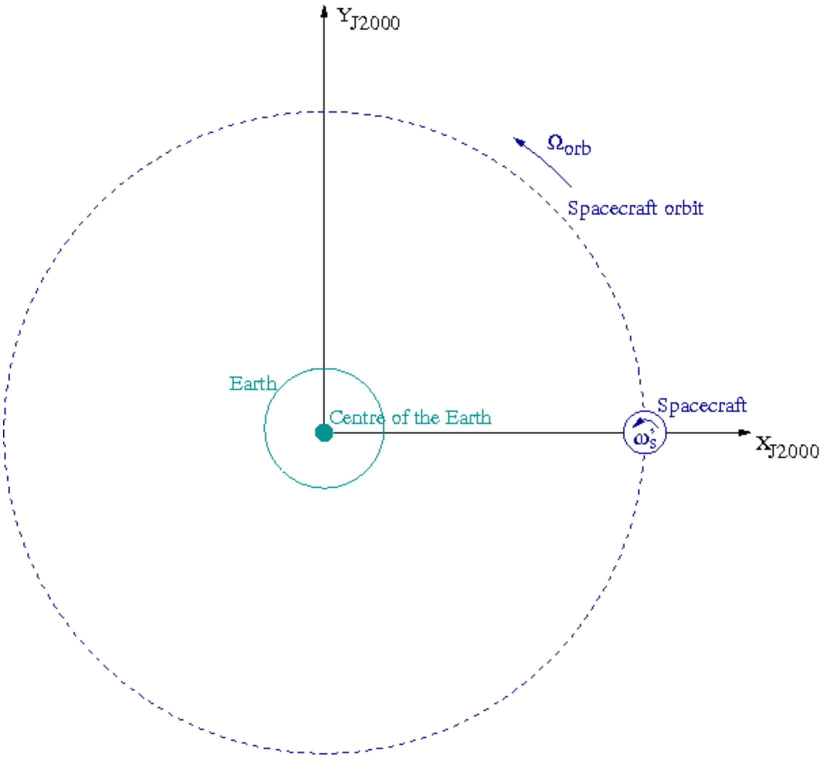

Figure 8-9: Schema of the initial conditions for the satellite orbit of this simulation. At t = 0 the Hinge 1 locates the satellite w.r.t. the IRF with the position vector r = ($R_\oplus$ + h, 0, 0), with $R_\oplus$ the Earth equatorial radius and h the GG orbit altitude. The satellite velocity is so v = (0, v_y, 0).

The continuous controllers of the whirling motion of the PGB and test masses are fed by ideal capacitance sensors and realized through ideal capacitance actuators.

8.6.1 Satellite acceleration in the LVLH reference frame

One of the main features of the simulator is the capability to compare the accelerations that have to be compensated/rejected and the acceleration that has to be detected: the non gravitational forces acting on the external surface of the spacecraft provides an inertial acceleration that is several orders of magnitude bigger than the EP violating signal. The LVLH components of the spacecraft non gravitational acceleration have been computed by using the Post-Processing module and shown in Figure 8-10, Figure 8-11 and Figure 8-12 below.

Figure 8-12, which shows a zoom of the time histories of the spacecraft acceleration along the Z_{LVLH} axis, highlights also the oscillating term due to the mechanical coupling with the PGB. It has to be pointed out here that the realized simulation is not yet the worst case scenario for the environment, and that it is just one possible representation for the satellite dynamics. The worst case scenario for the environment shall be taken into account once the satellite configuration and the possible launch date will be frozen. The short eclipse periods are also visible: during the eclipse the mean value of acceleration is zero.

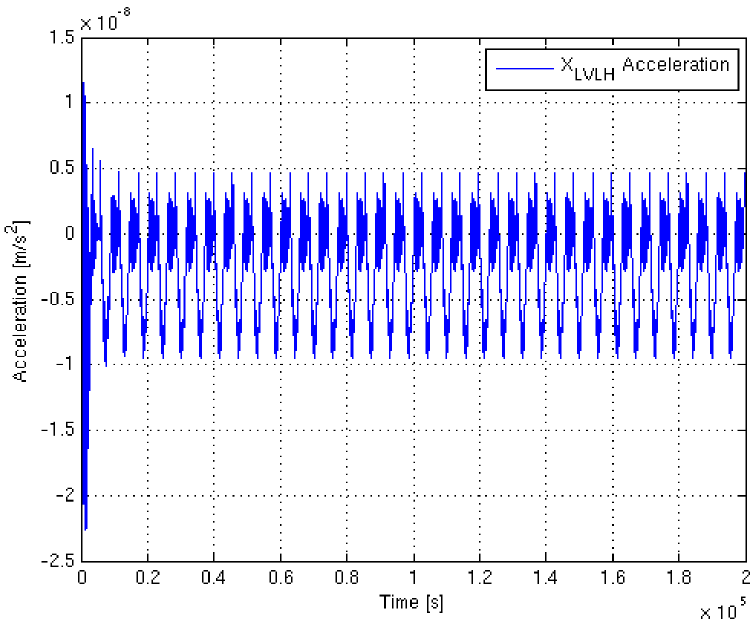

Figure 8-10: Time history of the spacecraft non gravitational acceleration along the X_{LVLH} axis, i.e. along the same direction of the EP violating signal, whose amplitude is $8.4{\cdot}10^{-17}$ m/s^2.

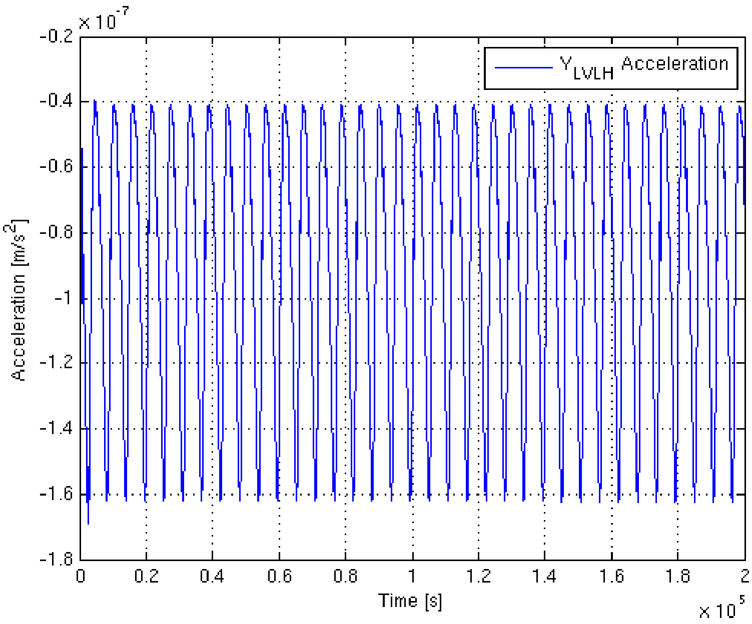

Figure 8-11: Time history of the spacecraft non gravitational acceleration along the Y_{LVLH} axis, i.e. perpendicular to the direction of the EP violating signal, whose amplitude is $8.4{\cdot}10^{-17}$ m/s^2.

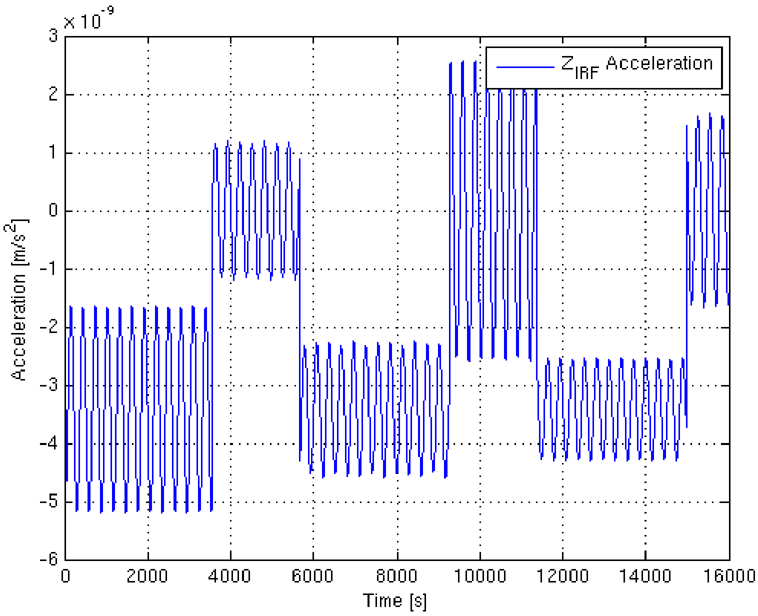

Figure 8-12: Zoom of the time history of the satellite non gravitational acceleration along the Z_{IRF} axis (Z_{LVLH} is parallel to it, there is only translation of the origin), i.e. perpendicular to the orbit plane. The relative motion of PGB w.r.t. the spacecraft is represented by the oscillations of the signal. The short eclipse periods are also visible (acceleration mean value is zero).

8.6.2 PGB-S/C DISPLACEMENT

The PGB-s/c displacement has been already largely analyzed in the previous section dedicated to the Drag Free control.

8.6.3 COMMON MODE MOTION OF THE TEST MASSES

The displacement of each test mass w.r.t. the PGB provides the information about the required overall rejection of the common mode acceleration. The overall external non-gravitational force affecting the spacecraft motion is sensed from the test masses as inertial force: in principle it is a pure common mode for them, such as in this simulation. In true life, it is anyway necessary to reduce this common mode acceleration for mainly three reasons:

- the common mode acceleration displaces each test mass, and this displacement has a limited range: the gap of the science capacitance plates
- the common mode rejection of the test masses mechanical suspension is not 0 (i.e. a fraction of the common mode acceleration is transformed into differential acceleration, which competes with the interesting signal to be detected)
- the capacitance read-out, which is in charge of detecting the test masses relative displacement due to an EP violation, is sensitive to both common and differential mode. Hence (a) Its dynamic range must be not saturated; (b) Its rejection of the common mode is limited.

In order to have a very small gap for the capacitance plates of the science read-out (i.e. high sensitivity), the external non-gravitational acceleration is partially compensated by means of an active Drag Free Control, which reduces the inertial acceleration sensed from the PGB and test masses at the orbit frequency. The remaining common mode acceleration is rejected from the mechanical suspension. In the IRF, the residual common mode acceleration sensed from the PGB and test masses at the orbit frequency is $a_{CMxy} = \chi_{DFCxy} \times a^{ext}_{NG\,xy}$. The a_{CMxy} acceleration is responsible of the elongation of the “springs” connecting the PGB to the spacecraft and the test masses to the PGB in the test masses equatorial plane XY.

In this simulation, whose main objective is the simulator validation, $\chi_{DFCxy} = 1$ (no DFC) and so $a_{CMxy} = a^{ext}_{NG\,xy}$. The inertial acceleration, which becomes a differential term due to the mechanical balance suspension imperfections, is $a^{\mathrm{iner}}_{\mathrm{DM}} = a_{CMxy} \times \chi_{CMRRxy}$, wih χ_{CMRRxy} the suspension Common Mode Rejection Ratio. As already mentioned above, in this simulation $\chi_{CMRRxy} = 0$, instead of $\chi_{CMRRxy} = 10^{-5}$ (perfect common mode rejection): so, $a^{\mathrm{iner}}_{\mathrm{DM}} = 0$. This means that the PGB-test mass displacement is the largest possible one, but that at the same time the differential displacement is not affected by this large value. In other words, in such a configuration the simulator can be used at the same time to check the level of violation of the requirements on the test masses common mode displacement in case of non drag free mode, and at the same time it can be used to detect the EP violating signal.

The Post-Processing module provides the time histories of the satellite position, velocity and acceleration in both the IRF and LVLH reference frames. It also provides the s/c-PGB and the PGB-test masses displacement, velocity and acceleration in both the IRF and LVLH reference frames, thus removing the high frequency components, which would make figures of BF time histories almost useless.

The following pictures show the time histories of the TMe common mode displacement along the three axes of the LVLH reference frame, as computed from the post-processing module.

Figure 8-13 shows the displacement of the outer test mass w.r.t. the PGB along X_{LVLH}: the maximum displacement (some tens of microns) is by far smaller than the gap between the science capacitance plate and the inner surface of the outer proof body (2.5 mm). While in this simulation the only difference of proof masses displacement is due to the EP violating signal and to gravity gradient (the differential displacement due to EP violation is $\Delta x_{EP} = F_{EP} \times (T_{diff})^2 / (4 \times m_{TM} \times \pi^2) \cong 0.5$ pm), in true life a fraction $\chi_{CMRRxy} = 10^{-5}$ of the observed common mode displacement is detected as differential displacement.

Figure 8-13 shows also that there is an offset on the X_{LVLH} displacement, whose value is 1 micron, which means 10 pm of differential displacement with the same frequency and phase of the EP signal: the necessity of the DFC for the compensation of the orbital component (in the IRF) of the non gravitational acceleration is here clearly stated. The larger displacement of the proof mass, i.e. the oscillation with amplitude of about 5 microns, generates (through $\chi_{CMRRxy} = 10^{-5}$) a differential displacement which is about 2 orders of magnitude bigger than Δx_{EP}. Also this term benefits from the action of the DFC, since the drag at orbit frequency in the IRF, i.e. the main drag component, shall not contribute to the orbit frequency term of non-gravitational acceleration in the LVLH reference frame. This differential displacement, anyway, has not the same frequency of the EP violating signal and does not affect the science performance of the experiment.

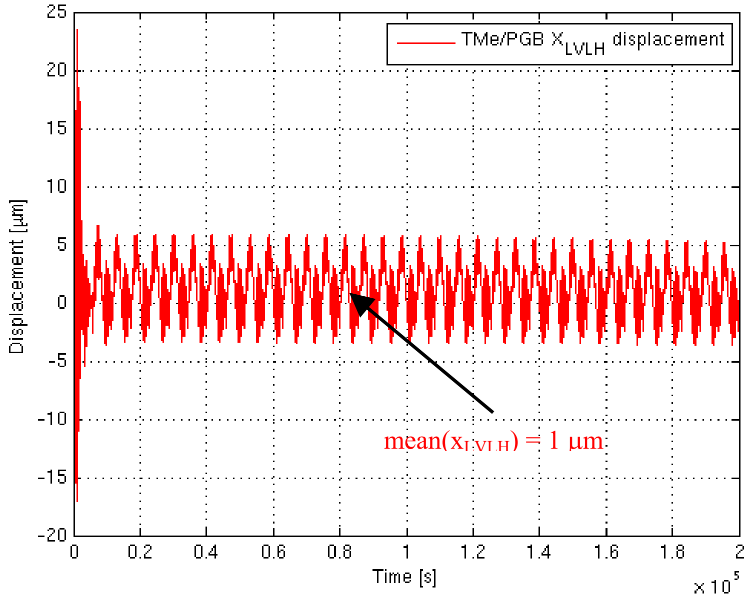

Figure 8-13: TMe-PGB displacement along the X_{LVLH} axis (part of the initial transient has been removed from the picture). The displacement along X_{LVLH} is not a problem from the point of view of the gap of the science capacitance plates. The offset (mean value) of the displacement, which is about 1 micron, has the same signature of the EP violating signal. In real life, without the Drag Free control, the fraction of common mode offset along X_{LVLH} transformed into differential mode due to the imperfect CMRR ($\chi_{CMRRxy} = 10^{-5}$, i.e. not zero) of the mechanical balance, would completely mask the EP violating signal, being about 20 times greater than Δx_{EP}.

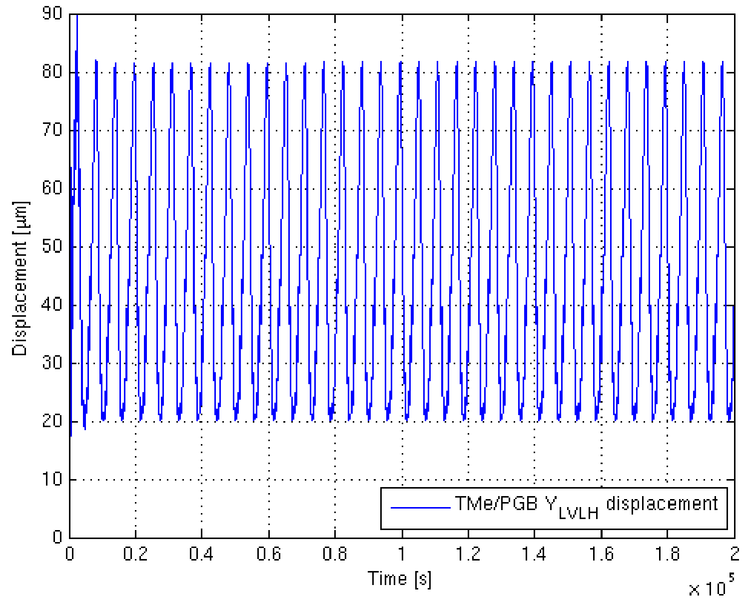

Figure 8-14: TMe-PGB displacement along the Y_{LVLH} axis (part of the initial transient has been removed from the picture). The displacement along Y_{LVLH} is not a problem from the point of view of the gap of the science capacitance plates. The offset (mean value) of the displacement, which is about 1 micron, has the same signature of the EP violating signal. In real life, without the Drag Free control, the fraction of common mode offset along X_{LVLH} transformed into differential mode due to the imperfect CMRR ($\chi_{CMRRxy} = 10^{-5}$, i.e. not zero) of the mechanical balance, would completely mask the EP violating signal.

Figure 8-14 shows the displacement of the outer test mass w.r.t. the PGB along Y_{LVLH}: the maximum displacement (one hundred of microns) is smaller than the gap between the science capacitance plate and the inner surface of the outer proof body (2.5 mm). Moreover, the largest part of this displacement is an offset, i.e. it is due to the orbital term (in the IRF) of the non-gravitational forces acting on the spacecraft: the presence of the DFC would reduce this displacement to about 30 microns. In this not realistic situation (absence of DFC) it is anyway demonstrated that the gap of the science capacitance read-out is not saturated. The offset along Y_{LVLH}, when "converted" into differential displacement through χ_{CMRRxy}, provides a ΔY_{LVLH} = 500 pm, i.e. a huge displacement having only a phase difference of 90° w.r.t. the EP violating signal. Again, the usefulness of the DFC is transparent and underlined.

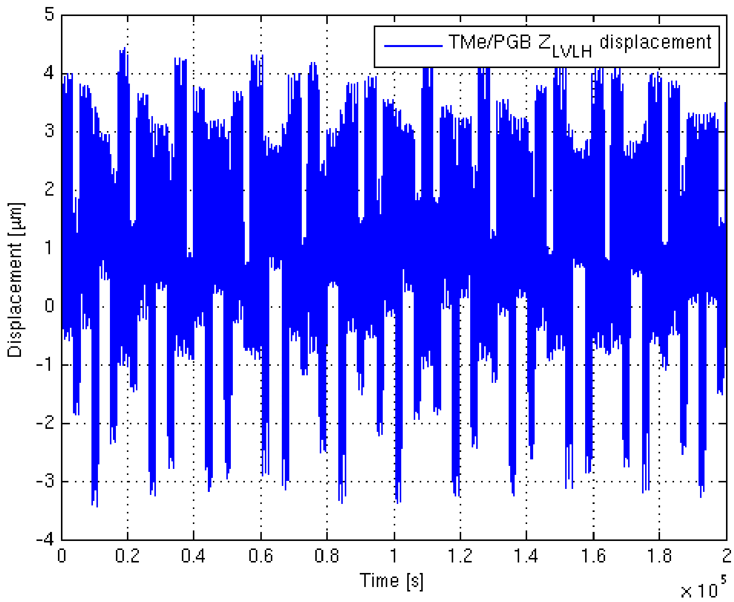

Figure 8-15: TMe-PGB displacement along the Y_{LVLH} axis (part of the initial transient has been removed from the picture). The displacement along Y_{LVLH} is not a problem from the point of view of the gap of the science capacitance plates. The offset (mean value) of the displacement, which is about 1 micron, has the same signature of the EP violating signal. In real life, without the Drag Free control, the fraction of common mode offset along X_{LVLH} transformed into differential mode due to the imperfect CMRR ($\chi_{CMRRxy} = 10^{-5}$, i.e. not zero) of the mechanical balance, would completely mask the EP violating signal.

Figure 8-15 shows the displacement of the outer test mass w.r.t. the PGB along Z_{LVLH}: the maximum displacement (about 5 microns) is smaller than the gap (2.5 ÷ 5 mm) of the capacitance sensors devoted to measure the proof masses displacement along the symmetry axis. In true life, the offset along Z_{LVLH}, which is about 1 micron, when "converted" into differential displacement through $\chi_{CMRRz} = 2 \cdot 10^{-2}$, provides a ΔZ_{LVLH} = 20 nm. This differential displacement along the symmetry axis, due to the gravity gradient tensor, gives rise to a differential acceleration in the test masses equatorial plane, at a frequency that is two times the orbit one (w.r.t. IRF). The requirement on the test masses differential displacement along the symmetry axis at the orbit frequency (w.r.t. IRF) is Δz^* = 0.5 nm. The maximum displacement along the symmetry axis is about $200 \cdot \Delta z^*$. The DFC is in charge of reducing by a factor 500 the non-gravitational forces acting at the orbit frequency along the satellite spin axis: it is transparent that taking into account the DFC compensation, the differential displacement along Z_{LVLH} becomes smaller and smaller than Δz^*. The science target of being capable of measuring $\eta=10^{-17}$ requires the DFC compensating action on both the orbit plane and the symmetry axis.

8.6.4 DIFFERENTIAL MODE MOTION OF THE TEST MASSES

The test masses differential displacement due only to the EP violating signal is $\Delta x_{EP} = a_{EP}\times(T_{diff})^2/(4\times\pi^2)$ = 0.531936 pm (this value is obtained by using the same parameters feeding the simulator, i.e. T_{diff} = 500 s, $a_{EP} = 8.4\cdot10^{-17}$ m/s^2). The science read-out does not provide directly the displacement due to the EP violation only, but the overall differential displacement, which takes into account also the gravity gradient contribution. The overall expected differential displacement along X_{LVLH} is in fact:

$$\Delta x_{LVLH} = \frac{F_{EP}}{m_{TM}\cdot\left(\omega_{DM}^2 - 3\cdot\frac{GM_\oplus}{(R_\oplus+h)^3}\right)} = 5.4449\cdot10^{-13}\,m$$

The time histories of the test masses differential displacement w.r.t. the IRF (after synchronous demodulation at the spin frequency) shown in Figure 8-16, highlight the orbit frequency of the expected signal. The EP violating signal is a rotating vector (at orbit frequency) w.r.t. IRF, so that X_{IRF} and Y_{IRF} are out of phase of 90°: the time delay between a maximum for the X_{IRF} component and the following Y_{IRF} one is about 1425 s (one quarter of the orbital period), as shown in Figure 8-16.

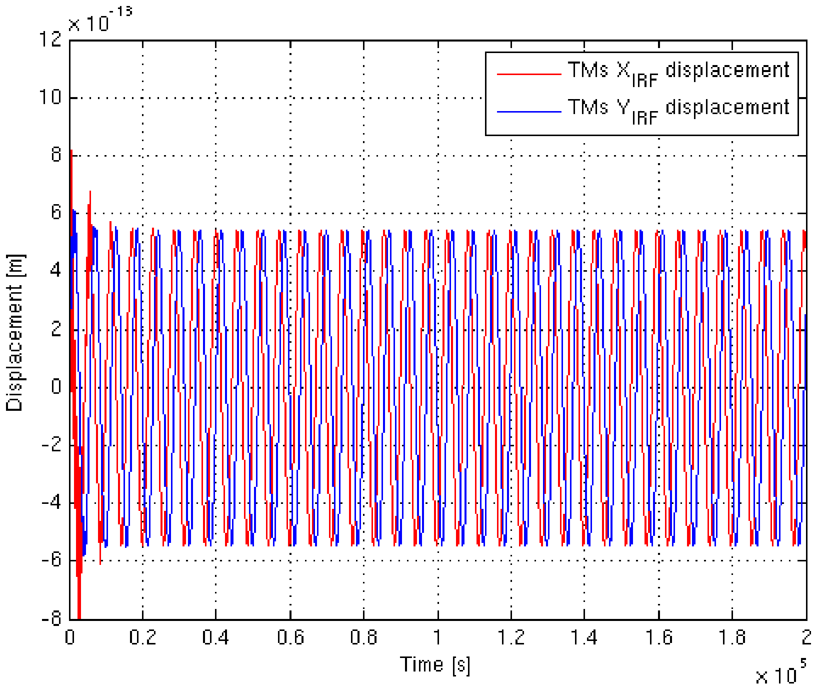

Figure 8-16: Test mass differential displacement w.r.t. the IRF. The signal signature at orbit frequency is apparent: the oscillation period of the signal is the orbit one, and the time span between a maximum for the X_{IRF} component and the following Y_{IRF} one is about 1425 s (one quarter of the orbital period).

The test masses differential displacements have to be observed in the LVLH frame in order to clear understand the test bodies' behavior and to validate the simulator (at lhe level of pm!). At first, the ΔX_{LVLH} and ΔY_{LVLH} differential displacements can be plotted in the same figure, to check their values w.r.t. the expected ones. Since the $CMRR_{xy}$ in this science performance simulation is 0, and there are not differential forces acting on the test masses along Y_{LVLH}, the expected test masses differential displacement along Y_{LVLH} is $\Delta Y_{LVLH} = 0$. Figure 8-17 shows the perfect match between the predicted differential displacements and the measured ones (accuracy is better than 1 femtometer): it has to be noticed that the gravity gradient contribution to ΔX_{LVLH} is correctly taken into account by the GG simulator.

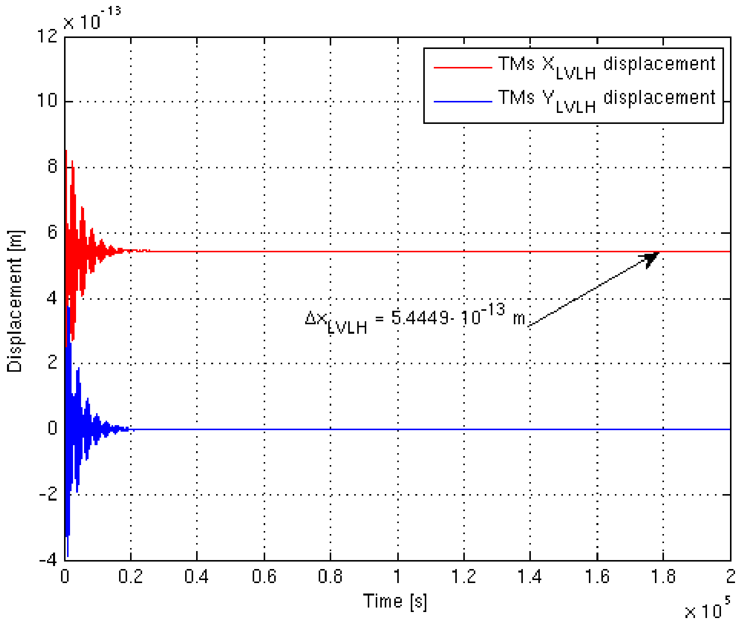

Figure 8-17: Test masses differential displacements in the LVLH frame. The measured ΔX_{LVLH} and ΔY_{LVLH} differential displacements match the predicted values with accuracy better than the femtometer. the gravity gradient contribution to ΔX_{LVLH} is correctly taken into account by the GG simulator.

The above describes results show a perfect match of the simulator vs. the expected results in the boundary conditions selected for this validating simulation. The switch-on of the imperfections, noises and of all the spurious effects, which can affect the experiments, shall be carried out with particular care, in a step by step approach, in order to check each contribution w.r.t. the overall science performance and w.r.t. the budgeted error.

8.7 DYNAMICS RANGE OF THE SIMULATOR

The first version of the GG simulator was essentially devoted to check the experiment performance taking into account the supercritical rotation (i.e. PGB and test masses whirling motion, and whirl motion control) in the 3-dimensional space, a good model of sensors and actuators, the EP violating signal, and an ad hoc implemented environment. The GG orbit did not exist, i.e. Earth gravity field (and also gravity gradient) was not implemented in the simulator. For this reason the drag was introduced as a force with a DC term and two sinusoidal components at the nominal orbit period and at nominal half orbit period w.r.t. the IRF. At the initial time t_0, the GG satellite was coincident with the IRF origin.

The introduction of the Earth gravity field (and of gravity gradient), i.e. of the GG satellite orbit, in the simulator was not cost free. A huge dynamical range has now to be covered: from half a pico-meter differential displacement of the test masses with some significant decimal digits ($\leq 10^{-14}$ m), to the orbital radius of the satellite around the Earth ($\approx 10^7$ m). The dynamics range required to the default implementation of the DCAP software package is so $\geq 10^{21}$ m, which is beyond the double precision capability. It has been verified that the double precision is still useful when the effort of the simulation is focused on the DFC and or whirl control performance, i.e. if it is not required to explore the test mass behaviour at the sub nano-meter level.

When the simulations are carried out in order to explore the GG mission science performance, it is required to run the simulator in quadruple machine precision. This requirement has a huge cost in terms of the CPU time: the simulator speed slows down by a factor ≈ 20 vs. the double precision run. A quadruple precision run on a Dual Xeon @3.4 GHz has almost the real time speed: the simulation of a time span of $2 \cdot 10^5$ s requires 205704 s of real CPU time.

The simulation results presented in Section 8.6 above have been carried out by a quadruple precision run of the GG simulator.

8.8 CONCLUSIONS

The GG Simulator described above is capable to explore the sub picometer world while the satellite orbits the Earth at about 7000 km distance from its center of mass. This is an astonishing capability, given the huge dynamical range (□ 10^{20} m) that the simulator must cover to account for both the test masses relative displacements at the sub-picometer level and the satellite orbital radius of about 7000 km.

The simulator is now capable to extract the EP violation signal at the GG target level of $\eta = 10^{-17}$ taking into account:

- Earth gravity field and gravity gradient
- Non-gravitational forces acting on the satellite surface due to atmospheric drag, solar radiation pressure and Earth albedo
- EP violating signal
- PGB and test masses supercritical rotation with whirl motion due to the mechanical suspension dissipation
- PGB and test masses whirl motion control by means of capacitance sensors/actuators co-rotating with the satellite
- Science capacitance read-out

At this level the GG simulator is by far more advanced and mature than it is typically expected at Phase A level. This is due to the considerable work carried out in the past on the GG satellite experiment and, in addition, to the precious heritage from GOCE End2End simulator. This powerful tool shall support the GG science team for the entire duration of the Phase A-2 study for the design phase, as a means for determining the achievable mission performance, and, consequently, trade off implementation options. In this way, specifications for all system elements can be derived, consistent with the overall goal and mutually balanced as a preparation for phases B/C/D. The GG simulator Post-Processing module shall suggest/support realistic procedures for scientific data reduction, based on fully representative “raw” data. In the future, during the verification phase, it shall be used as a means to establish the expected system performance, given the measured performance of all elements, tested separately and together, as far as viable.

Further work on the GG Simulator is planned before completion of the GG Phase A-2 Study. In particular, we plan to fully integrate in the simulator the DFC and PGB whirl motion control as they have been described in Section 7.

In addition, the GG simulator will:

5. Include a final model of the selected DFC actuators
6. Update the test masses properties (inertia, magnetic, thermal) after final the selection of the materials
7. Update the modeling of the science capacitance-read-out sensor according to the final specific design for the space experiment
8. Update the capability of introducing CMRR degradation due to mechanical unbalancing (stiffness variation vs. temperature, etc.)
9. Update the disturbing terms depending on various choices of the test masses material
10. Consolidate the Post-Processing module

9. PAYLOAD LABORATORY PROTOTYPE

9.1 GGG ("GG ON THE GROUND") VS GG: SIMILARITIES AND DIFFERENCES

The core of the GG payload is the differential accelerometer shown and discussed in Figure 3.7. It is clearly designed for zero-g: very weak mechanical coupling in spite of 10 kg mass test bodies and "perfect" cylindrical symmetry. Nevertheless, it has been possible to design and build a 1-g version of it because it is sensitive in a plane (the X,Y plane perpendicular to the spin/symmetry axis Z) rather than along the symmetry axis itself. Thus, one can use this axis to suspend the system against local gravity so as to maintain sensitivity in the X,Y horizontal plane of the laboratory. Given that a full scale model requires to suspend at least 20 kg (the two test cylinders), the issue remains as to how weakly the masses can be suspended and coupled to form a balance similar to that of Figure 3.7 while at the same time sustaining its weight.

Indeed this happens to be possible, and a sketch of the laboratory apparatus (also known as GGG –"GG on the Ground") is shown in Figure 4.10. The key item are 3 cardanic suspensions (picture shown in Figure 4.10, to the right) whose lamellae are wide enough to sustain the weight but also thin enough to make coupling in the two orthogonal directions of the horizontal plane very weak. All three cardanic joints are manufactured in CuBe by electroerosion in 3D from a single solid piece in order to minimize losses (i.e. for best mechanical quality).

The test cylinders, shown in green and blue, should be compared to the inner accelerometer of Figure 3.7 (same colors). The masses of the test cylinders are the same (10 kg each), though so far in the laboratory they have the same composition (Al) for cost reasons and because the goal is to test the physical properties and sensitivity of the apparatus. Both instruments are sensitive in the plane perpendicular to the spin/symmetry axis.

The masses and the balance arm form a vertical beam balance –in which the masses have the peculiarity of being concentric, as required in the space experiment– whose spring constant in the horizontal direction can be made very small. The masses are constrained by the balance arm to move only in opposite directions and therefore the apparatus is relatively insensitive to 'common mode' forces on the masses. This shaft is mounted in ball bearings and can be rotated at precisely controlled speeds by a micro-stepping stepper motor. The verticality of the shaft is ensured by sensing its tilt with a sensor and correcting it by means of piezo actuators (labeled as T and P respectively in Figure 4.10).

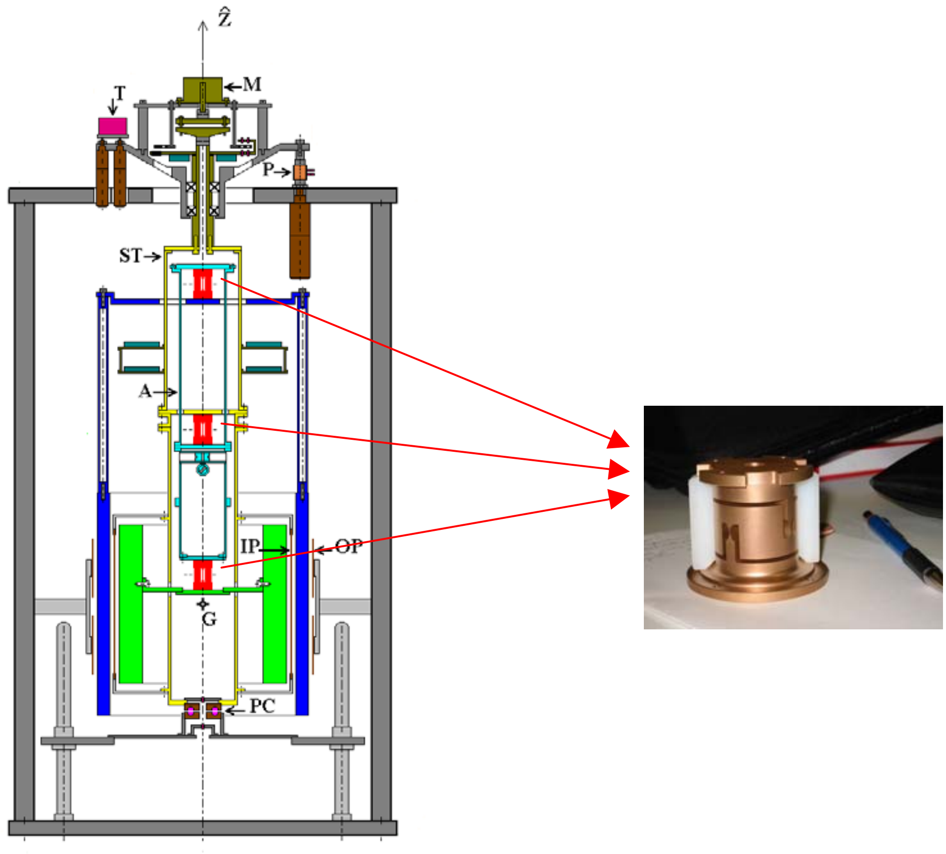

Figure 4.10: Section through the spin axis Z of the GGG differential accelerometer inside the vacuum chamber. The drawing is to scale, and the outer diameter of the outer test cylinder (in blue) is 27.4 cm. The structure shown in gray is a frame rigidly fixed to the vacuum chamber (the current chamber is shown in Figure 4.12 and has a 1 m internal diameter). More in detail: M: motor; x: ball bearings; ST: suspension tube, with two annular rings where the read out rotating electronics is located; A: coupling (balance) arm, located inside the suspension tube, with its 3 laminar cardanic suspensions (in red; the central one suspends the whole weight from the suspension tube, the top and bottom ones suspend outer and inner cylinder respectively from the coupling arm–see picture on the right); G: center of mass of the two-cylinder system (in blue the outer cylinder, in green the inner one, 10 kg each). IP are the internal capacitance plates of the differential motion detector, OP are the outer ones for whirl control, PC is the contactless inductive power coupler providing power to the electronics inside the rotor. T and P, at the top of the rotor, are the tiltmeter and 3 PZTs (at 120° from one another -only one shown) for automated control of low frequency terrain tilts.

Our understanding of the GGG dynamical system is extensively described in [42, 43]

It is crucial to notice that local gravity does not play a stabilizing role on the test masses of GGG. Since no stabilizing effect can be expected in space due to absence of weight, a ground based apparatus where the test mass is instead stabilized by gravity would differ substantially from its counterpart in space and be of very little use as a laborarory prototype. The reason why this is not the case for GGG is easily explained.

In essence, the dynamical scheme of the GGG laboratory prototype is as shown in Figure 4.11, whereby the period of natural oscillation the test masses relative to each other (differential period) is well expressed by the simple analytical formula

$$T_{diff} \cong \frac{2\pi}{\sqrt{\left(\frac{g}{l}\cdot\frac{\Delta l}{2l}+\frac{k}{m}\right)}}$$

In this formula the term containing g is small and the role of gravity is only to slightly affect the differential period; indeed, it is used to provide a small "negative spring" (if $\Delta l < 0$) to further decrease the mechanical stiffness k so as to obtain a longer differential period, hence a more sensitive balance (sensitivity to differential accelerations between the test masses improves with the differential period squared). Thus, in no way gravity has a stabilizing effect in GGG simply because the GGG dynamical system is not a simple pendulum. Indeed, the equilibrium position of the GGG test masses, around which an effect such as an EP violation would act, is dictated by supercritical rotation (more precisely by: i) the coupling frequency ii) the spin frequency , iii) construction and mounting errors whereby the centers of mass do not lie exactly on the rotation axis). This fact has been verified experimentally (see Figures 4.17 and 4.18)

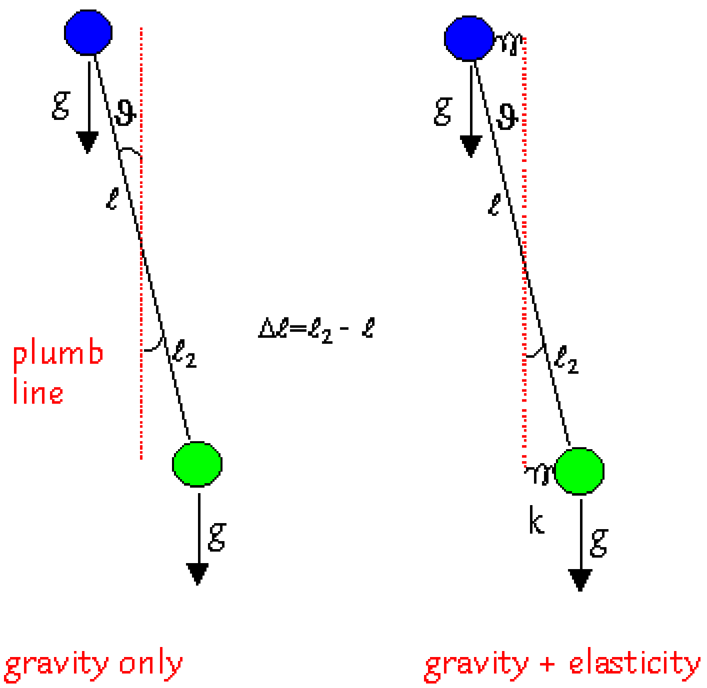

Figure 4.11: Simple sketch of the GGG dynamical system

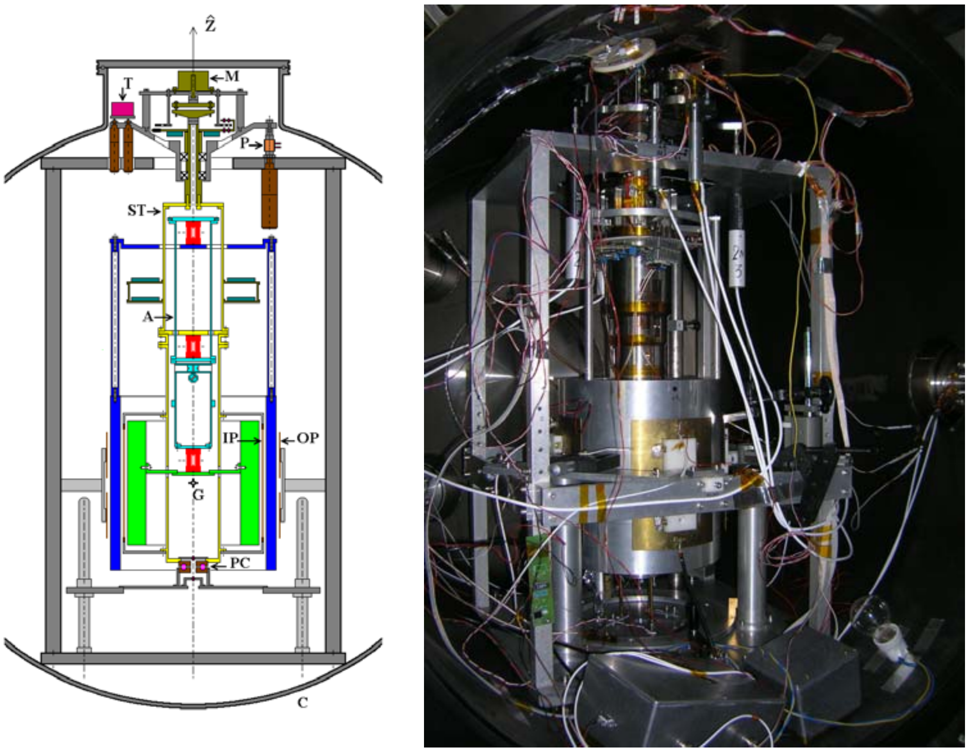

Figure 4.12: (left) The GGG laboratory prototype –sketched with its essential features described in Figure 4.10– surrounded by the vacuum chamber (labeled as C) whose internal diameter measures 1 m. (right) Picture of the apparatus inside the chamber (the external test cylinder –depicted in blue in the sketch– is visible).

The similarity between GGG and the space accelerometer of Figure 3.7 is apparent, but we point out the following differences.

i) In GGG the coupling arm is not located, as in Figure 3.7, inside the inner test cylinder with top/down symmetry (for practical mounting reasons) and this results in a reduced capability of the system (as compared to its counterpart in space) to reject common mode effects

ii) The cardanic suspensions which suspend and couple the test masses (shown in red in Figure 4.10) cannot be as weak as in absence of weight, resulting in a natural differential period at present about 40 times shorter than in space, which means that operation in weightlessness conditions would give higher sensitivity to differential accelerations by a factor 1700. The mechanical quality and losses of the cardanic suspension, which are crucial to achieve the scientific goal of the mission, have been measured with the GGG apparatus (Figure 4.15) demonstrating that the requirements can be met.

iii) The motor and bearings shown in Figure 4.10 are obviously not needed in space.

iv) Appropriate sensor and actuators (tilt meter and PZTs, depicted as T and P in Figure 4.10) are used on the ground to reduce disturbances from local terrain tilts, which by changing the inclination of the suspension tube will, because of the non-zero elastic coefficient of the laminar suspensions, produce changes of the inclination of the coupling arm (the beam of the balance) resulting in unwanted differential displacements of the test cylinders. Such a closed loop control is not needed in space since the whole satellite is an isolated system.

9.2 CAPACITANCE BRIDGE TRANSDUCERS, READ-OUT SYSTEM AND ELECTRONIC NOISE

The differential displacement of the masses is sensed by means of a capacitance bridge circuit mounted on the shaft. Two pairs of capacitance plates (see Figure 4.13) on opposite sides of the inner test cylinder and located halfway in between the inner and the outer one, form two variable capacitances (with the masses at ground potential) in a bridge circuit. A displacement of the masses from their equilibrium position causes an unbalance of the bridge and this is sensed by a phase sensitive detection circuit.

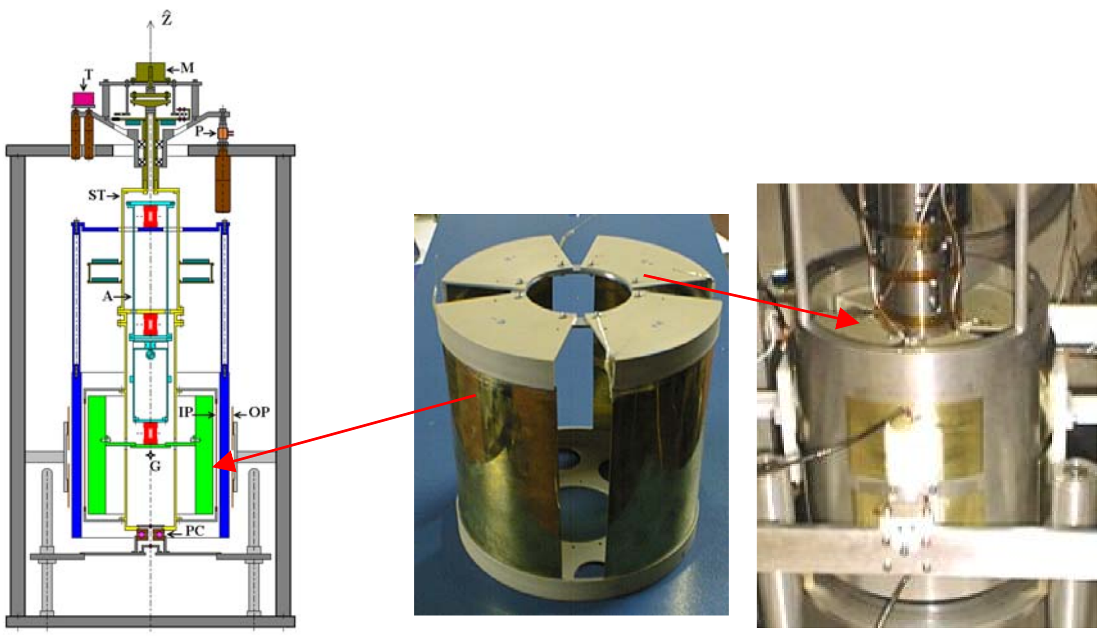

Figure 4.13: Two pairs of capacitance plates forming two bridges to read the displacements of the test cylinders relative to each other. This read-out system, including the rotating electronic circuit located on a annular ring around the shaft, is in all similar to the one designed for the GG payload in space. On the right hand picture, facing the outer test cylinder, are visible the smaller capacitance plates used as sensor and actuators for whirl motion damping

A sinusoidal signal (1 Volt) of high frequency (500kHz) is applied to the bridge in order to shift the signal of interest to a high frequency band with reduced 1/f noise. The high frequency bridge measurements are first amplified, demodulated and then converted from analog to digital (24 bit). A block diagram of the electronics is shown in Figure 4.14.

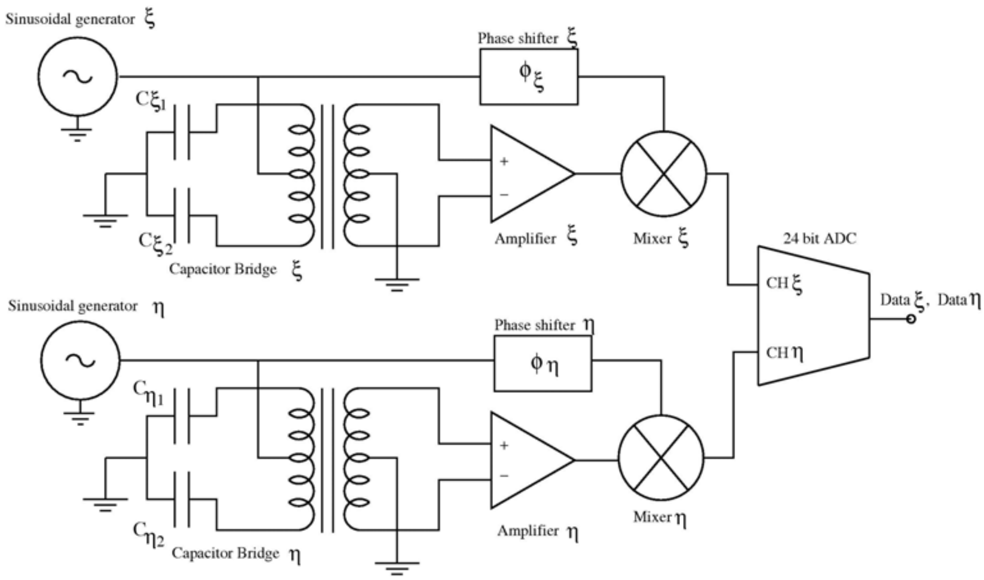

Figure 4.13: Simplified block diagram of the electronics of the 2 capacitance bridges of the GGG experiment. The bridge is excited by the sinusoidal generator; the signal form the bridge is amplofied and detected in pahse by the mixer and then cconcerted to digital at 24 bit

In order to be able to transform the relative displacement as measured by the bridges in the rotating frame of the rotor to the non-rotating frame, we need to know, in correspondence of each ADC conversion, also the phase angle of the rotor. For this purpose a rotary encoder has been mounted, which measures the phase of the rotor.

The digital signal from the ADC is transmitted by a LED placed on the axis of the shaft as an optical signal. The position signal thus received is time stamped and stored in a PC for post processing.

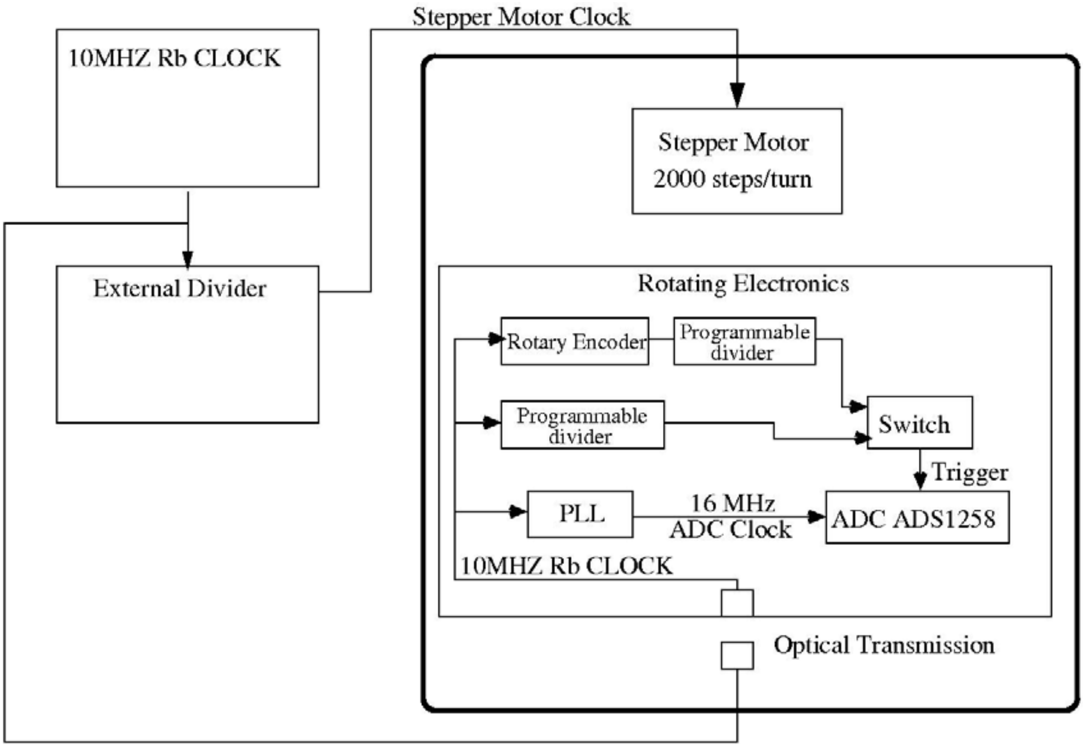

Figura 4.14: Scheme devised to read the GGG test masses displacements (in bold is depicted the vacuum chamber housing the apparatus)

The noise measured with the electronics currently in operation is shown in Figure 4.15

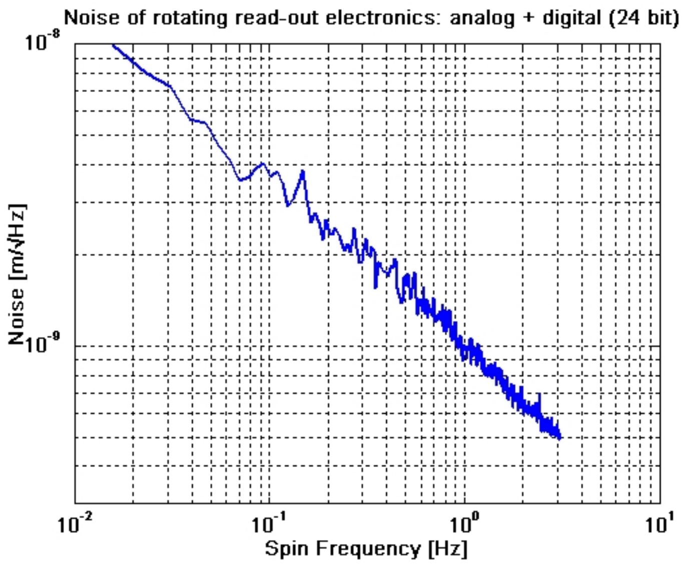

Figure 4.15: The read-out of the relative displacements of the test cylinders consists of 2 capacitance bridges co-rotating with the test masses. The analog output of each bridge is digitized 32 times per turn. Plot shows noise of read-out electronics alone located inside a chamber maintained at 35 ± 0.1°C. The noise of the digital part (alone) was measured independently for a few days, sampling at 32 times per spin period, as function of spin frequency (up to 3 Hz). The noise of the analog part was measured with the spectrum analyzer. The curve shows the sum of the two. The advantage of spin in reducing electronic noise is apparent.

9.3 MEASURED Q

A crucial parameter which characterizes a physical apparatus, especially if devoted to perform high precision measurements of small gravitational effects, is the quality factor Q of the whole. It measures the losses in the system (since no real system is perfect) and therefore its thermal noise, which ultimately limits the sensitivity that it can achieve. Though losses are known to occur at the non rigid components of the system (in this case the cardanic joints shown in Figure 4.10, which are therefore manufactured with great care for such losses to be minimized) reliable Q measurements are better performed with the entire apparatus fully assembled as in its nominal configuration. This has been done for the GGG prototype and the results are reported in Figure 4.16. In addition to being very satisfactory, it has to be noted that the small U shaped suspensions designed for coupling and suspending the test cylinders in space (see Figure 3.7) are certainly less complex and easier to manufacture than the cardanic joints used in the lab and will therefore have an even better mechanical quality. The measurements reported thus demonstrate an upper limit for losses (i.e. lower limit for Q) in the space experiment.

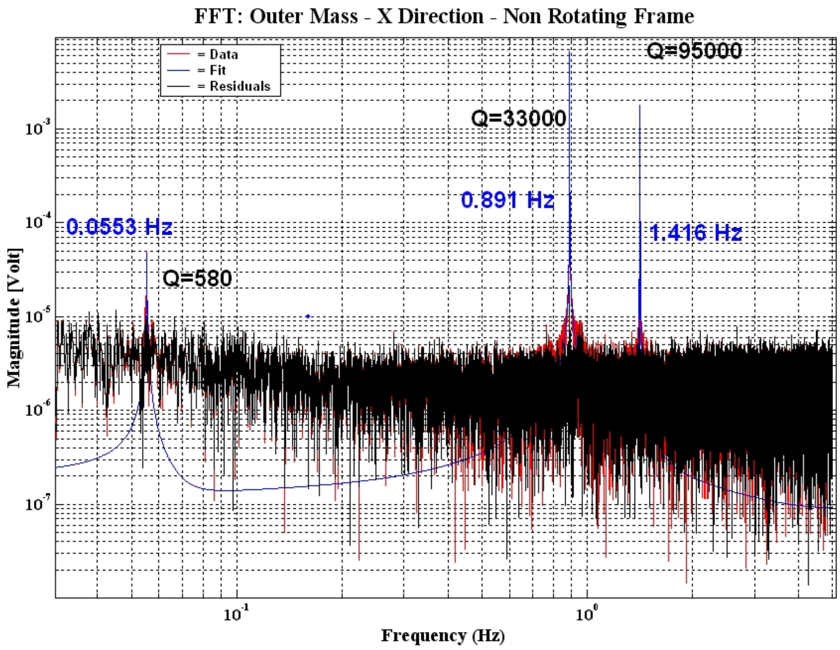

Figure 4.16: Resulting quality factors of the GGG accelerometer at the natural frequencies (at zero spin) as obtained by measuring the oscillation decay of the system. The blue curve is the FFT of the fitted output data. In supercritical rotation the relevant Q is measured from the growth of whirl at the natural differential frequency of the test cylinders; in a later assembly, at a spin frequency of 0.16 Hz we have measured 3020.

9.4 WHIRL MOTIONS CONTROL

In order to reduce the orbital whirl motion of the GGG system a controlled force is applied to the outer mass. Note that we have to do this without influencing the equilibrium position of the masses. Therefore the applied force is proportional only to the velocity of the outer mass in the laboratory reference frame and is, of course, opposite to its direction. In essence it acts as a damper. In addition, whirl motion occurs at specific frequencies which are the natural modes of the system and therefore the active control system confines its activity to these specific frequencies. The two-dimensional motion of the outer mass in the horizontal plane is broken down into its components in the X and Y directions in the laboratory frame and addressed through two independent active control loops. The loop gains in the two directions are however maintained equal to ensure that there is no azimuthal asymmetry. For simplicity only one of the loops is described below.

Both the actuators and sensors used in the active control scheme are capacitance based and are identical in their structure. The position sensor consists of a pair of brass plates on opposite sides of the outer mass, which are sectors of a cylinder concentric with it (see Figure 4.13, right hand picture). Each plate forms one capacitor of a bridge with the outer mass at ground potential. The pair therefore form one half of a capacitance bridge, the other half being a pair of constant capacitors of roughly the same capacitance. A displacement of the mass results in an unbalance of the bridge. The bridge is supplied with an AC excitation and the unbalance AC voltage signal is demodulated and filtered to obtain a DC signal proportional to the displacement of the mass. The capacitance sensor occupies the lower half of the outer cylinder yielding a sensitivity of about 1 nm /√Hz in the 10^{-2} – 10^{-3} Hz range. An identical pair of plates, acting as actuators, occupies the upper half.

The displacement signal is digitised and acquired by a PC using 16bit National Instruments DAQ cards. It is then processed to identify the whirl frequencies of the rotor and a control signal is generated. The algorithm used for this processing has several steps. First the signal is buffered as a time series of about 200 s. A windowed average of the signal is subtracted in order to ensure that we do not affect the equilibrium position. Then an FFT is applied to the signal and the spectrum displayed on the computer screen. Thus the operator has an online monitor of the spectrum of oscillations of the rotor. The operator then has to identify any three frequency bands that need to be damped. The program then selects these bands and performs an inverse FFT to generate a time series corresponding only to those frequency bands which have been selected. In the next step a derivative of this time series is calculated and negated to produce the control signal. However, in this process the errors in phase and amplitude are large at the portion of the signal close to the most recent data. This is because we have not sampled the longer periods sufficiently well in order to obtain a good estimate of their phase. The fundamental differential mode being about 13 seconds long we can act only after having sampled several periods of the 13 second period. It is therefore necessary to delay the action by an integral multiple of this period. This delay is also estimated by looking at the displayed signals on the screen and ensuring that the control force has the right phase in order to damp the velocity of the mass. The control signal is then multiplied by an appropriate 'gain' and supplied to the actuator plates. The various steps of this algorithm are shown in Figure 4.17. Whirl damping in action is shown in Figure 4.18.

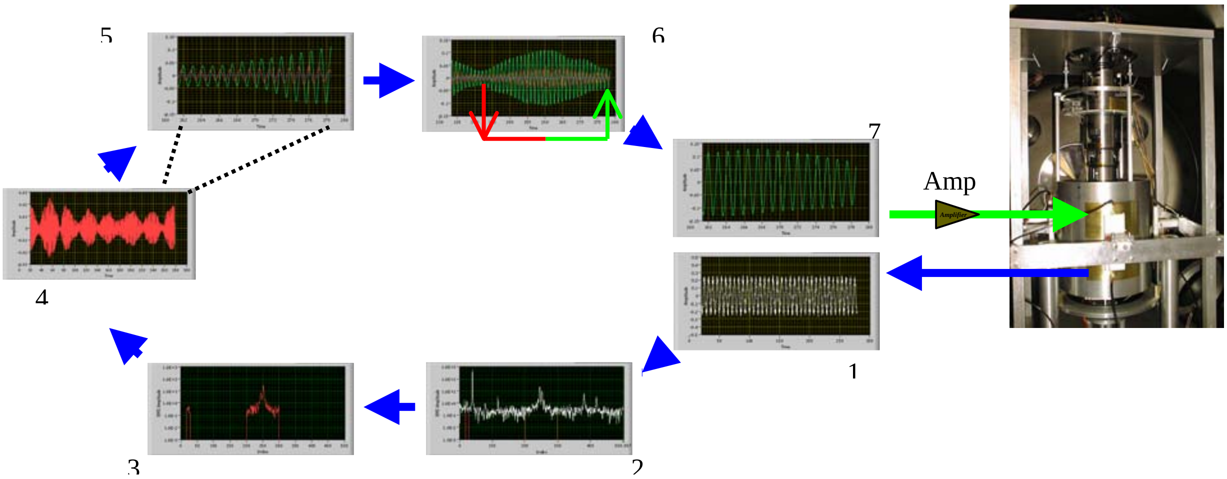

Figure 4.17: The various steps in the Whirl Control loop. 1. Digitised signal from the sensor plates, 2. FFT, 3. Frequency band selected by the user for damping 4. Inverse FFT of the selected band, 5. zoom into the most recent part of the signal to study the phase noise 6. Select delay such that the phase match is exact, 7. set digital gain and output via DAQ analog output to high voltage Amp. The green arrow points to the upper actuator plates to which the high voltage is supplied.

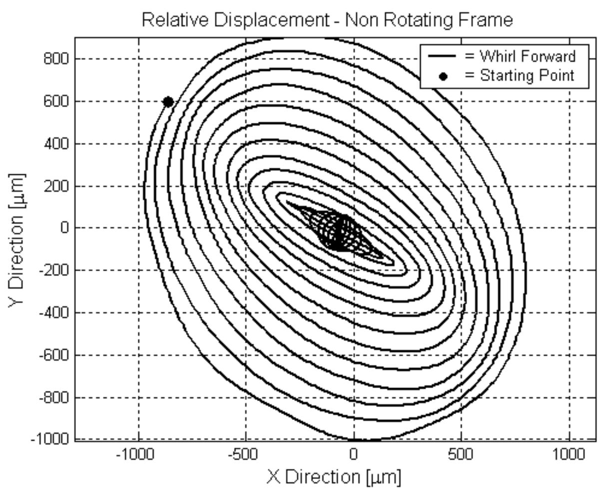

Figure 4.18: The whirl damping in action. The figure shows the amplitude of the orbital motion decreasing as the whirl control gradually removes energy from the fundamental differential mode of the GGG balance.

One of the main advantages of the computerised active control scheme is that it allows rapid adaptation of the 'filter' in the closed feed back loop so as to respond dynamically in real time. The other advantage is our ability to visually see the state of the rotor in real time and perform obtain diagnostic information, which then enables us to take decisions on setting filter location, bandwidth, gain and delays. As a result we were able to confidently extend the experimental runs from a few days to several months. This was crucial in obtaining sufficiently long data sets to address the problems at the diurnal frequencies near 10^{-5} Hz. The residual noise at low frequencies obtained after damping and the consequent signal to noise ratio are illustrated in the Figures 4.19 and 4.20.

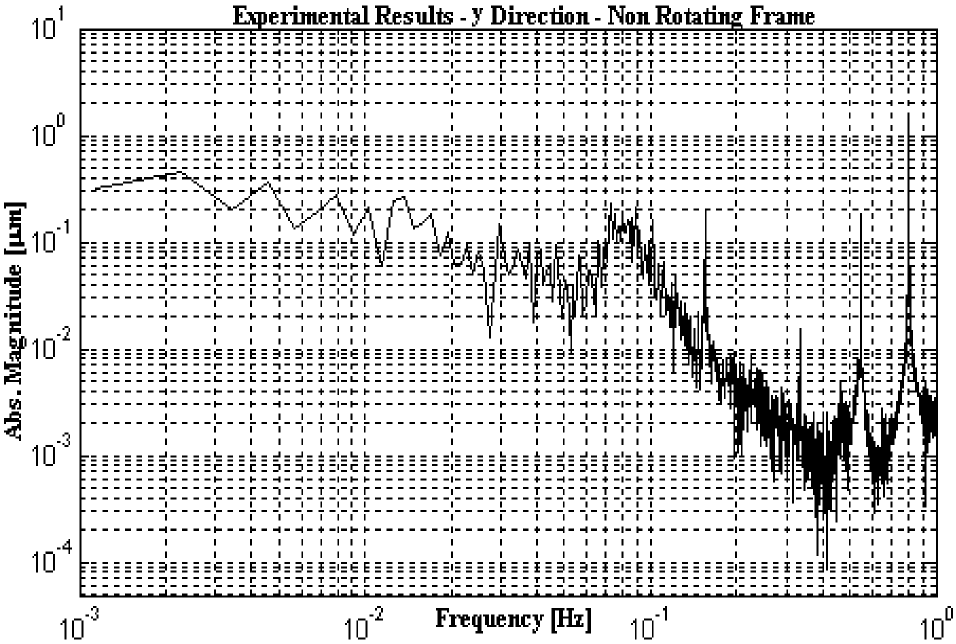

Figure 4.19: Results of Whirl Damping: FFT of the relative displacement of the test cylinders in y direction of the horizontal plane in the non-rotating reference system. The relevant whirl at the natural frequency of 0.08 Hz has been reduced to about 0.1µm.

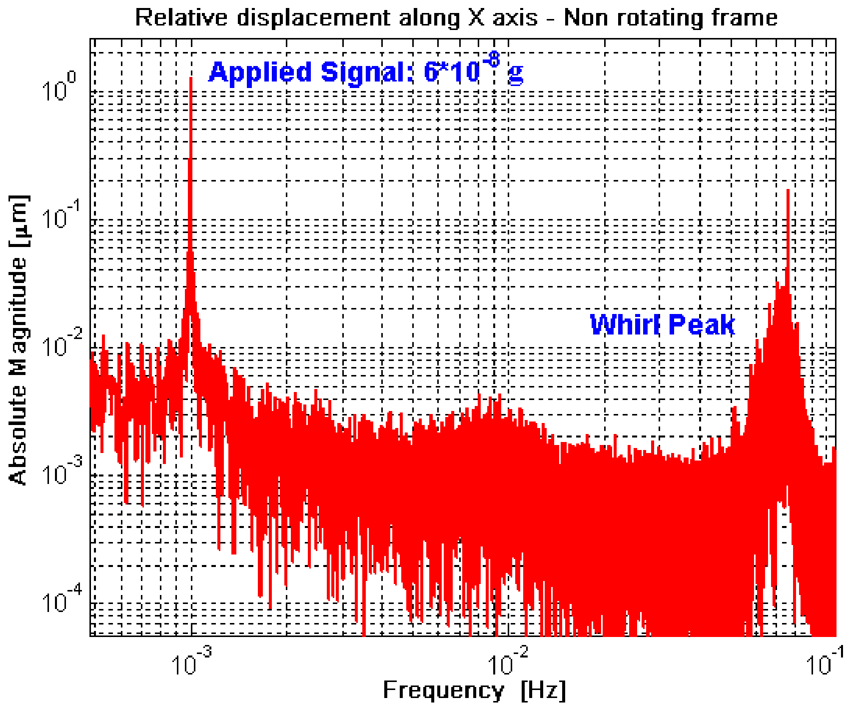

Figure 4.20: An example of recovery of an applied signal at frequency below whirl frequency. A signal applied at 0.01Hz in the y direction of the non-rotating reference frame is recovered from the output data though about 100 times smaller than the whirl at about 0.1Hz. This example indicates that recovery is possible even though the applied force produces a displacement much smaller than the whirl radius (not damped), hence, in order to measure an EP violation signal at the picometer level it is not necessary to reduce the whirl radius to the same level .

9.5 Experimental evidence for self-centering

Once the whirl has been damped the relative position of the masses is a constant. It has been seen that under supercritical conditions they converge to the same relative position regardless of their initial separation. This phenomenon known as 'self centering' of the masses has been repeatedly demonstrated and is shown in Figures. 4.21 and 4.22.

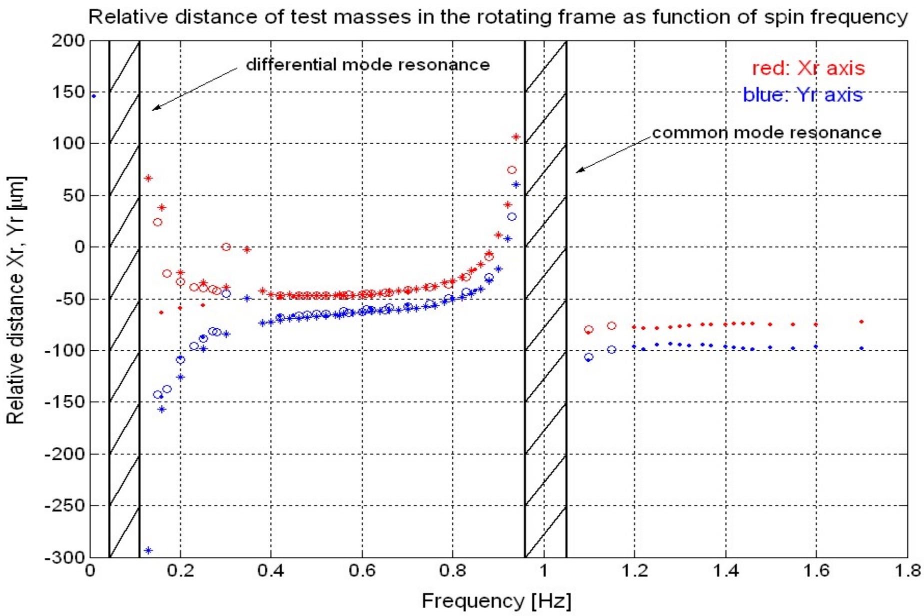

Figure 4.21: Relative distance of the test cylinders in the rotating reference frame as a function of the spin speed. Xr component is red colored. Yr component is blue colored. Different symbols are used for different measurement sessions: crosses correspond to measurement #1 of Figure 4.1.8, circles correspond to measurement #2 and dots to measurements #3. Each data point refers to a run of several hours. The black dashed areas mark the instability regions which correspond to the normal modes of the system. As the spin frequency increases from 0Hz towards the first resonance at 0.075Hz (data labeled L in Figure 4.18) the relative distance increases. Between the two resonances (i.e. between 0.12Hz and 0.89Hz; M in Figure 4.18) the system reaches always the same equilibrium position: as the spin frequency is increased past the instability region the cylinders start self-centering and the relative distance decreases rapidly. For spin frequencies in the range 0.4Hz – 0.6Hz, the relative distance is independent of the initial conditions and the three lines (crosses, circles and dots) in the figure coincide. When the spin frequency approaches the second instability region the relative distance grows again. At higher frequencies, above both the resonances (H-high) the system reaches another equilibrium position.

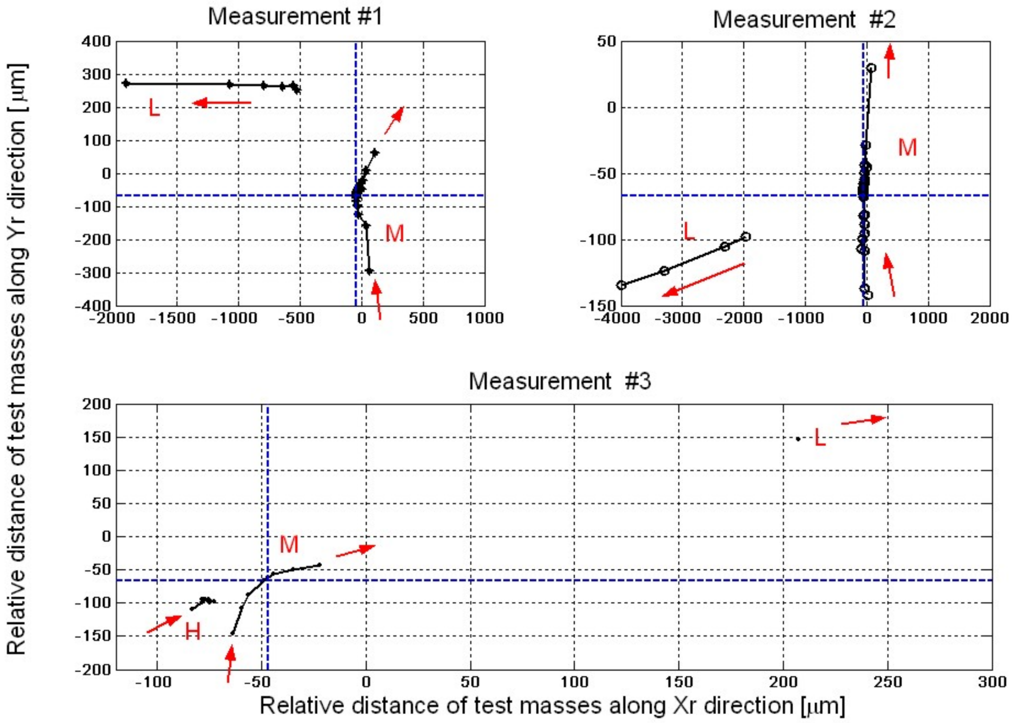

Figure 4.22: Experimental evidence for auto-centering of the test cylinders in supercritical rotation in the horizontal plane (Xr,Yr) of the rotating reference frame fixed with rotor. As the spin frequency increases (along red arrow) from 0Hz below the first resonance (L data), the relative distance increases. In between the two resonances (M data), the two test cylinders self-center reaching the equilibrium position determined by the intersection of the 2 dashed lines (always the same position in the three panels, independent of their initial conditions). Above both resonances (H data) they reach another equilibrium position.

9.6 UNIFORMITY OF ROTATION

The need for a motor in the GGG experiment is a matter of concern. Figures 4.23 and 4.25 show the uniformity of rotation at level of the rotor, which is what matters for the experiment. Obviously, an encoder on the motor itself shows a better uniformity.

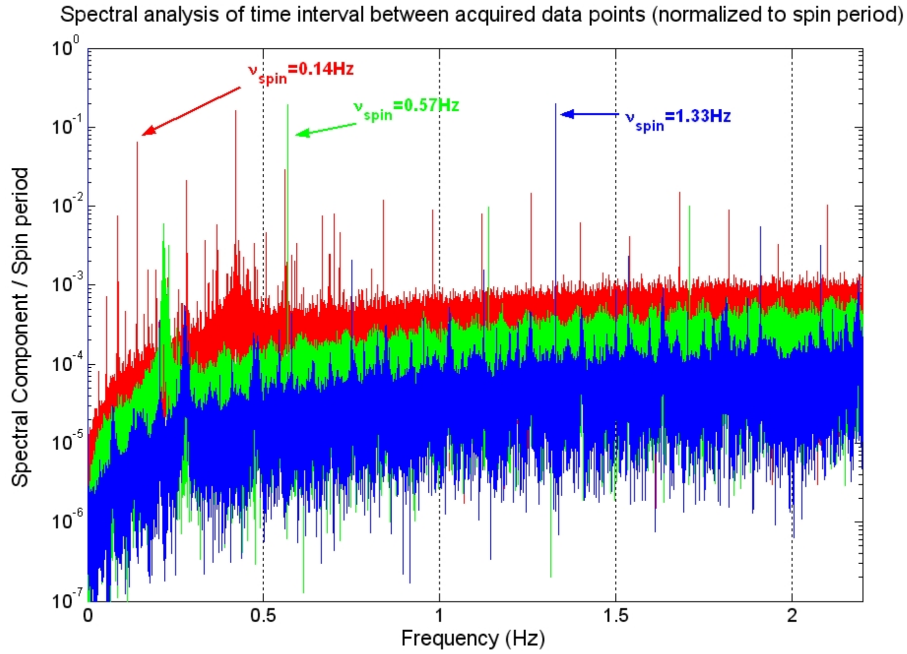

Figure 4.23: In increasing the rotation speed of the rotor by a factor 9.5 its spin energy increases by almost 2 orders of magnitude, and yet the rotation noise has decreased by about 1 order of magnitude

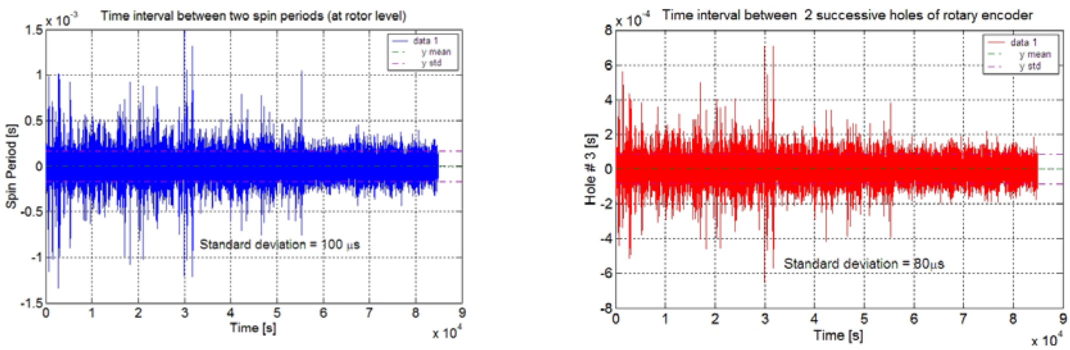

Figure 4.24: At rotor level, both the spin period measurement and the measurement of time interval between successive holes of the rotary encoder give a standard deviation of 80 to 100 microsec

9.7 DEALING WITH TERRAIN TILTS

Low frequency tilts of the local terrain do indeed disturb the test masses of the laboratory prototype and need to be attenuated for the prototype to achieve a sensitive (in terms of relative displacements of the test cylinders) of relevance for the space experiment. A closed control loop is applied, using a tilt meter as sensor and PZTs as actuators.

Figure 4.19 shows the results achieved in a 1 week run at the spin frequency of 0.9 Hz. However, though the loop works very well, the “zero” of the tilt meter is not the actual horizontal plane because the tilt meter is temperature dependent. Unless this dependence is characterized and compensated for within the loop, so that the PZTs receive the correct command, “spurious” tilts are in fact applied producing unwanted relative displacements of the test cylinders.

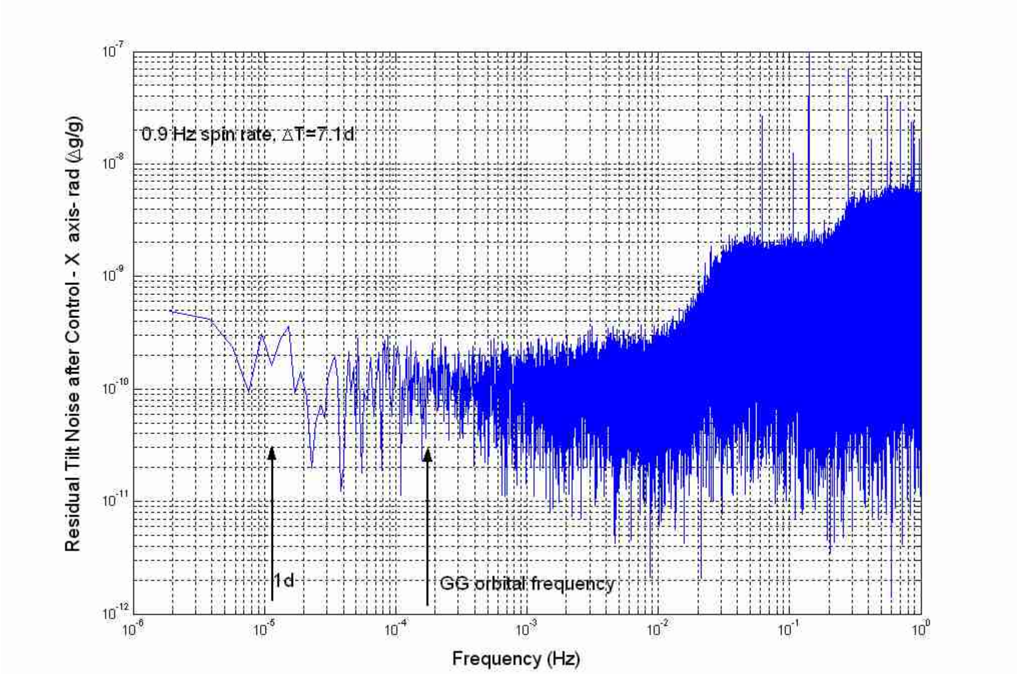

Figure 4.19: Fast Fourier Transform of the residual tilt noise after applying tilt control in closed loop for 7.1 days with the GGG apparatus spinning at 0.9 Hz. The test shows that at the low frequencies of interest (the GG orbital frequency and the diurnal frequency), the tilt measurement signal of the sensor used to close the loop can be “zeroed” to a few 10^{-10} rad (10^{-10} rad corresponding, in the current set up, to a relative displacement of the test cylinders of about $0.5 \cdot 10^{-10}$ m). This is the best result which can be obtained given the sensitivity of the tilt meter used.

In addition, in the current set up the vacuum chamber and the instrumentation (Figure 4.20) is not optimized to reduce diurnal thermal expansion/contraction effects.

Figure 4.21 shows how disturbances on the relative motion of the test cylinders acting over the timescale of 1 day have been reduced by 2 orders of magnitude by an appropriate thermal control loop of the vacuum chamber which has reduced its diurnal temperature variations to 0.02 °C/d. If then the temperature dependence of the tilt meter is characterized in this range, and compensated for within the control loop before sending the signal to the PZT actuators, the spurious tilts mentioned above are reduced, the zero of the tilt meter becomes a “true” zero and a corresponding reduction of the low frequency relative displacements of the test masses is expected.

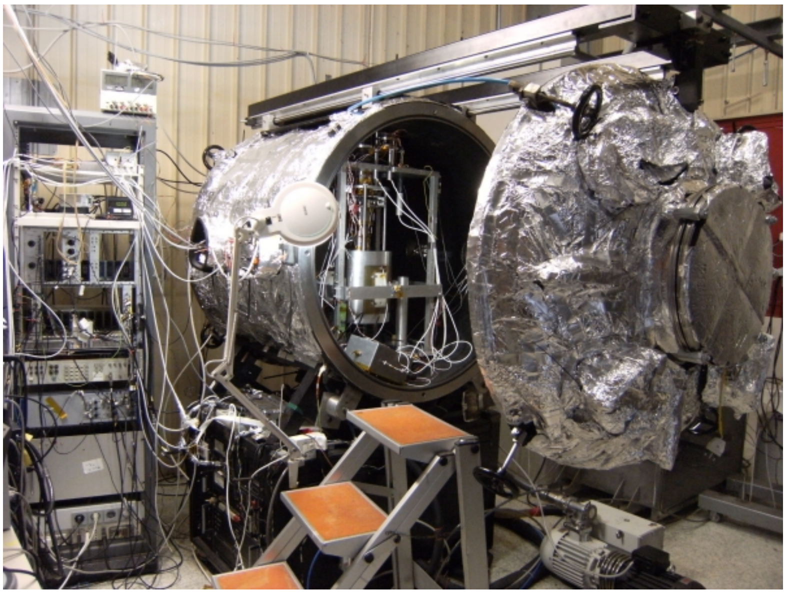

Figure 4.20: The vacuum chamber enclosing at present the GGG laboratory prototype. Below the wrapping with Al paper (to increase reflectivity) is a thermal insulating rubber blanket and below that a resistance wire wrapping (for heating) and water pipe (for cooling). The GGG apparatus mounted inside is symmetric around the vertical axis, at 90° with the chamber axis, which maximizes disturbances from the thermal distortions of the chamber.

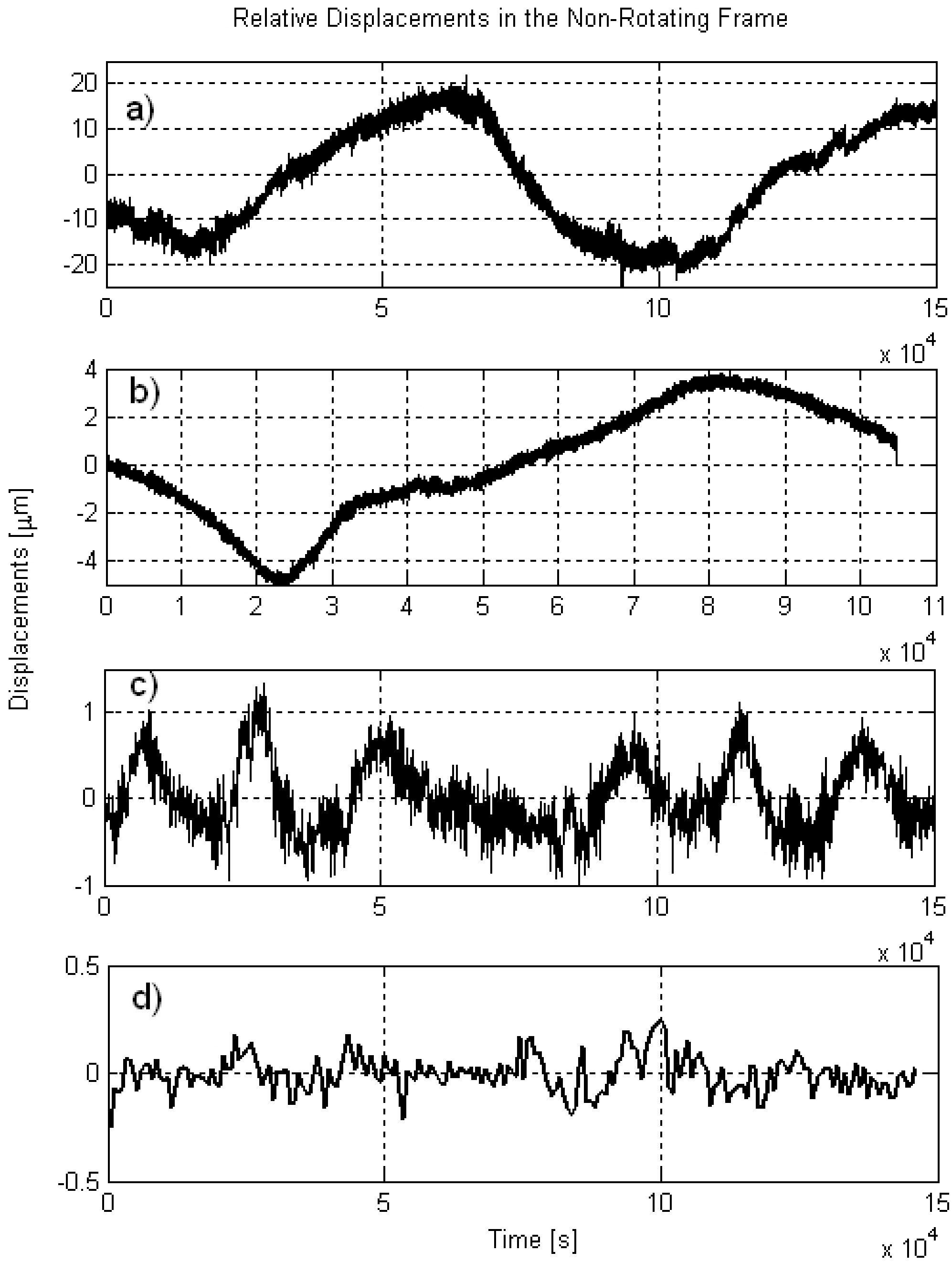

Figure 4.21: The figure demonstrates the advantages of thermal stabilization of the vacuum chamber enclosing the GGG experiment. The plots show the relative displacements (in microns) between the centers of mass of the test cylinders in the horizontal plane of the laboratory (once transformed from the rotating reference frame). Each run lasts about 2 days. Diurnal variations are apparent in the two upper plots, while they are no longer visible in the bottom ones; from plot a) to plot d) the amplitude of the largest relative displacements has decreased from 20 to 0.2 μm. The improvement therefore amounts to 2 orders of magnitude. It has been obtained by improving the thermal stability of the chamber. Starting with the run reported in plot b) a thermal stabilization loop of the chamber was implemented and gradually improved during the following runs till reaching the level of $\pm$ 0.02 °C/d during the run reported in plot d).

It is therefore the need to reduce low frequency terrain tilts (typical of the ground environment) which makes thermal stabilization of the laboratory prototype very important. This is a very important point to make as this source of thermal noise is not applicable to GG in space, in which case the main thermal stress comes from eclipses, and needs to be addressed differently (see Section 6)

One way applied in the GGG experiment to reduce tilt terrain noise has been, in addition to thermal stabilization, the use of a temperature compensated tilt control loop as shown in Figure 4.22 which has provided so far the best measurement results reported in Section 9.9

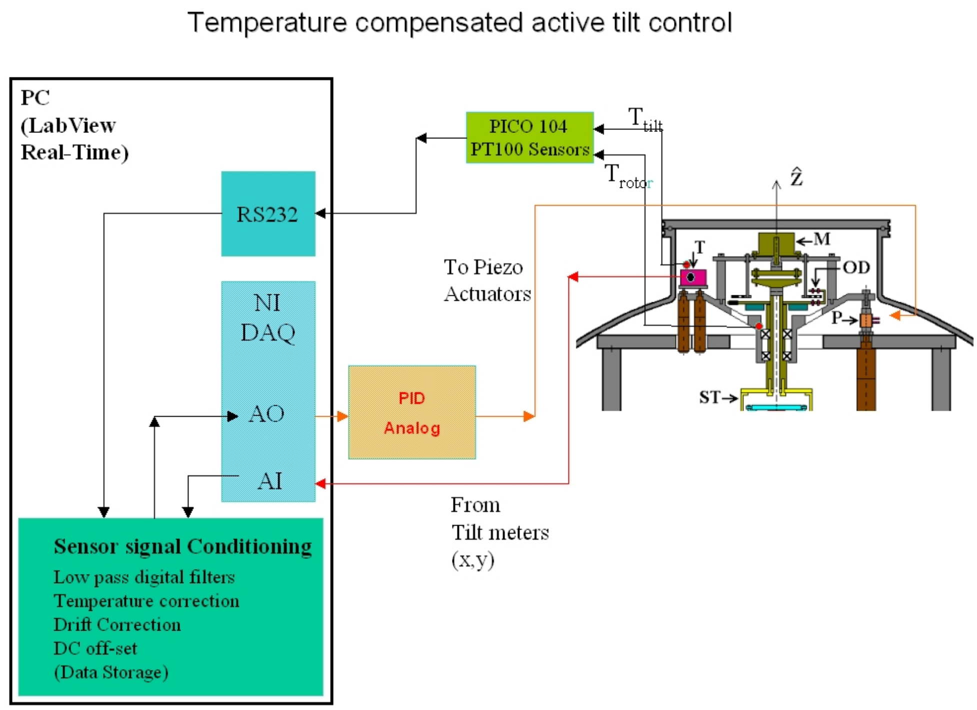

Figure 4.22: Scheme of the temperature compensated active tilt control loop currently used in GGG

The vacuum chamber shown in Figure 4.20 is indeed inappropriate for the GGG prototype for 2 major reasons. First the apparatus has cylindrical symmetry with the axis in the vertical direction while the chamber has a cylindrical symmetry with the axis at 90° from it. Second, the chamber rests on a base frame whose structure is not rigid enough. As a result, vibrations (coming from the terrain) and distortions (thermally induced expansions/contractions) are transmitted to the prototype inside, including low frequency ones (see Section 9.10 for a description of the new chamber)

9.8 MEASURING ELECTRIC CHARGE SURFACE PATCHES

The relevance of surface charge patch effects is well known and has been discussed in Section 3.2.1. We can now measure charge patches with GGG.

We use a small capacitance plate to apply a force on the outer test cylinder at a frequency below the differential mode frequency so that it is not attenuated, and then measure the resulting displacement of the test masses (at that frequency) with the capacitance bridge sensors in between the test cylinders. GGG is not rotating, though obviously under vacuum.

If the potential applied is unipolar, as a square wave, a displacement corresponding to the force applied by such potential is measured, as shown in Figure 4.23. Since charge changes sign with the applied potential while a patch charge on the surface does not, and the force is proportional to the charge squared, by applying a bipolar potential (square wave of the same period) only the patch charge effect (if any) will remain and give rise to a relative displacement of the test masses. This is shown in Figure 4.24 The ratio of the displacements in the two cases gives the ratio of the patch charge to the applied charge, hence of the patch potential to the applied potential, and therefore the potential of the patch. This is a simple direct measurement.

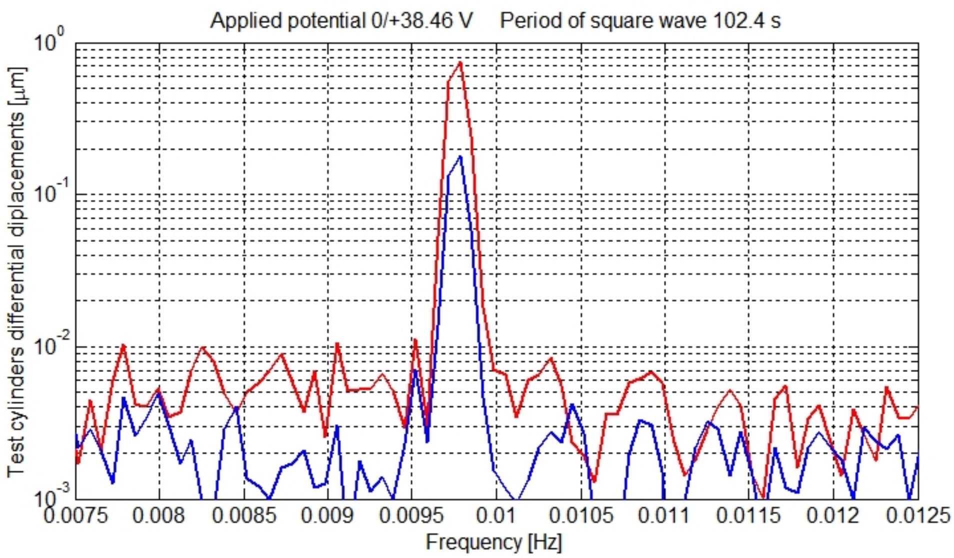

Figure 4.23: Relative displacements (in the two directions of the plane) caused by an applied unipolar potential of 0/+38.46 V and a period of the square wave of 102.4 s

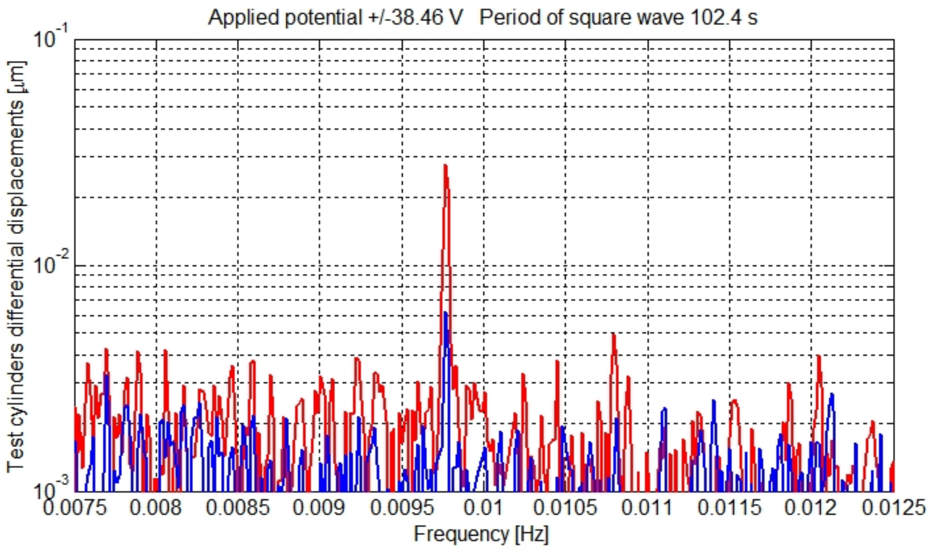

Figure 4.24: Relative displacements (in the two directions of the plane) caused by an applied bipolar potential of +/-38.46 V and a period of the square wave of 102.4 s

This run gives a patch potential of about 0.3 V. We plan to investigate the time variation by running a long measurement, the dependence on the are of the surface involved (it was 2cm x 2 cm in this case) and finally to assess the effectiveness of gold coating in reducing the patches.

Even though in GG as well as in GGG patch effects would be mostly DC it is clearly very important that we have a tool to quantitatively measure this source of perturbation.

9.9 GGG SENSITIVITY TO LOW FREQUENCY DIFFERENTIAL EFFECTS

The sensitivity of GGG to differential displacements of the test cylinders has been improving, particularly at low frequencies, as shown in Figure 4.25.

The FFT of the relative displacements during one run in 2008 is shown in Figure 4.26, from which we can see that the centers of mass of the GGG rotating test cylinders remain, at very low frequencies, within less than 10^{-8} m from each other.

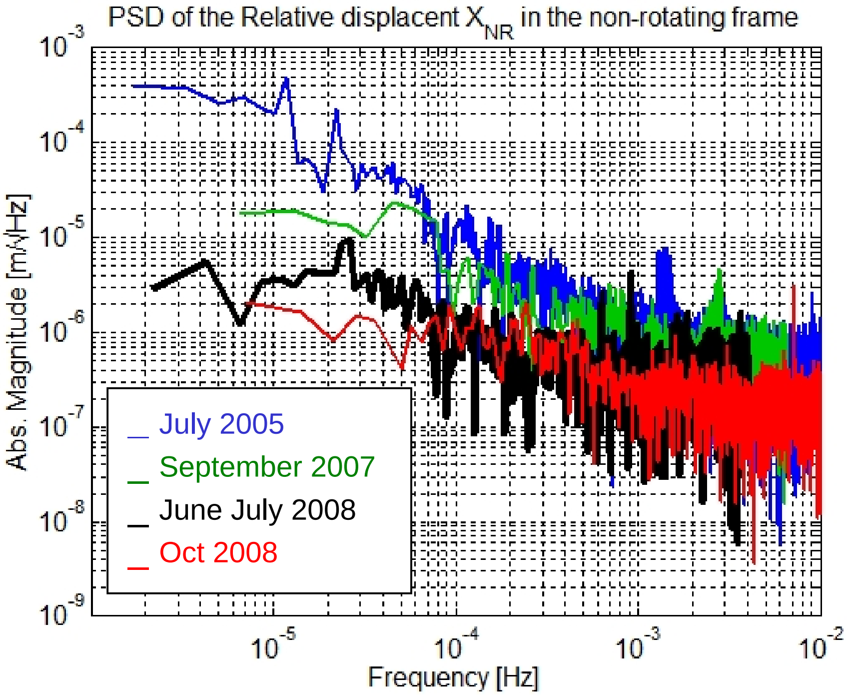

Figure 4.25: Power spectral density of the relative displacements of the test cylinders in the non rotating frame of the laboratory. Note the low frequency of the measurements, and the difficulty in reducing disturbances at diurnal frequency (1.16×10^{-5} Hz)

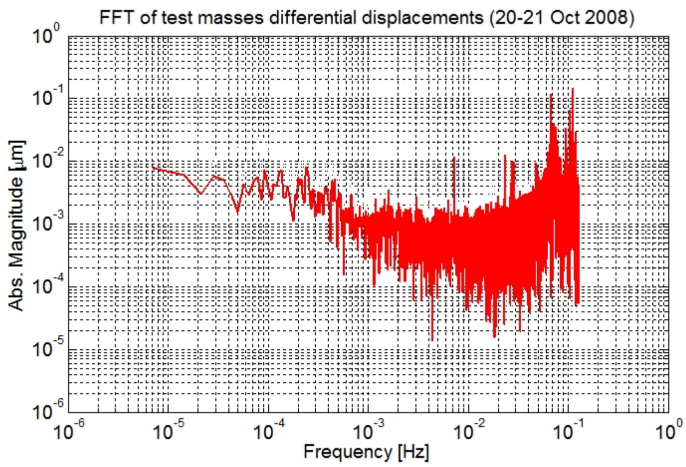

Figure 4.26: FFT of the relative displacements of the GGG test cylinders in the horizontal plane of the laboratory. At diurnal frequency, and at the orbital frequency of GG at which the EP violation signal is expected in space, they are below 10 nanometer.

9.10 ADVANCED GGG UNDER CONSTRUCTION

A properly designed new chamber, optimized for hosting the prototype and minimize disturbances on it has been manufactured and is now operational in the lab (see Figure 4.22). In addition to reducing disturbances on the apparatus and improving thermal stability (the base structure of the chamber is thermally stabilized –in addition to the chamber itself and ceramic breaks on three legs at the bottom of the chamber contribute to thermally decouple the apparatus form the base thus reducing thermal stress coming form the floor) the new chamber is designed to allow the apparatus to be suspended from a non rotating cardanic joint (shown in red in Figure 4.22, left) so as to reduce low frequency terrain tilts first actively and then also passively)

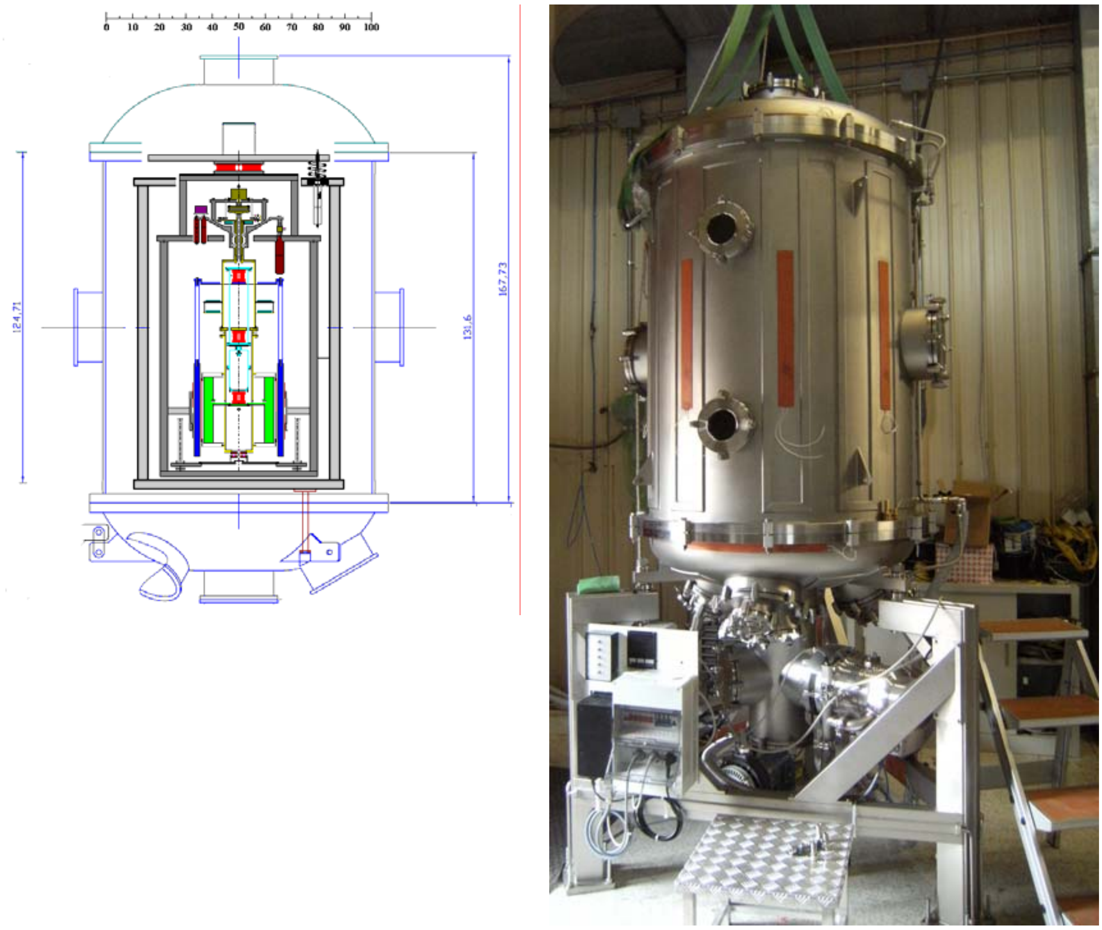

Figure 4.27: The new vacuum chamber designed to host an advanced laboratory prototype. The sketch on the left shows how the prototype can now be suspended (from a non rotating cardanic joint; shown in red; sketch on the left) for terrain tilts to be reduced passively in addition to the active tilt control loop:

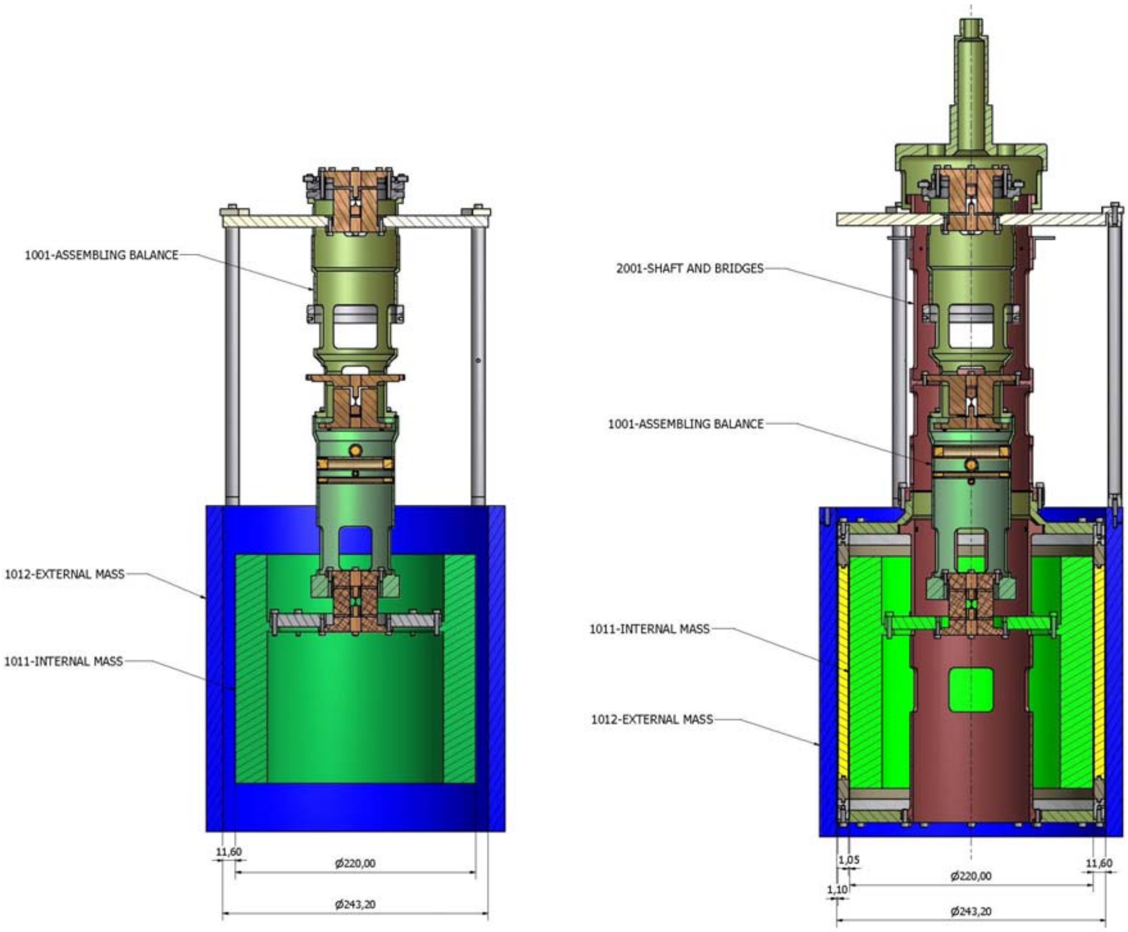

Figure 4.28: A new prototype has been designed and is under construction to be operated inside the new vacuum chamber of Figure 4.27. On the left is the GGG “balance”: two concentric test cylinders (blue and green) and the balance arm. Inside the arm are visible: the central cardanic joint (for connecting the whole balance to the shaft, as shown on the right); the top cardanic joint (for connecting the blue test cylinder to the balance arm); the bottom cardanic joint, for connecting the green test cylinder to the balance arm). On the right, the same balance is shown, with the balance arm placed inside the shaft and connected to it at its center, and the capacitance plates of the read out sensor (in yellow) in between the green and the blue test cylinders. These are construction drawings and are therefore to scale: the outer diameter of the blue test cylinder is 27.4 cm. Pictures of the capacitance plates of the read out sensor are shown below in Figure 4.29

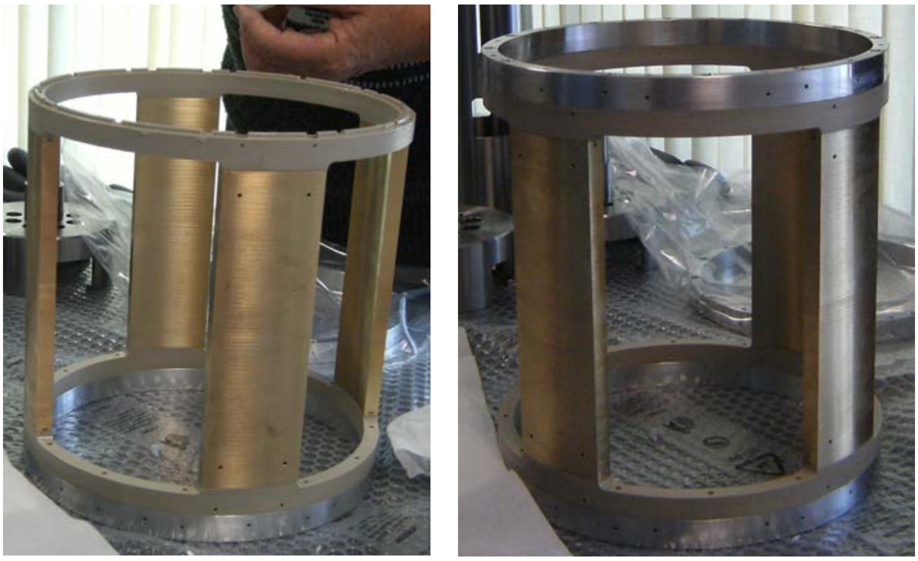

Figure 4.29: The capacitance bridges of the advanced prototype, to be used for measuring the relative displacements of the test cylinders (shown in yellow in Figure 4.28, right). They are assembled in a “cage” not to be ever dismantled, as this would impair the symmetry and construction precision. The brown rings are made of peek and serve as electric insulators. The external diameter of the cage is 24 cm

An improved sensitivity to test masses displacements is expected, first by running the current accelerometer prototype in the new vacuum chamber and finally by operating the new, suspended prototype. These results will be reported at completion of the Study.

In addition, a numerical GGG Simulator will be built similarly to the GG Experiment Simulator discussed in Section 8 so that its predictions can be compared with experimental measurements.

10. THE GROUND SEGMENT

10.1 KEY GG OPERATIONS REQUIREMENTS

The GG mission is devoted to a single experiment that, once initialized, runs to the end of the scientific data collection. In the Launch and Early Orbit Phase, operators control the correct spacecraft activation and perform attitude and spin-up maneuvers. Experiment set-up and first calibration operations follow. Thereafter the Science Phase starts and the experiment is run in 7-day (TBC) long data collection intervals. Spacecraft health checks will be cadenced at regular intervals to monitor the correct data acquisition and spacecraft status.

The nominal duration of the mission is two years. No orbit change maneuvers are required after insertion into operational orbit by the launcher. De-orbiting at end of life is not envisaged. Orbit determination is performed by using range and Doppler data from the Ground Station, no localization systems are foreseen on board.

The processing of scientific data is done in bulk; therefore no scientific quick-look is required. All satellite operations are autonomous, executed on the basis of time-tagged operation sequences that are loaded at least one day in advance. The minimum integration time of the experiment is determined by the experimental noises and is about 7 days. Hence, examination of the scientific data at shorter intervals is, strictly speaking, not significant. Therefore, quick look procedures are not needed and the scientific data can be routed to the Scientific Data Centre within a couple of days of reception. On the other hand, for the purposes of checking the health of the scientific payload and the correct execution of the measurement procedures, shorter reaction times may be desirable. Tests based on consistency checks, threshold parameter values etc. may be elaborated and implemented in automatic self-check procedures that can be run periodically by the onboard computer, and can be used to alert the ground control of any non-nominal state of the scientific payload. Data affected by anomalies of any sort will be rejected on post-processing and will have no effect but a shortening of the data collection period.

There are no requirements for real-time interaction between the satellite and the MOCC during a communication pass over the ground station. Because of that, and given the high level of on-board autonomy, the tasks of the ground control are essentially limited to:

- commanding and monitoring of the initial attitude maneuvers (spin axis orientation and spin-up);
- performing orbit determination and propagation and scheduling spacecraft/ ground station contacts;
- analyzing satellite data to establish that the satellite is operating correctly;
- generating and transmitting command sequences and parameters in accordance with science needs.

10.2 Ground Segment Description

The ground segment comprises the following functional blocks (Figure 10-67):

- Ground Stations System (GSTS)
- Ground Communication Subnet (GCS)
- Mission Operations Control Center (MOCC)
- Launcher Operations Control Center (LOCC)
- Science Operations Control Center (SOCC)
- Support Facilities (SF).

The GSTS supplies the required space to ground communication for telemetry reception and telecommand uplink. It includes a dedicated ground station for the normal operations, supplemented by additional stations during the LEOP. The nominal ground station is the ASI Station in Malindi, Kenya. Among the additional ground stations which can be employed to support the initial mission phases, the ESA/CNES Station at Kourou, French Guyana, is particularly well suited because of its near-equatorial location.

The Ground Communication Subnet (GCS) interconnects the ground stations with the functional blocks providing management of the satellite operations (the MOCC), and the science operations (the SOCC). This network can be largely realized using the existing ASI multi-mission operational network (ASINET).

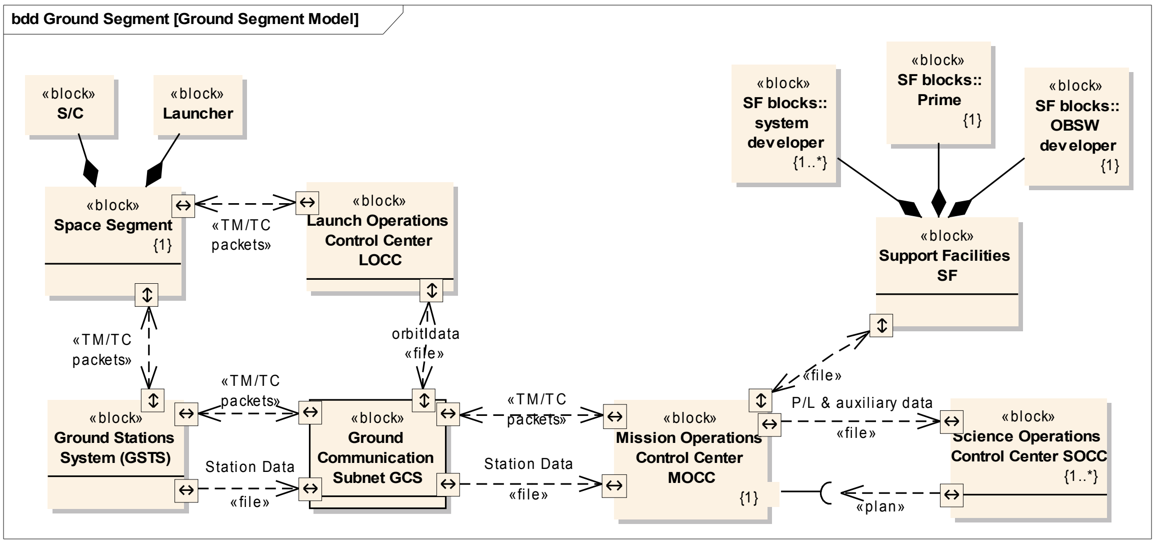

Figure 10-67: Functional model of the GG ground segment. Each block is a logical unit and/or a physical unit. The fundamental building blocks comprise the Ground Stations System (GSTS) with the Ground Communications Subnet (GCS), the Mission Operations Control Center (MOCC), the Launcher Operations Control Center (LOCC), the Science Operations Control Center (SOCC) and Support Facilities (SF).

The MOCC is responsible for the execution of all GG mission operations. It provides mission planning, orbit and attitude determination for both operational purposes and science data processing applications, spacecraft monitoring and control and payload monitoring and control. The MOCC will route the scientific telemetry to the SOCC and will receive the payload command requests from the SOCC to be subsequently processed and uplinked to the satellite.

Launch operations are managed by the LOCC. In the pre-launch and launch phases, until satellite separation, the MOCC provides the interface to the LOCC.

The SOCC is responsible for the generation of the scientific operations sequences to be executed on board, as well as for the scientific data processing and analysis. In the GG mission, real-time involvement of the SOCC in the mission operations is not a requirement. Therefore both science data and science operations sequences can be exchanged between MOCC and SOCC in an “off-line” mode.

The SF is a collection of facilities usually involved in the spacecraft development and providing engineering support during the mission, such as software or system developers for thrusters. During Commissioning and Calibration phases, the SF teams could be partly co-located at the MOCC.

Physically, the MOCC functions as well as most SF functions will reside in an operations control center provided by ASI. The specific program needs do not require the SOCC to be logistically separated: both functions may be co-located in the same facility. Anyway, the engineering and science teams will have web access to the necessary MOCC functionalities, whatever their physical location.

10.3 User Segment Description

GG is a mission devoted to a single experiment and has one single User Group led by the PI. Co-PIs are selected to become members of the GG User Group on the basis of:

- His/her specific contribution to hardware and/or software components of the payload and/or spacecraft;
- His/her knowledge of specific scientific topics of the science addressed by the mission;
- His/her specific expertise on: data analysis in the field of fundamental physics in space; GG full scale numerical simulations; recovery of scientific information from numerically simulated GG data;
- His/her contribution to key instrumental aspects of the mission which are known to affect the scientific outcome of the mission.

GG mission data will remain in the hands of the User Group for the entire duration of the mission and up to a maximum of 2 years after mission completion. After that, data will be made public via free internet access to a dedicated GG Mission Data Webpage. It has to be noted that the scientific outcome of the GG mission as to the Equivalence Principle being confirmed or violated, as well as in relation to the sensitivity achieved, will be of extreme importance and therefore it has to be established beyond any possible doubt. This requires other scientists and scientific collaborations outside the mission team to be in a position to independently check the results, starting from original data. To this end, the GG Mission Data Webpage will freely provide:

- Full GG science raw data with appropriate description and format specification for use from anyone interested in checking the User Group analysis;
- Full GG mission operation data with appropriate description and format specification to be used in combination with science data for completeness of information whenever needed;
- Reduced science data set as created by the GG User Group for signal search and analysis of relevant physical effects. Information on how the set has been created will be provided along with it;
- Data analysis software and codes developed and used by the GG User Group, including all the software tools which typically are not published on scientific journals along with the results.

10.4 Science Operations And Science Management Plan

After the launch and early orbit phase, experiment set-up and first calibration operations are executed. Thereafter, the experiment is run in 7-day long data collection intervals. Calibration sessions are regularly interspersed with the measurement intervals. Continuation of the mission improves the measurement accuracy with the square root of the measurement time. The nominal duration of the mission is two years.

The processing of scientific data is done in bulk; therefore no scientific quick-look is required. All scientific operations are autonomous, executed on the basis of time-tagged operation sequences that are loaded at least one day in advance. Given the high level of autonomy, the science operations are essentially limited to:

- Command and monitoring of the initial experiment set-up;
- Analysis of satellite data to establish that the experiment is operating correctly;
- Generation and transmission of command sequences and parameters for experiment tuning.

After commissioning at the beginning of life, the main operational modes of the satellite are:

- Experiment Set-up and Calibration Mode
- Normal mode (scientific operation of the experiment)
- High-rate Data Collection Mode
- Safe (Hold) Mode.

The experiment set-up phase will be based on semi-autonomous procedures, with intermediate checks by the ground after each phase before the next operation is executed. The experiment set-up includes the balancing of the test masses and the mechanical balancing of the capacitance read-out sensors. Both operations need to be repeated at regular intervals. Automatic procedures for such operations will be elaborated, possibly with some interaction with the ground control.

In the science measurements phase, the operation will be essentially autonomous. The Normal Mode is characterized by the drag-free control, executed by proportional milli-Newton thrusters. However, the survival of the mission does not depend on the drag-free control, since the maintenance of the operational attitude is guaranteed by the gyroscopic stability. In case of malfunctions, the scientific operations will be put on hold and housekeeping data will be collected and transmitted to ground on the next station passes; resumption of the operations will be commanded by the ground.

Generally, the command and parameter sequences of the Normal mode will need to be updated on a time basis of several weeks, except in the set-up phase when the frequency will be higher (some hours).

The scientific telemetry data stream consists of:

- Test mass differential displacements (in-plane, 2 axes)
- External test mass displacement w.r.t. PGB (3 orthogonal axes)
- Internal test mass displacement w.r.t. PGB (3 orthogonal axes)
- PGB to spacecraft displacement (3 orthogonal axes)
- Spin velocity vector
- On board reference time.

All such data are collected as 16-bit words at high rate (50 Hz). Payload housekeeping data (monitors, temperatures, …) are collected at lower rates, depending on the time constant of the phenomena to be kept under control. Finally, a complete record of the drag-free control operation (commands as received, actuator response, auxiliary variables, monitors and controls) is collected to enable reconstructing the time history of the disturbance rejection performance.

A preliminary budget of the telemetry data is in Table 10-21.

Data description	**Variable list**	**Number of variables**	**Frequency [Hz]**	**Record length [bit]**	**Data rate [kbit/s]**
Diff. TMs displacement	Δx, Δy	2	50	16	1,6
Tme/PGB displacement	Δx, Δy, Δz	3	50	16	2,4
Tmi/PGB displacement	Δx, Δy, Δz	3	50	16	2,4
PGB/Spacecraft displacement	Δx, Δy, Δz	3	50	16	2,4
ω_{SPIN}	ω_x, ω_y, ω_z	3	50	16	2,4
Reference time	t	1	50	16	0,8
Science data					**12**
Payload Housekeeping					**1**
Drag-free control					**7**

Total Data Rate	**kbps**	**20**
Period	**s**	**5702**
Data volume per orbit	**Mbit/orbit**	**112**
Telemetry rate	**kbit/s**	**186**

Table 10-21: Telemetry data rate budget

11. Development, programmatics and risk analysis

11.1 Satellite development approach

11.1.1 Development objectives and elements

The objectives of the GG program are:

- To carry out a test of the Equivalence Principle with sensitivity of a least 1 part in 10^{17}, in low, near-equatorial, near-circular Earth orbit, for a duration of at least 2 years;
- To design, develop, and test a small satellite, devoted to the above objectives, over a time span (Implementation Phase) not exceeding 3 years (TBC), within a level of resources commensurate with that of a small satellite program of ASI;
- To launch and operate the satellite using as much as possible the infrastructure and resources at the disposal of ASI;
- To use this opportunity to advance the implementation and use of Italian technology and know-how in the service of an outstanding scientific project.

The space segment, the GG Satellite, is defined as a modular product consisting of two modules: the Platform (or Service Module) and the Payload (Pico Gravity Box). At lower level each module is composed of subsystems, and each subsystem can be composed of one of more units plus auxiliary parts.

A number of elements support the project during its life cycle.

- The GG Payload ground prototype (GGG). GGG is an experiment to test the Equivalence Principle, at lower sensitivity, with an apparatus very close to a prototype of the payload designed for the GG space experiment. The experiment is carried out at the University Of Pisa and can be used as a development model for the flight model.
- Software simulators. Satellite and Payload simulators, both HW and SW, will be used during the project lifecycle to consolidate the design, verify requirements in advance respect to the HW manufacturing, execute tests not performable on real HW.
- Standard engineering mathematical tools will be used to support the project development.
- Ground Support Equipment (GSE). The GSE comprises all the test equipment needed to support the ground activities on GG and its components. The GSE includes Electrical and Mechanical Ground Support Equipment.
- Standard laboratory equipment and special tools used during the GG integration and test activities.

- Test facilities. Along its ground lifecycle GG and its flight components will use different test facilities such as thermal vacuum chambers, shakers, acoustic chambers, anechoic chambers. A dedicated facility will be selected to perform the environmental test campaign. All flight items will be subjected to a Cleanliness Control Plan and to a Quality Control. Consequently the facility used by the prime contractor and its subcontractors shall conform to these requirements. In particular all the items qualified to flight shall be maintained in a qualified clean room (typically class 8).
- The VEGA facilities in Kourou to support the Launch Campaign.
- The GG Ground Segment: it provides all the necessary features to ensure satellite control during the mission and scientific data acquisition, storage and analysis. It comprises as subsystems the ground station network, the Operations Control Center (OCC), responsible for the execution of the mission operations, and the Science Operation Center (SOC), responsible for the scientific data processing and analysis.

11.1.2 PROGRAM FLOW

The GG project will be implemented in the following steps:

- System Definition Phase (Phase A/B), that includes the definition of the GG flight system and its relevant support equipment and the finalization of the System and Payload design;
- Development and Production phase (Phase C/D) that includes the detailed design, the development, production, verification and delivery of the GG flight Satellite with the Payload installed on it, the associated support equipment, and the launcher adapter;
- Launch and in orbit commissioning (Phase E/F), that include the launch preparation, the launch itself and the system checkout and calibration in the early orbit phases;
- The operating life, in which the scientific measurements will be acquired, stored, and analyzed until the end of the mission.

The GG Satellite detailed design definition will start from the preparation of high level (system level) specifications. Starting from these documents, lower level specifications (subsystem and unit level) will be prepared as input for the subcontractors. The Subcontractors will provide to the prime the requested items after completion of relevant development and validation process. All the units, subsystems, parts collected by the prime will be integrated to compose the final satellite and validated with the testing campaign at system level.

Dedicated reviews and milestones are defined in the various project phases to certify the above process.

11.1.3 Model Philosophy

At the satellite system level, a Proto Flight approach is proposed. Prior to the PFM program,

- the satellite functional performances will be validated using a dedicated End to End simulator (purely SW) plus an Avionics Test Bench where representative HW will be incrementally included in the loop. This HW will be composed of breadboards and 'Off the Shelf' components, functionally representative of the flight HW;
- the satellite-level thermo-structural performances and the compliance with the relevant requirements will be evaluated by analysis.

The Proto Flight Model will be the final product after integration, and the unit that will be launched. Since a single complete satellite model is foreseen, it will be subjected to a complete proto-flight test campaign in order to confirm the functional validation performed on simulators, and the thermo-structural performances evaluated by analysis.

At lower level (payload and platform), different model approaches apply as detailed in §11.2 and §11.2 below.

11.1.4 Schedule

The GG program will be phased according to the following durations and main reviews:

- Phase B 9 months KO, PDR
- Phase C/D 36 months CDR, TRR, FAR
- Phase E 3 months LRR.

Figure 11-68 shows the current GG master schedule for the phases B, C/D, E, and F. The Ground Segment schedule is included with the following baseline:

- 2 years of mission (including commissioning)
- 1 year of long term data archiving.

ID	Task Name
1	**GG planning**
2	GG phase B K.O. - T0
3	GG Preeliminary Design Review (PDR) - Start C/D
4	GG Critical Design Review (CDR)
5	GG Proto-Flight Model TRR - Start System I&T
6	GG Flight Acceptance Review (FAR) and (ORR)
7	GG Launch Readness Review (LRR)
8	GS System Requirement & Preliminary Design Review (GSPDR)
9	GS Critical Design Review (GSCDR)
10	GS and Operations Qualification Review (GSQR)
11	**Ground Segment phase B/C/D**
12	**Ground Segment phase B**
13	GS Phase B K.O.
14	GS Requirements and Design
15	**Ground Segment phase C/D**
16	GS Design
17	GS Procurement, development and test
18	GS System Validation Tests
19	GS Verification Completed
20	GS manteinance
21	**Operations phase B/C/D**
22	**Operations phase B**
23	Operations analysis and development
24	**Operations phase C/D**
25	Development of Operations Products
26	Operations Products Validation
27	GS Training
28	GS Ready for Operations
29	**Payload phases B/C/D**
30	PGB Kick Off
31	Flight PGB Design
32	Flight PGB Development & Testing
33	Flight PGB ready for I&T on Satellite
34	**GG platform phase B**
35	System I/F Consolidation
36	Units and S/S draft specification
37	GSE adaptation/definition for GG
38	**GG phase C/D**
39	GG Equipments / SS Detailed Specification
40	GG Platform Equipment Procurement
41	GG PT structure Procurement (including H/N & propulsion)
42	GG PT Non Standard Items Development Models
43	GG GSE procurement
44	GG SW Development & Test
45	ATB adaptation for GG
46	GG SW testing on ATB
47	GG Platform I&T and functional test (incl. FEEP)
48	GG PGB Integration and Functional Verifications
49	GG System Testing
50	Environmental Test (TV/TB, Mechanical, EMC)
51	GG ready for Launch Campaign
52	**GG phase E**
53	Launch Campaign
54	GG ready to Launch
55	GG Launch
56	In-orbit Commissioning and Calibration
57	Operation and Science
58	GS Maintenance
59	Mission end
60	**GG phase F**
61	Long Term Data Archiving
62	Disposal of ground segment

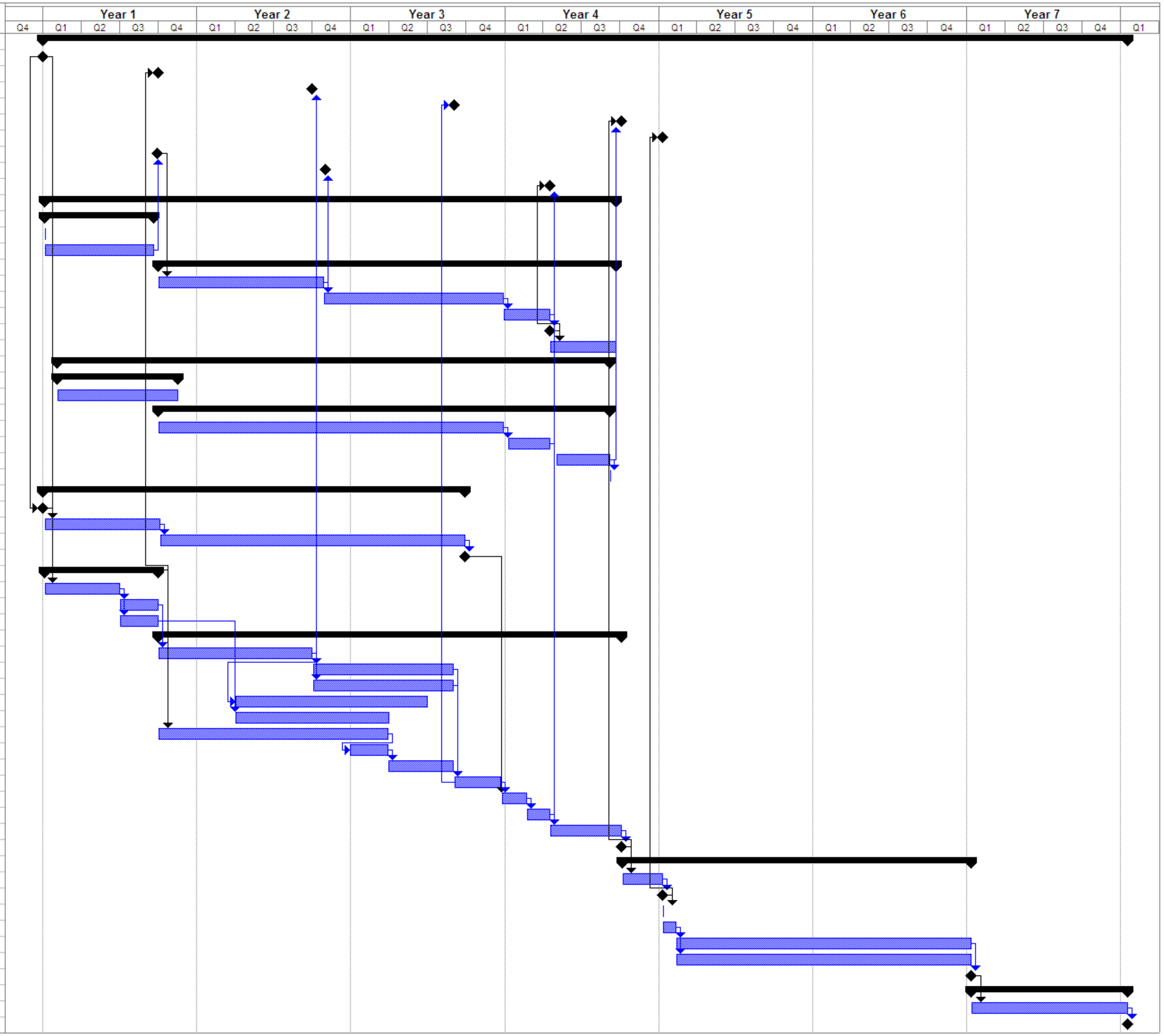

11.2 Payload development plan

At payload (PGB) level, a two-model approach is proposed. The PGB-STM (Structural Thermal Model) will be used to qualify the mechanical and thermal design, including the thermo-structural deformation aspects. The STM has therefore to be representative in terms of mechanics and thermal design. The PBG-PFM (Proto Flight Model) will be used to complete the acceptance from the mechanical, thermal and functional point of view, and will be the flight unit. Figure 11-69 summarizes the PGB test approach.

From the equipment point of view, the following units are new developments, and will be subjected to a complete qualification test campaign, including environmental testing (TV/TB, mechanical test):

- ECE and (partially) CPE
- Accelerometer
- Lock/unlock mechanisms.

The ECE and CPE will have Engineering Models, mechanically, thermally and functionally representative of the flight units. The Accelerometer is functionally covered by the GGG laboratory experiment; however an STM is needed anyway and will be provided as part of the complete PGB assembly. The mechanisms shall be completely flight representative, and shall be included in the PGB-STM. Table 11-22 summarizes the approach.

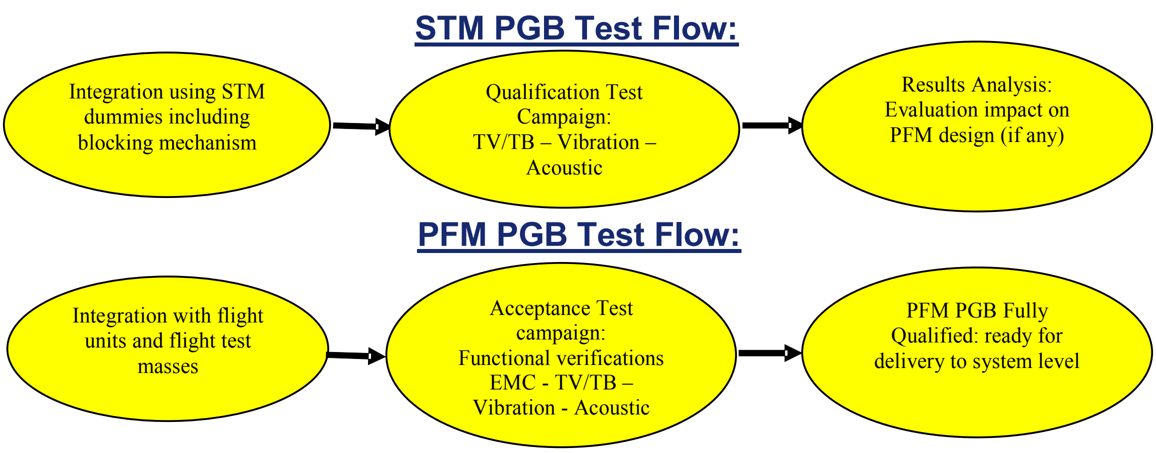

Figure 11-69: Two-model approach to PGB system testing

Assembly – Unit	EM / Functional model	PFM
Accelerometer Mechanics	GGG-Pisa (tbc)	1
ECE unit	1	1
CPE unit	1 (tbc)	1
Locking mechanism	n. 1 set	NN sets

Table 11-22: PGB unit model philosophy

11.3 Platform development plan

Different model philosophies will be applied for units and subsystems according to whether they are recurring items or not. As general rule, a protoflight approach will be defined for the recurring items. At equipment and subsystem levels, the verification approach will be defined in function of the individual unit/subsystem Technology Readiness Level (TRL). The general approach is to have a complete qualification test campaign and consequently a qualification approach on the new items, and to perform a reduced acceptance campaign on the recurring units.

The following non-recurring or (partially) new development items have been identified.

- FEEP. At least one FEEP development model will be foreseen as part of the qualification process, before the flight model.
- Spin Sensor. At least two models will be foreseen as part of the qualification process: 1) an Engineering Qualification Model (EQM), which shall be submitted to a complete qualification test campaign to assess the design and the technological solutions; 2) a Flight Model (FM), which shall be submitted to a test campaign at flight conditions before being installed on the satellite.

At platform and system level, the PFM will be subjected to a complete proto flight test campaign, including thermal testing, mechanical testing and electro-magnetic compatibility, according to the sequence depicted in Figure 11-70.

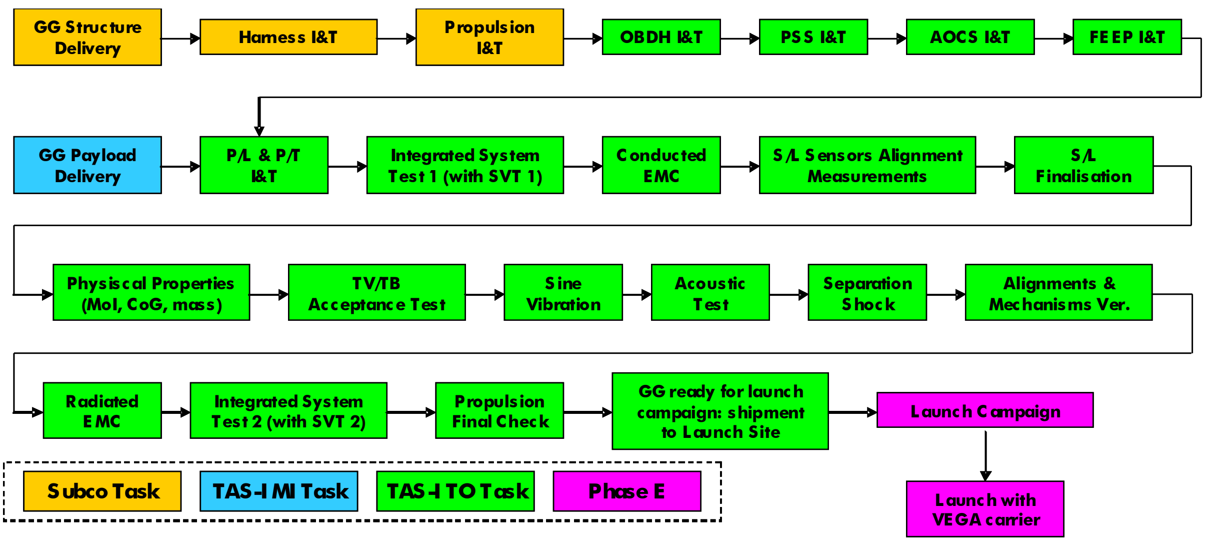

Figure 11-70: Development Plan at satellite level. In the above scheme color coding is used to mark different responsibilities. Gold stands for an item/subsystem provided by and external subcontractor. Green marks a task under Industrial Prime responsibility. Blue signals the payload and its components. Phase E is identified in a different color since it will be probably be subjected to a different contract.

11.4 Development plan for the Ground Segment

The ground segment will be developed in step with the flight system, as shown in Figure 11-71.

According to the requirements assessment performed in Phase A2, all major hardware provisions and facilities may be inherited from existing ASI assets. Therefore no significant costs are envisaged for hardware/facility procurement.

The mission specific items to be designed and developed / procured as part of the GG program include all the necessary GS documentation, plans, software and procedures. Major items are listed below.

Phase B

- Ground segment requirements document (GSRD)
- Space–to–ground interface control document (SGICD)
- Mission analysis report (MAR)

Phase C

- Space–to–ground interface control document (SGICD) – final version
- Consolidated Report on Mission Analysis report (CREMA)
- Operations engineering plan (OEP)
- Mission operations plan (preliminary)

Phase D

- Validated Mission Operations Plan (MOP)
- Validated space and ground segment monitoring and control databases
- Operations training plan (OTP)
- Fully validated ground segment, including personnel and procedures, ready for in–orbit operations and exploitation.

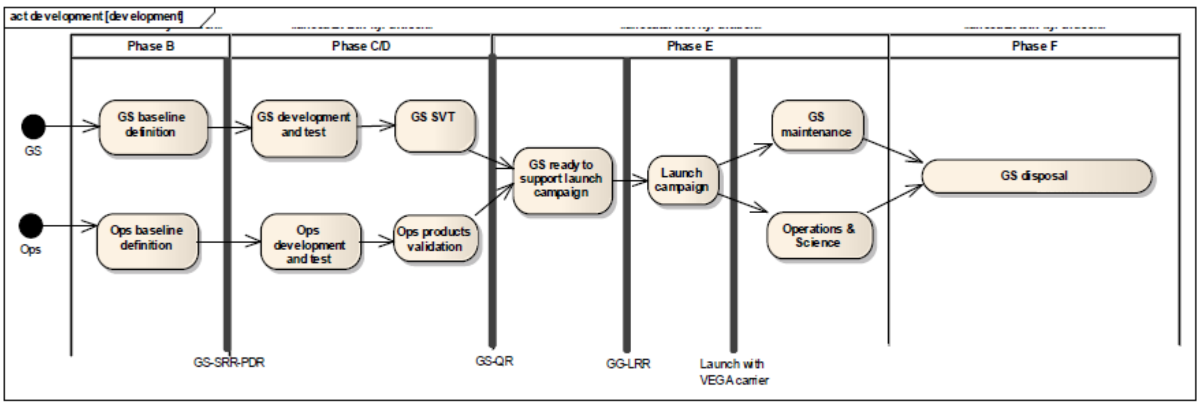

Figure 11-71: Ground segment development plan

11.5 Development plan for the User Segment

The GG "user segment" is constituted by the PI and the associated scientific consortium, as described in §10.3. The tools to be developed include descriptions and format specifications of Level 1 data for scientific use, and data analysis software and codes. These tools will be produced all along the life cycle of the project. Concurrently, the satellite software simulator (an early version of which is already available today) will be employed for generating simulated science data streams, to test and validate the data analysis software.

11.6 Program management

In the frame of GG Phase A2, a program organization has been established which constitutes the model for the program management of the subsequent phases, summarized below. In this organization, Thales Alenia Space Italia (Torino) is the prime contractor, in charge of the system design, and the satellite development and validation until its delivery to the customer. TAS-I Milano is in charge of the Payload development and verification until its delivery to the system. Telespazio is in charge of the Ground Segment development, validation and management, supported by ALTEC for the management of the scientific product related tasks of the ground segment.

Thales Alenia Space Italia possesses an effective management system that is the result of experience gained in more than 30 years of activity in the space domain. This management approach is routinely applied for all space-related products (platforms, payloads, ground systems…), and, among them, in scientific satellite programs. The approach was successfully exercised in the management of both large and small European industrial teams, with interfaces with the scientific communities, the ground segment and the launcher authorities. The TAS management system has obtained the ISO 9001 certification and complies with the ESA ECSS standard policies and management requirements.

To accomplish its task of Prime Contractor, Thales Alenia Space Italia will nominate a Project Team comprising the various expertises, managerial, technical and quality, necessary to carry out the relevant tasks and duties.

TAS-I will be responsible for the management and direction of the Subcontractors, controlling their programmatic and technical performances. It will provide to ASI visibility at any level of its industrial team and will make accessible and available all information generated under the GG Study.

The TAS-I project management will be exercised via:

- a Project Management Plan that defines the management rules and organization in accordance with the ASI requirements;
- standard, well proven techniques for work breakdown structuring, program planning and scheduling, risk management and control, change management, program reporting, documentation and communication exchange;
- implementation of a uniform management approach to the Subcontractors, extending to them the Prime Contractor management requirements;

- the definition of financial and cost management rules in accordance with the applied contract typologies;
- the definition of rules and procedures for contract change management, configuration management, progress and performance evaluation.

11.7 Milestones and meetings plan

The milestones associated to the GG program phases are summarized below.

11.7.1 Phase B

The objective of this phase is to consolidate and freeze the specifications and plans already initiated in Phase A2. Specifically, the Phase B activities will have the following purpose:

- To complete the review and analysis of the GG requirements and the translation of them into subsystem and unit specifications (a task already initiated in Phase A2). Special care will be put in the evaluation of possible reuse of existing and already qualified items, to reduce the cost and increase the reliability;
- To complete the trade-offs, to freeze a detailed GG design baseline compliant with the requirements and to consolidate the performance budgets;
- To establish a detailed design of the GSE needed for the AIV/AIT campaign;
- To complete the management, PA, development, integration, test and qualification plans;
- To initiate, if needed, breadboarding and test activities on critical items;
- To initiate procurement of long-lead items (if any).

The Phase B will be formally closed by the GG Preliminary Design Review (PDR).

11.7.2 Phase C/D

The main objective of Phase C will be to implement the designs, the plans and the specifications generated in Phase B into a fully integrated, qualified and tested GG proto-flight model together with all required supporting hardware and software.

Phase C will be concluded with the GG Critical Design Review (CDR), giving formal authorization to start with unit and subsystems procurement and AIT activities.

Phase D will comprise:

- development and manufacturing of all flight hardware;

- integration and testing of the satellite according to the specified model philosophy;
- execution of the functional and environmental test campaigns;
- production and delivery of the satellite user's manual;
- delivery of the GG proto-flight model.

Phase D will be concluded with the GG Final Acceptance Review (FAR).

11.7.3 Phase E

Phase E comprises the launch campaign and the satellite in-orbit commissioning.

The objectives of the launch campaign include in particular:

- final GG verification at the launch site to check the satellite performance after the shipment to Kourou for launch with VEGA;
- mating operations with the launcher;
- joint operation with the launcher authority, including final countdown.

The formal review that completes the Launch campaign is the Launch Readiness Review (LRR), held a few days before launch. A successful LRR will authorize GG to launch.

The main objectives of the commissioning phase include:

- In orbit check of all GG subsystems and functions;
- configuration of the satellite in its operating modes;
- payload set-up and first calibration;
- start of scientific data acquisition.

11.7.4 Program milestone summary

The main events of GG project until GG launch are shown in Table 11-23, starting from the kick-off of Phase B. The associated bar chart is in Figure 11-68. This preliminary sequence of program events will be consolidated as part of the GG Implementation Proposal.

	Key Events	Epoch from T0
Reviews (Satellite level)	Phase B Kick-Off	T0
	Preliminary Design Review	T0+9m
	Phase C/D Kick-Off	T0+9m
	Critical Design Review	T0+21m
	Test Readiness Review	T0+32m
	Final Acceptance Review	T0+45m
	Launch Readiness Review	T0+48m
	Launch	T0+48m
Reviews (GS level)	Ground Segment Preliminary Design Review	T0+9m
	Ground Segment Critical Design Review	T0+22m
	Ground Segment Operations Qualification Review	T0+40m

Model	Main Goals	Epoch from T0
ATB	ATB Availability for GG	T0+24m
	ATB Ready for SW Test	T0+27m
	ATB Test Completion	T0+48m
FM	FM/PFM Equipment Procurement Start	T0+21m
	Results of development models availability	T0+30m
	GSE for system activities availability	T0+30m
	FM/PFM Equipment Procurement Completion	T0+32m
	Flight PGB Availability at System Level	**T0+35m**
	S/L Ready for Environmental Test	T0+39m
	S/L Ready for Launch Campaign	T0+45m
	S/L Ready for Launch	**T0+48m**

Table 11-23: GG program milestones

12. REFERENCES

1. Connecting Quarks with the Cosmos: Eleven Science Questions for the New Century, Board on Physics and Astronomy, The National Academic Press, 2003

2. Report from the Dark Energy Task Force, available online at http://www.nsf.gov/mps/ast/aaac/dark_energy_task_force/report/detf_final_report.pdf, 2006

3. D. Bramanti et al.: Galileo and the Universality of Free Fall, in STEP Simposium, ESA WPP-115, 319, 1993

4. F. Cajori: Sir Isaac Newton's Mathematical Principles of Natural Philosophy, (University of California, Berkeley) 1934

5. A. Einstein: Über das Relativitätsprinzip und die aus demselben gezogene Folgerungen. Jahrb. Radioaktiv 4, 411, 1907

6. C. M. Will: The Confrontation Between General Relativity and Experiment: Living Reviews in Relativity, vol. 9, p. 3. http://relativity.livingreviews.org/Articles/lrr-2006-3/ 2006

7. Bertotti B., Iess L., Tortora P.: A test of general relativity using radio links with the Cassini spacecraft, Nature, 425, pp.374-376, 2003

8. T. Damour., Class. Quantum Grav.: 13 A33-A41, 1996

9. T. Damour, F. Piazza, G. Veneziano: Phys. Rev. D 66, 046007, 2002

10. Eötvös, R.V., Pekar, D., Fekete, E.: Beitrage zum gesetze der proportionalität von trägheit und gravität. Ann. Phys. 68, 11-66, 1922

11. Roll, P.G., Krotkov, R., Dicke, R.H.: The equivalence of inertial and passive gravitational mass. Ann. Phys. 26, 442-517, 1964

12. Braginsky, V.B., Panov, V.I.: Verification of the equivalence of inertial and gravitational mass. Sov. Phys. JEPT 34, 463-466, 1972

13. Su, Y., Heckel, B.R., Adelberger, E.G., Gundlach, J.H., Harris, M., Smith, G.L., Swanson, H.E.: New tests of the universality of free fall. Phys. Rev. D Part. Fields 50, 3614-3636, 1994

14. Baeßler, S., Heckel, B.R., Adelberger, E.G., Gundlach, J.H., Schimidt, U., Swanson, H.E.: Improved Test of the Equivalence Principle for Gravitational Self-Energy. Phys. Rev. Lett. 83, 3585, 1999

15. Schlamminger S., Choi K.-Y., Wagner T. A., Gundlach , J.H. and Adelberger E. G.: Test of the Equivalence Principle Using a Rotating Torsion Balance. Phys. Rev. Lett. 100, 041101, 2008

16. Carusotto, S., Cavasinni, V., Mordacci, A., Perrone, F., Polacco, E., Iacopini, E., Stefanini, G.: g Universality with a Galileo Type Experiment. Phys. Rev. Lett. 69, 1722, 1992

17. Dimopoulos, S., Graham, P.W., Hogan, J.M., Kasevich,M.A.: Testing General Relativitá with Atom Interferometry. Phys. Rev. Lett. 98, 111102, 2007

18. Peters, A., Chung, K.Y., Chu, S.: Measurement of gravitational acceleration by dropping atoms. Nature 400, 849, 1999

19. V. Iafolla, E.C. Lorenzini, V. Milyukov and S. Nozzoli, Review of Scientific Instruments 69, 4146, 1998

20. R.D. Reasenberg: A Sounding Racket to Test the WEP, Presented at Q2C3 International Workshop, Airlie Center, Virginia USA, 2008 available online at http://funphysics.jpl.nasa.gov/Q2C3/program.html

21. MICROSCOPE Website http://www.onera.fr/dmph/accelerometre/index.html

22. "Galileo Galilei" (GG) Website http://eotvos.dm.unipi.it See in particular: "GG Phase A Report (ASI 2000)" availbale online at http://eotvos.dm.unipi.it/ggweb/phaseA/

23. STEP Website http://einstein.stanford.edu/STEP/step2.html

24. Fischbach, E., Krause, D.E., Talmadge, C., Tadic, D.: Higher order weak interactions and the equivalence principle. Phys. Rev. D Part. Fields 52, 5417, 1995

25. Damour, T., Polyakov, A.M.: Runaway Dilaton and Equivalence Principle Violations. Gen. Relativ. Gravit. 26, 1171, 1994

26. Williams, J.G., Turyshev, S.G., Boggs, D.H.: Progress in Lunar Laser Ranging Tests of Relativistic Gravity. Phys. Rev. Lett. 93, 261101. 2004

27. Murphy, T.W. Jr., Michelson, E.L., Orin, A.E., Adelberger, E.G., Hoyle, C.D., Swanson, H.E., Stubbs, C.W., Battat, J.E.: APOLLO: Next-Generation Lunar Laser Ranging. Int. J. Mod. Phys. D 16(12a), 2127, 2007

28. A.M. Nobili, G.L. Comandi, D. Bramanti, Suresh Doravari, D.M. Lucchesi and F. Maccarrone: Limitations to testing the equivalence principle with satellite laser ranging, Gen. Rel. Grav. 40, 1533-1554, 2008 availabel online at http://eotvos.dm.unipi.it/documents/generalpapers/nobili.pdf

29. A.M. Nobili: Precise gravitation measurements on Earth and in space: Tests of the Equivalence Principle in Proceedings of the International School of Physics "Enrico Fermi" Course CXLVI Recent Advances in Metrology and Fundamental Constants, Eds. T.J. Quinn, S. Leschiutta and P. Tavella, IOS Press, Amsterdam, pp. 609-652, 2001, available online at http://eotvos.dm.unipi.it/murst/varenna2000/nobili2.pdf

30. Dale K. Gill, Saps Buchman: Evidence for Patch Effect Forces On the Gravity Probe B Gyroscopes, APS meeting 2007, available online at http://meetings.aps.org/Meeting/APR07/Event/65181

31. Den Hartog, J.P.: 1985, Mechanical Vibrations (Dover Publications, Inc., New York, first published 1934)

32. P.K. Chapman and A.J. Hanson: An Eötvös Experiment in Earth Orbit, in Proceedings of the Conference on Experimental Tests of Gravitational Theories, R.W. Davies Editor, Cal. Tech. JPL TM no. 33-499, 228, 1970

33. A.M. Nobili, G. Catastini, A. di Virgilio, V. Iafolla, F. Fuligni: Noise attenuators for gravity experiments in space, Physics Letters A, 160, 45-54, 1991

34. G. Catastini, D. Bramanti, A.M. Nobili, F. Fuligni, V. Iafolla: Pico Gravity Box (PGB): Efficiency of a passive noise attenuator in space, ESA Journal, 16, 401-417, 1992

35. A.M. Nobili, D. Bramanti, E. Polacco, G. Catastini, A. Anselmi, S. Portigliotti, A. Lenti, P. di Giamberardino, S. Monaco, R. Ronchini: Evaluation of a proposed test of the weak equivalence principle using earth-orbiting bodies

in high-speed co-rotation: re-establishing the physical bases, Classical and Quantum Gravity, 16, 1463-1470, 1999

36. G. Vannaroni et al.: Plasma effects on the GG satellite, in preparation 2009, available online at http://eotvos.dm.unipi.it/documents/specificissues/plasma effects on GG.pdf

37. A. M. Nobili, D. Bramanti, G.L. Comandi, R. Toncelli, E. Polacco, G. Catastini: Radiometer effect in space missions to test the Equivalence Principle, Physical Review D, Rapid Communications, 63, 101101(R), 2001

38. A. M. Nobili, D. Bramanti, G.L. Comandi, R. Toncelli, E. Polacco: Radiometer effect in the Microscope space mission, New Astronomy, 7, 521-529, 2002

39. A. Anselmi, G. Catastini: Design of the GG satellite, Physics Letters A, 318, Pages 205-212, 2003

40. A. M. Nobili, D. Bramanti, G. L. Comandi, R. Toncelli, E. Polacco, M. L. Chiofalo: Galileo Galilei-GG: design, requirements, error budget and significance of the ground prototype, Physics Letters A, 318, 172-183, 2003

41. E. Fischbach, C. L. Talmadge: The Search for Non-Newtonian Gravity; Springer- Verlag, New York, 1998.

42. G. L. Comandi, M. L. Chiofalo, R. Toncelli, D. Bramanti, E. Polacco and A. M. Nobili: Dynamical Response of the Galileo Galilei rotor for a Ground test of the Equivalence Principle: theory, simulation and experiment. Part I: the normal modes, Review of Scientific Instruments, 77, 034501(1-15), 2006

43. G. L. Comandi, R. Toncelli, M. L. Chiofalo, D. Bramanti and A. M. Nobili: Dynamical Response of the Galileo Galilei rotor for a Ground test of the Equivalence Principle: theory, simulation and experiment. Part II: the rejection behavior, Review of Scientific Instruments, 77, 034502(1-10), 2006

13. ACRONYMS AND ABBREVIATIONS

AD	Applicable Document
AIV	Assembly Integration and Test
AOCS	Attitude and Control Subsystem
ASI	Agenzia Spaziale Italiana
BCR	Battery Charge Regulator
BDR	Battery Discharge Regulator
CCSDS	Consultative Committee for Space Data Systems
CDMU	Command and Data Management Unit
CFRP	Carbon Fiber Reinforced Plastics
CGPS	Cold Gas Propulsion System
CMRR	Common Mode Rejection Ratio
CNES	Centre National d'Etudes Spatiales
COG	Center of Gravity
COM	Center of Mass
CPE	Control and Processing Electronics
CPU	Central Processing Unit
DFACS	Drag Free and Attitude Control Subsystem
DFM	Drag Free Mode
DoD	Depth of Discharge
E2E	End To End Simulator
ECE	Experiment Control Electronics
ECSS	European Cooperation for Space Standardization
EGSE	Electrical Ground Support Equipment
EOL	End Of Life
EP	Equivalence Principle
EPS	Electrical Power System
EQM	Engineering Qualification Model
ESA	European Space Agency
FEEP	Field Emission Electric Propulsion
FEM	Finite Element Model
FCA	FEEP Cluster Assembly
FCL	Fold-back Current Limiter
FOS	Factor of Safety
FOV	Field of View
G/S	Ground Station
GG	Galileo Galilei (Satellite)
GGG	Galileo Galilei on the Ground (Payload laboratory prototype experiment)
GMM	Geometrical Mathematical Model
GOCE	Gravity and Ocean Circulation Explorer
GTR	General Theory of Relativity
HK	Housekeeping
I/F	Interface
INFN	Istituto Nazionale di Fisica Nucleare
IRF	Inertial Reference Frame
ISV	Independent Software Validation
ITO	Indium Tin Oxide
JERF	J2000 Equatorial Reference Frame
LCL	Latching Current Limiter
LEOP	Launch and Early Orbit Phase
LGA	Low Gain Antenna
LL	Limit Loads
MLI	Multi Layer Insulation
MOI	Moment Of Inertia
MRD	Mission Requirement Document

OBCP	On Board Control Procedure
OBDH	On Board Data Handling
P/L	Payload
PA	Product Assurance
PCDU	Power Control and Distribution Unit
PCE	Payload Control Electronics
PCU	Power Control Unit
PGB	Pico Gravity Box
POI	Product of Inertia
PSLV	Polar Satellite Launch Vehicle
PPRF	Payload Physical Reference Frame
QL	Qualification Loads
RD	Reference Document
RFDN	Radiofrequency Distribution Network
SA	Solar Array
SD	Standard Document
S/C	Spacecraft
SM	Standard Model (of particle physics)
STS	System Technical Specification
SEL	Single Event Latch-Up
SEU	Single Event Upset
SPF	Single Point Failure
SPRF	Satellite Physical Reference Frame
S^3R	Sequential Switching Shunt Regulator
S/S	Subsystem
STB	Software Test Bed
SVF	Software Validation Facility
TAS-I	Thales Alenia Space Italia
TBC	To Be Checked
TBD	To Be Defined
TC	Telecommand
TCS	Thermal Control System
TM	Telemetry
TM	Test Mass
TMM	Thermal Mathematical Model
TRL	Technological Readiness Level